Electron Correlation Treatment via Many-Body Expansions

Dissertation zur Erlangung des Grades
„Doktor der Naturwissenschaften“
im Promotionsfach Chemie

am Fachbereich Chemie, Pharmazie, Geographie und Geowissenschaften der
Johannes Gutenberg-Universität Mainz

von

Jonas Greiner

geb. in Dannenberg (Elbe)

Mainz 2024

1. Gutachter: [redacted]

2. Gutachter: [redacted]

3. Gutachter: [redacted]

Tag der mündlichen Prüfung: 22.11.2024

Die vorliegende Arbeit wurde im Zeitraum vom 15. Oktober 2020 bis zum 1. August 2024 am Institut für Physikalische Chemie der Johannes Gutenberg-Universität Mainz im Arbeitskreis von [redacted] erstellt.

Acknowledgments

I would like to express my sincere gratitude to my supervisor, [redacted], for his invaluable guidance, support, and encouragement throughout my PhD journey. His expertise and enthusiasm have been instrumental in shaping my research and academic growth. I am deeply indebted to his mentorship and unwavering belief in my abilities. I am particularly grateful for his generous support in enabling my participation in two summer schools, attendance at several conferences, and international research collaborations, which significantly enriched my doctoral studies.

My deep appreciation goes to [redacted] for his vital contributions to my PhD research. Despite the geographical distance, his support provided essential guidance and perspective. His dedication and availability were instrumental in overcoming challenges and advancing my work. I am grateful for the opportunity to discuss our research during a visit of his group in Lyngby.

Heartfelt thanks are due to [redacted], [redacted], and [redacted] for the fruitful collaboration on the MBE-CASSCF project. The opportunity to visit Pisa and work closely with them was invaluable. Their expertise and support have been instrumental in the success of our research.

I would like to express my sincere thanks to [redacted] for kindly agreeing to review my PhD thesis.

I would like to thank [redacted] for being a wonderful office mate during the early stages of my PhD. While your absence during the final stretch was felt, I am grateful for the positive and supportive environment you helped to create. Additionally, I want to express my sincere gratitude to [redacted] for always having an open door and a listening ear during those long evenings. Your insights and support were crucial. Furthermore, the friendly and supportive atmosphere in office [redacted] provided a much-needed balance and contributed significantly to a positive work environment.

I am deeply grateful to the entire group in Mainz for their support, encouragement, and fruitful discussions that have enriched my PhD experience. The collaborative spirit and shared expertise within the group created a stimulating and productive environment.

Finally, I would like to express my deepest gratitude to my family and to my girlfriend for their unwavering love, support, and encouragement throughout my PhD journey. Their belief in me has been a vital source of strength, and I am eternally grateful for their sacrifices.

Contents

Acronyms

1-RDM	1-body reduced density matrix
2-RDM	2-body reduced density matrix
AFQMC	Auxiliary-field quantum Monte Carlo
AM	Arithmetic mean
AO	Atomic orbital
ASCI	Adaptive sampling configuration interaction
ASCI-SCF	Adaptive sampling configuration interaction self-consistent field
AS-FCIQMC	Adaptive-shift full configuration interaction quantum Monte Carlo
CAD-FCIQMC	Cluster-analysis-driven full configuration interaction quantum Monte Carlo
CAS	Complete active space
CASCC	Complete active space coupled-cluster
CASCI	Complete active space configuration interaction
CASPT2	Complete active space second-order perturbation theory
CASSCF	Complete active space self-consistent field
CC	Coupled-cluster
CCSD	Coupled-cluster with single and double excitations
CCSD(T)	Coupled-Cluster with single, double, and perturbative triple excitations
CCSDT	Coupled-Cluster with single, double, and triple excitations
CCSDT(Q)	Coupled-Cluster with single, double, triple, and perturbative quadruple excitations
CCSDTQ	Coupled-Cluster with single, double, triple, and perturbative quadruple excitations
CI	Configuration interaction
CIPSI	Perturbatively selected configuration interaction
DMRG	Density matrix renormalization group
DMRGSCF	Density matrix renormalization group self-consistent field
ER	Edmiston-Ruedenberg
FB	Foster-Boys
FCCR	Full coupled-cluster reduction
FCI	Full configuration interaction

FCIQMC	Full configuration interaction quantum Monte Carlo
FCIQMC-SCF	Full configuration interaction quantum Monte Carlo self-consistent field
GM	Geometric mean
HCI	Heat-bath configuration interaction
HCISCF	Heat-bath configuration interaction self-consistent field
HF	Hartree-Fock
iCI	Iterative configuration interaction with selection
iCISCF	Iterative configuration interaction-based multiconfigurational self-consistent field
iFCI	Incremental full configuration interaction
i-FCIQMC	Full configuration interaction quantum Monte Carlo with the initiator approximation
LMO	Localized molecular orbital
MBE	Many-body expansion
MBE-CASCI	Many-body expanded complete active space configuration interaction
MBE-CASSCF	Many-body expanded complete active space self-consistent field
MBE-CC	Many-body expanded coupled-cluster
MBE-CCSD	Many-body expanded coupled-cluster with single and double excitations
MBE-CCSD(T)	Many-body expanded coupled-cluster with single, double excitations, and perturbative triple excitations
MBE-CCSDT	Many-body expanded coupled-cluster with single, double excitations, and triple excitations
MBE-CCSDT(Q)	Many-body expanded coupled-cluster with single, double, triple, and perturbative quadruple excitations
MBE-CCSDTQ	Many-body expanded coupled-cluster with single, double, triple, and quadruple excitations
MBE-FCI	Many-body expanded full configuration interaction
MO	Molecular orbital
MPS	Matrix product state
NO	Natural orbital
PM	Pipek-Mezey
QIT	Quantum information theory
QMC	Quantum Monte Carlo

RDM	Reduced density matrix
RHF	Restricted Hartree-Fock
ROHF	Restricted open-shell Hartree-Fock
SCI	Selected configuration interaction
SHCI	Semistochastic Heat-bath configuration interaction
UHF	Unrestricted Hartree-Fock
UNO	Unrestricted natural orbital
v2RDM	Variational 2-body reduced density matrix method

1 Introduction

The desire of the human mind to uncover the truth behind our reality and to comprehend the physical laws that govern it is unparalleled and has long been a driver for technological advancement. Unfortunately, the "truth … is much too complicated to allow anything but approximations."[1] No statement could more accurately express the challenges faced by any attempt to explain the chemical phenomena that make up our world than this quote proclaimed by John von Neumann in 1947. Already during the dawn of quantum mechanics in the 1920s, it was clear to Paul A. M. Dirac and many of his contemporaries that "the underlying physical laws necessary for the mathematical theory of a large part of physics and the whole of chemistry are … completely known, and the difficulty is only that the exact application of these laws leads to equations much too complicated to be soluble."[2] Consequently, the primary goal of theoretical chemistry for the past 100 years has been to find suitable approximations to the complex equations envisioned in the early 20th century. The need for these approximations has uncovered that "chemical questions are problems in applied mathematics"[3] and as such, the rise of the computer has undoubtedly revolutionized how we think about these problems and how they are solved. As correctly recognized by Robert S. Mulliken in his Nobel Prize acceptance speech in 1966, "the era of computing chemists, when hundreds if not thousands of chemists will go to the computing machine instead of the laboratory, for increasingly many facets of chemical information, is … at hand. There is only one obstacle, namely, that someone must pay for the computing time."[4] Mulliken correctly emphasizes how it is not only necessary to find accurate but also computationally efficient approximations of exact theory and his statement is as relevant as ever in light of energy conservation efforts during the transition towards renewable energy sources.[5,6]

At the very foundation of the majority of quantum chemical methods lies the solution of the electronic Schrödinger equation which aims to describe the complex movements of the electrons within the static potential of the nuclei. Solving the electronic Schrödinger equation will not only yield the electronic energy but will by extension also provide access to ionization potentials, electron affinities, excitation energies, inter- and intramolecular forces, force constants, dipole moments, polarizabilities, magnetizabilities, nuclear magnetic shielding tensors, and many other quantities of chemical interest.[7,8] These properties enable the calculation of bond energies, dissociation energies, thermodynamic quantities such as enthalpies of formation, equilibrium and transition state structures, potential barriers for internal rotation and for chemical reactions, frequencies and intensities of spectroscopic transitions, and many other properties which can be directly compared to experiments.[7–9] Unsurprisingly, the motivation of the theoretical chemistry community to find widely applicable and efficient solutions to the electronic Schrödinger equation is immense.[10] The exact solution, full configuration interaction (FCI), is intractable for all but the smallest of molecular systems.[11] For this reason, quantum chemistry offers a diverse toolbox of approximations to the electronic Schrödinger equation which cater towards a variety of chemical applications while attempting to strike a balance between accuracy and computational efficiency.[12,13] These traditional quantum chemical methods can be roughly divided into two categories: the mean-field, effective one-body methods such as Hartree-Fock (HF) and Kohn-Sham density functional theory and the many-body methods which encompass the configuration interaction (CI), many-body perturbation theory, coupled-cluster (CC),

and complete active space self-consistent field (CASSCF) methods, among others.[12,14,15] These approaches generally excel in their specific domain but do not offer a comprehensive and universal solution for the broad range of relevant chemical systems.

On the high-accuracy end of the spectrum of quantum chemical methods, a group of approximations has recently gained popularity by directly targeting the exact solution of the electronic Schrödinger equation. These approaches can be referred to as approximate FCI methods and generally attempt to preserve the underlying, desirable features of the FCI solution at a fraction of its cost.[16–24] This is often achieved, with varying degrees of success, by employing numerical techniques that are frequently unconventional in the context of quantum chemistry, to exploit sparsity in the FCI solution.[25] The appeal of these methods, a property shared with the FCI method, is rooted in the wide variety of molecular systems that they can generally be applied to. Additionally, these methods can often be systematically improved such that they can approach the exact solution and thus obtain highly accurate results.[25,26] The theoretical background for relevant traditional quantum chemical methods and selected approximate FCI methods will be given in Chapter 2 of this thesis.

One group of FCI approximations, the incremental methods, involve the orbital-based many-body expansion (MBE) of the electron correlation energy. The origins of this method can be traced to the *n*th-order Bethe-Goldstone equations by Robert K. Nesbet.[27–29] Hermann Stoll applied the orbital-based MBE to the CC correlation energy of solids in what he called the incremental correlation scheme.[30–32] This method was extended by Michael Dolg and co-workers to the treatment of molecular systems.[33–36] Klaus Ruedenberg and co-workers[37,38] first applied the MBE to the FCI correlation energy in combination with their correlation energy extrapolation by intrinsic scaling approach.[39] Two different flavors of approximate FCI theory through the lens of orbital-based MBEs were later developed: Many-body expanded full configuration interaction (MBE-FCI)[23,40–43] by Janus J. Eriksen and Jürgen Gauss and incremental full configuration interaction (iFCI)[24,44,45] by Paul Zimmerman. Since then, the MBE has also been applied to tensor-product-based wave functions on the basis of orbital clusters[46] and in the context of quantum computing.[47] In addition, a plethora of molecular fragment-based MBE varieties exist which attempt to describe intermolecular interactions in condensed phases.[48–106] The MBE-FCI method, which will be the focus of this thesis, offers a compelling combination of features, including the ability to systematically improve its results through longer expansions and the possibility to perform calculations in an embarrassingly parallel fashion. Obtaining an MBE-FCI result involves numerous small, independent calculations which can easily be distributed among many computational cores while requiring only minimal communication. This property of a quantum chemical method is particularly relevant considering the predicted plateauing of Moore's law, the doubling of the number of transistors in state-of-the-art computer chips every few years, in the very near future.[107–109] The structure and inner workings of PyMBE,[110] a massively parallel implementation of MBE-FCI, will be presented in Chapter 3.

The incremental methods are not limited to the calculation of energies. In principle, the MBE can be applied to any electronic property. Dipole moments, transition dipole moments, and excitation energies have been calculated on the basis of MBE-FCI.[43,111,112] These methods can also be applied to wave function properties such as the 1- and 2-electron reduced density matrices (1- and 2-RDMs) or the generalized Fock matrix that are needed to construct orbital gradients in the CASSCF method.[113] As such, incremental methods can be considered as a drop-in replacement for the complete active space configuration interaction (CASCI) solver in two-step CASSCF algorithms. A first attempt at exploiting a truncated MBE for this purpose was proposed by Zimmerman and Rask[113] and was later extended to analytic nuclear gradients.[114] In Chapter 4 of this thesis, a novel approach for utilizing MBE-FCI to enable approximate CASSCF calculations with large active spaces is presented. This method, many-body expanded complete active space self-consistent field (MBE-CASSCF), is first

compared to conventional CASSCF calculations through applications on several polyacene systems and is then applied to the triplet-quintet spin gap of the iron(II) porphyrin system employing active spaces as large as 50 electrons in 50 orbitals.

Successfully applying quantum chemical methods does not only require a certain degree of insight into the electronic structure of the system at hand but also some experience with the methods themselves. Without this experience, judging the reliability and assessing the errors of a computed result becomes a challenging task. This is particularly true for active space methods such as CASCI or CASSCF which are the *de facto* standard for multireference systems.[115,116] These challenging systems are ubiquitous in transition metal chemistry and an accurate description is needed for many applications including catalysis, bioinorganic chemistry, material science, and medicine.[117] Additionally, both the description of electronically excited states and bond-breaking processes often require the use of multireference methods.[14] While generalized MBE-FCI can in principle be applied to arbitrary states of a wide range of chemical systems, efficient convergence of the MBE is often highly dependent on choosing a so-called reference space.[42] In Chapter 5, an automatic identification scheme for reference spaces in MBE-FCI is presented. The results from this scheme are then applied to and compared with the active space selection problem which is closely related. Automatic reference space detection significantly increases the accessibility of MBE-FCI for inexperienced users as the expansion is automatically restarted with an appropriate reference space whenever difficult convergence is observed.

The MBE is not limited to the FCI problem but can also be used to approximate traditional quantum chemistry methods such as CC theory. An orbital-based expansion will generally not be competitive with conventional CC methods due to their polynomial scaling compared to the prohibitive scaling of MBE-based methods with respect to the number of expansion objects. This issue can be rectified by accumulating orbitals into orbital clusters and using these as expansion objects.[46] Chapter 6 proposes an orbital clustering scheme which can then be applied to both FCI and CC expansions to enable calculations on larger systems and basis sets. This development significantly extends the scale of systems that can be efficiently treated with MBE-based methods.

Whenever approximations of exact theory are developed, the introduced error must be estimated and controlled. While some approximate FCI methods do propose error estimation techniques,[118–123] the accuracy of MBE-FCI can only be assessed through its convergence profile. This information is not known before the expansion is started, and it is therefore difficult to predict at what point the expansion should be terminated. In Chapter 7, a dynamic screening and error estimation technique based on empirical relationships and importance sampling[124,125] is developed. Whenever this technique is employed, the MBE can be converged up to a given maximum error bound. The ability to systematically improve the error bounds of an approximate method is highly desirable because chemical applications have different accuracy requirements and employing additional, potentially unnecessary work can be avoided. Additionally, controlling the error through a single input parameter increases accessibility for inexperienced users.

The application of quantum chemical methods to symmetric molecules can often lead to a significant reduction in computational effort whenever the applied algorithms appropriately exploit point-group symmetry.[126–134] When employing localized orbitals, which are often used in approximate FCI methods to introduce sparsity, symmetry is generally not exploited and much potential room for optimization is not explored. Chapter 8 introduces a novel algorithm for the symmetrization of localized orbitals which is then used to reduce the number of individual calculations and therefore significantly accelerate MBE-FCI calculations of highly symmetric molecules.

A recent blind challenge on the frozen-core ground state electronic energy of benzene in a cc-pVDZ basis set has showcased results from different categories of approximate FCI methods and has also exemplified the wide range of results that can be expected from these methods.[135] In this benchmark, the MBE-FCI result agrees with other highly accurate approximate FCI methods and falls in the middle of the projected energy range. Unfortunately, MBE-FCI is also by far the most computationally expensive method benchmarked in this study, requiring a staggering 1.7 million core hours for the benzene calculation. This observation exemplifies the need to improve performance of the MBE-FCI method to bring costs more in line with other approximate FCI approaches. The combined improvements to the MBE-FCI method introduced in this thesis enable the calculation of the ground state electronic energy of benzene in a cc-pVTZ basis set which is presented in Chapter 9 and brings the original result in the blind challenge much closer to the exact non-relativistic electronic energy.

Reliably reaching chemical accuracy, which is defined as 1 kcal/mol, has been a long-standing goal in the theoretical chemistry community.[136–140] We have now progressed to a point where accuracies beyond chemical accuracy can be routinely attained for small- to medium-sized systems. The present thesis presents several improvements to the original MBE-FCI method which increase its applicability, accessibility, reliability, and overall performance. This progress enables the massively parallel calculation of electronic energies for a wide range of chemical systems in the sub-millihartree accuracy range while requiring minimal experience and input from the user. These highly accurate calculations of small systems are important both for benchmarking purposes[136,141–174] and for the calculation of thermochemical quantities which have applications in atmospheric chemistry and astrochemistry.[9,140,175–179] Complementary to the foregoing, the development of the MBE-CASSCF method enables the treatment of multireference systems with large active spaces which has numerous applications in transition metal chemistry and for spectroscopic methods which require the treatment of electronically excited states. In Chapter 10, these developments and the corresponding results will be summarized, followed by a discussion of implications and future directions.

2 Theory

2.1 The Quantum Many-Body Problem

The greatest challenge in quantum chemistry is the accurate description of numerous interacting quantum particles such as the electrons and nuclei of a molecular system. The state of a quantum many-body system is described through a wave function $|\Psi(\mathbf{r}, t)\rangle$ which is a complex mathematical object that encodes the position of all particles $\mathbf{r}$ and describes the state of the system as it propagates in time t. In order to relate results from quantum chemical calculations to experiments, the expectation values of so-called observables can be directly compared to experimental measurements. Many chemical phenomena can be described using stationary states for which all observables are constant in time. In quantum mechanics, observables are represented through Hermitian operators, one example of which is the Hamilton operator $\hat{H}$ with its eigenvalue E, the energy. Both the wave function and the energy can be determined by solving the corresponding eigenvalue equation

$$\hat{H}\,|\Psi(\mathbf{r})\rangle = E\,|\Psi(\mathbf{r})\rangle\,, \tag{2.1}$$

the time-independent Schrödinger equation.[180] Solving the time-independent Schrödinger equation will not only yield the energy of the system but will also grant access to the eigenvalues of other observables through their respective expectation value. The Hamilton operator consists of two parts, the kinetic energy operator $\hat{T}$ and the potential energy operator $\hat{V}$. In the absence of magnetic fields and relativistic effects, the potential energy operator of a free molecule solely consists of the Coulomb interactions between the different particles. The molecular Hamiltonian in atomic units[181]

$$\begin{aligned}\hat{H} &= \hat{T}_\mathrm{n} + \hat{T}_\mathrm{e} + \hat{V}_\mathrm{nn} + \hat{V}_\mathrm{ne} + \hat{V}_\mathrm{ee} \\ &= -\sum_{A=1}^{N_A} \frac{1}{2M_A}\nabla_A^2 - \frac{1}{2}\sum_{\alpha=1}^{N_\alpha}\nabla_\alpha^2 + \sum_{A<B}^{N_A}\frac{Z_A Z_B}{r_{AB}} - \sum_{\alpha=1}^{N_\alpha}\sum_{A=1}^{N_A}\frac{Z_A}{r_{A\alpha}} + \sum_{\alpha<\beta}^{N_\alpha}\frac{1}{r_{\alpha\beta}}\end{aligned} \tag{2.2}$$

describes the kinetic energies and Coulomb interactions of all N_A nuclei and n_α electrons. The nuclear kinetic energy operator depends on the nuclear masses M_A and the nuclear Laplace operators ∇_A^2. The electronic kinetic energy operator involves the electronic Laplace operators ∇_α^2. The Coulomb interactions can be calculated from the atomic numbers Z_A and the distances between the particles r_{AB}, $r_{A\alpha}$, and $r_{\alpha\beta}$. A very common and effective simplification in the field of quantum chemistry is the Born-Oppenheimer approximation[182] which allows for a separation of the nuclear and electronic coordinates. The wave function is replaced by a product of the nuclear and electronic wave functions $\Psi_\mathrm{n}(\mathbf{R})$ and $\Psi_\mathrm{e}(\mathbf{r};\mathbf{R})$ of which only the latter depends on the electronic coordinates $\mathbf{r}$. This approximation originates from the much larger mass of the nuclei compared to the electrons such that the nuclear kinetic energy operator can be neglected for the solution of the electronic Schrödinger equation[182]

$$\hat{H}_\mathrm{e}\,|\Psi_\mathrm{e}(\mathbf{r};\mathbf{R})\rangle = E_\mathrm{e}(\mathbf{R})\,|\Psi_\mathrm{e}(\mathbf{r};\mathbf{R})\rangle \tag{2.3}$$

for a given set of nuclear coordinates $\mathbf{R}$. The electronic Hamiltonian

$$\hat{H}_\mathrm{e} = \hat{T}_\mathrm{e} + \hat{V}_\mathrm{ne} + \hat{V}_\mathrm{ee} \tag{2.4}$$

only includes the terms from Equation (2.2) that explicitly depend on the electronic coordinates. After the solution of the electronic Schrödinger equation, the electronic energy can be added to the nuclear Coulomb interaction $\hat{V}_{\mathrm{nn}}$ to form the Born-Oppenheimer potential $\hat{V}_{\mathrm{BO}}$ which is necessary to solve the Schrödinger equation for the full molecular system and determine the nuclear wave function.[182] The remainder of this thesis will address solutions to the electronic Schrödinger equation and hence the index "e" will be dropped in the upcoming chapters and the Hamiltonian, wave function, and energy will refer to the respective electronic quantity.

A functional *ansatz* for the electronic wave function is required to solve the electronic Schrödinger equation. An important observable that significantly affects the behavior of quantum particles is their spin which can be described through the spin operator $\hat{S}^2$ and the spin projection operator along the z-axis $\hat{S}_z$. Because these spin operators commute with the electronic Hamilton operator, the electronic wave function is also required to be an eigenfunction of these operators:[183]

$$\hat{S}^2 \left|\Psi\right\rangle = S(S+1) \left|\Psi\right\rangle \tag{2.5}$$

$$\hat{S}_z \left|\Psi\right\rangle = M_S \left|\Psi\right\rangle . \tag{2.6}$$

The respective eigenvalues S and M_S are the spin and spin magnetic quantum numbers which can be used to classify different eigenfunctions of the Hamilton operator. Single electrons can be described using spin orbitals

$$\left|\varphi(\boldsymbol{\tau})\right\rangle = \left|\phi(\mathbf{r})\right\rangle \cdot \left|s(\sigma)\right\rangle \tag{2.7}$$

which are formed as a product of spatial orbitals ϕ and spin functions s. The variable $\boldsymbol{\tau}$ is a combination of both the spatial variable $\mathbf{r}$ and the spin variable σ. The spin function can take two possible values: $\left|\alpha(\sigma)\right\rangle$ and $\left|\beta(\sigma)\right\rangle$. These are eigenfunctions to the single electron $\hat{s}^2$ operator with quantum number $s = 1/2$ and to the single electron $\hat{s}_z$ operator with quantum numbers $m_S = 1/2$ and $m_S = -1/2$, respectively. The set of spin orbitals $\{\varphi_p\}$ are required to form a basis, meaning that every single-electron wave function in the function space can be written as a linear combination of these orbitals. Consequently, when treating many-electron systems, every N-electron wave function can be written as a linear combination of all possible products combining N elements from the set of spin orbitals. Special care must be taken when this product is constructed for electrons since these particles have a half-integer spin quantum number and are therefore considered fermions. For fermions, the wave function[184,185]

- has to be antisymmetric under the interchange of any two electrons, and
- has to vanish whenever two electrons occupy the same one-electron wave function.

Both properties are fulfilled for an antisymmetric product which can also be written as a Slater determinant[186]

$$\left|\Phi\right\rangle = \frac{1}{\sqrt{N!}} \begin{vmatrix} \varphi_1(\boldsymbol{\tau}_1) & \varphi_2(\boldsymbol{\tau}_1) & \cdots & \varphi_N(\boldsymbol{\tau}_1) \\ \varphi_1(\boldsymbol{\tau}_2) & \varphi_2(\boldsymbol{\tau}_2) & \cdots & \varphi_N(\boldsymbol{\tau}_2) \\ \vdots & \vdots & \ddots & \vdots \\ \varphi_1(\boldsymbol{\tau}_N) & \varphi_2(\boldsymbol{\tau}_N) & \cdots & \varphi_N(\boldsymbol{\tau}_N) \end{vmatrix} . \tag{2.8}$$

Any fermionic wave function

$$\left|\Psi\right\rangle = \sum_{I}^{N_{\mathrm{det}}} c_I \left|\Phi_I\right\rangle \tag{2.9}$$

in the function space provided by the set of spatial orbitals can be written as a linear combination of all possible Slater determinants.[187] The index I describes all combinations of N spin orbitals that can be used to construct determinants. Slater determinants are by definition eigenfunctions of the spin

projection operator $\hat{S}_z$ but will not necessarily be eigenfunctions of the spin operator $\hat{S}^2$. Alternatively, the wave function can also be constructed as a linear combination of spin eigenfunctions to a desired spin quantum number constructed from these Slater determinants, so-called configuration state functions, which ensures that a wave function of the desired spin is obtained.

For a given exact electronic wave function, properties can be determined by calculating the expectation value $\langle\Psi|\hat{\Omega}|\Psi\rangle$ of an observable $\hat{\Omega}$. To find an expression for the expectation value, operators containing only one- and two-electron operators

$$\begin{aligned}\hat{\Omega} &= \sum_{\alpha} \hat{\Omega}(\boldsymbol{\tau}_\alpha) + \frac{1}{2}\sum_{\alpha,\beta} \hat{\Omega}(\boldsymbol{\tau}_\alpha, \boldsymbol{\tau}_\beta) \\ &= \sum_{p,q} \left\langle \varphi_p(\boldsymbol{\tau}_1) \middle| \hat{\Omega}(\boldsymbol{\tau}_1) \middle| \varphi_q(\boldsymbol{\tau}_1) \right\rangle \hat{a}_p^\dagger \hat{a}_q + \frac{1}{2}\sum_{p,q,r,s} \left\langle \varphi_p(\boldsymbol{\tau}_1)\varphi_q(\boldsymbol{\tau}_2) \middle| \hat{\Omega}(\boldsymbol{\tau}_1, \boldsymbol{\tau}_2) \middle| \varphi_r(\boldsymbol{\tau}_1)\varphi_s(\boldsymbol{\tau}_2) \right\rangle \hat{a}_p^\dagger \hat{a}_q^\dagger \hat{a}_s \hat{a}_r\end{aligned} \tag{2.10}$$

can be written in second quantization as the of sum of products of creation and annihilation operators $a_p^\dagger$ and a_p and the respective expectation values in the spin-orbital basis. The operators $\hat{a}_p^\dagger$ and $\hat{a}_p$ respectively create and annihilate an electron in orbital φ_p in the wave function on which they act.

In this thesis, the integrals are written in physicist's notation for which the electronic coordinates are dropped and the electron that is described by an orbital is indicated by the position in the integral: $\left\langle \varphi_p(\boldsymbol{\tau}_1) \middle| \hat{\Omega}(\boldsymbol{\tau}_1) \middle| \varphi_q(\boldsymbol{\tau}_1) \right\rangle := \langle\varphi_p|\hat{\Omega}|\varphi_q\rangle$ and $\left\langle \varphi_p(\boldsymbol{\tau}_1)\varphi_q(\boldsymbol{\tau}_2) \middle| \hat{\Omega}(\boldsymbol{\tau}_1, \boldsymbol{\tau}_2) \middle| \varphi_r(\boldsymbol{\tau}_1)\varphi_s(\boldsymbol{\tau}_2) \right\rangle := \langle\varphi_p\varphi_q|\hat{\Omega}|\varphi_r\varphi_s\rangle$. Whenever spatial orbitals are used because the spin function has been removed through integration over the spin coordinates, the one-electron integrals will be described as matrix elements of the operator: $\langle\phi_p|\hat{\Omega}|\phi_q\rangle := \Omega_{pq}$. For the two-electron integrals the spatial orbital symbol ϕ will be dropped: $\langle\phi_p\phi_q|\hat{\Omega}|\phi_r\phi_s\rangle := \langle pq|\hat{\Omega}|rs\rangle$. Whenever the operator describes the two-electron potential, the operator $\frac{1}{r_{12}}$ is omitted: $\langle pq|\frac{1}{r_{12}}|rs\rangle := \langle pq|rs\rangle$.

The expectation value

$$\left\langle \Psi \middle| \hat{\Omega} \middle| \Psi \right\rangle = \sum_{p,q} D_{pq} \left\langle \varphi_p \middle| \hat{\Omega} \middle| \varphi_q \right\rangle + \frac{1}{2}\sum_{p,q,r,s} d_{pqrs} \left\langle \varphi_p\varphi_q \middle| \hat{\Omega} \middle| \varphi_r\varphi_s \right\rangle \tag{2.11}$$

can be calculated solely from the 1-RDM

$$D_{pq} = \left\langle \Psi \middle| \hat{a}_p^\dagger \hat{a}_q \middle| \Psi \right\rangle, \tag{2.12}$$

the 2-RDM

$$d_{pqrs} = \left\langle \Psi \middle| \hat{a}_p^\dagger \hat{a}_q^\dagger \hat{a}_s \hat{a}_r \middle| \Psi \right\rangle, \tag{2.13}$$

and the one- and two-electron integrals over the respective operator. Consequently, knowledge of the exact electronic wave function and the respective RDMs can enable the calculation of a plethora of electronic properties without additional computational effort. Solving the electronic Schrödinger equation by determining the coefficients in Equation (2.9) variationally yields the exact solution to the non-relativistic electronic Schrödinger equation in a given MO basis, resulting in the FCI method.[187]

2.1.1 Full Configuration Interaction Theory

The FCI equations can be derived by inserting the wave function *ansatz* (Equation (2.9)) into the electronic Schrödinger equation (Equation (2.3)) and projecting onto a determinant $\langle\Psi_J|$. The orbital

basis is often chosen to be orthonormal such that the constructed determinants will also form an orthonormal basis and the resulting equations

$$\mathbf{Hc} = \mathbf{Ec} \tag{2.14}$$

can be written in matrix form as an eigenvalue equation.[188] The eigenvector matrix $\mathbf{c}$ and the eigenvalue matrix $\mathbf{E}$ describe the CI coefficients from Equation (2.9) and the energy of every state in the given orbital basis. The elements of the Hamilton matrix $\mathbf{H}$ are matrix elements of the electronic Hamiltonian $H_{IJ} = \langle \Phi_J | \hat{H} | \Phi_I \rangle$ and can be acquired in an orthonormal orbital basis by applying the Slater-Condon rules.[186,189] The determinants in Equation (2.9)

$$|\Psi\rangle = c_0 \, |\Phi_0\rangle + \sum_{i}^{N_{\text{occ}}} \sum_{a}^{N_{\text{virt}}} c_i^a \, \hat{a}_a^\dagger \hat{a}_i \, |\Phi_0\rangle + \sum_{i<j}^{N_{\text{occ}}} \sum_{a<b}^{N_{\text{virt}}} c_{ij}^{ab} \, \hat{a}_a^\dagger \hat{a}_b^\dagger \hat{a}_j \hat{a}_i \, |\Phi_0\rangle + \dots \tag{2.15}$$

can be sorted with respect to excitations of some reference determinant $|\Phi_0\rangle$. Due to the fact that the electronic Hamiltonian only contains operators that act on one and two electrons, only matrix elements where the determinants differ by at most two orbitals produce non-vanishing contributions. The Hamilton matrix

$$\begin{array}{c|c|c|c|c|c} & |\Phi_0\rangle & |\Phi_i^a\rangle & |\Phi_{ij}^{ab}\rangle & |\Phi_{ijk}^{abc}\rangle & \dots \\ \hline \langle\Phi_0| & \langle\Phi_0|\hat{H}|\Phi_0\rangle & \langle\Phi_0|\hat{H}|\Phi_i^a\rangle & \langle\Phi_0|\hat{H}|\Phi_{ij}^{ab}\rangle & 0 & 0 \\ \hline \langle\Phi_i^a| & \langle\Phi_i^a|\hat{H}|\Phi_0\rangle & \langle\Phi_i^a|\hat{H}|\Phi_i^a\rangle & \langle\Phi_i^a|\hat{H}|\Phi_{ij}^{ab}\rangle & \langle\Phi_i^a|\hat{H}|\Phi_{ijk}^{abc}\rangle & 0 \\ \hline \langle\Phi_{ij}^{ab}| & \langle\Phi_{ij}^{ab}|\hat{H}|\Phi_0\rangle & \langle\Phi_{ij}^{ab}|\hat{H}|\Phi_i^a\rangle & \langle\Phi_{ij}^{ab}|\hat{H}|\Phi_{ij}^{ab}\rangle & \langle\Phi_{ij}^{ab}|\hat{H}|\Phi_{ijk}^{abc}\rangle & \dots \\ \hline \langle\Phi_{ijk}^{abc}| & 0 & \langle\Phi_{ijk}^{abc}|\hat{H}|\Phi_i^a\rangle & \langle\Phi_{ijk}^{abc}|\hat{H}|\Phi_{ij}^{ab}\rangle & \langle\Phi_{ijk}^{abc}|\hat{H}|\Phi_{ijk}^{abc}\rangle & \dots \\ \hline \vdots & 0 & 0 & \vdots & \vdots & \ddots \end{array} \tag{2.16}$$

becomes block-diagonal and diagonally dominant. Nevertheless, the solution of the FCI equations is prohibitively expensive for all but the smallest of orbital bases because all matrices in Equation (2.14) are of dimension $N_{\text{det}} \times N_{\text{det}}$ and the total number of determinants in a closed-shell system

$$N_{\text{det}} = \binom{M}{N_{\text{occ}}}^2 = \left(\frac{M!}{N_{\text{occ}}!(M - N_{\text{occ}})!} \right)^2 \tag{2.17}$$

scales factorially with the total number of spatial orbitals M and the total number of occupied spatial orbitals N_{occ}. From a chemical perspective, often only one or a few of the lowest eigenvalues of $\mathbf{E}$ are of interest and there is no reason to diagonalize the entire Hamilton matrix. In addition, matrix-free algorithms are used which directly compute the Hamilton matrix CI vector product, called the sigma vector $\boldsymbol{\sigma} = \mathbf{Hc}$, without constructing and saving the entire Hamilton matrix while exploiting its block sparsity.[190] The most commonly used method, the Davidson algorithm,[11,127,191] has enabled FCI calculations with over a trillion determinants.[192,193] Unfortunately, due to the steep scaling of the number of determinants with system size, this only corresponds to a system of 24 electrons in 24 spatial orbitals which is rather small from a chemical point of view and significantly limits the applicability of the FCI method.

2.2 Standard Approximate Solutions to the Electronic Schrödinger Equation

Due to the prohibitive cost of solving the electronic Schrödinger equation exactly, many approximate solutions have been proposed to tackle larger chemical problems. Above all, the development of the HF method made quantum chemical calculations applicable to a much wider range of problems and has spearheaded the development of more accurate methods.

2.2.1 Hartree-Fock Theory

In HF theory, the electronic wave function

$$|\Psi_{\mathrm{HF}}\rangle = |\Phi_0\rangle \tag{2.18}$$

is reduced to a single Slater determinant.[194] When applying the FCI method, the actual choice of orbitals from which the determinants are constructed is meaningless as long as they are complete and linearly independent. If the wave function is approximated, the energy is no longer invariant with respect to the chosen orbital basis. For this reason, the variational principle

$$E_0 \leq \tilde{E} = \frac{\left\langle \tilde{\Psi} \middle| \hat{H} \middle| \tilde{\Psi} \right\rangle}{\left\langle \tilde{\Psi} \middle| \tilde{\Psi} \right\rangle} \tag{2.19}$$

is applied to the ground state energy E_0 to minimize the approximate energy $\tilde{E}$ and systematically improve the approximate wave function $|\tilde{\Psi}\rangle$ on the basis of the variational method.[195,196] In the HF context, this approach determines the optimal orbital basis to describe the electronic ground state using a single determinant. The expectation value of the HF energy[197]

$$E_{\mathrm{HF}} = \sum_i \langle \varphi_i | \hat{h} | \varphi_i \rangle + \frac{1}{2} \sum_{i,j} \left(\langle \varphi_i | \hat{J}_j | \varphi_i \rangle - \langle \varphi_i | \hat{K}_j | \varphi_i \rangle \right) \tag{2.20}$$

can be obtained through application of the Slater-Condon rules[186,189] and the definition of the matrix elements of the one-electron Hamiltonian

$$\hat{h} = -\sum_{\alpha=1}^{N_\alpha} \left(\frac{1}{2} \nabla_\alpha^2 + \sum_{A=1}^{N_A} \frac{Z_A}{r_{A\alpha}} \right) \tag{2.21}$$

and the matrix elements of the Coulomb and exchange operators[197]

$$\hat{J}_j(\boldsymbol{\tau}_1)\varphi_i(\boldsymbol{\tau}_1) = \int d\boldsymbol{\tau}_2 \varphi_j^*(\boldsymbol{\tau}_2) \frac{1}{r_{12}} \varphi_i(\boldsymbol{\tau}_1)\varphi_j(\boldsymbol{\tau}_2) \tag{2.22}$$

$$\hat{K}_j(\boldsymbol{\tau}_1)\varphi_i(\boldsymbol{\tau}_1) = \int d\boldsymbol{\tau}_2 \varphi_j^*(\boldsymbol{\tau}_2) \frac{1}{r_{12}} \varphi_j(\boldsymbol{\tau}_1)\varphi_i(\boldsymbol{\tau}_2). \tag{2.23}$$

The expression in Equation (2.20) can alternatively be derived from Equation (2.11), knowing that the 1-RDM for a wave function consisting of a single determinant equals the identity ($D_{ij} = \delta_{ij}$) and the 2-RDM can be constructed from the 1-RDMs: $d_{ijkl} = D_{ik}D_{jl}$. The orbitals from which the HF energy is calculated can be optimized by iteratively solving the canonical HF equations[197]

$$\hat{F}\varphi_i = \varepsilon_i \varphi_i \tag{2.24}$$

using the self-consistent field (SCF) algorithm. The Fock operator[197]

$$\hat{F} = \hat{h} + \sum_j (\hat{J}_j - \hat{K}_j) \tag{2.25}$$

explicitly depends on the spin orbitals through the Coulomb and exchange operators. The application of the Fock operator to a given spin orbital describes the interaction of a single electron with the mean-field of all other electrons. The orbital energies ε_i are the eigenvalues of the Fock operator and enable an energetic ordering of the orbitals. The definition and optimization of the spatial orbitals that are required to construct the spin orbitals is difficult in their three-dimensional functional form and instead, the orbitals are constructed as a linear combination of a precomputed basis set $\{|\chi_\mu\rangle\}$:[197–199]

$$|\phi_i\rangle = \sum_\mu^M c_{\mu i} \left|\chi_\mu\right\rangle . \tag{2.26}$$

This basis set is usually chosen to represent approximate solutions of the hydrogen atom which are called atomic orbitals (AO) and the resulting *ansatz* is a linear combination of atomic orbitals.[199] The spin and spatial orbitals are labeled molecular orbitals (MO) in this context to differentiate these from the AO basis set. The optimization problem is shifted from the three-dimensional MOs $\phi_i(\mathbf{r})$ to the scalar MO coefficients $c_{\mu i}$. Using Equation (2.26), the HF equations can be transformed into a generalized eigenvalue problem, the so-called Roothaan-Hall equations[197,200]

$$\mathbf{Fc} = \mathbf{Sc}\boldsymbol{\varepsilon}, \tag{2.27}$$

which are solved self-consistently by repeatedly diagonalizing and reconstructing the Fock matrix $F_{\mu\nu} = \langle\chi_\mu|\hat{F}|\chi_\nu\rangle$ until convergence. To begin with, the AO basis has to be orthogonalized to ensure the AO overlap matrix $S_{\mu\nu} = \langle\chi_\mu|\chi_\nu\rangle$ equals the identity and vanishes from Equation (2.27). The diagonalization of the Fock matrix does not only yield those MO coefficients $\mathbf{c}$ that are needed to calculate the HF energy in the AO basis

$$E_{\mathrm{HF}} = \sum_{\mu,\nu} D^{\mathrm{AO}}_{\mu\nu} \left\langle \chi_\mu \middle| \hat{h} \middle| \chi_\nu \right\rangle + \frac{1}{2} \sum_{\mu,\nu,\sigma,\rho} D^{\mathrm{AO}}_{\mu\sigma} D^{\mathrm{AO}}_{\nu\rho} \left(\left\langle \chi_\mu\chi_\nu \middle| \chi_\sigma\chi_\rho \right\rangle - \left\langle \chi_\mu\chi_\nu \middle| \chi_\rho\chi_\sigma \right\rangle \right) \tag{2.28}$$

but a surplus of orbitals that do not contribute to the HF determinant. The additional set of virtual orbitals $\{\phi_a\}$ complements the set of occupied orbitals $\{\phi_i\}$ and can be used to construct the additional determinants required to describe the exact electronic wave function in Equation (2.9). As a consequence, the HF method builds the foundation for many quantum chemical methods beyond the mean-field approximation. The 1-RDM in the AO basis

$$D^{\mathrm{AO}}_{\mu\nu} = \sum_i^N c^*_{\mu i} c_{\nu i} \tag{2.29}$$

can be constructed from the MO coefficients for the occupied orbitals. The HF minimization condition can alternatively be written in the following form:

$$\left\langle \varphi_a \middle| \hat{F} \middle| \varphi_i \right\rangle = 0. \tag{2.30}$$

This expression is equivalent to the matrix elements $\langle\Phi_i^a|\hat{H}|\Phi_0\rangle$ and the resulting expression is commonly known as the Brillouin theorem[201,202] which causes the corresponding block in the Hamilton matrix in Equation (2.16) to vanish whenever HF orbitals are used.

The ground states of chemical systems can have varying spin quantum numbers. In the simplest case, molecules have an equal number of electrons with alpha- and beta-spin. For these singlet systems, the ground state can often be described with a determinant where two sets of spatial orbitals that are occupied by electrons with either spin are equivalent: $\phi_i^\alpha = \phi_i^\beta$. When these closed-shell systems are described with HF, the restricted HF formalism (RHF) can constrain the equality of the spatial orbitals while obtaining the same solution as if the equality had not been enforced. The resulting determinant is automatically a spin eigenfunction to the correct spin eigenvalue. For open-shell systems, which can be systems with higher multiplicity or open-shell singlets, a corresponding restricted approach, restricted open-shell HF (ROHF),[203] constrains the variability of the HF wave function and the resulting minimum will not necessarily coincide with the minimum if the spatial orbitals had been allowed to differ: $\phi_i^\alpha \neq \phi_i^\beta$. The latter method is called unrestricted HF (UHF) and will generally yield a lower energy for open-shell systems.[204,205] Unfortunately, UHF will often produce wave functions that are not exact eigenfunctions of the $\hat{S}^2$ operator and are therefore undesirable as solutions to the electronic Schrödinger equation because of spin contamination. For the remainder of this thesis, orbitals will always be assumed to have been calculated in a restricted formalism such that spatial orbitals are doubly occupied unless otherwise stated and the "α" and "β" are therefore dropped from the spatial orbital symbol.

While the single-determinant wave function provided by HF theory can provide a qualitatively correct starting point for many systems of chemical interest, a solution beyond the mean-field approximation is generally necessary to evaluate electronic properties of molecules with sufficient accuracy. While Fermi correlation is correctly described in the HF solution through the utilization of an antisymmetrized wave function, the mean-field approach completely disregards the Coulomb correlation, i.e., the correlated movement of electrons in the molecular quantum system due to Coulomb repulsion. Additional determinants are required to accurately capture the complex interdependence of the electronic degrees of freedom. These additional contributions can be quantified through the correlation energy

$$E_{\text{corr}} = E - E_{\text{HF}} \tag{2.31}$$

which is defined as the difference between the FCI energy and the HF energy.[206] Whenever the HF solution provides a qualitatively correct description of the underlying electronic wave function, the system is said to be dynamically correlated. In contrast, systems where multiple determinants are required are called statically correlated systems. The UHF description does introduce some degree of electron correlation because the UHF wave function can be decomposed into a linear combination of spin-pure RHF and ROHF wave functions of different spin quantum numbers.[205,207] This can be enough to qualitatively describe chemical applications that would otherwise require multiple restricted determinants such as bond-breaking processes. Nevertheless, a treatment of additional determinants in the electronic wave function is generally required to provide a quantitative description of electronic properties.

2.2.2 Coupled-Cluster Theory

The CC method is primarily aimed at treating dynamically correlated systems. In contrast to FCI, an exponential *ansatz*

$$|\Psi_{\text{CC}}\rangle = e^{\hat{T}} |\Phi_0\rangle \tag{2.32}$$

is chosen for the wave function.[208,209] The cluster operator

$$\hat{T} = \hat{T}_1 + \hat{T}_2 + \hat{T}_3 + \ldots + \hat{T}_N = \sum_{i,a} t_i^a \hat{a}_a^\dagger \hat{a}_i + \frac{1}{4} \sum_{i,j,a,b} t_{ij}^{ab} \hat{a}_a^\dagger \hat{a}_b^\dagger \hat{a}_j \hat{a}_i + \ldots \tag{2.33}$$

can be decomposed into excitation operators $\hat{T}_x$.[209,210] These excitation operators consist of the cluster amplitudes $t_{i\ldots}^{a\cdots}$ and quasi-particle creation operators, $\hat{a}_i$ and $\hat{a}_a^\dagger$, which create holes in the occupied orbitals and electrons in the virtual orbitals. As such, the application of an excitation operator $\hat{T}_x$ transforms the HF determinant into excited determinants of order x. The CC energy expression[210]

$$E = \left\langle \Phi_0 \middle| e^{-\hat{T}} \hat{H} e^{\hat{T}} \middle| \Phi_0 \right\rangle \tag{2.34}$$

is obtained by inserting the CC wave function, Equation (2.32), into the electronic Schrödinger equation, Equation (2.3), multiplying with $e^{-\hat{T}}$ from the left, and projecting onto the HF determinant. The CC amplitudes that are required to calculate the CC energy are acquired by instead projecting onto the respective excited determinants and solving the resulting amplitude equations:[210]

$$\begin{aligned} 0 &= \left\langle \Phi_i^a \middle| e^{-\hat{T}} \hat{H} e^{\hat{T}} \middle| \Phi_0 \right\rangle \\ 0 &= \left\langle \Phi_{ij}^{ab} \middle| e^{-\hat{T}} \hat{H} e^{\hat{T}} \middle| \Phi_0 \right\rangle \\ &\vdots \end{aligned} \tag{2.35}$$

These equations can be simplified using the Baker-Campbell-Hausdorff formula[211–213] and solved self-consistently for every excitation order. The CC ansatz alone does not offer any improvement over the FCI wave function in Equation (2.9). Only when the cluster operator is truncated after a certain excitation order does the exponential approach offer two major advantages over linearly truncated CI approaches. Through the expansion of the exponential operator, the CC wave function

$$|\Psi_{\mathrm{CC}}\rangle = \left(1 + \hat{T}_1 + \hat{T}_2 + \frac{1}{2}\hat{T}_1^2 + \hat{T}_3 + \frac{1}{6}\hat{T}_1^3 + \hat{T}_1\hat{T}_2 + \ldots\right)|\Phi_0\rangle \tag{2.36}$$

includes higher excitations as a product of lower excitations that are explicitly included in the cluster operator. The contributions from these higher excitations will generally provide a better approximation to the FCI wave function at no additional computational scaling cost.[210] In addition, the exponential operator leads to a wave function that is multiplicatively separable which results in a method for which the sum of the energies of non-interacting subsystems equals the total energy of the full system. This property is called size-consistency and is extremely important for the correct scaling of the energy of a quantum chemical method with system size.[210] Both the systematic improvability of the CC wave function and its size-consistency are major reasons for the widespread success of CC theory.

Common truncated approaches are CC with single and double excitations (CCSD),[214] CC with single, double, and triple excitations (CCSDT),[215–217] and CC with single, double, triple, and quadruple excitations (CCSDTQ).[218,219] In contrast to FCI, these approaches scale polynomially with system size: $\mathcal{O}(M^6)$, $\mathcal{O}(M^8)$, and $\mathcal{O}(M^{10})$, respectively. Additional CC methods with intermediate scaling exist where the highest excitation is approximated (non-)iteratively from the lower order excitations based on perturbation theoretic arguments. A prominent example is CC with single, double, and perturbative triple excitations (CCSD(T)) which is coined the *gold standard of quantum chemistry* due to its ability to consistently reach chemical accuracy for dynamically correlated systems with an affordable scaling of $\mathcal{O}(M^7)$.[210,220,221] Analogously, a non-iterative approximation for the quadruple excitations exists, labeled CC with single, double, triple, and perturbative quadruple excitations (CCSDT(Q)), which scales $\mathcal{O}(M^9)$.[222] Many attempts to adapt CC theory to the treatment of statically correlated systems have not repeated the scientific revolution caused by its dynamically correlated counterpart due to methodological ambiguities and the complexity of the resulting equations.[223]

2.2.3 Complete Active Space Configuration Interaction Theory

The treatment of static correlation requires the explicit inclusion of specific determinants into the electronic wave function. This requirement is generally caused by (near-)degenerate orbitals. For systems, for which the inclusion of all determinants as in FCI is intractable, the number of determinants can be reduced by restricting excitations to a small subset of the full orbital basis. The orbital basis is partitioned into three different sets:

- Inactive orbitals $\{\phi_i\}$: these orbitals are always doubly occupied, only determinants including these orbitals are added to the wave function.
- Active orbitals $\{\phi_u\}$: these orbitals are variably occupied, all possible determinants that result from the distribution of the remaining electrons among this set of orbitals are included in the wave function.
- Virtual orbitals $\{\phi_a\}$: these orbitals are unoccupied, no determinants including these orbitals are added to the wave function.

This partitioning has two major advantages: Defining the wave function has been shifted from choosing a set of determinants to choosing a set of orbitals which is more aligned with *chemical intuition.* In addition, the method is size-consistent as long as all excitations in the active orbital space are accounted for. The electronic Schrödinger equation can then be solved for all determinants in this complete active space (CAS), resulting in the CASCI method.[224] When the Hamilton matrix is diagonalized in this smaller subspace, the inactive orbitals no longer explicitly contribute. To ensure all contributions are correctly accounted for, the CASCI Hamiltonian is modified by replacing the one-electron Hamiltonian with an inactive Fock operator

$$\hat{F}^I = \hat{h} + \sum_i \left(2\hat{J}_i + \hat{K}_i\right) \tag{2.37}$$

which adds the mean-field interaction with the inactive orbitals.[224] In addition, the HF energy of the inactive orbitals is added to the Hamiltonian. As a result, the CASCI energy

$$E = \sum_{u,v} D_{uv} F^I_{uv} + \sum_{u,v,x,y} d_{uvxy} \langle uv \,|\, xy\rangle + \sum_i \left(h_{ii} + F^I_{ii}\right) \tag{2.38}$$

can be constructed from the 1- and 2-RDMs of the active space orbitals, the inactive Fock matrix elements

$$F^I_{pq} = h_{pq} + \sum_i \left(2 \langle pi \,|\, qi\rangle - \langle pi \,|\, iq\rangle\right), \tag{2.39}$$

and the familiar one- and two-electron integrals. While the CASCI wave function is in many cases able to provide a qualitatively correct description of the exact wave function, both the MO choice itself and the question of what orbitals to include in the active space are rather ambiguous and difficult to generalize.[225] To ensure that the orbitals are optimal for a given CAS wave function, the CASCI procedure can be combined with orbital optimization which results in the CASSCF method.

2.2.4 Complete Active Space Self-Consistent Field Theory

In CASSCF theory, the wave function

$$|\Psi\rangle = e^{-\hat{\kappa}} \sum_I^{\text{CAS}} c_I \Phi_I \tag{2.40}$$

depends on the orbital rotation operator $e^{-\hat{\kappa}}$ and the CI coefficients c_I of the CAS determinants.[226] The orbital rotation operator

$$\hat{\kappa} = \sum_{p<q} \kappa_{pq} \left(\hat{a}_p^\dagger \hat{a}_q - \hat{a}_q^\dagger \hat{a}_p \right) \tag{2.41}$$

is antisymmetric which guarantees a unitary transformation of the orbitals in the exponential form $e^{-\hat{\kappa}}$.[227] The CASSCF energy expression for a given set of orbitals is equivalent to the CASCI energy in Equation (2.38). Both groups of wave function parameters, the CI coefficients and the orbital rotations, have to be varied simultaneously during the energy minimization. In practice, first- and second-order algorithms exist for the optimization of the CASSCF wave function. First-order algorithms[224,228–242] only employ information from the electronic gradients with respect to orbital rotation $\mathbf{g}^{\mathrm{o}}$ and the variation of the CI coefficients $\mathbf{g}^{\mathrm{c}}$. The convergence rate of these algorithms is linear. First-order CASSCF algorithms do not take any coupling between the wave function parameters into consideration. As a result, the optimization of the CI coefficients can be performed separately in a two-step procedure. The CI coefficient gradient is minimized through a CASCI calculation for a given set of orbitals which optimizes the CI coefficients variationally using the Davidson procedure. Using the obtained CI coefficients, the orbital gradient[243]

$$g_{pq}^{\mathrm{o}} = 2(F_{pq} - F_{qp}) \tag{2.42}$$

can be calculated from the generalized Fock matrix[243]

$$F_{pq} = \sum_r D_{pr} h_{qr} + \sum_{r,s,t} d_{prst} \langle qr|st\rangle \,. \tag{2.43}$$

The energy can be minimized by following the gradient and these two steps are repeated until convergence. For CAS wave functions, the generalized Fock matrix elements[243]

$$F_{ip} = 2 \left(F_{pi}^I + F_{pi}^A \right) \tag{2.44}$$

$$F_{up} = \sum_v D_{uv} F_{pv}^I + \sum_{v,w,x} d_{uvwx} \langle pv|wx\rangle \tag{2.45}$$

$$F_{ap} = 0 \tag{2.46}$$

can be simplified to only depend on the active space density matrices, two electron integrals including three active orbitals, inactive Fock matrix elements, and active Fock matrix elements[243]

$$F_{pq}^A = \sum_{u,v} D_{uv} \left(\langle pu|qv\rangle - \frac{1}{2} \langle pu \,|\, vq\rangle \right). \tag{2.47}$$

In conventional CASSCF, all orbital rotations within the orbital subsets are redundant and the corresponding gradient blocks automatically vanish. Strong couplings between the orbital rotation and the optimization of the CI coefficients will severely limit the convergence of first-order methods. The convergence can be accelerated by utilizing a quasi-Newton algorithm such as the limited-memory Broyden-Fletcher-Goldfarb-Shanno method.[244] This method preconditions the gradient with approximate orbital Hessian information through a Hessian updating procedure. The initial Hessian calculation can be avoided by using the Hessian diagonal which is trivial to invert.[245] To reduce the computational cost of calculating the Hessian diagonal, all terms containing the integrals

with two non-active integrals can be modified to yield the following expressions:[236]

$$H^{\mathrm{oo}}_{ia,ia} = 4\left(F^I_{aa} + F^A_{aa}\right) - 4\left(F^I_{ii} + F^A_{ii}\right) \tag{2.48}$$

$$H^{\mathrm{oo}}_{ua,ua} = 2D_{uu}F^I_{aa} - 2\sum_v D_{uv}F^I_{uv} - 2\sum_{v,w,x} d_{uvwx}\,\langle uw|xy\rangle + D_{uu}F^A_{aa} \tag{2.49}$$

$$H^{\mathrm{oo}}_{iu,iu} = \left(F^I_{uu} + F^A_{uu}\right) - \left(F^I_{ii} + F^A_{ii}\right) + 2D_{uu}F^I_{ii} - 2\sum_v D_{uv}F^I_{uv} - 2\sum_{v,w,x} d_{uvwx}\,\langle uw|xy\rangle + 2D_{uu}F^A_{ii}\,. \tag{2.50}$$

The resulting quasi-Newton algorithm will provide superlinear convergence at only very little additional cost.[236] As an alternative for difficult-to-converge systems, second-order algorithms[227,243,246–272] utilize both electronic gradient and Hessian information and therefore also explicitly consider the coupling between orbital rotation and the optimization of the CI coefficients through the coupling block of the electronic Hessian $\mathbf{H}^{\mathrm{co}}$. These algorithms minimize a second-order energy functional in a one-step procedure and converge quadratically near the minimum. The expense of calculating the orbital Hessian often limits the applicability of second-order CASSCF algorithms.

Even though the CASSCF method is able to treat statically correlated systems efficiently, the resulting wave functions will generally only be qualitatively correct. Dynamic correlation beyond the active space is necessary to obtain results with chemical accuracy. Better results can be obtained through second-order perturbation theory (complete active space second-order perturbation theory, CASPT2), multireference CI, or multireference CC on top of an existing CASSCF wave function. Unfortunately, these approaches are often either not systematically improvable, not size-consistent, produce equations with very high complexity, or are simply too expensive for all but the smallest of system sizes and active spaces. In addition, choosing an active space for CASSCF calculations often requires *chemical intuition* and intricate knowledge of the system at hand.[115,119,273–278] While automated approaches exist, their application has yet to convert CASSCF theory to a truly black-box method.[116,279–287]

2.3 Approximate FCI Methods

While the conventional methods introduced in Section 2.2 significantly extend the range of systems that can be treated numerically, the usage of the FCI method still offers significant advantages. The ability of the FCI method to treat arbitrary spin and symmetry states of both statically and dynamically correlated systems on an equal footing is unrivaled and reinforces its status as a true black-box benchmark method for many applications. However, the fact that the total number of basis functions, whether it be Slater determinants, configuration state functions, or configurations, increases factorially with system and basis set size significantly limits the applicability of FCI. For this reason, a great amount of research has targeted the development of so-called approximate FCI methods that preserve these underlying desirable features of the FCI solution while reducing either the prefactor of the factorial scaling of traditional FCI algorithms or by lowering the computational scaling to be polynomial with system size.[25] These methods generally reformulate the FCI problem to exploit sparsity by neglecting negligible contributions up to given thresholds. Four different classes of approximate FCI methods are often cited: selected configuration interaction methods (SCI), methods based on tensor decomposition techniques (particularly density matrix renormalization group, DMRG), quantum Monte Carlo methods (QMC), and incremental methods based on the many-body expansion (MBE).[25]

2.3.1 Selected CI Methods

Selected CI methods construct a CI wave function not through excitation level-based truncation or definition of an active space but by selecting specific determinants based on some predefined criterion. The earliest of these methods, called perturbatively selected configuration interaction (CIPSI), starts from an initial guess for the important determinants $\{S\}$ that is then iteratively improved by adding more determinants that are deemed important.[16,288,289] In this scheme, the important determinants form the unperturbed Hamiltonian in the Epstein-Nesbet partitioning of the Hamiltonian[16,290–292] and the corresponding CI coefficients are obtained from a CASCI calculation. Determinants for which the weighing coefficient $c_I^{(1)}$ to the first-order correction of the wave function[16,288,289]

$$\left|\Psi^{(1)}\right\rangle = -\sum_{I\notin\{S\}} c_I^{(1)} \left|\Phi_I\right\rangle = -\sum_{I\notin\{S\}} \frac{\left\langle\Phi_I\middle|\hat{H}\middle|\Psi^{(0)}\right\rangle}{E_I - E_0} \left|\Phi_I\right\rangle \tag{2.51}$$

is above a given threshold are added to the unperturbed Hamiltonian and this procedure is repeated until convergence. At the end, the CASCI energy is corrected using the second-order energy correction[16,288,289]

$$E^{(2)} = -\sum_{I\notin\{S\}} \frac{\left|\left\langle\Phi_I\middle|\hat{H}\middle|\Psi^{(0)}\right\rangle\right|^2}{E_I - E_0}. \tag{2.52}$$

An alternative approach, adaptive sampling CI (ASCI),[21,121,122] only keeps determinants in $\Psi^{(0)}$ with CI coefficients above a given threshold and only considers this subspace in the criterion in Equation (2.51). While for CIPSI, the determinant proxy is rooted in perturbation theory, many alternative approaches to decide on which determinants are to be added to the unperturbed wave function have been proposed: Heat-bath CI (HCI) only considers those determinants with a large numerator in Equation (2.51) for at least one determinant in $\Psi^{(0)}$ to be added to the unperturbed wave function.[22] Semi-stochastic heat-bath CI (SHCI) stochastically samples the final perturbation correction.[120,293,294] Iterative CI with selection (iCI) uses a combined criterion from CIPSI and SHCI for the selection of configuration state functions and uses an additional secondary space to describe the changes in the unperturbed space caused by the introduction of dynamical correlation through the primary space in Equation (2.51).[20,123,295,296] Coordinate descent FCI reformulates the FCI problem as an unconstrained optimization problem that is solved using a coordinate-descent algorithm. Determinants with the largest approximate gradient for this optimization problem are added to the wave function.[297,298] Machine-learned CI uses a neural network to predict important determinants on-the-fly.[299,300] In adaptive CI (ACI), the proxy is derived by diagonalizing a 2×2 Hamiltonian which is constructed from the unperturbed wave function and the respective determinant. In addition, as in ASCI, only determinants with large CI coefficients are kept in the unperturbed wave function.[301,302] Tensor product SCI groups the orbitals into clusters from which many-particle cluster states can be defined, and the selection is then performed based on Equation (2.51) in a basis of tensor products of these cluster states.[303]

Approximate FCI methods have not only been applied to the calculation of FCI properties but can also be used as a replacement for the CASCI solver in two-step CASSCF calculations. The ASCI, HCI, and iCI approaches have been used to extend the applicability of the CASSCF method to the treatment of larger active spaces, resulting in the ASCI-SCF, HCISCF, and iCISCF methods, respectively.[304–306] ASCI-SCF and HCISCF have also been applied to the calculation of CASSCF nuclear gradients.[307–309]

SCI methods unite a couple of distinct disadvantages: The CASCI space may not increase beyond a certain point as the diagonalization is not easily parallelized which restricts the method to systems

with a limited number of important determinants. Additionally, the perturbative correction is not systematically improvable. For this reason, more accurate results can only be achieved by adding more determinants to the active space. This is of special importance for the high-accuracy description of predominately dynamically correlated systems where numerous determinants produce small but non-vanishing contributions to the total energy.[135] In addition, SCI wave functions are not size-consistent. Nevertheless, this effect becomes less important as the SCI wave function approaches the FCI limit.

2.3.2 Tensor Decomposition Methods

The FCI wave function

$$|\Psi\rangle = \sum_{n_1,n_2,\ldots,n_M} c_{n_1 n_2 \ldots n_M} |n_1 n_2 \ldots n_M\rangle \tag{2.53}$$

can be reformulated in second quantization.[310] The determinants are described by occupation number vectors $|n_1 n_2 \ldots n_M\rangle$ which define determinants in a given MO basis through their occupation numbers n_i for all orbitals i. In an unrestricted MO basis, the occupation numbers can take values of zero and one. The resulting CI coefficient tensor $c_{n_1 n_2 \ldots n_M}$ has dimension 2^M. When the electron number N is conserved, the actual dimension is given by Equation (2.17) since only occupation number vectors with N electrons are considered in the wave function. In tensor decomposition methods, the CI coefficient tensor is decomposed and approximated by a product of lower rank tensors. In the popular DMRG method, the tensor is decomposed[17,119,310–320]

$$c_{n_1 n_2 \ldots n_M} \approx \sum_{i_1,i_2,\ldots,i_{M-1}}^{m} A^{n_1}_{i_1} A^{n_2}_{i_1 i_2} \ldots A^{n_{M-1}}_{i_{M-2} i_{M-1}} A^{n_M}_{i_{M-1}} \tag{2.54}$$

into a matrix product state (MPS) of M tensors $\mathbf{A}$. The inner tensors have dimension $2 \times m \times m$ where m is the so-called MPS dimension. Through this approach, DMRG encodes a sequential structure into the description of electron correlation by describing the correlation between the orbitals φ_1 and φ_2 through the contraction over index i_1 while more contractions are necessary to describe the correlation between two orbitals with a greater *distance* in the occupation number vector.[310] The energy expectation value for this wave function *ansatz* can now be variationally optimized. This is often achieved using an algorithm which sweeps over pairs of adjacent orbitals, solves a local eigenvalue problem with the Davidson algorithm which yields a combined two-site tensor. Optimized but approximate one-site tensors $\mathbf{A}$ for both involved sites can be determined by applying a singular value decomposition to the two-site tensor and discarding small singular values and the corresponding singular vectors up to a given MPS dimension. This procedure is completed by sweeping back and forth along the orbitals until convergence.[314]

The DMRG method was the earliest among the approximate FCI methods that was combined with CASSCF for the description of large active spaces, resulting in the DMRGSCF method.[269,321–324] The method has also been applied to CASSCF analytic geometrical gradients[325] and combined with perturbation theory for the treatment of dynamical correlation outside the active space.[325–328]

Due to its unique structure, the DMRG wave function is able to efficiently treat very strongly correlated systems by exploiting locality in the FCI wave function. Unfortunately, the DMRG results strongly depend both on the chosen orbital basis and on the order of the orbitals in the occupation number vector. DMRG will only be size-consistent and accurate, when an appropriate local orbital basis is used and if the orbitals are ordered according to their spatial position in the occupation number vector.[310,314] The absolute sum of discarded singular values is correlated to the

error of a DMRG optimization and can therefore be exploited for extrapolation. The calculation is repeated with increasing MPS dimension and a linear extrapolation of the DMRG energy against the discarded singular values is used to approximate the exact DMRG energy if no singular values were discarded.[314,329,330] For dynamically correlated systems, it is often difficult to get results with very high accuracy as a very large MPS dimension would be required to accurately describe the FCI wave function. For this reason, DMRG often relies on extrapolation which eliminates the variational character of the method. Nevertheless, DMRG has asserted itself as the primary tool for the description of static correlation whenever FCI and CASSCF calculations are infeasible.[25]

Another important application of the DMRG method, the automated selection of active spaces for CASSCF calculations, is closely connected to the field of quantum information theory (QIT). In QIT, the entanglement of a quantum system is quantified through the von Neumann entropy[331]

$$S = -\mathrm{Tr}\left(\boldsymbol{\rho} \ln \boldsymbol{\rho}\right) \tag{2.55}$$

which can be calculated from the density matrix $\boldsymbol{\rho}$. To extract entanglement information of individual orbitals, the quantum system can be divided into a subsystem and its environment. The density matrix in Equation (2.55) is replaced by an RDM and the resulting entropy describes the entanglement of the subsystem with its environment. In the context of quantum chemistry, the subsystem is a set of orbitals and orbital RDMs[332]

$$\rho^{p}_{n_p,n'_p} = \left\langle \Psi \middle| \sum_{n_1,\ldots,n_{p-1},n_{p+1},\ldots,n_M} |n_1 \ldots n'_p \ldots n_M\rangle \langle n_1 \ldots n_p \ldots n_M| \middle| \Psi \right\rangle \tag{2.56}$$

$$\rho^{pq}_{n_p n_q,n'_p n'_q} = \left\langle \Psi \middle| \sum_{n_1,\ldots,n_{p-1},n_{p+1},\ldots,n_{q-1},n_{q+1},\ldots,n_M} |n_1 \ldots n'_p \ldots n'_q \ldots n_M\rangle \langle n_1 \ldots n_p \ldots n_q \ldots n_M| \middle| \Psi \right\rangle \tag{2.57}$$

are used to construct the one- and two-orbital entropies[332–335]

$$S_p = -\mathrm{Tr}\left(\boldsymbol{\rho}^{p} \ln \boldsymbol{\rho}^{p}\right) = -\sum_{n_p} \eta^{p}_{n_p} \ln \eta^{p}_{n_p} \tag{2.58}$$

$$S_{pq} = -\mathrm{Tr}\left(\boldsymbol{\rho}^{pq} \ln \boldsymbol{\rho}^{pq}\right) = -\sum_{n_p,n_q} \eta^{pq}_{n_p n_q} \ln \eta^{pq}_{n_p n_q} \tag{2.59}$$

which can alternatively be constructed from their eigenvalues η^{p}_{n} and η^{pq}_{n} when the RDMs are expanded in the basis of their eigenvectors. The 1- and 2-orbital RDMs differ from the 1- and 2-electron RDMs introduced in Equations (2.12) and (2.13) as they are constructed by calculating the trace over orbitals instead of electrons. These quantities can be efficiently evaluated through the calculation of matrix elements of the DMRG wave function. The orbital entropies are an important measure to quantify the extent to which orbitals are correlated with the remaining quantum system. The individual correlation between two orbitals can be quantified through the mutual information[332–335]

$$I_{pq} = \frac{1}{2}\left(S_p + S_q - S_{pq}\right)\left(1 - \delta_{pq}\right) \tag{2.60}$$

which subtracts the two-orbital entropy from the sum of both one-orbital entropies. Because the single-orbital entropies and orbital mutual information generally do not significantly change beyond a certain MPS dimension, cost-effective DMRG calculations on the entire system can be used to quantify the extent to which orbitals are correlated in a multireference system. Active spaces for CASSCF calculations can then be constructed by choosing the most strongly correlated orbitals which proves to be a major step towards black-box CASSCF calculations.[116,281,283,285–287,335–337]

2.3.3 Quantum Monte Carlo Methods

Sparsity in the FCI wave function cannot only be exploited deterministically through the selection of specific determinants according to a predefined criterion but also by stochastically sampling the determinant space on the basis of probability theory. The CASCI problem can be solved for a random set of determinants and all CI coefficients above a predefined threshold can be retained and augmented by an additional set of random determinants. This procedure can be repeated until the CI vector no longer grows in size. The resulting approach is coined Monte-Carlo configuration interaction[338–342] and is a stochastic version of the SCI group of methods.

More sophisticated QMC approaches for the solution of the electronic Schrödinger equation are the different flavors of projector QMC which are based on the solution of the imaginary time Schrödinger equation[343]

$$-\frac{\partial \left|\Psi(\mathbf{r},\tau)\right\rangle}{\partial \tau} = \hat{H}\left|\Psi(\mathbf{r},\tau)\right\rangle . \tag{2.61}$$

This equation can be obtained by a variable change from time t to imaginary time τ in the time-dependent Schrödinger equation. The imaginary time dependence in the solution of the imaginary time Schrödinger equation[343]

$$\left|\Psi(\mathbf{r},\tau)\right\rangle = e^{-\hat{H}\tau}\left|\Psi(\mathbf{r},0)\right\rangle = e^{-\hat{H}\tau}\sum_K c_K(0)\left|\Psi_K(\mathbf{r})\right\rangle = \sum_K c_K(0)e^{-E_K\tau}\left|\Psi_K(\mathbf{r})\right\rangle \tag{2.62}$$

corresponds to an exponential decay. An arbitrary wave function can be written as a linear combination of the eigenstates $|\Psi_K(\mathbf{r})\rangle$ of the Hamiltonian. Since the ground state energy E_0 is the lowest for all eigenstates, the contribution of the ground state wave function $|\Psi_0(\mathbf{r})\rangle$ will decay slowest as the wave function is propagated in imaginary time. The ground state wave function[343]

$$\left|\Psi_0\right\rangle = \lim_{\tau\to\infty} e^{-(\hat{H}-E_0)\tau}\left|\Psi\right\rangle = \lim_{n\to\infty} e^{-(\hat{H}-E_0)n\Delta\tau}\left|\Psi\right\rangle \tag{2.63}$$

can be extracted from any trial wave function by shifting the Hamiltonian by the ground state energy when the imaginary time tends to infinity. The ground state energy is generally not known and replaced by an approximate ground state energy $E_S(\tau)$. The ground state wave function is then determined by discretizing the imaginary time variable, propagating a starting wave function using the propagator $e^{-\hat{H}\tau}$ in imaginary time, and continuously estimating the ground state energy from the current wave function. A popular example of these methods for molecular systems is full configuration interaction quantum Monte Carlo (FCIQMC).[19,344,345] In FCIQMC, the wave function is sampled in the space of Slater determinants by solving the working equation[346,347]

$$c_I(\tau+\Delta\tau) = \left(1-\Delta\tau(H_{II}-E_S(\tau))\right)c_I(\tau) - \Delta\tau\sum_{I\neq J} H_{IJ}c_J(\tau) \tag{2.64}$$

stochastically through the probabilistic spawning and death of signed walkers.[a] Alternatively, the FCI problem can also be solved without walkers using the fast randomized iteration method which is a generalization of the FCIQMC method that exploits sparsity through matrix and vector compression techniques.[348,349] A deterministic analogue of the FCIQMC method called projector CI also exists.[350]

[a] The spawning and death probabilities of the walkers are proportional to $|(H_{II}-E_S(\tau))|$ and $|H_{IJ}|$ which can be compared to Equation (2.64). Walkers can either die when $H_{II}-E_S(\tau) > 0$ or spawn an additional same-signed walker on determinant $|\Phi_I\rangle$ when $H_{II}-E_S(\tau) < 0$ with probability $|(H_{II}-E_S(\tau))|$. Walkers can also spawn another walker on determinant $|\Phi_J\rangle$ with probability $|H_{IJ}|$. The sign of the spawned walker is related to the sign of the respective Hamilton matrix element and the sign of the parent walker. Walkers with opposite sign annihilate which is important to correctly recover the fermionic wave function.[19,344,345]

The FCIQMC method has also been combined with the CASSCF method for the description of large active spaces of statically correlated systems, referred to as FCIQMC-SCF.[351–353]

An alternative projector QMC method commonly applied to quantum chemical systems is auxiliary field QMC (AFQMC).[18,354–360] In AFQMC, the electronic ground state wave function is obtained by solving the master equation[360]

$$|\Psi_0\rangle = \left(\sum_{n,w} W_n^w e^{i\theta_n^w}\right)^{-1} \sum_{n,w} W_n^w e^{i\theta_n^w} \frac{\left|\Phi_n^w\right\rangle}{\langle\Psi \mid \Phi_n^w\rangle} \tag{2.65}$$

which can be derived from Equation (2.63).[b] The equation is sampled using random walkers w with weight W_n^w, phase θ_n^w, and determinant Φ_n^w.

Both FCIQMC and AFQMC are plagued by the Fermion sign problem as much as all QMC methods applied to fermionic systems.[346,360,369,370] This can be solved by introducing a bias. In the case of FCIQMC, the initiator approximation[345,371] (*i*-FCIQMC) is used, while in AFQMC, the phaseless approximation is applied.[372] For FCIQMC, an adaptive shift method has been suggested to reduce the bias introduced by the initiator approximation, resulting in the adaptive-shift FCIQMC method (AS-FCIQMC).[373] For QMC methods, the error can easily be estimated from the stochastic error. In projector QMC methods, due to the autocorrelation of the energy during the imaginary time propagation, the stochastic error cannot be determined from neighboring time steps as this would underestimate the variance of the sampling. Instead, a blocking analysis over a certain range of the most recent time steps is necessary to get an accurate estimate of the stochastic error.[118] Unfortunately, this error does not account for the bias introduced by the initiator and phaseless approximations.

2.3.4 Incremental Methods

The fourth group of approximate FCI methods are the incremental methods which make use of the many-body expansion to directly approximate energies and properties while circumventing the actual approximation of the wave function. To illustrate these methods, Section 2.4 presents the MBE-FCI method.

2.3.5 Other Methods

The variational 2-RDM (v2RDM)[374–384] approach also explicitly avoids the construction of the FCI wave function in Equation (2.9) by directly targeting the 1- and 2-RDMs since these quantities provide enough information to construct the electronic energy through Equation (2.11). Accordingly, a solution to the electronic structure problem can be obtained through variational optimization of the RDMs under certain constraints, the so-called N-representability conditions.[374,375,377,385–388] Fulfilling all conditions proves to be as expensive as solving the FCI equations directly but alternatively the FCI limit can be approached approximately by only explicitly enforcing a certain number of constraints. The resulting v2RDM method can approximate FCI results at polynomial scaling and has also been

[b] The imaginary time propagator is Trotter-decomposed.[361,362] The one-electron part of the Hamiltonian can be exactly applied to a Slater determinant which will yield another Slater determinant due to Thouless theorem.[363,364] The two-electron part is rewritten as a square of one-electron operators through a Cholesky decomposition of the two-electron integrals.[365,366] A Hubbard–Stratonovich transformation[367,368] can then be used to transform these operators and to reformulate the system of interacting electrons to a system of non-interacting electrons coupled with random auxiliary fields.[360]

applied to the CASCI step in CASSCF calculations for the description of large active spaces.[389–391] The v2RDM approach can generally be applied to both statically and dynamically correlated systems but unfortunately has issues with the correct description of bond dissociation processes.[392–394]

In addition, multiple hybrid methods exist that combine approximate FCI methods with the conventional methods introduced in Section 2.2 or with other approximate FCI methods. One such example is the cluster-analysis-driven FCIQMC method (CAD-FCIQMC)[395–398] which tries to leverage the fact that the CC energy only depends on the $\hat{T}_1$ and $\hat{T}_2$ amplitudes. The exact determination of these amplitudes from the respective amplitude equations will reproduce the exact FCI energy. Unfortunately, the solution of the $\hat{T}_1$ and $\hat{T}_2$ amplitude equations requires knowledge of the $\hat{T}_3$ and $\hat{T}_4$ amplitudes. Approximations for these amplitudes can be determined from the cluster analysis of the FCIQMC wave function.[396] A major advantage of this approach stems from the deterministic treatment of the single and double CC amplitudes and the fact that the stochastic error is only restricted to the comparatively small triples and quadruples contributions. As a result, the CAD-FCIQMC method will accelerate convergence of FCIQMC towards the FCI limit.

Another hybrid method, full coupled-cluster reduction (FCCR)[399,400] targets the FCI energy through an iterative expansion of the CC expansion manifold such that higher excitations are only added to the projection manifold when the respective amplitude equation of the single commutator of the current set of cluster operators produces an amplitude above a certain threshold. In addition, only amplitudes and products of amplitudes above a larger threshold are considered during the solution of the amplitude equations for a given projection manifold.[399] The resulting method can be interpreted as a selected CC method that preserves the underlying desirable properties of the CC expansion such as size-consistency and fast convergence towards the FCI limit. Accurate results for large systems unfortunately require perturbative error corrections.[400]

2.4 Many-Body Expanded Full Configuration Interaction

The theory behind the incremental methods finds its roots in the observation that the energy is generally not countably additive whenever many particles in a quantum system interact. The addition of particles to a quantum system will not only add the interactions between these particles but also influence the interaction between the existing particles and vice versa. The energy of such a supersystem can be written as follows:

$$E_{AB} = E_A + E_B + (E_{AB} - E_A - E_B). \tag{2.66}$$

The expression $(E_{AB} - E_A - E_B)$ describes the energy correction ΔE_{AB} due to the interaction of the fragments A and B and originates from the nonadditivity of the energy. Generalizing this assumption and replacing the subsystems by a number of fragments (indexed using p, q, ...) in a molecular system will lead to the general form of the MBE[23,24,27,31,48,49]

$$\begin{aligned} E &= E^{(1)} + E^{(2)} + E^{(3)} + E^{(4)} + \dots \\ &= \sum_p \epsilon_p + \sum_{p<q} \Delta\epsilon_{pq} + \sum_{p<q<r} \Delta\epsilon_{pqr} + \sum_{p<q<r<s} \Delta\epsilon_{pqrs} + \dots \end{aligned} \tag{2.67}$$

which enables the decomposition of any eigenvalue of the Hamiltonian matrix of a molecular system into contributions $E^{(n)}$ from a varying number of n fragments. These fragments are the objects of the expansion, and they must be chosen to describe a set of distinct particles and a corresponding set of linearly independent basis functions that span the function space of interest. One popular choice are

the sets of atomic orbitals located at the atoms of individual molecules and the corresponding electrons of those atoms.[48–51] Another common choice for the objects of the expansion that is prevalent for the solution of the electronic Schrödinger equation and will be used throughout this thesis are the molecular orbitals from a preceding Hartree-Fock calculation on the full molecular system.[23,24,27,31] This choice defines a set of occupied and virtual orbitals and therefore also automatically divides the electrons among the fragments. The contributions at different orders of the MBE are constructed from increments of all possible orbital combinations that involve the same number of orbitals. The individual increments[23,24,27,31,48,49]

$$\begin{aligned} \Delta\epsilon_{pq} &= \epsilon_{pq} - \epsilon_p - \epsilon_q \\ \Delta\epsilon_{pqr} &= \epsilon_{pqr} - \Delta\epsilon_{pq} - \Delta\epsilon_{pr} - \Delta\epsilon_{qr} - \epsilon_p - \epsilon_q - \epsilon_r \\ &\vdots \end{aligned} \tag{2.68}$$

are defined recursively on the basis of increments from previous orders and describe the mutually exclusive interaction of the combined tuple of orbitals. The energies (ϵ_p, ϵ_{pq}, …) are calculated by solving the electronic structure problem involving the corresponding orbitals and electrons. In general, the MBE is not applied to the electronic energy itself since the HF energy is routinely available even for larger systems. Instead, the correlation energy is targeted by performing CASCI calculations involving the increment orbitals in the active space.[23,24,27] Increments of fragments involving no electrons (such as increments of only virtual HF orbitals) will automatically vanish. The Hartree-Fock energy is then subtracted from the CASCI energies to form the energies

$$\begin{aligned} \epsilon_p &= E_p - E_{\mathrm{HF}} \\ \epsilon_{pq} &= E_{pq} - E_{\mathrm{HF}} \\ &\vdots \end{aligned} \tag{2.69}$$

that are used to construct the increments in Equation (2.68). Doing so will cause all increments involving twice as many electrons as orbitals (increments of only occupied HF orbitals) to vanish due to the fact that the HF determinant already perfectly describes the electronic wave function in this orbital basis.

2.4.1 Reference and Expansion Spaces

In early applications of orbital-based MBE correlation theory, the expansion objects in Equation (2.67) were limited to the occupied orbitals in the molecular system.[24,27,31] For the individual increments, the occupied orbitals are treated in a *bath* of all virtual orbitals. Later work turned this definition around and performed an expansion of the virtual orbitals instead.[23,40,41] This different treatment of the orbitals in the MBE warrants a distinct classification of the orbital space into a so-called reference and a corresponding expansion space which generalizes both flavors of MBE-FCI.[42] The reference space orbitals are always included in every individual increment calculation while the expansion space orbitals form the expansion objects. As a result, the reference space correlation energy E_{ref} has to be added to the MBE master equation (Equation (2.67))[42]

$$\begin{aligned} E_{\mathrm{corr}} &= E_{\mathrm{ref}} + E^{(1)} + E^{(2)} + E^{(3)} + E^{(4)} + \dots \\ &= E_{\mathrm{ref}} + \sum_p \epsilon_p + \sum_{p<q} \Delta\epsilon_{pq} + \sum_{p<q<r} \Delta\epsilon_{pqr} + \sum_{p<q<r<s} \Delta\epsilon_{pqrs} + \dots \end{aligned} \tag{2.70}$$

to obtain the desired correlation energy. The reference space correlation energy is subtracted from the individual CASCI energies

$$\begin{aligned} \epsilon_p &= E_p - E_{\text{ref}} \\ \epsilon_{pq} &= E_{pq} - E_{\text{ref}} \\ &\vdots \end{aligned} \tag{2.71}$$

to calculate the increments according to Equation (2.68) and to avoid double counting of the reference space contributions. Four different edge cases for orbital partitioning can be defined as showcased in Figure 2.1. The full reference space in Figure 2.1a encompasses the entire orbital space and the reference space alone reproduces the full correlation energy of the entire system. As the expansion space is empty, the system is not described through an MBE but instead through the initial reference space calculation which corresponds to a regular FCI calculation. This method is not practical for all but the smallest of systems before the factorial scaling of the FCI method makes calculations infeasible. The partitioning in Figure 2.1b corresponds to the early applications of the MBE to the correlation energy by Nesbet[27] and Stoll[31] and is for this reason referred to as Type-1 MBE-FCI. The resulting method is most useful for electron-rich systems in small basis sets where the number of occupied orbitals is equal to or greater than the number of virtual orbitals. The reverse partitioning in Figure 2.1c was first used by Eriksen, Lipparini, and Gauss[23,40,41] for the treatment of systems in larger basis sets. Increasing the basis set size for a given system only increases the number of increment calculations while the size of the individual CASCI calculations is held constant. This method is referred to as Type-2 MBE-FCI. The last edge case described in Figure 2.1d is the most unbiased application of the MBE to the treatment of the electron correlation problem. Both occupied and virtual orbitals are treated on an equal footing, and the MBE is applied to the full orbital space. As a result, the expansion[42]

$$E_{\text{corr}} = E^{(2)} + E^{(3)} + E^{(4)} + \ldots = \sum_i \sum_a \epsilon_{ia} + \sum_{i<j} \sum_a \Delta\epsilon_{ija} + \sum_i \sum_{a<b} \Delta\epsilon_{iab} + \ldots \tag{2.72}$$

starts at the second expansion order since active spaces of single occupied or virtual orbitals do not produce a valid correlation energy. Both empty reference spaces and all partitionings in between these four edge cases are referred to as Type-3 MBE-FCI.[42] Intermediate partitionings usually require some greater insight into the nature of the electron correlation problem at hand to provide an

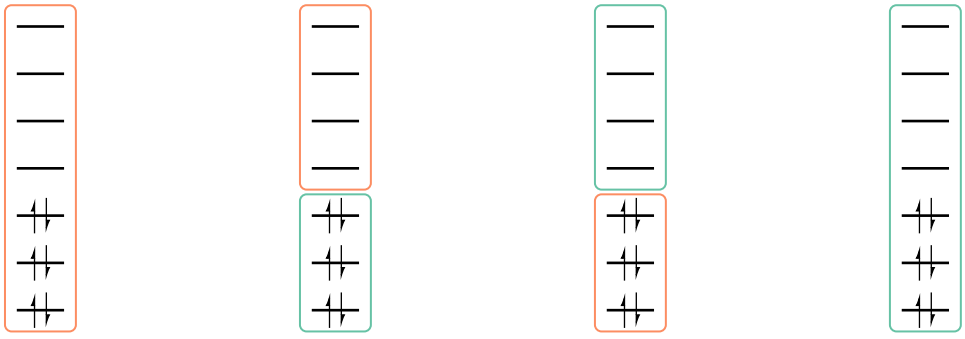

(a) Full reference space
Empty expansion space
Regular FCI calculation

(b) Virtual reference space
Occupied expansion space
Type-1 MBE-FCI

(c) Occupied reference space
Virtual expansion space
Type-2 MBE-FCI

(d) Empty reference space
Full expansion space
Type-3 MBE-FCI

Figure 2.1: Different reference and expansion space choices in MBE-FCI.

additional benefit beyond the common partitionings described in Figure 2.1. Nevertheless, such reference space choices can be of utter importance whenever the HF reference is qualitatively wrong. Choosing such reference spaces is strongly correlated to the difficult task of choosing active spaces for the purpose of optimizing CASSCF wave functions.

2.4.2 Scaling

The many-body expansion suffers from the curse of dimensionality as much as any exact formulation of FCI theory. Rewriting the energy as in Equation (2.67) will only be of use when the mutual interaction between the different fragments decreases as the number of fragments is increased. Unless the expansion converges quickly and is properly truncated, a combinatorial explosion will lead to an overwhelming number of small calculations that are too numerous to compute and will lead to numerical errors due to finite convergence criteria of the Davidson algorithm used for the individual CASCI calculations and limited floating point precision. If instead convergence can be reached before the number of calculations grows too large, the MBE turns out to be a powerful method for the approximation of FCI energies and properties. Fortunately, electron correlation is a nearly pairwise additive process which enables the truncation of the MBE after few orders without large losses in accuracy.[91] Nevertheless, reaching an overwhelming number of increment calculations before convergence is a common bottleneck for empty reference space MBE-FCI calculations because these often exhibit many expansion objects. For closed-shell systems, the total number of non-vanishing increments

$$N_{\text{inc}}^{(n)} = \sum_{n_{\text{occ}}=1}^{\min(n-1,N/2)} \binom{N/2}{n_{\text{occ}}} \binom{M - N/2}{n - n_{\text{occ}}} \tag{2.73}$$

at a given order n can be calculated by summing over possible occupations n_{occ} in the system and multiplying the binomial coefficients $\binom{N}{n_{\text{occ}}}$ and $\binom{M-N/2}{n-n_{\text{occ}}}$ where N describes the number of electrons while M describes the total number of spatial orbitals.

The leading contribution of empty reference space MBE-FCI in Equation (2.73)

$$O(M^{n-1}N/2) \tag{2.74}$$

is polynomial with respect to system size and the exponent corresponds to the order of the expansion. If the expansion can be truncated at early orders and if this truncation order does not increase with system size, MBE-FCI will yield a method with polynomial scaling and a favorable exponent. In addition, the cost of the individual CASCI calculations[c] rises factorially with the number of increment orbitals and electrons which gives the full expansion a complicated scaling relationship by affecting the prefactor through the following expression:

$$\binom{n}{n_{\text{occ}}}^2 n_{\text{occ}}^2 (n - n_{\text{occ}})^2. \tag{2.75}$$

For high expansion orders, the resulting prefactor can become large enough to significantly limit the applicability of MBE-FCI. While choosing a reference space will lower the number of increments by reducing the number of expansion space orbitals, the general scaling with respect to the expansion space orbitals will remain the same. Additionally, adding orbitals to the reference space will make individual CASCI calculations more expensive and therefore affect the prefactor in Equation (2.75). Carefully choosing reference and expansion spaces for an efficient computation will therefore require

[c] Generally $O\left(\binom{M}{N/2}^2 (N/2)^2 (M - N/2)^2\right)$ for closed-shell systems

striking a balance between the computational effort of the individual CASCI calculations and the number of increment calculations that need to be performed. Additionally, these undesirable scaling properties of the MBE motivate the need to utilize and exploit any available information to reduce the number of calculations by avoiding redundant calculations or calculations that result in negligible contributions and to properly estimate the error of any contributions that are not explicitly calculated.

2.4.3 Base Models

Faster MBE convergence can be achieved by utilizing so-called base models of conventional quantum chemical methods such as CC.[40] The correlation energy of the chosen approximate method is calculated for the full system and for the individual increments. The increment base model energy is subtracted from the increment energy. In the same way that reference space MBE-FCI targets the gap between the CASCI energy of the reference space and the full correlation energy, the base model MBE-FCI targets the gap between the base model energy and the FCI energy which can be small for dynamically correlated systems and high-level CC base models. As a result, the magnitude of individual increments will be reduced and MBE convergence is accelerated. This approach significantly reduces the number of calculations that are necessary to reach a certain accuracy. The base model energy of the full system can be added back onto the resulting energy to obtain the full correlation energy of the system.

2.4.4 Recursive Formulation

Constructing the MBE from Equation (2.70) will require saving previous-order increments to recursively construct the increments at the current order through Equation (2.71). An alternative is to use a recursive version of the MBE[50]

$$E_{\text{corr}}^{(n)} = \epsilon_{\Sigma}^{(n)} - \sum_{m=1}^{n-1} \binom{M-n}{M-m} E_{\text{corr}}^{(m)} \tag{2.76}$$

which yields the nth-order contribution to the correlation energy $E_{\text{corr}}^{(n)}$ from the sum of all CASCI correlation energies $\epsilon_{\Sigma}^{(n)}$ at the current order and from the previous-order correlation energy contributions. This comes at the disadvantage that individual, potentially vanishing increments can no longer be removed during the calculation and the expansion can only be truncated after some given order.

2.5 Basis Sets

The AOs that are used to construct the MOs in Equation (2.26) constitute another common source of error in electronic structure calculations. In practice, finite sets of linearly independent basis functions are used which can be systematically improved by adding additional basis functions in an attempt to approach the complete basis set limit. The functional form of these basis functions determines the ability of the basis set to describe the MOs of arbitrary molecules and to produce accurate results even for small numbers of basis functions. AO basis functions[180]

$$\chi(\mathbf{r}) = R_l(r) Y_{l,m_l}(\theta, \phi) \tag{2.77}$$

are constructed as a product of a spherical harmonic function $Y_{l,m_l}(\theta, \phi)$ and a radial function $R_l(r)$. The quantities l and m_l describe the orbital angular momentum quantum number and orbital magnetic quantum number with respect to the spherical symmetry of the atom for which these basis functions are defined. The physically correct parametrization of the radial function results in so-called Slater-type orbitals.[401] For practical reasons, these are often replaced by the computationally more efficient contracted Gaussian-type orbitals[402,403]

$$R_l(r) = r^l \sum_{p=1}^{P} d_p N(l, \alpha_p) \exp(-\alpha_p r^2) \tag{2.78}$$

which attempt to approximate the Slater function through linear combinations of P primitive Gaussian functions with exponent α_p and coefficient d_p. The constant $N(l, \alpha_p)$ ensures normalization of the individual Gaussian functions. Standard AO basis sets in quantum chemistry provide a set of basis functions with optimized exponents and contraction coefficients for a given number of primitive Gaussian functions for individual elements across the periodic table. The common Dunning correlation-consistent basis sets of the form cc-pVXZ[404–407] will include a single basis function for every orbital in the core electron shell and X basis functions for every orbital in the valence electron shell. Additionally, polarization functions of higher quantum number l are added such that the total number of basis functions per quantum number l decreases by one as the angular momentum increases until only a single basis function is included for the maximum angular momentum quantum number. The resulting basis sets are designed such that the HF and correlation energies can be extrapolated to the complete basis set limit with empirical relationships.[404]

2.6 Molecular Orbital Bases

In addition to canonical orbitals that are readily available from a preliminary HF calculation, other MO bases are often useful in approximate quantum chemical calculations as they can improve sparsity in the involved tensors which can make approximations significantly more effective. These MO bases can be constructed as linear combinations of any given orbital basis. If this linear combination is a unitary transformation of an orthonormal basis such as the canonical orbital basis or the orthogonalized AO basis, the resulting basis will preserve the orthonormal qualities of the original basis. In addition, if the linear combination only involves separate unitary transformations of the occupied and virtual subspaces of the canonical orbital basis, both the HF and the correlation energy will remain invariant to this transformation. This property is irrelevant in the FCI limit as the FCI energy is invariant with respect to orbital rotation. Orbitals of this type are generally coined HF orbitals and these fulfill the Brillouin theorem. A variety of different HF orbitals which can be used to accelerate convergence of MBE-FCI are introduced in this section. CC correlation energies are also generally invariant with respect to which HF orbitals are used. The same statement does not hold true for standard formulations of CC methods with non-iterative perturbative corrections such as CCSD(T) or CCSDT(Q). For these methods, non-canonical MOs will require an iterative solution.[408] While using non-canonical MOs for MBE-FCI with CC base models and employing the non-iterative formulation by replacing orbital energies with diagonal Fock matrix elements is theoretically questionable, the ability of the resulting model to mirror the FCI description is of much greater importance in the MBE-FCI context.[40] To perform calculations of this kind, the base model calculation on the entire system also needs to be performed by employing the same non-canonical MO basis.

2.6.1 Natural Orbitals

The natural orbital (NO) basis can be constructed for arbitrary quantum chemical methods whenever a 1-RDM is available. The orbital basis is defined through diagonalization of the 1-RDM[385]

$$\boldsymbol{\eta} = \mathbf{U}^\dagger \mathbf{D} \mathbf{U} \tag{2.79}$$

where $\mathbf{U}$ describes the unitary matrix from which the NO coefficients can be constructed. The diagonal elements of the diagonal matrix $\boldsymbol{\eta}$ describe the fractional occupation numbers of the NOs for the respective quantum chemical method. If the NOs are occupied according to their occupation numbers, the resulting determinant provides the best possible single-determinant description of the original wave function from which the 1-RDM was constructed. For this reason, NOs with close to integer occupation numbers are not important for the description of electron correlation in the system. The NO basis will generally provide a compact representation of the underlying wave function.[385,409]

For an RHF wave function, the canonical orbitals describe the NOs since the 1-RDM is already diagonal. To improve upon this orbital basis, the unrestricted natural orbital (UNO) basis can be constructed by diagonalizing the sum of α and β 1-RDMs from a UHF calculation.[279] This will yield a restricted orbital basis that recovers some electron correlation through the UHF solution. UNOs generally provide a much better initial guess for CASSCF calculations than canonical orbitals. In addition, the importance of a UNO for the description of correlation in a system can be gauged through the deviation of its occupation number from integer values. Hence, UNOs with occupation numbers between 0.02 and 1.98 are commonly used as active orbitals in CASSCF in an attempt to automate the active space selection process.[116,279,280] The resulting orbital criterion has also been extended to more accurate correlated wave functions.[410–412]

2.6.2 Localized Molecular Orbitals

Localized molecular orbitals (LMOs) are optimized to be spatially separated which decreases the contribution of any quantities related to the orbital overlap whenever a sufficient distance between the orbitals is reached. This also applies to the increments of well-separated LMOs which qualifies these as an effective basis for the expansion space of MBE-FCI and MBE-CC calculations.[41,42] The locality of an LMO ϕ_p can be quantified through the second- and fourth-moment orbital spread[413–415]

$$\sigma_n^p = \sqrt[n]{\langle p \,|\, (\mathbf{r} - \langle p \,|\, \mathbf{r} \,|\, p \rangle)^n \,|\, p \rangle} \qquad (n = 2, 4). \tag{2.80}$$

While localization procedures often only involve separate unitary transformations of the occupied and virtual subspaces, non-HF, non-orthogonal, and overcomplete orbital bases have been applied to overcome the computational effort required to treat larger molecular systems.[33,408,416–426] The removal of the orthogonality constraint avoids the appearance of so-called orthogonalization tails which can limit the locality of the optimized basis.[427] This can be important for the virtual orbital space as virtual orbitals are notoriously difficult to localize. Unfortunately, the usage of non-orthogonal and overcomplete bases significantly complicates the calculation of matrix elements from the corresponding Slater determinants as the Slater-Condon rules cannot be applied. For this reason, only HF LMOs will be used in this thesis.

Foster-Boys Localized Orbitals

The Foster-Boys (FB) localization procedure[428] minimizes the square of the second-moment orbital spread

$$\mathcal{J} = \left\langle p \left| \left(\mathbf{r} - \langle p \,|\, \mathbf{r} \,|\, p \rangle\right)^2 \right| p \right\rangle . \tag{2.81}$$

The resulting orbitals generally do not preserve the separation of the σ- and π-orbitals for planar systems.[429] Additional localization procedures which minimize the fourth-moment orbital spread also exist which penalize the tails of the resulting LMOs to a much greater extent.[415,430]

Pipek-Mezey Localized Orbitals

Pipek-Mezey (PM) LMOs[429,431] are obtained by maximizing the partial charges located at the nuclei

$$\mathcal{J} = \sum_A \sum_i \left| q_i^A \right|^2 \tag{2.82}$$

where q_i^A describes the contribution of orbital ϕ_i to the partial charge at atom A. Since partial charges are a chemical concept that is not related to any observable that can be assigned to an operator, many partial charge estimates have been suggested in the literature. The original PM method[429,431] is based on Mulliken charges[432] which assign electrons according to the AO density matrix of AOs centered at the atoms. Another alternative are so-called Löwdin charges[433,434] which transform the density matrix into the symmetrically orthogonalized AO basis and trace over the AOs centered at the atoms in question. In this thesis, PM localization is based on meta-Löwdin charges.[d] The actual choice of the partial charge estimate does not significantly affect the visual appearance of the resulting PM orbitals.[437]

The main advantage of the PM method is the fact that the σ- and π-orbitals are not mixed during the optimization which improves the interpretability of the resulting orbital basis.[429]

Edmiston-Ruedenberg Localized Orbitals

Another type of localization method, the Edmiston-Ruedenberg (ER) procedure[438,439] localizes the orbitals by minimizing the interorbital repulsion which is equivalent to maximizing the orbital self-repulsion

$$\mathcal{J} = \sum_p \langle pp|pp \rangle . \tag{2.83}$$

In practice, this localization procedure is generally avoided due to its prohibitive scaling ($O(M^5)$) and the fact that the spatial locality of ER LMOs is often inferior to those obtained by the PM and FB methods when second- and fourth-moment orbital spreads are compared.[440–442]

[d] Meta-Löwdin charges[435] are equivalent to Löwdin charges except that the core, valence, and Rydberg AO subspaces are separately symmetrically orthogonalized. The orbitals are classified according to these AO subspaces by transforming the AO basis into the unique natural AO basis.[436] The core orbitals are then symmetrically orthogonalized and projected out from the valence and the Rydberg natural AO subspace. This procedure is repeated for the remaining subspaces.[435]

2.6.3 CASSCF Orbitals

CASSCF orbitals minimize the CASCI energy of a quantum chemical system with respect to orbital rotation by accumulating as much electron correlation as possible inside the active space. For this reason, CASSCF orbitals are prime candidates for the separation of the reference and expansion spaces in MBE-FCI. For MBE-CC calculations, this orbital basis is unsuitable due to the fact that CASSCF orbitals do not constitute HF orbitals which makes both the HF and CC energies ill-defined.

2.7 Molecular Symmetry

Another common enhancement in quantum chemical calculations is the exploitation of molecular symmetry. Small molecular systems often exhibit symmetry which can be classified through group theory. The nuclear coordinates of these molecules are related through symmetry operations $\hat{G}$ of the molecular point group. As a result, these symmetric molecules exhibit a degree of redundancy which can be exploited in electronic structure calculations.

The MOs produced after convergence of an HF optimization are often automatically symmetry-adapted unless symmetry-broken solutions yield a lower energy.[197,363,443–445] In this case, an HF solution of appropriate symmetry can be obtained by symmetry-adapting the AOs[446] and restricting the occupation accordingly. If the molecular point group is Abelian, the application of a symmetry operation $\hat{G}$ to one of these MOs

$$\hat{G}\phi_p = \chi\phi_p \tag{2.84}$$

will produce the same orbital times a factor. This factor is called a character χ of an irreducible representation Γ which describes the symmetry of the MO. Non-Abelian point groups have multi-dimensional irreducible representations, such that sets of multiple orbitals can be eigenfunctions of the symmetry operations. For symmetric molecules in Abelian point groups, integrals of totally-symmetric operators (such as $\frac{1}{r_{12}}$)

$$\left\langle pq \middle| \hat{\Omega} \middle| rs \right\rangle = 0 \Leftarrow \Gamma(\phi_p) \otimes \Gamma(\phi_q) \otimes \Gamma(\hat{\Omega}) \otimes \Gamma(\phi_r) \otimes \Gamma(\phi_s) \neq \Gamma_{\text{symm}} \tag{2.85}$$

will vanish unless the direct product of the irreducible representations of the MOs is also totally symmetric.[133,446,447] Due to the structure of the equations for iteratively obtaining the CI coefficients and CC amplitudes from these integrals during quantum chemical calculations, these tensors will also not contribute unless the direct product of the irreducible representations of all involved orbitals is totally symmetric. Both the integrals and the coefficients can be sorted by the irreducible representations of the orbitals such that a block structure will emerge. This block structure can be exploited to reduce the memory required for the storage of these quantities and the computational effort necessary to contract them.[134,191]

In most quantum chemical codes, symmetry is only exploited for subgroups of the D_{2h} point group which are Abelian and for which the irreducible representations are real. The exploitation for Abelian point groups with complex irreducible representations requires either complex orbitals or two-dimensional irreducible representations both of which are usually avoided in conventional algorithms. Non-Abelian point groups also introduce multidimensional irreducible representations and for these often highly symmetrical systems, much room for potential speed-ups is often neglected due to the complexity of the resulting implementation.

Abelian point-group symmetry with real irreducible representations can also be exploited in the individual CASCI calculations of MBE-FCI if a suitable CASCI solver is used. Unfortunately, it is only

applicable to the use of symmetry-adapted orbitals such as canonical or natural MOs. In MBE-FCI, LMOs are often used to accelerate the convergence of the MBE. These orbitals do not transform as irreducible representations of the point group and as a result, the vanishing integral theorem does not hold.

3 The PyMBE Program

The PyMBE program is a statically typed Python package for the description of electron correlation through many-body expansions.[110] The program was originally written by [redacted] and has since been restructured and extended to accommodate the extensions introduced in this thesis. The code heavily relies on the *Numerical Python* (NumPy) library[448] for storing large, multidimensional arrays and for the mathematical functions required to handle these. The individual quantum chemical calculations are performed using the *Python-based Simulations of Chemistry Framework* (PySCF) electronic structure modules[449,450] and modified versions of the *ecc* and *ncc* modules from the *Coupled-Cluster techniques for Computational Chemistry* (CFOUR) program package.[451,452] The code has been parallelized using the *Message Passing Interface* (MPI) standard[453] with the *MPI for Python* (mpi4py) package.[454–457] The general structure of the PyMBE program is described in this chapter.

The PyMBE program is written in an object-oriented manner and can be started from a Python script. All input data such as system information, integrals, and algorithmic settings are passed to the initialization function of an `MBE` class and are stored as attributes of the resulting object. An actual calculation is started by calling the `MBE` member function `kernel` which initially performs a sanity check of all `MBE` attributes to catch possible user input errors. Afterwards, the attributes are saved to a restart folder which can be used to restart a calculation that has been terminated. To ensure all data is available to every process, the `MBE` attributes are broadcasted among all processes. Large arrays such as integrals are stored in shared memory according to the MPI-3 standard and are accessible to all processes on a shared-memory node. Every process then creates its own expansion object that is a member of the `ExpCls` class. The `ExpCls` class has multiple derived classes which have MBE target specific implementations of the many abstract methods that are member functions of the `ExpCls` class. The class hierarchy tree is showcased in Figure 3.1. The `RDMExpCls` and `GenFockExpCls` classes

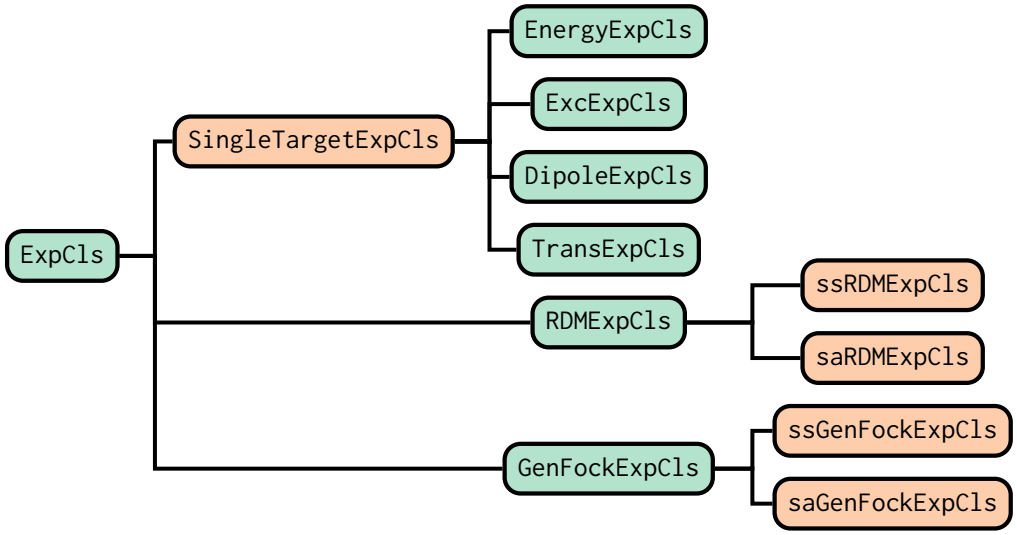

Figure 3.1: Class hierarchy of the `ExpCls` class in the PyMBE program.

additionally have derived classes for the functions belonging to state-specific and state-averaged implementations. After the respective `ExpCls` class is initialized, its `driver` member function is called which starts the calculation at the first MBE order.

3.1 Expansion Driver

Specific implementations of the `driver` function exist for the master and worker processes. The sequence of tasks in the master `driver` function are presented in Figure 3.2. At every order n, the algorithm starts by calculating the number of orbital tuples at the current order. This is an important step to ensure that the arrays for the storage of the increments can be allocated accordingly. This step is followed by the actual calculation of the increments. In PyMBE, the truncation of the expansion is achieved through orbital-based screening. Therefore, after the calculation of the increments, orbitals whose contributions are deemed unnecessary for the remaining orders are screened away and removed from the expansion space. The increments that include these orbitals no longer need to be stored and are removed from memory in the purging step. The intrinsics of these functions will

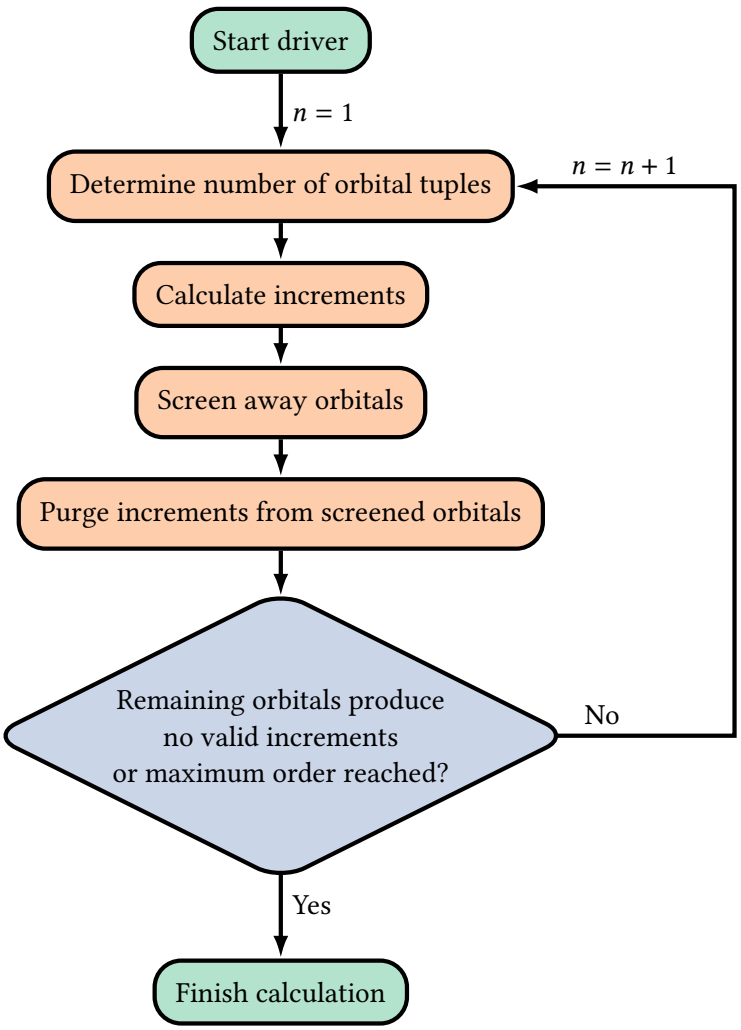

Figure 3.2: Flowchart of the MBE driver in the `ExpCls` class.

be discussed in the upcoming sections. While the master process performs these steps, the worker `driver` function waits for the master `driver` function to broadcast a *wake-up* message whenever help is needed on performance-critical tasks such as increment calculation or purging.

3.1.1 Calculation of Number of Orbital Tuples

At the beginning of every MBE order, the theoretical number of tuples for every order of the entire MBE

$$N_{\text{theo}} = \binom{M_{\text{exp}}}{n} \tag{3.1}$$

can be easily calculated. M_{exp} is the number of orbitals in the initial expansion space. Whenever orbitals are screened away at later orders in the MBE, N_{theo} decreases because M_{exp} is replaced by a reduced expansion space. The number of tuples which will produce non-vanishing increments

$$N_{\text{non-van}} = \sum_{n_{\text{occ}}=0, n_{\text{occ}} \notin V_{\text{occ}}}^{\min(n, N/2)} \binom{N/2}{n_{\text{occ}}} \binom{M_{\text{exp}} - N/2}{n - n_{\text{occ}}} \tag{3.2}$$

describes all those orbital combinations in the screened number of tuples that are not vanishing due to occupation. The set V_{occ} includes all numbers of occupied orbitals that produce active spaces for which correlation energies and properties vanish:

- Active spaces in which no excitations are possible
- Active spaces in which only single excitations are possible due to the Brillouin theorem (Equation (2.30)) when HF orbitals are used
- Active spaces in which only up to double excitations are possible in MBE-FCI calculations with a CCSD or CCSD(T) base model
- Active spaces in which only up to triple excitations are possible in MBE-FCI calculations with a CCSDT or CCSDT(Q) base model
- Active spaces in which only up to quadruple excitations are possible in MBE-FCI calculations with a CCSDTQ base model

Only the non-vanishing increments are stored in PyMBE. Therefore, the number of increments that need to be stored per MBE order is equal to $N_{\text{non-van}}$ unless LMO symmetry is exploited which will be described in Chapter 8.

3.1.2 Calculation of Increments

After the number of increments has been determined for the current MBE order, the arrays for the storage of the increments can be allocated. These arrays are necessary for the calculation of increments at later orders due to the recursive nature of Equation (2.68). At every order, the increments are stored in an associative array for every possible orbital tuple occupation. Each associative array consists of a hash array and an increment array. The hashes are constructed as a function of the orbital tuple. These arrays are stored in shared memory such that the memory requirements and necessary communication between the individual processes of the algorithm are minimized while all increments remain accessible by every process on a shared-memory node. The orbital combinations that contribute to the MBE are generated with a so-called *generator function*.

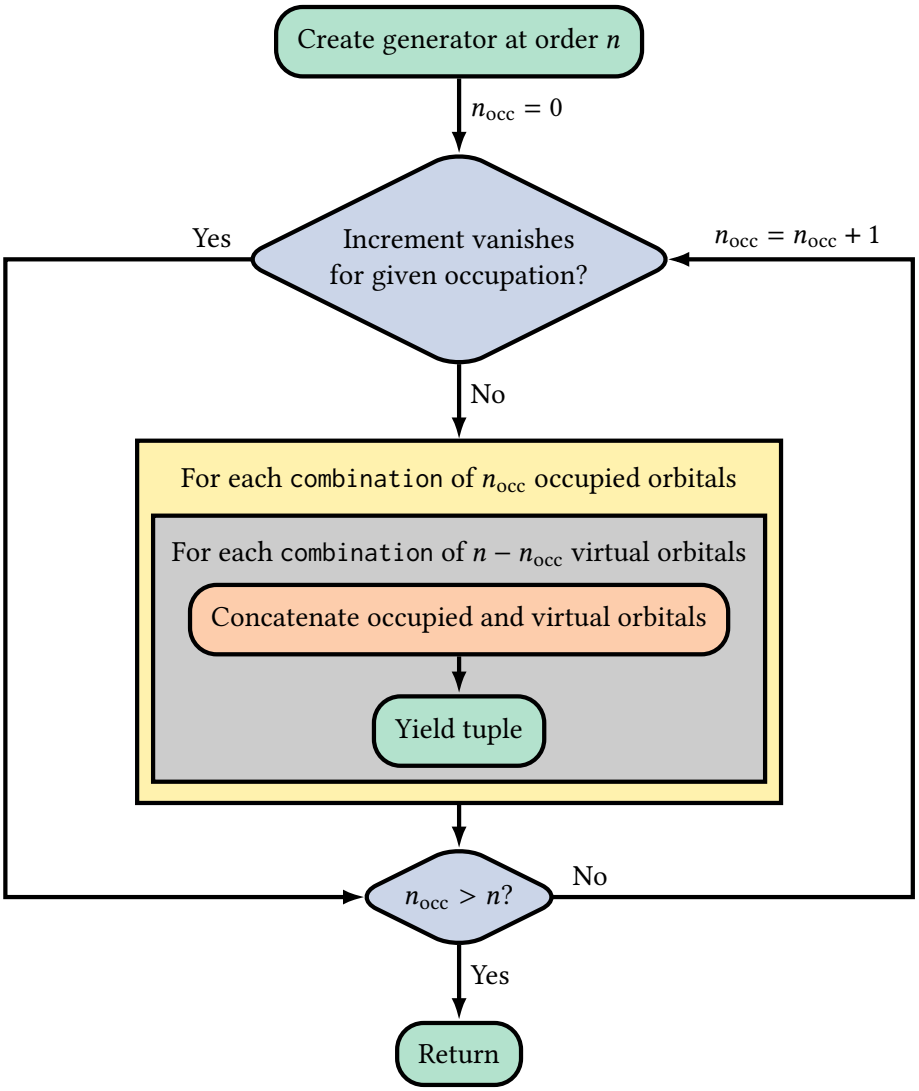

Figure 3.3: Flowchart of the tuple generator function.

These functions generate a new return value every time they are called which avoids storing all possible orbital combinations in memory. The basic generator for the generation of orbital tuples is described in Figure 3.3. The generator function exploits the `combinations` generator from the *itertools* module of the Python standard library which efficiently returns all combinations of a supplied length that can be constructed from an input sequence. The increment calculations are then divided among the processes in a round-robin fashion which will generally be sufficient for load balancing since the active space sizes for all increment calculations at a given MBE order are equal and because the orbital tuple generator function will produce orbital combinations ordered by occupation. If a sufficient number of orbital tuples is available at a given order, all processes will receive a roughly equal number of calculations with an equal number of determinants. The round-robin distribution will also minimize communication between the processes during the increment calculation. After distribution, the CASCI calculation will be started using one of the quantum chemistry backends.

Once the CASCI calculation is complete, increments are calculated by subtracting lower-order subtuple increments according to Equation (2.68). This process is showcased in Figure 3.4. Lower-order subtuples are again generated using the generator function in Figure 3.3 and the increment

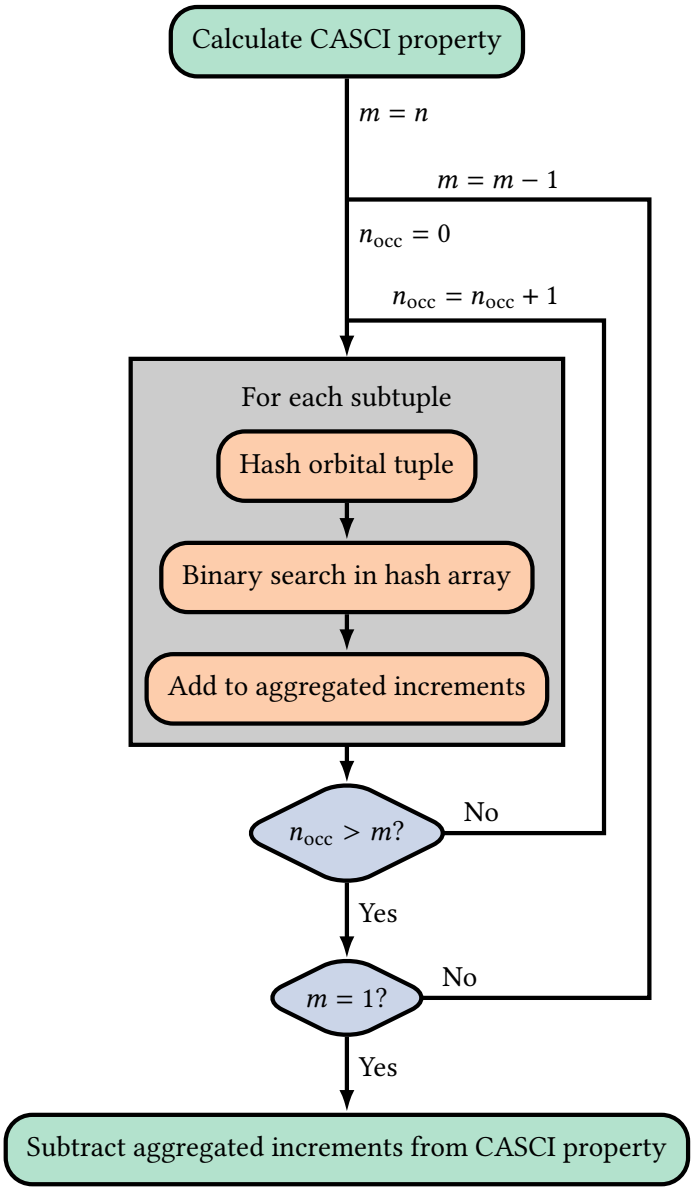

Figure 3.4: Flowchart of increment calculation.

energies are extracted from the increment arrays by locating the insertion index of the subtuple hash in the respective hash array using a binary search algorithm. The calculated increment and the hash generated for the orbital tuple are then appended to increment and hash lists and added to the total MBE property.

To ensure that calculations can be restarted, restart files are written during the increment calculations at a predetermined frequency. Whenever this is done, all processes are synchronized and the increment and hash lists are gathered among all local master processes and written to disk. In addition, all other information about the current MBE order that is necessary to restart the calculation is saved.

After all increments have been calculated, the remaining increments and hashes are gathered and all associative arrays for the current order are written to shared memory. The hash array is sorted, and

the increment array is rearranged accordingly so that increments can be extracted from the hash array using binary search in the screening and purging steps and in the upcoming MBE orders.

Additionally, a modified MBE function was implemented which completely avoids saving any increments to memory. Instead, the MBE energy or property is evaluated through Equation (2.76) while completely avoiding the construction of increments. This comes at the advantage of significantly reduced memory costs which can be necessary for the MBE of non-scalar properties such as RDMs or generalized Fock matrices which scale with system size. Unfortunately, the recursive evaluation of the MBE also completely disallows screening away increments at later MBE orders.

3.1.3 Screening

Efficient evaluation of the MBE requires non-contributing increments to be screened away. In PyMBE, an orbital-based screening procedure is utilized which successively removes orbitals from the expansion space. The main advantage behind orbital-based screening is that the generator in Figure 3.3 can still be used to efficiently generate all orbital tuples that have not been screened away. PyMBE screens away orbitals at a predetermined rate that is defined through a *screening start order* and a *screening percentage*. A certain percentage of the current expansion space with the largest maximum increment magnitude is screened away at every order after the screening start order. Alternative screening proxies such as the sum of the (absolute) increments which include a specific orbital can also be used. While this *fixed* screening procedure enables control over the length of the expansion and over the computational effort necessary to complete the expansion, this scheme will not adapt to the convergence rate of the MBE that might very much differ for individual molecules. For this reason, an *adaptive* screening procedure was implemented in PyMBE and is described in Chapter 7.

Orbital-based screening is based on the assumption that some orbitals will require larger active spaces to accurately describe their correlation with the remaining orbitals than others. Screening away individual orbitals will be more effective for the NO orbital basis as orbitals with near-integer occupation numbers such as core and high-lying virtual orbitals can be screened away much earlier than the orbitals that are variably occupied. Conceptually, this type of screening is similar to frozen NO approaches[47,458–461] as the correlation contributions of low- or high-lying NOs are successively removed after a certain MBE order. For LMO bases, the truncation will not be as effective as the LMOs are designed such that individual increments involving orbitals that are sufficiently separated will vanish. Therefore, it might be possible to avoid individual increment calculations before all increments produced by an orbital can be screened away. This additional, increment-based screening is not currently implemented in PyMBE. After orbitals have been removed from the expansion space, the increments that include these orbitals can be removed from the increment associative arrays in the purging step.

3.1.4 Purging

A generator function is used to generate all orbital tuples that can be constructed from the remaining expansion space orbitals and these will be used to construct new hash and increment lists. This step is parallelized by distributing these orbital tuples among the processes. After all increments and hashes are added to the lists, these are gathered and stored in shared memory. In general, the computational effort required for purging is negligible in comparison to the increment calculation.

3.2 Quantum Chemistry Backends

MBE calculations exhibit high accuracy and performance demands towards the quantum chemistry backends that are used to perform the underlying CASCI and CASCC calculations. While many implementations of MBE-based methods function as script- or driver-based programs that write input files for quantum chemistry program packages, start the corresponding executables, and read the results after completion in order to construct the MBE, there are two major disadvantages of such an approach. First, this out-of-core approach can lead to significant losses in precision which can become problematic when many small numbers are added as is frequently done in the increment calculations and the MBE itself.[80] Second, the input/output (I/O) overhead when writing to disk can become significant since the individual calculations themselves are generally inexpensive. Additionally, the individual calculations themselves should not require any disk I/O since the necessary tensors are generally small enough for the active space sizes in question that these can be stored in memory. For these reasons, MBE programs should invoke efficient in-core algorithms for the increment calculations that are properly interfaced to the MBE driver. The PyMBE program relies on two efficient quantum chemistry backends, the PySCF and the MBECC backend.

3.2.1 PySCF Backend

PyMBE is interfaced with the *fci* and *cc* modules in the PySCF program package. The *fci* package enables efficient determinant-based FCI calculations and can be adapted to the solution of the CASCI problem through Equations (2.37) and (2.38). While the necessary framework also exists in the *casscf* module, the interface in PyMBE is streamlined to the solution of many small CASCI calculations without any unnecessary overhead. The FCI implementation requires an initial guess for the CI vectors. The initial guess for the ground state is constructed by choosing the determinant with the correct symmetry and number of α and β electrons that produces the lowest energy expectation value. For degenerate determinants due to spin, an appropriate configuration is constructed as initial guess to describe the correct spin state. Since the FCI implementation in PySCF is determinant-based and because determinants are only eigenfunctions of the $\hat{S}_z$ operator and not necessarily of the $\hat{S}^2$ operator, the Davidson diagonalization might not stay on the correct spin eigenstate and produce a solution of a different spin.[a] While the CI vector will only describe determinants of a given M_S eigenvalue, linear combinations of these determinants can be eigenfunctions to different $S(S+1)$ eigenvalues. For this reason, the $S(S+1)$ eigenvalue of the produced CI vector is calculated after every CASCI calculation. Whenever the solver does not produce the correct state, the calculation is restarted while applying a second-order spin penalty such that all states of unwanted $S(S+1)$ eigenvalues are shifted to higher energies in the eigenvalue spectrum.[462] The final CI vector is used to calculate the MBE target. The *fci* module in the PySCF backend can be used to calculate (excitation) energies, (transition) dipole moments, 1- and 2-RDMs, and generalized Fock matrices for both open- and closed-shell systems.

The *cc* module in PySCF can be used to perform MBE-CCSD and MBE-CCSD(T) and the corresponding MBE-FCI base model calculations in PyMBE. The *cc* module in the PySCF backend can be used to calculate ground state energies, dipole moments, 1- and 2-RDMs, and generalized Fock matrices for open- and closed-shell systems.

[a] While an appropriate initial guess should guarantee convergence to the correct spin eigenstate by decoupling the spin blocks of the sigma vector, both an inappropriate preconditioner in the Davidson procedure and the accumulation of errors due to limited floating-point precision can in practice lead to spin contamination and therefore result in other, energetically lower spin eigenstates.[462]

3.2.2 MBECC Backend

PyMBE is also interfaced to modified versions of the *ecc* and *ncc* modules from the CFOUR program package which are written in Fortran and C++, respectively. Initial work on the interface to the *ecc* module was done by [redacted] and was finished and extended to the *ncc* module by the author of this thesis. Modified versions of these modules are packaged in the MBECC backend and these diverge from the common design philosophy of the CFOUR program package which uses disk I/O to communicate between the different modules which are compiled as separate executables. The MBECC backend is compiled separately from CFOUR into a dynamic library using the *cmake* build system.[463] The dynamic library can be loaded once in PyMBE and repeatedly called to efficiently perform MBE-CC calculations and the increment CC calculations for MBE-FCI base model calculations. The MBECC backend creates all the necessary data structures such as integral lists and common blocks required by the CFOUR modules and calls all necessary subroutines that are usually executed whenever a CFOUR executable is started. All routines that facilitate disk I/O were replaced by in-core versions. In addition, unnecessary steps in both modules that can affect runtimes for small systems have been removed. After completion, the energy and a convergence boolean is returned through the interface.

The interface to the *ecc* module is currently limited to closed-shell CCSD, CCSD(T), and CCSDT ground state energies. The interface to the *ncc* module is currently limited to closed-shell CCSD, CCSD(T), CCSDT, CCSDT(Q), and CCSDTQ ground state energies. Both modules are generally faster than the respective *cc* module in PySCF. The *ecc* module is often faster than the *ncc* module in the MBECC backend for the small calculations that are required in MBE calculations.

4 Treating Large Active Spaces with MBE-CASSCF

The conventional CASSCF method is limited to active space sizes of around 22 electrons in 22 orbitals due to the factorial scaling of the CASCI step.[192] This restriction can be alleviated by replacing the standard CASCI solver with an approximate CASCI solver. As described in Section 2.3, many approximate FCI methods have been coupled to standard CASSCF optimization algorithms to increase the applicability of the CASSCF method to systems that require larger active spaces.[113,114,269,304–306,321–323,325,327,352,353,389–391] A variety of alternative approaches, which directly modify the CASSCF procedure, exist for the treatment of large active spaces.[192,235,464–475] In this chapter, the MBE-FCI method is adapted such that it can be utilized as a replacement for the CASCI solver in first-order CASSCF algorithms. The work in this chapter was published in Ref. 476.

4.1 Theory

First-order CASSCF algorithms require orbital gradient information which can be extracted from the CI vector in the CASCI step through Equation (2.42). When an approximate CASCI solver is used, this wave function information has to be obtained from the respective approximate CASCI method. Incremental methods such as MBE-FCI do not yield an approximation of the wave function itself but instead directly approximate a given property such as the 1- and 2-RDMs of the active space orbitals

$$D_{uv} = D_{uv}^{\mathrm{ref}} + \sum_{u' \in \mathrm{CAS}} (\mathbf{D}_{u'})_{uv} + \sum_{u'<v' \in \mathrm{CAS}} (\Delta\mathbf{D}_{u'v'})_{uv} + \sum_{u'<v'<w' \in \mathrm{CAS}} (\Delta\mathbf{D}_{u'v'w'})_{uv} + \dots \tag{4.1}$$

$$\begin{aligned} d_{uvwx} = d_{uvwx}^{\mathrm{ref}} &+ \sum_{u' \in \mathrm{CAS}} (\mathbf{d}_{u'})_{uvwx} + \sum_{u'<v' \in \mathrm{CAS}} (\Delta\mathbf{d}_{u'v'})_{uvwx} \\ &+ \sum_{u'<v'<w' \in \mathrm{CAS}} (\Delta\mathbf{d}_{u'v'w'})_{uvwx} + \dots \end{aligned} \tag{4.2}$$

which are needed to calculate the generalized Fock matrices in Equation (2.42) to approximate the orbital gradient. The indices u', v', w', … describe the active space orbitals of the increment active space within the full CASSCF active space. In agreement with Equation (2.69), the MBE is generally not applied to the full RDMs. Instead, residual density matrices $\mathbf{D}^{\mathrm{res}}$ and $\mathbf{d}^{\mathrm{res}}$ are constructed by subtracting the energy expectation value of a single determinant which yields a similar description to Equation (2.69) except that the HF energy is replaced by an energy expectation value of this designated determinant. As a result, elements of the increment density matrices that are not included in the increment active space will vanish in the resulting MBE

$$D_{uv}^{\mathrm{res}} = D_{uv}^{\mathrm{ref}} + \sum_{u' \in \{uv\}} \left(\mathbf{D}_{u'}^{\mathrm{res}}\right)_{uv} + \sum_{u'<v' \in \{uv\}} \left(\Delta\mathbf{D}_{u'v'}^{\mathrm{res}}\right)_{uv} + \sum_{u'<v'<w' \in \{uv\}} \left(\Delta\mathbf{D}_{u'v'w'}^{\mathrm{res}}\right)_{uv} + \dots \tag{4.3}$$

$$
\begin{aligned}
d^{\mathrm{res}}_{uvwx} = d^{\mathrm{ref}}_{uvwx} &+ \sum_{u' \in \{uvwx\}} \left(\mathbf{d}^{\mathrm{res}}_{u'}\right)_{uvwx} + \sum_{u'<v' \in \{uvwx\}} \left(\Delta\mathbf{d}^{\mathrm{res}}_{u'v'}\right)_{uvwx} \\
&+ \sum_{u'<v'<w' \in \{uvwx\}} \left(\Delta\mathbf{d}^{\mathrm{res}}_{u'v'w'}\right)_{uvwx} + \dots
\end{aligned}
\tag{4.4}
$$

which limits the memory required to store these increments during the expansion as their size is determined by the MBE order and not by the number of orbitals in the full active space. The increment density matrices $\Delta\mathbf{D}^{\mathrm{res}}_{u'v'\dots}$ and $\Delta\mathbf{d}^{\mathrm{res}}_{u'v'\dots}$ are defined recursively according to Equations (2.68) and (2.71). The reference space density matrices describe a reference space as in Equation (2.70).

The MBE of the reduced density matrices in Equations (4.3) and (4.4) can then be used to approximate any observable through Equation (2.11). Unfortunately, doing so will not yield the same result as if the MBE had been applied to the energy or property itself. This can be understood by inspecting the energy MBE at expansion order 2 for a minimal active space of 4 electrons in 3 spatial orbitals:

$$
\begin{aligned}
E^{(2)} = \;& \epsilon^{\mathrm{res}}_{i'a'} + \epsilon^{\mathrm{res}}_{j'a'} \\
= \;& \left(\mathbf{D}^{\mathrm{res}}_{i'a'}\right)_{i'i'} \left(\mathbf{F}^{I}_{i'a'}\right)_{i'i'} + \left(\mathbf{D}^{\mathrm{res}}_{i'a'}\right)_{i'a'} \left(\mathbf{F}^{I}_{i'a'}\right)_{i'a'} + \left(\mathbf{D}^{\mathrm{res}}_{i'a'}\right)_{a'i'} \left(\mathbf{F}^{I}_{i'a'}\right)_{a'i'} \\
& + \left(\mathbf{D}^{\mathrm{res}}_{i'a'}\right)_{a'a'} \left(\mathbf{F}^{I}_{i'a'}\right)_{a'a'} + \left(\mathbf{D}^{\mathrm{res}}_{j'a'}\right)_{j'j'} \left(\mathbf{F}^{I}_{j'a'}\right)_{j'j'} + \left(\mathbf{D}^{\mathrm{res}}_{j'a'}\right)_{j'a'} \left(\mathbf{F}^{I}_{j'a'}\right)_{j'a'} \\
& + \left(\mathbf{D}^{\mathrm{res}}_{j'a'}\right)_{a'j'} \left(\mathbf{F}^{I}_{j'a'}\right)_{a'j'} + \left(\mathbf{D}^{\mathrm{res}}_{j'a'}\right)_{a'a'} \left(\mathbf{F}^{I}_{j'a'}\right)_{a'a'} + \text{two electron terms} \\
= \;& \sum_{k',b'} \left(\left(\mathbf{D}^{\mathrm{res}}_{i'a}\right)_{k'b'} + \left(\mathbf{D}^{\mathrm{res}}_{j'a'}\right)_{k'b'}\right) h_{k'b'} \\
& + \sum_{k',b'} \left(\mathbf{D}^{\mathrm{res}}_{i'a'}\right)_{k'b'} \left(2\langle k'j'|b'j'\rangle - \langle k'j'|j'b'\rangle\right) + \sum_{k',b'} \left(\mathbf{D}^{\mathrm{res}}_{j'a}\right)_{k'b'} \left(2\langle k'i'|b'i'\rangle - \langle k'i'|i'b'\rangle\right) \\
& + \text{two electron terms}
\end{aligned}
\tag{4.5}
$$

The indices i' and j' describe the occupied orbital and the index a' describes the virtual orbital inside the active space if this system were described using a single designated determinant. The truncated MBE energy cannot be partitioned into individual residual density matrix contributions unless the density matrices are immediately contracted with the respective two-electron integrals. This is caused by the inactive Fock matrix which explicitly depends on the definition of the active space due to the sum over inactive orbitals (Equation (2.37)). This will always be the case whenever the expansion space includes occupied orbitals from which the two-electron part of the inactive Fock matrix is constructed. Consequently, a truncated energy MBE and an energy calculated using Equation (2.11) from a truncated MBE of the 1- and 2-RDMs will not yield the same results. The same is true for the generalized Fock matrix and the orbital gradient when it is calculated from RDMs which have been approximated by means of a truncated MBE.

If the calculated RDMs are instead immediately contracted with the necessary integrals, the calculations will yield the residual CASCI generalized Fock matrices

$$
\begin{aligned}
\left(\mathbf{F}^{\mathrm{res}}_{u'\dots}\right)_{ip} &= 2\left(F^{I}_{pi} + \left(\mathbf{F}^{A}_{u'\dots}\right)_{pi}\right) - 2\left(F^{I}_{pi} + \sum_{j''} \left(2\langle pj''|ij''\rangle - \langle pj''|j''i\rangle\right)\right) \\
&= 2\left(\sum_{v',w'} \left(\mathbf{D}_{u'\dots}\right)_{v'w'} \left(\langle pv'|iw'\rangle - \frac{1}{2}\langle pv'|w'i\rangle\right) - \sum_{j''} \left(2\langle pj''|ij''\rangle - \langle pj''|j''i\rangle\right)\right)
\end{aligned}
\tag{4.6}
$$

$$\begin{aligned}\left(\mathbf{F}^{\mathrm{res}}_{u'\ldots}\right)_{i'p} &= 2\left(F^{I}_{pi'} + \left(\mathbf{F}^{A}_{u'\ldots}\right)_{pi'}\right) - 2\left(F^{I}_{pi'} + \sum_{j''}\left(2\left\langle pj''|i'j''\right\rangle - \left\langle pj''|j''i'\right\rangle\right)\right) \\ &= 2\left(\sum_{v',w'}\left(\mathbf{D}_{u'\ldots}\right)_{v'w'}\left(\left\langle pv'|i'w'\right\rangle - \frac{1}{2}\left\langle pv'|w'i'\right\rangle\right) - \sum_{j''}\left(2\left\langle pj''|i'j''\right\rangle - \left\langle pj''|j''i'\right\rangle\right)\right)\end{aligned} \tag{4.7}$$

$$\begin{aligned}\left(\mathbf{F}^{\mathrm{res}}_{u'\ldots}\right)_{i''p} &= \sum_{v'}\left(\mathbf{D}_{u'\ldots}\right)_{i''v'}F^{I}_{pv'} + \sum_{v',w',x'}\left(\mathbf{d}_{u'\ldots}\right)_{i''v'w'x'}\left\langle pv'|w'x'\right\rangle \\ &\quad - \left(2F^{I}_{pi''} + \sum_{j''}\left(4\left\langle pj''|i''j''\right\rangle - 2\left\langle pj''|j''i''\right\rangle\right)\right)\end{aligned} \tag{4.8}$$

$$\left(\mathbf{F}^{\mathrm{res}}_{u'\ldots}\right)_{a''p} = \sum_{v'}\left(\mathbf{D}_{u'\ldots}\right)_{a''v'}F^{I}_{pv'} + \sum_{v',w',x'}\left(\mathbf{d}_{u'\ldots}\right)_{a''v'w'x'}\left\langle pv'|w'x'\right\rangle \tag{4.9}$$

$$\left(\mathbf{F}^{\mathrm{res}}_{u'\ldots}\right)_{a'p} = 0 \tag{4.10}$$

according to Equations (2.44) and (2.45). The indices i'', j'', … and a'', b'', … respectively describe the occupied and virtual increment active space orbitals in relation to the occupation of the designated determinant that is to be subtracted to construct the residual generalized Fock matrices. The residual CASCI generalized Fock matrix elements exclusively depend on the RDM elements of the increment active space. The occupied-general block of the residual generalized Fock matrix block does not require any contractions between the 1-RDM and the inactive Fock matrix. Hence, this block can be constructed from an MBE of the 1-RDM according to the arguments in Equation (4.5). The elements $\left(\mathbf{F}^{\mathrm{res}}_{u'}\right)_{i'p}$, $\left(\mathbf{F}^{\mathrm{res}}_{u'}\right)_{a'p}$, $\left(\mathbf{F}^{\mathrm{res}}_{u'}\right)_{i''p}$, and $\left(\mathbf{F}^{\mathrm{res}}_{u'}\right)_{a''p}$ all contribute to the active-general block of the residual generalized Fock matrix of the full system. All of these blocks do require contractions between the 1-RDM and two-electron integrals that depend on the definition of the increment orbitals themselves and can therefore not be constructed from an MBE of the 1-RDM. From the residual CASCI generalized Fock matrix elements, the increments can be calculated recursively as in Equation (2.71). The increments can then be used to approximate the generalized Fock matrix elements

$$F_{ip} = F^{\mathrm{ref}}_{ip} + \sum_{u'\in\mathrm{CAS}}\left(\mathbf{F}^{\mathrm{res}}_{u'}\right)_{ip} + \sum_{u'<v'\in\mathrm{CAS}}\left(\Delta\mathbf{F}^{\mathrm{res}}_{u'v'}\right)_{ip} + \sum_{u'<v'<w'\in\mathrm{CAS}}\left(\Delta\mathbf{F}^{\mathrm{res}}_{u'v'w'}\right)_{ip} + \ldots \tag{4.11}$$

$$F_{up} = F^{\mathrm{ref}}_{up} + \sum_{u'\in\mathrm{CAS}}\left(\mathbf{F}^{\mathrm{res}}_{u'}\right)_{up} + \sum_{u'<v'\in\mathrm{CAS}}\left(\Delta\mathbf{F}^{\mathrm{res}}_{u'v'}\right)_{up} + \sum_{u'<v'<w'\in\mathrm{CAS}}\left(\Delta\mathbf{F}^{\mathrm{res}}_{u'v'w'}\right)_{up} + \ldots \tag{4.12}$$

of the full system. While this equation yields a different description than the one afforded by Equations (4.3) and (4.4), it also requires significantly more memory. This is a result of the increment size no longer being dependent on the expansion order but instead on the size of the full system. For this reason, the recursive formulation of the MBE in Equation (2.76) is necessary to efficiently describe large systems while limiting memory usage.

Employing an approximate CASCI solver such as MBE-FCI will cause the CASSCF optimization to no longer be redundant with respect to the rotation of the active orbitals among each other.[321] The gradient g^{o}_{uv} will no longer vanish and most likely should be explicitly accounted for if the CASSCF wave function is to be optimized with respect to all variational parameters. Active orbital optimization will often lead to severe convergence issues because it is not redundant with the optimization of the CI coefficients.[269,304,307] One approach to circumvent this dilemma is to perform the CASCI step without allowing for single excitations.[114] Since single excitations constitute the leading term in the Taylor expansion of the orbital rotation operator in Equation (2.40)

$$\exp(-\hat{\kappa}) = 1 - \sum_{p<q}\kappa_{pq}\left(\hat{a}^{\dagger}_{p}\hat{a}_{q} - \hat{a}^{\dagger}_{q}\hat{a}_{p}\right) + \ldots, \tag{4.13}$$

their exclusion might reduce the redundancy and possibly tame any arising convergence issues. The contribution of the single excitations to the CASSCF energy can be recovered by reintroducing these in the final energy calculation. Active orbital optimization will lead to a variational method because the wave function is optimized with respect to all variational degrees of freedom. As a result, the Hellmann-Feynman theorem[477,478] can be applied for the evaluation of properties. Because the final energy is still determined from a truncated MBE, the final energy will not be an upper bound to the exact ground-state energy.[114] Alternative approaches to active orbital optimization exploit an inner-outer loop structure which overcomes some issues but still slows convergence.[305] A more reliable and consistent approach could be to explicitly treat the coupling between the optimization of orbitals and CI coefficients.[271,479]

Quasi-Newton algorithms additionally require the orbital Hessian diagonal to precondition the orbital gradient. While the approximate Hessian diagonals in Equations (2.48) to (2.50) are generally sufficient for conventional CASSCF calculations,[236] the explicit optimization of active-active rotations will additionally require the Hessian diagonal of the active space orbitals. Since the integrals only involve active orbitals, the exact Hessian diagonal can be utilized for this block.[305] Starting from Equations (21a) and (21b) in Ref. 243 the active-active block of the Hessian diagonal

$$
\begin{aligned}
H^{\mathrm{oo}}_{uv,uv} = \frac{\partial E}{\partial \kappa_{uv} \partial \kappa_{uv}} &= \frac{\partial E}{\partial U_{uv} \partial U_{uv}} + \delta_{vu}(F_{uv} + F_{vu}) - \frac{\partial E}{\partial U_{vu} \partial U_{uv}} - \delta_{uu}(F_{vv} + F_{vv}) - \frac{\partial E}{\partial U_{uv} \partial U_{vu}} \\
&\quad - \delta_{vv}(F_{uu} + F_{uu}) + \frac{\partial E}{\partial U_{vu} \partial U_{vu}} + \delta_{uv}(F_{vu} + F_{uv}) \\
&= 2D_{uu}h_{vv} + 4\sum_{p,q} \left(d_{upuq} \langle vp|vq\rangle + \left(d_{upqu} + d_{uuqp}\right) \langle vv|pq\rangle\right) \\
&\quad - 2D_{vu}h_{uv} - 4\sum_{p,q} \left(d_{upvq} \langle up|vq\rangle + \left(d_{upqv} + d_{uvqp}\right) \langle uv|pq\rangle\right) \\
&\quad - 2D_{uv}h_{vu} - 4\sum_{p,q} \left(d_{vpuq} \langle vp|uq\rangle + \left(d_{vpqu} + d_{vuqp}\right) \langle vu|pq\rangle\right) \\
&\quad + 2D_{vv}h_{uu} + 4\sum_{p,q} \left(d_{vpvq} \langle up|uq\rangle + \left(d_{vpqv} + d_{vvqp}\right) \langle uu|pq\rangle\right) \\
&\quad + 2\delta_{uv}(F_{uv} + F_{vu}) - 2F_{uu} - 2F_{vv} \\
&= 2D_{uu}F^I_{vv} + 2D_{vv}F^I_{uu} - 4D_{uv}F^I_{vu} + 2\delta_{uv}(F_{uv} + F_{vu}) - 2F_{uu} - 2F_{vv} \\
&\quad - \sum_i \left(2\langle vi|vi\rangle - \langle vi|iv\rangle\right) + 4\sum_{p,q} \left(d_{upuq} \langle vp|vq\rangle + \left(d_{upqu} + d_{uuqp}\right) \langle vv|pq\rangle\right) \\
&\quad + \sum_i \left(2\langle ui|vi\rangle - \langle vi|iu\rangle\right) - 4\sum_{p,q} \left(d_{upvq} \langle up|vq\rangle + \left(d_{upqv} + d_{uvqp}\right) \langle uv|pq\rangle\right) \\
&\quad + \sum_i \left(2\langle vi|ui\rangle - \langle vi|iu\rangle\right) - 4\sum_{p,q} \left(d_{vpuq} \langle vp|uq\rangle + \left(d_{vpqu} + d_{vuqp}\right) \langle vu|pq\rangle\right) \\
&\quad - \sum_i \left(2\langle ui|ui\rangle - \langle ui|iu\rangle\right) + 4\sum_{p,q} \left(d_{vpvq} \langle up|uq\rangle + \left(d_{vpqv} + d_{vvqp}\right) \langle uu|pq\rangle\right) \\
&= 2D_{uu}F^I_{vv} + 2D_{vv}F^I_{uu} - 4D_{uv}F^I_{vu} + 2\delta_{uv}(F_{uv} + F_{vu}) - 2F_{uu} - 2F_{vv} \\
&\quad + 4\sum_{x,y} \left(d_{uxuy} \langle vx|vy\rangle + \left(d_{uxyu} + d_{uuyx}\right) \langle vv|xy\rangle - d_{uxvy} \langle ux|vy\rangle \right. \\
&\quad - \left(d_{uxyv} + d_{uvyx}\right) \langle uv|xy\rangle - d_{vxuy} \langle vx|uy\rangle - \left(d_{vxyu} + d_{vuyx}\right) \langle vu|xy\rangle \\
&\quad \left. + d_{vxvy} \langle ux|uy\rangle + \left(d_{vxyv} + d_{vvyx}\right) \langle uu|xy\rangle\right)
\end{aligned}
\tag{4.14}
$$

can be derived. The final expression differs from the one given in Ref. 305 but is equivalent to the Hessian diagonal in Ref. 306.

4.2 Implementation

The significant changes that are necessary to perform expansions of 1- and 2-RDMs and generalized Fock matrices, necessitated the inclusion of the MBE target-specific `ExpCls` implementations described in Figure 3.1. These calculations require both the simultaneous expansion of multiple targets and the treatment of targets for which simple mathematical operations such as addition and subtraction require indexing due to the dependence of the tensor elements on the tuple orbitals. For this reason, `RDMCls` and `GenFockCls` classes were created that can describe multiple targets and include so-called *dunder methods* that define operations such as indexing, addition, subtraction, multiplication, division, copying, and filling for these targets. With the help of these functions, these multi-target objects can be handled in the same way as energies or dipole moments in PyMBE. Additionally, arrays of these objects are described through the `packedRDMCls` and `packedGenFockCls` classes. This is of special importance for the 1- and 2-RDMs as these can be saved memory-efficiently by exploiting permutational symmetry which is automatically handled in PyMBE when individual `RDMCls` objects interact with elements of a `packedRDMCls` object. These packed objects are for example used to store the 1- and 2-RDM and generalized Fock matrix increments in associative arrays for later retrieval. The `RDMExpCls` and `GenFockExpCls` classes also include functions to perform parallel operations on these objects such that these can be parsed among the processes as well as allocated and opened in shared memory. The additional integrals involving orbitals outside the active space that are needed to construct the generalized Fock matrix are also saved in shared memory.

The size of the increment RDMs required to construct the 1- and 2-RDMs for the entire active space using Equations (4.3) and (4.4) scales with the size of the orbital tuples. For these, real orbital permutational symmetry

$$D_{pq} = D^*_{qp} \tag{4.15}$$

$$d_{pqrs} = d_{rpsq} = d^*_{qspr} = d^*_{sqrp} \tag{4.16}$$

is exploited such that the actual memory requirements of the individual increments

$$\frac{(N^{\mathrm{ref}} + n)^2 + (N^{\mathrm{ref}} + n)}{2} \tag{4.17}$$

$$\frac{7(N^{\mathrm{ref}} + n)^4 + 8(N^{\mathrm{ref}} + n)^3 - (N^{\mathrm{ref}} + n)^2 - (N^{\mathrm{ref}} + n)}{12} \tag{4.18}$$

are minimized. N^{ref} is the number of orbitals in the reference space. 1- and 2-RDM expansions are always performed simultaneously through the `RDMCls` and `packedRDMCls` classes. The increment 1- and 2-RDMs are constructed by subtracting the RDMs from a single designated determinant which can be constructed from the occupation vectors and then subtracting the appropriate smaller subtuple increments from the respective elements of the residual RDMs. A crude approximation for the electronic energy can be obtained from the expanded 1- and 2-RDMs and this quantity can be used to monitor convergence in CASSCF.

For generalized Fock matrices, only the elements described in Equations (4.7) to (4.9) are calculated. The residual generalized Fock matrix is determined by constructing the respective generalized Fock

matrix for the designated determinant and subtracting it from the calculated generalized Fock matrix. The total number of elements that need to be saved for a single increment

$$(N_{\text{occ}}^{\text{act}} + N_{\text{virt}}^{\text{ref}} + N_{\text{virt}}^{\text{tup}}) * M \tag{4.19}$$

scale with system size, with active space size through the number of occupied orbitals in the active space $N_{\text{occ}}^{\text{act}}$, and with orbital tuple size through the number of virtual orbitals in the orbital tuple $N_{\text{virt}}^{\text{tup}}$. $N_{\text{virt}}^{\text{ref}}$ is the number of virtual orbitals in the reference space. The increments need to be constructed from subtuple increments which can have fewer elements since the increment shape depends on the number of virtual orbitals in the orbital tuple. For this reason, increments of different occupation are stored in different associative arrays and a generator function for tuples of a certain occupation exists in PyMBE so that recursive increment construction can be performed efficiently without significant overhead. The electronic energy is needed to monitor convergence during the CASSCF orbital optimization. Since the electronic energy cannot be calculated from the generalized Fock matrix, an energy expansion is performed simultaneously. The occupied-general block of the generalized Fock matrix (Equation (4.6)) is calculated at the very end of the MBE calculation since this block can be constructed from a 1-RDM expansion. This procedure is more memory-efficient than storing the entire occupied-general block for every increment. The active-general block of the generalized Fock matrix, 1-RDM, and the energy are all described through the `GenFockCls` and `packedGenFockCls` classes. For large systems, the problematic scaling of the generalized Fock matrix increments can generally be avoided by utilizing Equation (2.76).

The designated determinant and the corresponding residual property in MBE-CASSCF theory replaces the HF determinant and correlated property in standard MBE-FCI theory in the absence of HF orbitals. This designated determinant should be designed so that it dominates the correlated wave function. In MBE-CASSCF, this is achieved by constructing UNOs as initial orbitals for the orbital optimization and occupying these according to their occupation numbers. While the resulting determinant will generally not yield a qualitatively correct description for statically correlated systems, a correlated description can be obtained by additionally introducing a reference space.

Since approximate CASSCF calculations are not invariant to the choice of active orbitals, a proper initial guess can accelerate convergence of the MBE and therefore yield a better approximation to the orbital gradient. As an alternative to UNOs, PM LMOs can be used in PyMBE to accelerate convergence. The *lo* module in PySCF is used to localize the orbitals such that the occupied, singly occupied, and virtual subspaces in the designated determinant are rotated separately. This will ensure that the designated determinant will still yield a good description of the underlying wave function.

To enable CASCI calculations without single excitations, an additional variable called `hop` was added to the PySCF *fci* solvers. The callable that is passed to this variable can replace the standard operation for sigma vector formation. PyMBE defines an alternative function which zeroes the elements corresponding to singly excited determinants and thus ensures that these will not contribute during the Davidson iterations.

The `RDMExpCls` and `GenFockExpCls` classes additionally possess state-specific (`ssRDMExpCls` and `ssGenFockExpCls`) and state-averaged (`saRDMExpCls` and `saGenFockExpCls`) subclasses which introduce interfaces to the PySCF *fci* module that yield state-specific or state-averaged target properties. State-averaged MBE-CASSCF calculations are only relevant for the averaging of states of equal symmetry and spin because the same increment CASCI solver can be used for these states. For states of different symmetry or different spin it will be as efficient to perform two MBE-CASCI calculations and average the resulting properties.

4.2.1 Interface between PyMBE and CASSCF Module in CFOUR

Performing MBE-CASSCF calculations requires embedding of the PyMBE program into a CASSCF driver. To achieve this, an interface between PyMBE and the *sa_casscf* module in CFOUR was mainly written by [redacted] with help from [redacted] and the author of this thesis. Since PyMBE can be started from a script, it can be compiled into a dynamic library using the *C Foreign Function Interface for Python*[480] and embedded into Fortran. The *sa_casscf* module can then repeatedly pass all necessary variables to an `MBE` object and call its kernel function to start an MBE-CASCI calculation. The MBE-CASSCF method was implemented for two first-order solvers: super-CI[224,233,235,237,241] and quasi-Newton.[236,245] While the former provides linear convergence, the latter is able to achieve robust superlinear convergence near the minimum. The favorable convergence properties of both optimization strategies can be combined by initially performing super-CI optimization until the quadratic region is reached and then switching to the quasi-Newton solver.[235,238]

Approximate CASSCF calculations for systems which require large active spaces often also possess a significant number of inactive and virtual orbitals which can hinder inactive and active Fock matrix construction in Equation (2.47) and the contraction of the 2-RDM with two-electron integrals in Equation (2.44). This can be accelerated through optimized Cholesky decomposition of the two-electron integrals.[272,365,366] The reconstruction of the additional integrals that are passed to PyMBE and required to construct the generalized Fock matrix can represent both a computational and a memory bottleneck. For this reason, the reconstruction was parallelized by the author of this thesis by utilizing the MPI shared memory paradigm.

4.3 Results

The MBE-CASSCF algorithm is first tested on naphthalene,[a] anthracene,[b] and tetracene[b] and then applied to the triplet-quintet spin gap of a model system for the iron(II) tetraphenylporphyrin complex.

For the linear polyacenes, the cc-pVDZ basis set[404] is used and the CASSCF optimization is started from UNOs as initial orbitals. All orbitals with an occupation number between 0.01 and 1.99 were correlated which results in (10,10), (14,14), and (18,18) π-orbital active spaces, respectively. The results for naphthalene and anthracene can be compared to conventional CASSCF results while tetracene already requires a large-scale implementation to generate these.

4.3.1 Orbital Optimization with Truncated MBEs

CASSCF orbital optimization employing an MBE-CASCI solver requires truncation of the constructed MBEs. Ideally, the MBEs are truncated at a given MBE order such that Equation (2.76) can be employed and the unfavorable memory-scaling of the RDM and the generalized Fock matrix increments can be circumvented. To test whether truncation during orbital optimization will produce orbitals that can recover the exact CASSCF energies, the orbitals were optimized using different MBE truncation orders while the final energy was determined using a conventional CASCI calculation. The energy error in comparison to conventional CASSCF orbital optimization and the CASSCF orbital gradient are plotted in Figure 4.1. The MBE-CASSCF orbital optimization significantly improves the UNOs

[a] CCSD/cc-pVDZ geometry
[b] Geometry from Ref. 307

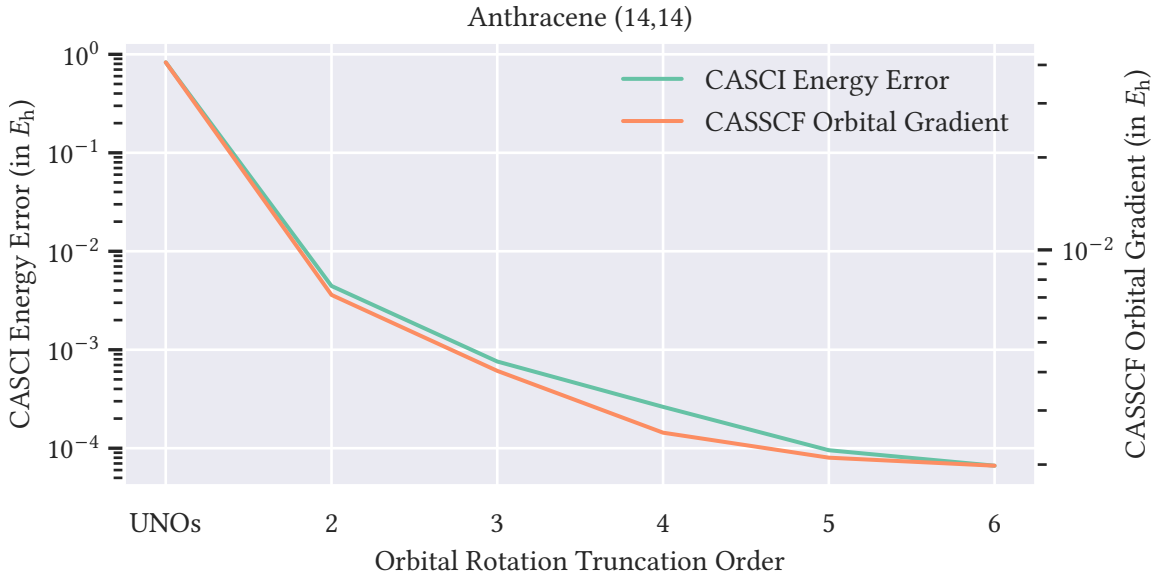

Figure 4.1: Error of an exact CASCI calculation and CASSCF orbital gradient of anthracene with a (14,14) active space for different orbitals in comparison to the exact CASSCF quantities. The orbitals are either UNOs or orbitals from an MBE-CASSCF quasi-Newton orbital optimization where the MBE is truncated at different fixed orders. Adapted with permission from Ref. 476. Copyright 2024 American Chemical Society.

such that truncation at later orders will yield energies within chemical accuracy of the conventional CASSCF result. The energy convergence is exponential with respect to the truncation order and the gradient vanishes in the asymptotic limit. The MBE-CASSCF orbitals can be considered sufficiently converged when the MBE is truncated at orders 4 or 5. While the final, exact CASCI calculation is computationally impractical for large active spaces, it can be replaced by an accurate, screened MBE-CASCI energy calculation which does not suffer from the same shortcomings as the RDM and generalized Fock matrix expansions. A similar approach has been successfully applied to an HCISCF implementation.[304]

Consequently, all MBE-CASSCF calculations considered in this thesis make use of orbital optimizations truncated at MBE order 5 with a subsequent energy expansion screened according to the screening protocol described in Section 3.1.3. The screening parameters used for these calculations are described in Table 4.1. While the *loose* screening parameters match the truncated expansion used during orbital optimization, the other parameters start to screen away 30 % of the orbitals per order at successively higher orders.

Table 4.1: Different screening parameters used in MBE-CASSCF calculations. Adapted with permission from Ref. 476. Copyright 2024 American Chemical Society.

Screening	Start Order	Percentage
loose	5	100 %
medium	5	30 %
tight	6	30 %
very tight	7	30 %

4.3.2 Reduced Density Matrix and Generalized Fock Matrix Expansions

The MBE of RDMs and generalized Fock matrices will yield different approximations to the orbital gradient according to Equation (4.5). The CASSCF energy convergence from the orbital optimization with both MBE targets and the final energies for different screening criteria for all three linear polyacenes are described in Figure 4.2. The orbital optimizations in the left plots of Figure 4.2 employing both MBE targets exhibit practically identical convergence profiles except for a shift in the final energies. The energy at iteration 0 is equivalent because the initial gradients and Hessian

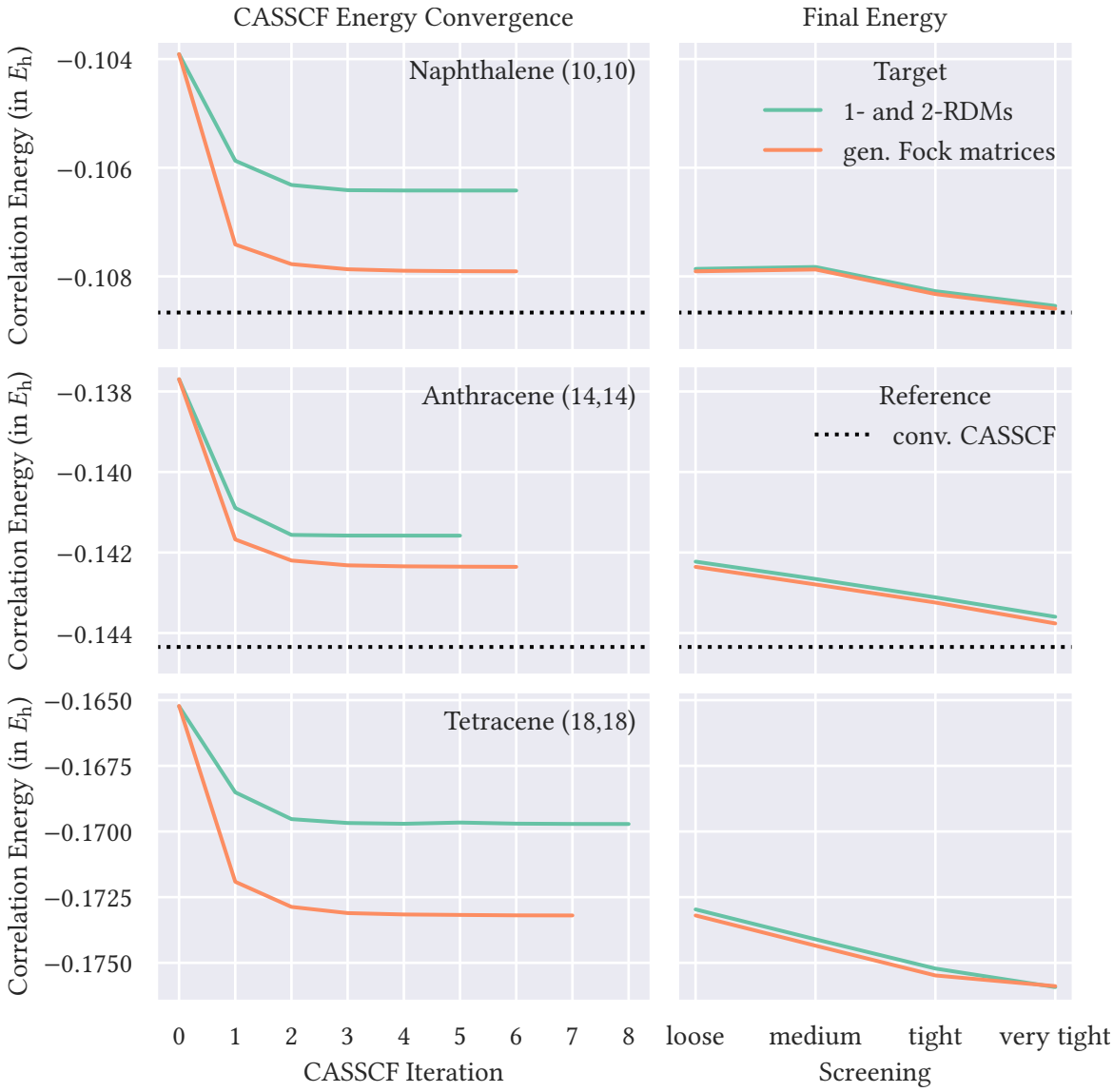

Figure 4.2: CASSCF energy convergence and final energy of naphthalene, anthracene, and tetracene for expansions based on 1- and 2-RDMs and generalized Fock matrices. PM LMOs are used as the initial guess for the active orbitals. The reference space involves those LMOs that have the greatest overlap with the UNOs with occupation numbers greater than 0.2 and smaller than 1.8. Adapted with permission from Ref. 476. Copyright 2024 American Chemical Society.

diagonals are calculated from the 1- and 2-RDM expansion for both targets. While there is a large shift between the final converged correlation energies calculated from the MBE of RDMs and the direct energy expansion involved in the MBE of generalized Fock matrices, the final energy expansions in the plots on the right side in Figure 4.2 almost entirely correct for this difference. Although the differences in the final energies are small, the generalized Fock matrix expansion generally yields results closer to the conventional CASSCF result. For this reason, all quasi-Newton MBE-CASSCF optimizations will be based on generalized Fock matrix expansions. Regardless, the quality of the optimized orbitals justifies using the 1- and 2-RDM expansions for the initial super-CI optimization and the initial gradient and Hessian diagonal evaluation. The final energies from both expansion targets can be systematically improved by tightening the screening criteria.

4.3.3 Active Orbital and Reference Space Choice

Besides screening and MBE target choice, the nature of the active space orbitals and the reference space can also significantly affect the accuracy of MBE-CASSCF. While the UNOs used as initial guess for the orbital optimization already provide a compact basis for the subsequent expansion, MBE-based methods often benefit from an LMO basis that minimizes specific orbital interactions through spatial separation of the involved orbitals. The reference space choice on the other hand introduces a certain ambiguity as the orbitals to be included are difficult to anticipate. An empty reference space often makes the expansion intractable in practice due to the sheer number of increments dictated by combinatorics. An obvious alternative in the context of CASSCF theory is to use equivalent but tighter criteria to how the original active space was chosen. Therefore, active orbitals with occupation numbers between 0.2 and 1.8 are used to define the UNO reference space. In the localized basis, those orbitals with the highest overlaps with the chosen UNOs can be used as reference space orbitals.

The convergence profiles and final energies for both active orbital and reference space choices are plotted in Figure 4.3. The LMO basis is able to significantly accelerate MBE convergence such that the final CASSCF energies in the left plots in Figure 4.3 can already quantitatively reproduce the conventional CASSCF results and the final energies in the right plots. When employing the UNO basis, it is generally necessary to tighten the screening criteria of the final energy evaluation as was done in the plots on the right side of Figure 4.3 to generate results of higher quality. Tightening the screening criteria can lead to oscillations of the final energy since truncated MBEs are not variational. For the LMOs, systematic rapid convergence to the conventional result can be observed for naphthalene and anthracene. Adding orbitals to the reference space also accelerates convergence to the CASSCF result in both orbital bases and will provide more accurate results. It should be noted, however, that a larger reference space will also increase the computational effort necessary to solve the individual CASCI problems of the MBE, and it is therefore necessary to steer clear of the tipping point where the combinatorial scaling of the CASCI methods overshadows the effect of the reduction in the total number of increments and the convergence benefits of adding orbitals to the reference space. Alternative and more theoretically sound methods for choosing upon a reference space will be discussed in Chapter 5.

4.3.4 Active Orbital Optimization

The MBE-CASSCF method is not invariant with respect to the optimization of the active orbitals. As discussed in Section 4.1, the explicit optimization of these orbitals will lead to redundancies in the wave function parametrization that can be partially avoided by excluding singly excited determinants

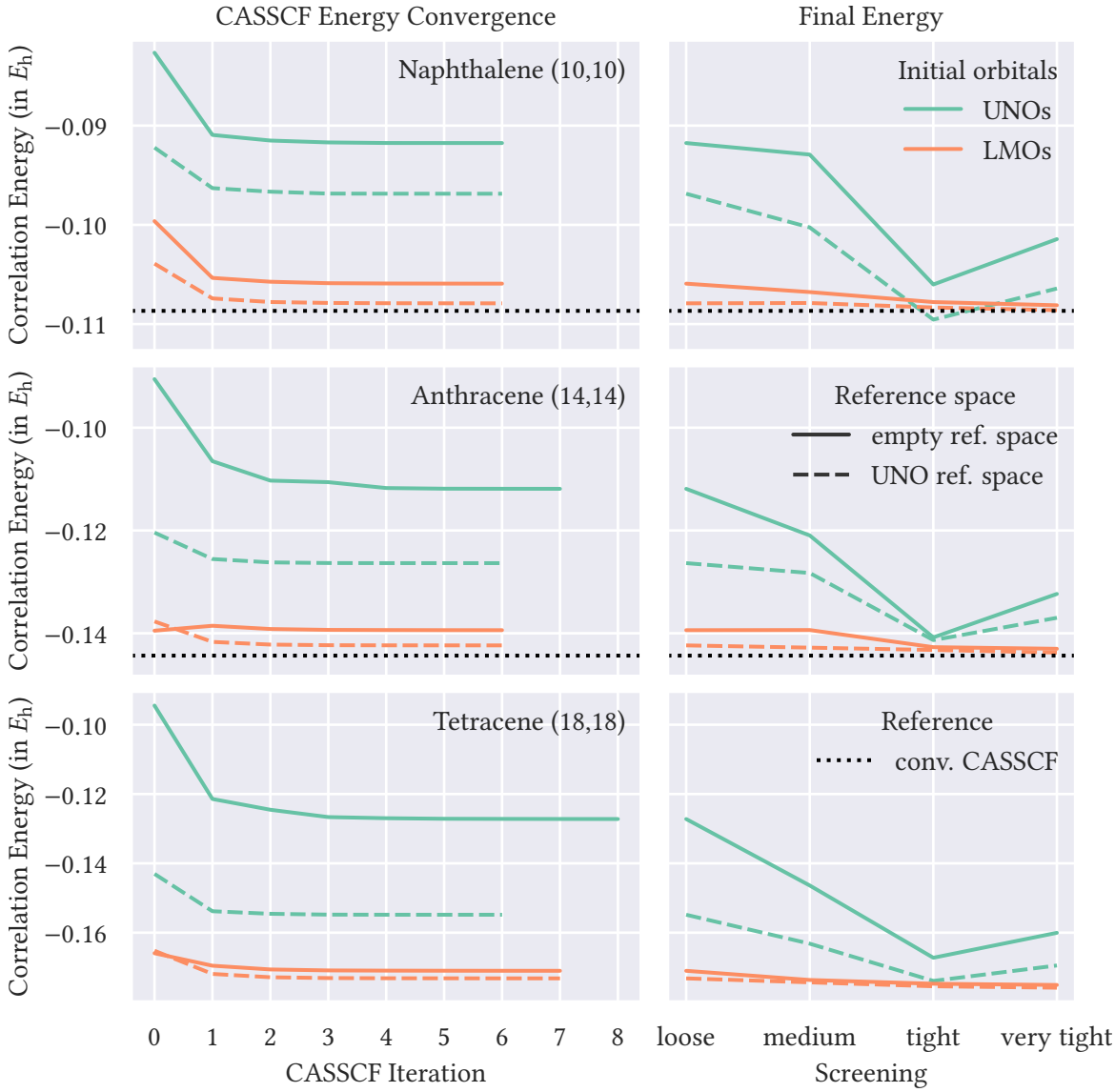

Figure 4.3: CASSCF energy convergence and final energy of naphthalene, anthracene, and tetracene for PM localized active MOs, UNOs, empty reference spaces, and references spaces based on UNO occupation numbers. Generalized Fock matrices are chosen as the MBE target of these expansions. Adapted with permission from Ref. 476. Copyright 2024 American Chemical Society.

from the CASCI optimization.[114] The effects of introducing such a procedure into the MBE-CASSCF method are investigated in Figure 4.4 for naphthalene and anthracene employing an LMO active space initial guess. For tetracene with LMOs as starting orbitals and for the calculations utilizing UNOs as starting orbitals for all three systems, the orbital optimizations including active-active rotations did not converge. The optimization profiles on the right side of Figure 4.4 demonstrate that the orbital optimization is able to converge to a lower energy minimum when active-active rotations are included. Unfortunately, the energy improves only very little and the optimization takes significantly longer to converge. The effect of tighter screening criteria on the final energies after reintroducing the contribution of singly-excited determinants on the left side of Figure 4.4 compensates and overshadows the possible gains from active orbital optimization. The minimization

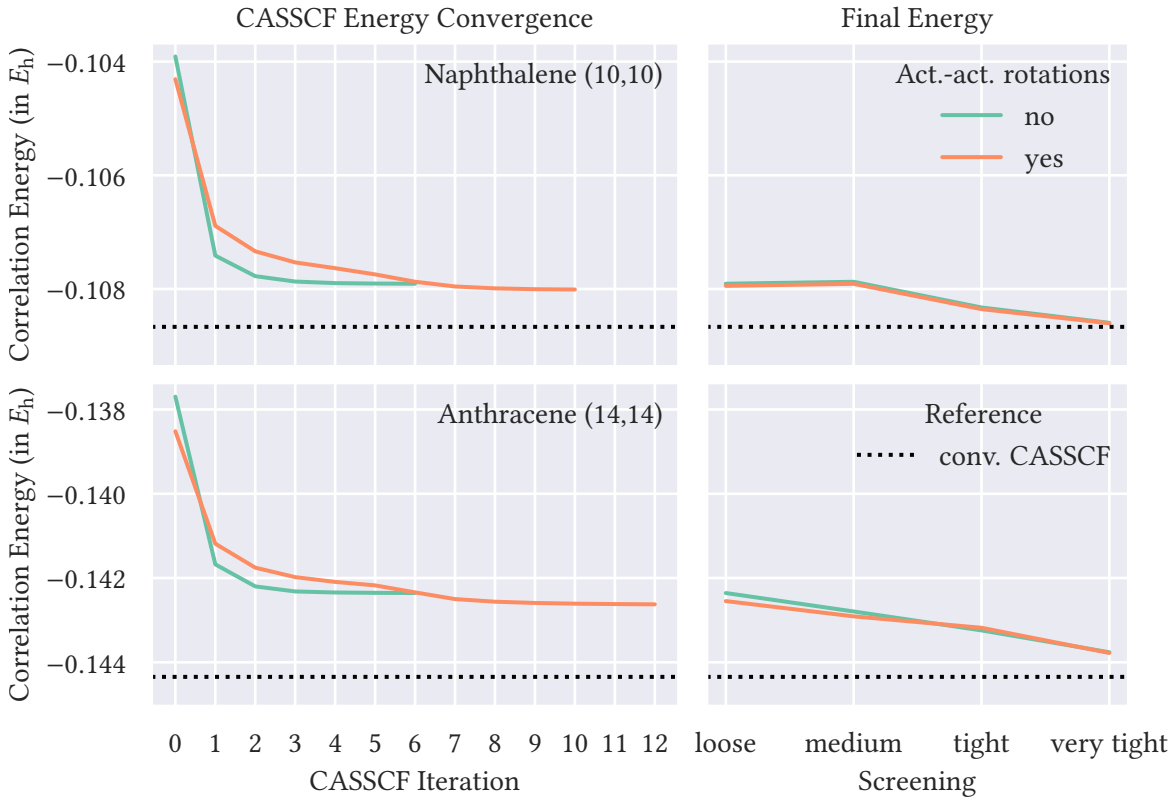

Figure 4.4: CASSCF energy convergence and final energy of naphthalene and anthracene with and without active-active rotations. Generalized Fock matrices are chosen as the target of these expansions. PM LMOs are used as the initial guess for the active orbitals. The reference space contains those LMOs that have the greatest overlap with the set of UNOs that have occupation numbers greater than 0.2 and smaller than 1.8. Adapted with permission from Ref. 476. Copyright 2024 American Chemical Society.

of the energy with respect to active orbital rotations appears to draw its benefits from the MBE orders immediately following the truncation order. These effects immediately vanish when the higher-order contributions are explicitly calculated by tightening the screening criteria. In agreement with other work on active-active rotations in the context of approximate CASSCF methods,[305–309] the explicit consideration of these does not seem worthwhile for the MBE-CASSCF method. Both an appropriate initial active orbital basis such as PM LMOs and the utilization of tighter screening criteria during the final energy evaluation will be more beneficial for improving the accuracy of the final results.

4.3.5 Triplet-Quintet Spin Gap of Iron(II) Porphyrin

The MBE-CASSCF implementation is applied to the triplet-quintet spin gap of the challenging iron(II) porphyrin system which is depicted in Figure 4.5. This is a model system for iron(II) tetraphenylporphyrin which is of high importance in bioinorganic chemistry due to its presence in the heme group.[481] It also is a highly selective and efficient candidate for a pre-catalyst for the electrochemical conversion of carbon dioxide to carbon monoxide.[482] These applications warrant high interest in the spin-state energetics of Fe(II) porphyrin.

This system has been extensively investigated experimentally, and all experimental studies agree that

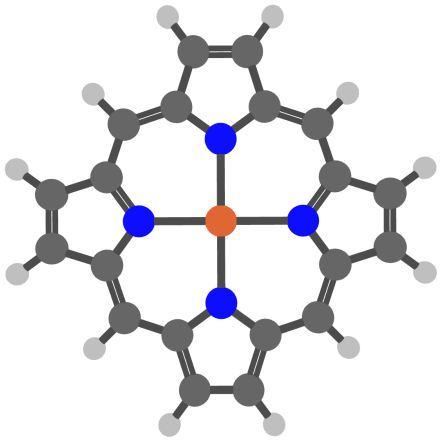

Figure 4.5: Molecular structure of the Fe(II) porphyrin system. Iron is depicted in orange, nitrogen in blue, carbon in dark gray, and hydrogen in light gray. Adapted with permission from Ref. 476. Copyright 2024 American Chemical Society.

the electronic ground state exhibits triplet character.[483–488] Recent work has described the ground state as "genuinely multiconfigurational" and suggests that it can be described as a mixture of a ${}^3A_{2g}$ and a ${}^3E_g$ configuration.[482] In contrast, CASSCF and CASPT2 studies on the model system in Figure 4.5 have generally predicted a quintet ground state instead.[489,490] Possible reasons for this inconsistency in comparison to the experimental result could be the approximate treatment of electron correlation, the missing phenyl groups in the model system, the finite basis sets used in these studies, the neglect of relativistic contributions, and missing environment and finite-temperature effects. The aim of describing the triplet-quintet spin gap of this system with MBE-CASSCF is to investigate the former effect by systematically increasing the active space size. Other work by Olivares-Amaya et al.[119] applying DMRGSCF and by Smith et al.[304] applying HCISCF to a large (44,44) active space have correctly predicted a triplet ground state while work by Levine et al.[305] which applied ASCI-SCF was unable to corroborate these results with a similar active space choice, suggesting that the result obtained by the earlier two works strongly depends on the chosen active space. Guo et al.[306] were correctly able to predict a triplet ground state with iCISCF for larger, chemically motivated active spaces. The fact that larger active spaces and methods predominately targeting dynamical correlation such as CCSD(T) have correctly predicted a triplet ground state,[481] suggests that dynamical correlation can play an important role in recovering the correct ordering of both spin states.

The MBE-CASSCF calculations on the model system[c] in Figure 4.5 employ an ANO-VDZP basis set.[493,494] These calculations are performed by utilizing increasingly large active spaces systematically chosen according to their UNO occupation numbers. The initial active space is defined by the orbitals with occupation numbers between 0.01 and 1.99 which results in an active space of 22 electrons in 22 orbitals. The active space is then extended by adding the most correlated 8, 18, and 28 orbitals and an equal number of electrons which results in (30,30), (40,40), and (50,50) active spaces, respectively. The systematic definition of active spaces distinguishes this treatment from previous work.[119,304–306] All orbitals with UNO occupation numbers between 0.2 and 1.8 are included in the reference space which results in (6,6) and (8,8) active spaces. UNOs are used as initial guess for the inactive/virtual orbitals while PM LMOs are used within the active space.

[c]Geometry based on symmetrized parameters from x-ray diffraction in Ref. 491, consistent with Refs. 352 and 492

For systems with multiple singly occupied orbitals such as the states targeted for this system, the individual CASCI calculations can become expensive at later orders in the expansion since the reference space grows large. This will become problematic for large-scale calculations as these are usually done on many low-memory nodes which means that the CI and sigma vectors can no longer be held in memory for all processes. For this reason, the larger active space calculations on the quintet state are limited to MBE order 6, resulting in increment CASCI calculations involving 14 orbitals at maximum. In Table 4.2, the results of terminating the final energy calculations at MBE order 6 for the (22,22) active space are compared to the screening criteria introduced in Table 4.1. The total energy when the MBE is truncated at order 6 is within chemical accuracy of the results from all screening criteria while the spin gaps are on par with the *tight* and *very tight* criteria. For the remaining calculations on this system, the MBE will therefore be truncated at order 6.

Table 4.2: MBE-CASSCF energy for the lowest triplet and quintet states and corresponding spin gap of the Fe(II) porphyrin system for different screening parameters in a (22,22) active space with (6,6) and (8,8) reference spaces for the triplet and quintet states, respectively. Adapted with permission from Ref. 476. Copyright 2024 American Chemical Society.

Screening	Triplet Energy (in au)	Quintet Energy (in au)	Spin Gap (in kcal/mol)
medium	−2245.156 547	−2245.201 957	28.50
tight	−2245.156 991	−2245.202 046	28.27
very tight	−2245.157 095	−2245.202 014	28.19
6 / 100 %	−2245.156 933	−2245.201 829	28.17

The calculation of energy gaps requires a balanced description of both states. It could be argued that the choice of different reference space sizes for both systems does not fulfill this criterion. A comparison of the triplet energies with (6,6) and (8,8) reference spaces is given in Table 4.3. Both reference space choices produce final energies within chemical accuracy of each other and therefore the (6,6) reference space will be used for the description of the triplet state.

Table 4.3: MBE-CASSCF energy for the lowest triplet state of the Fe(II) porphyrin system for different reference space sizes in a (30,30) active space. The MBE was terminated after order 6. Adapted with permission from Ref. 476. Copyright 2024 American Chemical Society.

Reference Space	(6,6)	(8,8)
Triplet Energy (in au)	−2245.265 808	−2245.265 273

The results from ROHF calculations and MBE-CASSCF calculations employing the discussed parameters and employing increasingly larger active spaces are presented in Table 4.4. For the most part, the spin gap decreases as the active space size is increased and more correlation is recovered. For the calculation employing the largest active space, the energy gap increases by 5.46 kcal/mol in comparison to the smaller active space. These energy gaps are comparable to results from the literature[304,305] and are generally far from converged with respect to active space size. It is therefore not difficult to imagine the spin gap to drastically change or switch signs as the active space is further enlarged. The quintet calculation in the largest active space required around 138 000 core

Table 4.4: MBE-CASSCF energy for the lowest triplet and quintet states and corresponding spin gap of the Fe(II) porphyrin system for different active spaces and screening parameters. The triplet and quintet states used (6,6) and (8,8) reference spaces, respectively. Adapted with permission from Ref. 476. Copyright 2024 American Chemical Society.

CAS	Triplet Energy (in au)	Quintet Energy (in au)	Spin Gap (in kcal/mol)
ROHF	−2244.986 964	−2245.043 905	35.73
(22,22)	−2245.156 933	−2245.201 829	28.17
(30,30)	−2245.265 808	−2245.292 189	16.55
(40,40)	−2245.398 154	−2245.411 361	8.29
(50,50)	−2245.558 638	−2245.580 548	13.75

hours for 18 CASSCF iterations involving 36 individual CASCI calculations.[d] For comparison, the triplet calculation required only around 36 000 core hours for 43 CASSCF iterations involving 87 individual CASCI calculations, showcasing a drastic decrease of the required computational effort when employing a smaller reference space. Systems which can be treated with smaller reference spaces could therefore be described by even larger active spaces in large-scale parallel calculations. The quintet and triplet calculations describing the smaller (40,40) active space respectively only require around 31 000 and 3700 core hours for 17 and 13 CASSCF iterations (35 and 26 individual CASCI calculations).[e] Calculations of this size can be routinely performed on parallel computers.

The correlation energies of both spin states are plotted in Figure 4.6. As the active space is enlarged, the magnitude of the correlation energy increases as a larger amount of correlation is recovered due to the variationality of the CASSCF method. While this is true for both systems, the triplet correlation energy decreases faster which shrinks the size of the spin gap. The fact that all remaining

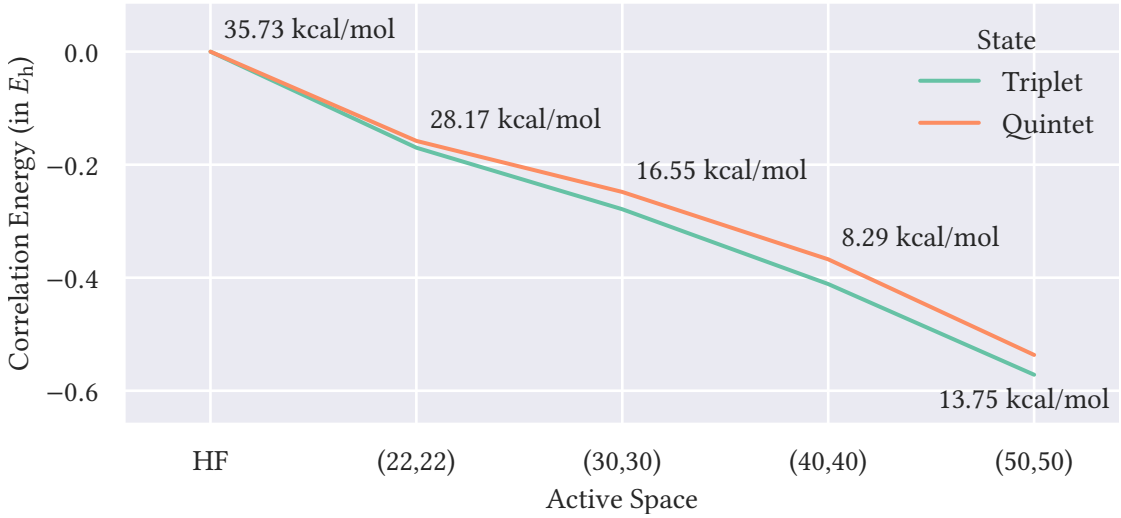

Figure 4.6: Correlation energies of the triplet and quintet states of the Fe(II) porphyrin system for different active spaces. The corresponding quintet-triplet spin gaps are annotated as text. Adapted with permission from Ref. 476. Copyright 2024 American Chemical Society.

[d] Computer architecture: 150 Intel Xeon CPUs 2630v4 on 75 nodes (1500 cores @ 2.2 GHz, 2.85 GB/core)
[e] Computer architecture: 50 Intel Xeon CPUs 2630v4 on 25 nodes (500 cores @ 2.2 GHz, 2.85 GB/core)

correlation outside the active space is left untreated both in the CASSCF method and its approximate versions appears highly problematic for the treatment of this system since the spin gap itself appears to be on the scale of the correlation energy contribution of individual orbitals. This conclusion was also drawn in other work on this system.[304,305,352] While the CASSCF method is often known to produce qualitatively correct results for difficult systems, this system qualifies for a treatment beyond conventional and even approximate CASSCF theory. Since the active space size is intrinsically limited by scaling, methods designed for the combined treatment of static and dynamic correlation should be considered instead. Since the CASPT2 method also predicts a quintet ground state for this system,[490] it might be necessary to devise more advanced methods that combine approximate CASSCF approaches with dynamical correlation treatments beyond perturbation theory. In the context of MBE-CASSCF theory, the final energy MBE-CASCI calculation could be to replaced by an MBE-FCI calculation where the orbitals outside the active space are screened away earlier than the active space orbitals. The resulting approach would recover some residual correlation energy of the orbitals outside the active space.

Nevertheless, the showcased calculations on this system convincingly demonstrate the ability of the MBE-CASSCF method to treat large active spaces in an embarrassingly parallel manner. Additionally, the outlined method can aid in the interpretation of results from conventional CASSCF calculations. While the missing dynamical correlation is the likely culprit for the incorrect ordering of the states, other effects such as basis set size and the missing phenyl groups could also be contributing factors whenever miniscule energy gaps are to be resolved.

5 Automatic Reference Space Detection in MBE-FCI

Generalized MBE-FCI theory introduces the concept of reference and expansion spaces to categorize the different expansions that can be constructed from a given orbital space.[42] For statically correlated systems, it is generally necessary to venture beyond an empty reference space to ensure optimal convergence towards the MBE target. In this chapter, an automatic reference space detection algorithm for arbitrary systems is presented and compared to measures based on the orbital entropy and mutual information obtained from DMRG wave functions. Correlation between incremental correlation energies and these entanglement measures was previously investigated by Stemmle and Paulus.[495] Additionally, the presented algorithm also ensures that the optimal state is chosen from the eigenvalue spectrum of every increment active space. The work in this chapter was published in Ref. 496.

5.1 Theory

The eigenvalue spectrum of the increment active space can significantly change as additional expansion space orbitals are incorporated at increasingly high orders of an MBE. For multireference systems, the states with similar character will often not stay in the same position in the eigenvalue spectrum and the CASCI root used to construct the increment should not be chosen by position alone. When the ground state is targeted, a higher root could potentially produce a more coherent description of the full system ground state for certain increment active spaces. As a result, the increment magnitude can become large whenever the wave function character of the used root is significantly different from the wave functions that were used to construct the subtuple increments. Choosing the *wrong* state can lead to significant issues in MBE convergence due to large increment magnitudes and should be avoided. A possible remedy would be to explicitly compare the wave functions of a tuple and its subtuples and use the state which is *closest* in wave function character. A simpler solution is to compare every tuple's wave function to the reference space wave function under the assumption that the states chosen for tuples at previous orders also resemble the reference space wave function. A measure of state similarity is given by the quantum fidelity[497–500]

$$F_{IJ} = \left|\langle \Psi_I | \Psi_J \rangle\right|^2 \tag{5.1}$$

for pure quantum states I and J. The quantum fidelity is a quantity from QIT that has also been used in the context of DMRG theory.[501] Optimal MBE convergence for a given state and reference space can hence be achieved by choosing a state from the reference space spectrum, either by position or similarity to a desired state from a low-level approximation, and then utilizing the states that maximize the fidelity with this reference space state from the increment active spaces.

The assumption that all increment roots used at previous orders are similar to the reference space wave function can be fulfilled by the requirement that the increment orbitals are added to the

reference space and the calculation is restarted whenever this assumption does not hold true. When the fidelity of a chosen state drops sharply, this generally indicates a significant change to the desired wave function. As a result, all increment orbitals for which the current reference space does not provide an adequate approximation are successively added to the reference space. Employing this procedure, the reference space is constructed as needed by iteratively restarting the calculation until the MBE can be converged reliably. This procedure can be started from an empty reference space and thus provides an unbiased, tailored treatment for arbitrary systems.

5.2 Implementation

For all increment calculations in PyMBE, the Davidson solver starts by solving for the lowest root of the given spin and symmetry while leveraging the reference space wave function as initial guess. If the quantum fidelity of the lowest state and the reference space wave function is already maximal, the energy or property for this state is used to calculate the increment. Otherwise, additional states are successively calculated until the maximum fidelity of all calculated states is larger than the sum of the fidelities of the remaining states. This quantity can be calculated from the accumulated fidelity of all calculated states. The root-finding algorithm is illustrated in Figure 5.1. Whenever two CASCI states for active spaces with differing numbers of orbitals are compared, the correct sign for the individual CI coefficients must be factored into the calculation of the quantum fidelity if the number

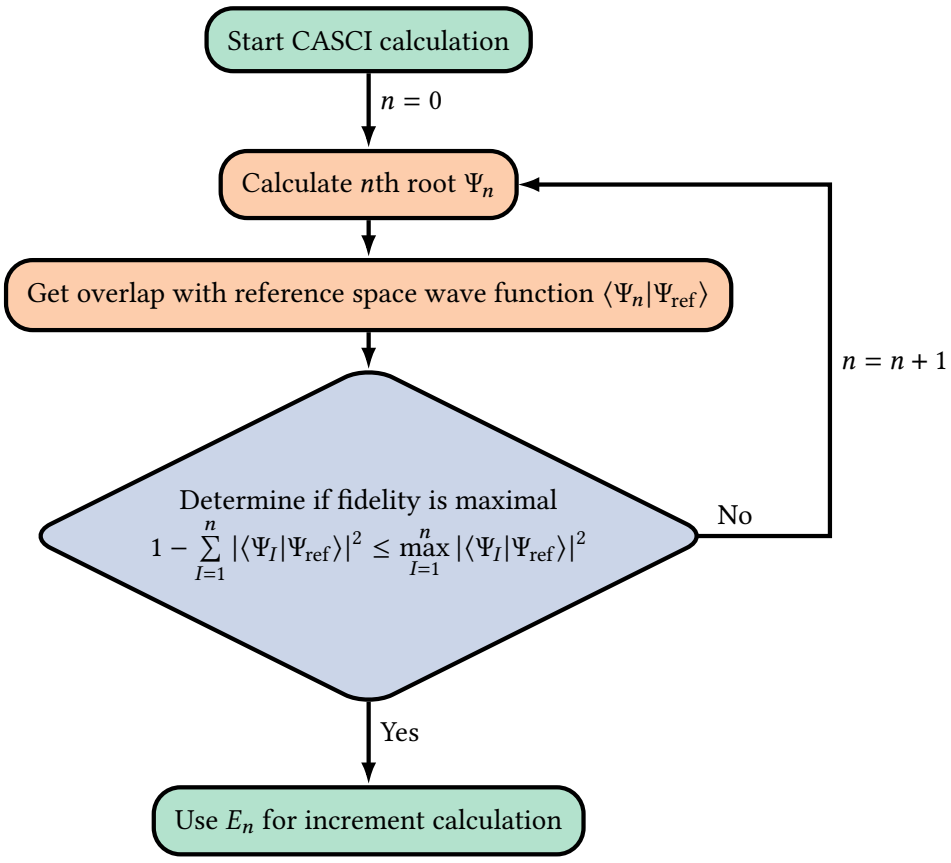

Figure 5.1: Flowchart of the root-finding algorithm for individual CASCI calculations. Adapted with permission from Ref. 496. Copyright 2024 American Chemical Society.

of electrons in both states differs. For *tame* systems, the maximal state will generally be found without calculating more than a single root for a given increment active space. The root-finding approach only functions reliably if the other spin states in a given S_z manifold significantly differ from the reference space wave function as the maximum number of roots for the targeted spin state can otherwise be reached before the decision step in Figure 5.1 triggers. Alternatively, the desired state which produces the maximum overlap with the reference space wave function can be targeted directly through a root-homing procedure.[502] This will often lead to convergence issues for difficult systems which is why the outlined iterative method is preferred.

Orbitals are added to the reference space whenever the quantum fidelity between the FCI wave function and the reference space wave function drops below a user-defined threshold as displayed in Figure 5.2. When multiple tuples produce a quantum fidelity below the threshold at a certain order, the orbitals of the tuple with the lowest quantum fidelity are added to a list of potential orbitals to be added to the reference space as the differences in wave function character between these tuples and the current reference space wave function might coincide. Additionally, all orbitals of tuples which produce fidelities within 1 % of the minimum quantum fidelity are added to this list. From all orbitals in this list, the most frequently occurring orbitals are added to the reference space. If all orbitals only occur once, they are added to the reference space in their entirety. This could either be because no additional orbitals produce fidelities within 1 % of the minimum quantum fidelity or because there is no intersection between the tuples considered to be included in the reference space. By only adding the most frequently occurring orbitals, the algorithm ensures only those orbitals most likely to be responsible for any changes in the wave function are included in the reference space. A dynamic quantum fidelity threshold is implemented in PyMBE to prevent the reference space from growing beyond manageable sizes. This threshold is obtained through a sigmoid function

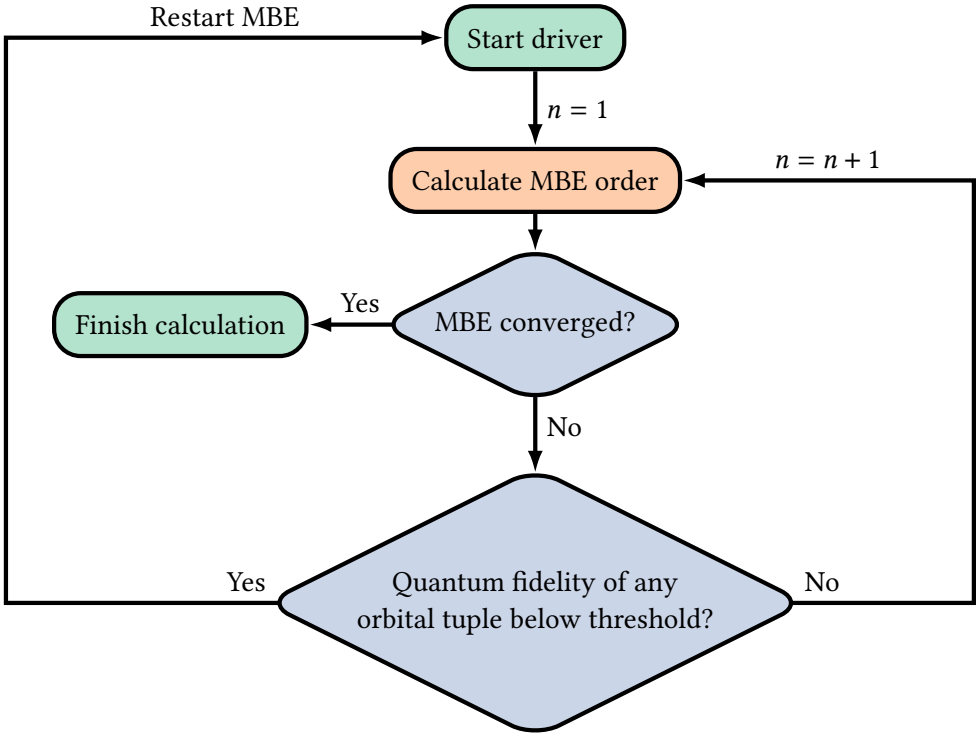

Figure 5.2: Flowchart of reference space detection. Adapted with permission from Ref. 496. Copyright 2024 American Chemical Society.

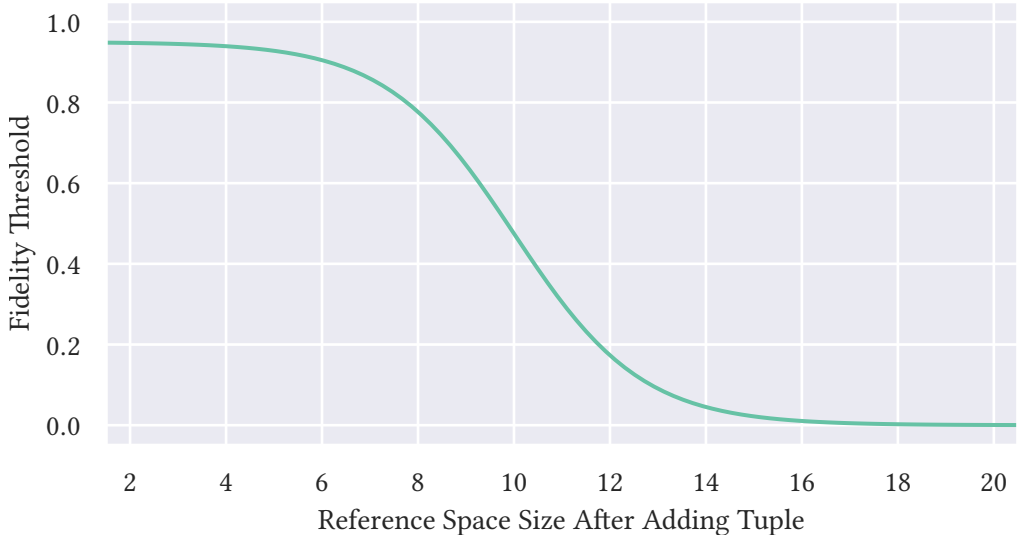

Figure 5.3: Sigmoid function used as quantum fidelity threshold for a starting threshold of 0.95. Adapted with permission from Ref. 496. Copyright 2024 American Chemical Society.

which depends on the potential reference space size if a certain tuple were added and is plotted in Figure 5.3. The starting value of the sigmoid function can be controlled through an input argument. A starting threshold of 0.90 to 0.95 generally captures all orbitals that might potentially cause problems with MBE convergence. The addition of orbitals to the reference space generally takes place during the first few MBE orders. The computational cost of the reference detection process is therefore negligible in comparison to the subsequent MBE-FCI calculation.

5.3 Results

The outlined reference space identification method can be compared to the orbital entropy and mutual information which are commonly exploited in the autoCAS procedure[281,285] to automatically choose active spaces for CASSCF calculations. In this thesis, these quantities are obtained from cost-effective DMRG calculations performed with the *block2* code[503] involving an MPS dimension of 500. While the optimal reference space definition in generalized MBE-FCI is highly correlated to the definition of active spaces in conventional complete active space methods, the MBE is generally able to capture some degree of static correlation outside the reference space. The required reference spaces are therefore often smaller than CASSCF active spaces for a given system. The order in which orbitals are added to the reference spaces for different quantum fidelity thresholds are directly compared to the orbital entropy and mutual information for three different systems: ozone, nickel acetylene, and the phenoxy radical.[a] These systems have been used to investigate the adequacy of UNO occupation numbers for the definition of active spaces for CASSCF calculations.[116] In Figure 5.4, both the orbital entropy and the mutual information for the canonical MOs in the full valence space employing the cc-pVTZ basis set[404] are compared to quantum-fidelity- and MBE-based reference space detection. Orbitals with significant orbital entropy are added to the active space at lower quantum fidelity thresholds, indicating a strong relationship between these quantities. For nickel acetylene, which exhibits only modest orbital entropies, orbitals are only added at quantum fidelities around 0.98. For all systems, clear patterns for strongly correlated orbitals can be observed which generally agree

[a] Geometries from Ref. 116

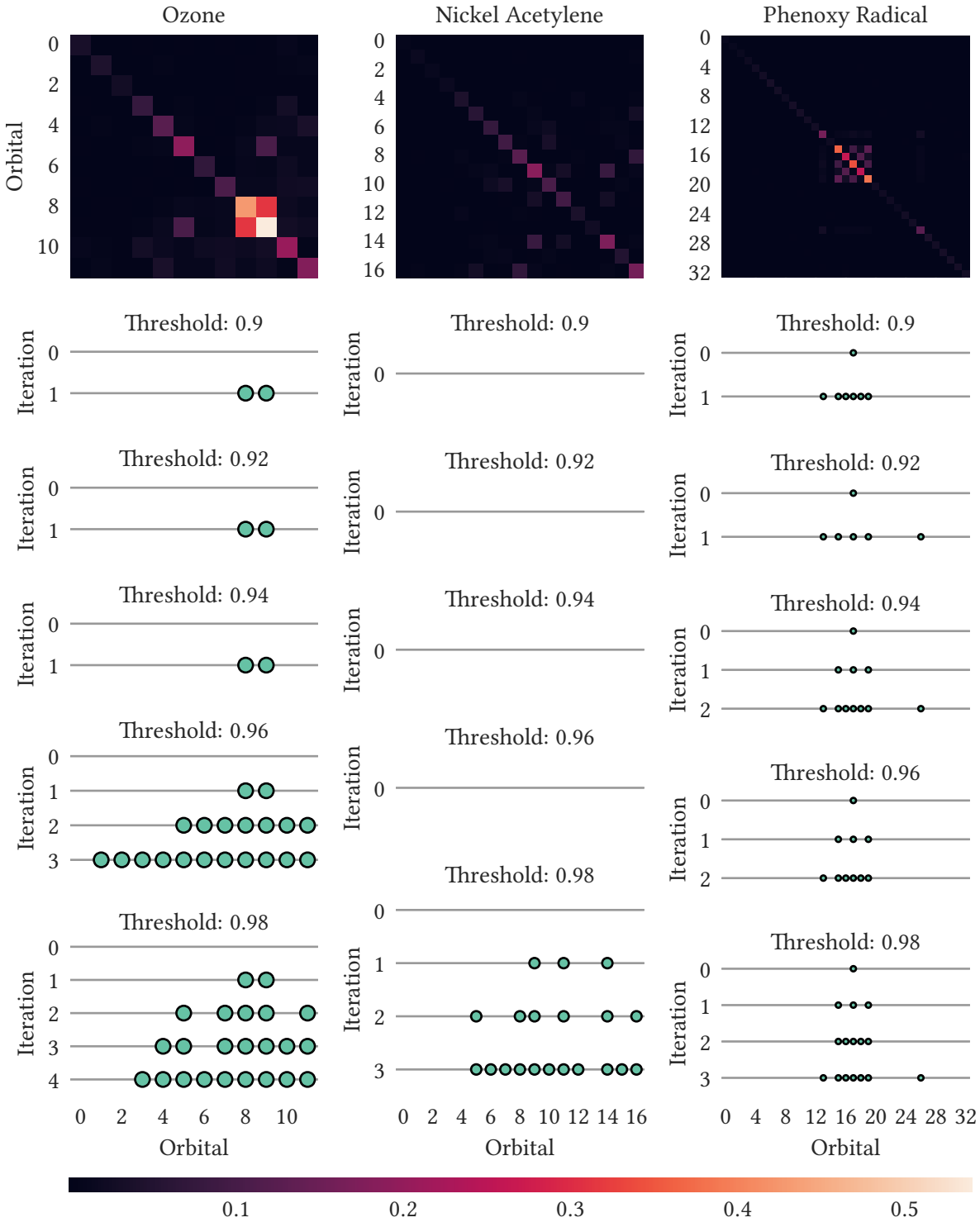

Figure 5.4: Comparison of quantum entanglement diagrams from DMRG calculations to iterative quantum fidelity MBE-based addition of orbitals to the active space for ozone, nickel acetylene, and the phenoxy radical in the canonical MO basis. Top: Diagonal elements describe single-orbital entropy, off-diagonal elements describe mutual information. Bottom: Green circles describe orbitals in the active space at the end of an iteration. Adapted with permission from Ref. 496. Copyright 2024 American Chemical Society.

and would lead to similar active spaces depending on the chosen thresholds. Pairs of orbitals which possess significant contributions to the mutual information are generally added simultaneously as the electrons occupying these orbitals will often already strongly interact for small active space sizes. In some cases, the quantum-fidelity-based reference space identification will add relatively unimportant orbitals in conjunction with orbitals that exhibit significant orbital entropies. Whenever this happens, the latter orbitals are unable to overcome the static quantum fidelity threshold unless the former orbitals are also included in the reference space. When a higher threshold is used instead, the important orbitals are added at earlier orders of the MBE, resulting in a smaller chosen active space. In actual MBE-FCI calculations, this potential issue is diminished by utilizing the dynamic quantum fidelity threshold described in Figure 5.3 which decreases when a larger number of orbitals are considered to be added to the reference space.

Similar to autoCAS and other active space selection approaches, the outlined approach can be applied to arbitrary orbital bases as it is not based on orbital energies or occupation numbers which are only defined for orbitals which diagonalize the Fock matrix or 1-RDM. Both introduced techniques for active space identification are compared for the PM LMO basis in Figure 5.5. In the LMO basis, the quantum-fidelity- and MBE-based active space identification again displays very strong correlation to the patterns in the orbital entropy and mutual information heatmaps. Automatic schemes based on both methods will produce identical active spaces for corresponding thresholds. The quantum-fidelity-based method is able to compete with results from full valence DMRG calculations while only exploiting information from numerous small active space calculations. Nevertheless, in its current form, the outlined algorithm is hindered from predicting active spaces larger than the limits of conventional FCI since this procedure requires CASCI calculations involving the full predicted active space. Identifying such large active spaces is necessary for approximate CASSCF methods. An alternative, non-iterative procedure could be formulated by adding all orbitals which produce active spaces below a quantum fidelity threshold up until some low MBE order. Such a procedure is expected to be sufficient for the identification of large active spaces since this application will commonly not require the mutual correlation between all active space orbitals but only among small subsets of these.

Applications of the reference space detection in the context of MBE-FCI for a variety of molecular systems are presented in Chapter 7 in conjunction with the orbital clustering, screening, and error estimation developments presented in the next chapters.

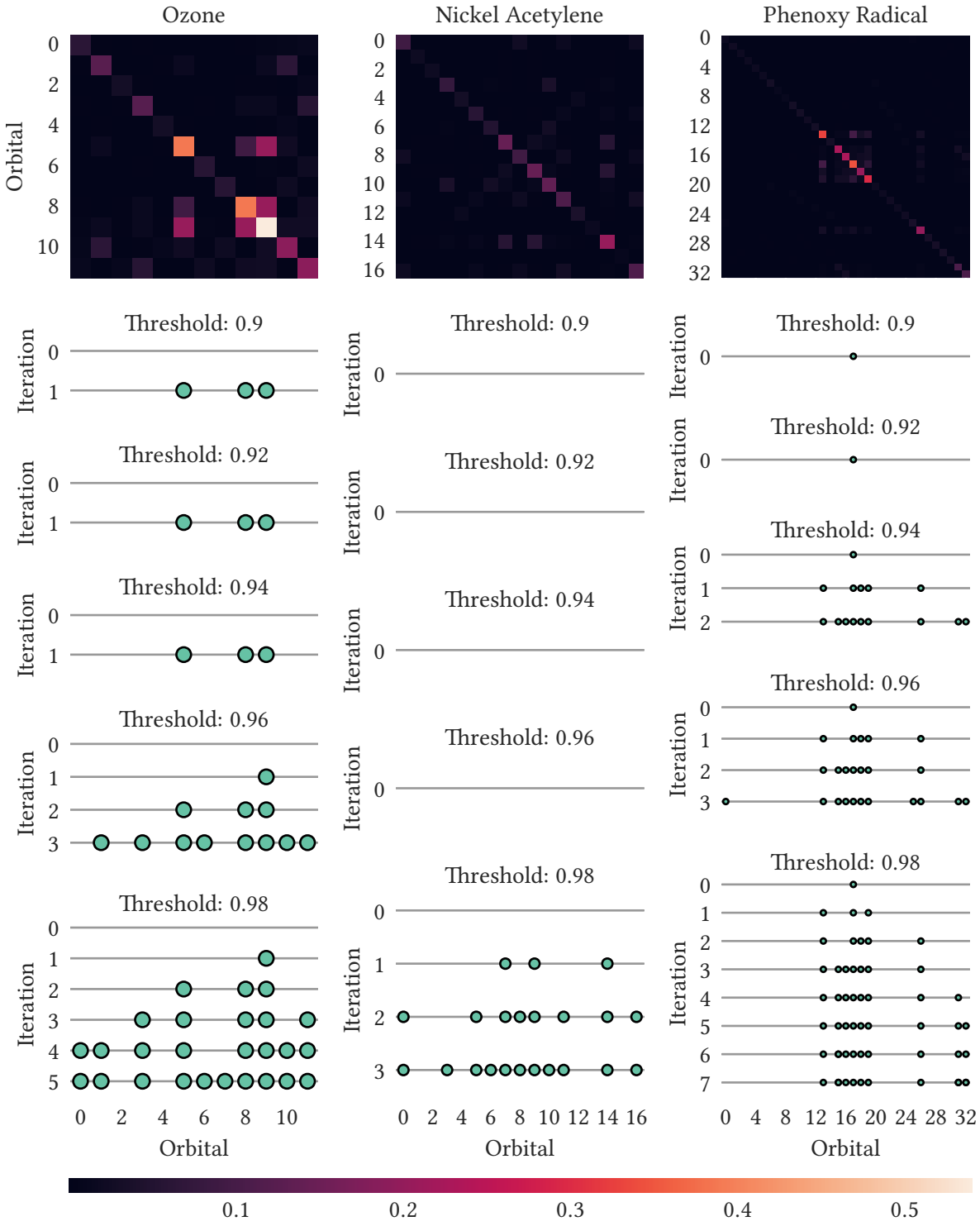

Figure 5.5: Comparison of quantum entanglement diagrams from DMRG calculations to iterative quantum fidelity MBE-based addition of orbitals to the active space for ozone, nickel acetylene, and the phenoxy radical in the PM LMO basis. Top: Diagonal elements describe single-orbital entropy, off-diagonal elements describe mutual information. Bottom: Green circles describe orbitals in the active space at the end of an iteration. Adapted with permission from Ref. 496. Copyright 2024 American Chemical Society.

6 Orbital Clustering in MBE-FCI

For dynamically correlated systems, the reference space will generally remain empty during the outlined automatic detection procedure because the addition of orbitals will only cause small perturbations to the underlying HF wave function. Whenever many orbitals need to be treated by employing MBE-based methods, either due to system or basis set size, empty reference space calculations will often be infeasible due to a combinatorial explosion of the number of increments at higher orders of the expansion. This constraint severely limits the accuracy up to which the MBE can be converged. This issue can be delayed by forming orbital clusters and using these as objects of the expansion. Work by Abraham and Mayhall[46] has impressively showcased that the MBE in a tensor product state basis is able to efficiently treat larger systems when orbital clusters based on a cluster mean-field reference[470] are employed. The orbital clusters are chosen on the basis of exchange matrix element magnitudes or as bonding/antibonding orbital pairs. Before these developments, Dolg and co-workers have constructed occupied LMO clusters and corresponding projected AO excitation spaces from distance criteria involving the LMO centers of charge and utilized these in incremental CCSD expansions.[34,35] This chapter introduces cluster-based expansions for the MBE-CC and MBE-FCI methods involving optimal orbital clusters constructed by exploiting low-order MBE information. The work in this chapter was published in Ref. 496.

6.1 Theory and Implementation

Assigning orbitals to orbital clusters and using these as expansion objects can significantly reduce the total number of increments that need to be calculated at a given MBE order. When considering cluster-based expansions, there are different approaches for defining the MBE order. Traditionally, the MBE order groups increments by the number of expansion objects which would correspond to the number of orbital clusters.[46] One disadvantage of this definition is the varying computational effort required to solve the CASCI problem for different cluster sizes which makes load balancing a lot more complex when running calculations in parallel. In addition, individual CASCI calculations might get too expensive to solve for combinations of large orbital clusters for a given MBE order while increment calculations on other tuples at this order formed from smaller orbital clusters are still feasible. This definition of the MBE will perform well, when the chosen clusters are very homogenous both in size and occupation which will rarely be possible for chemical systems in arbitrary basis sets. Alternatively, the MBE order can also be defined as the number of expansion space orbitals that are included in a tuple. As a result, all orbital tuples for a given MBE order will have the same active space size and will therefore require similar computational effort for a given occupation. Additionally, this definition can be seen as a generalization of π-pruning for linear molecules and will produce exactly the same results when degenerate π_x- and π_y-orbitals are put into clusters. π-pruning is used in the context of MBE-FCI to guarantee convergence to the correct ground state for linear systems while employing Abelian subgroups which is achieved by grouping degenerate π_x- and π_y-orbitals in the same orbital cluster.[41,42,112] π-pruning also significantly accelerates calculations on linear

systems due to the aforementioned reduction in increment calculations. Due to these advantages, this definition of the cluster MBE order was adopted in PyMBE.

Unfortunately, defining the MBE such that the MBE order corresponds to the number of expansion space orbitals in a tuple makes both tuple generation itself and the calculation of the total number of tuples at a given MBE order more complicated. An alternative generator for tuple generation was added to PyMBE and is described in Figure 6.1. This recursive generator is used whenever the

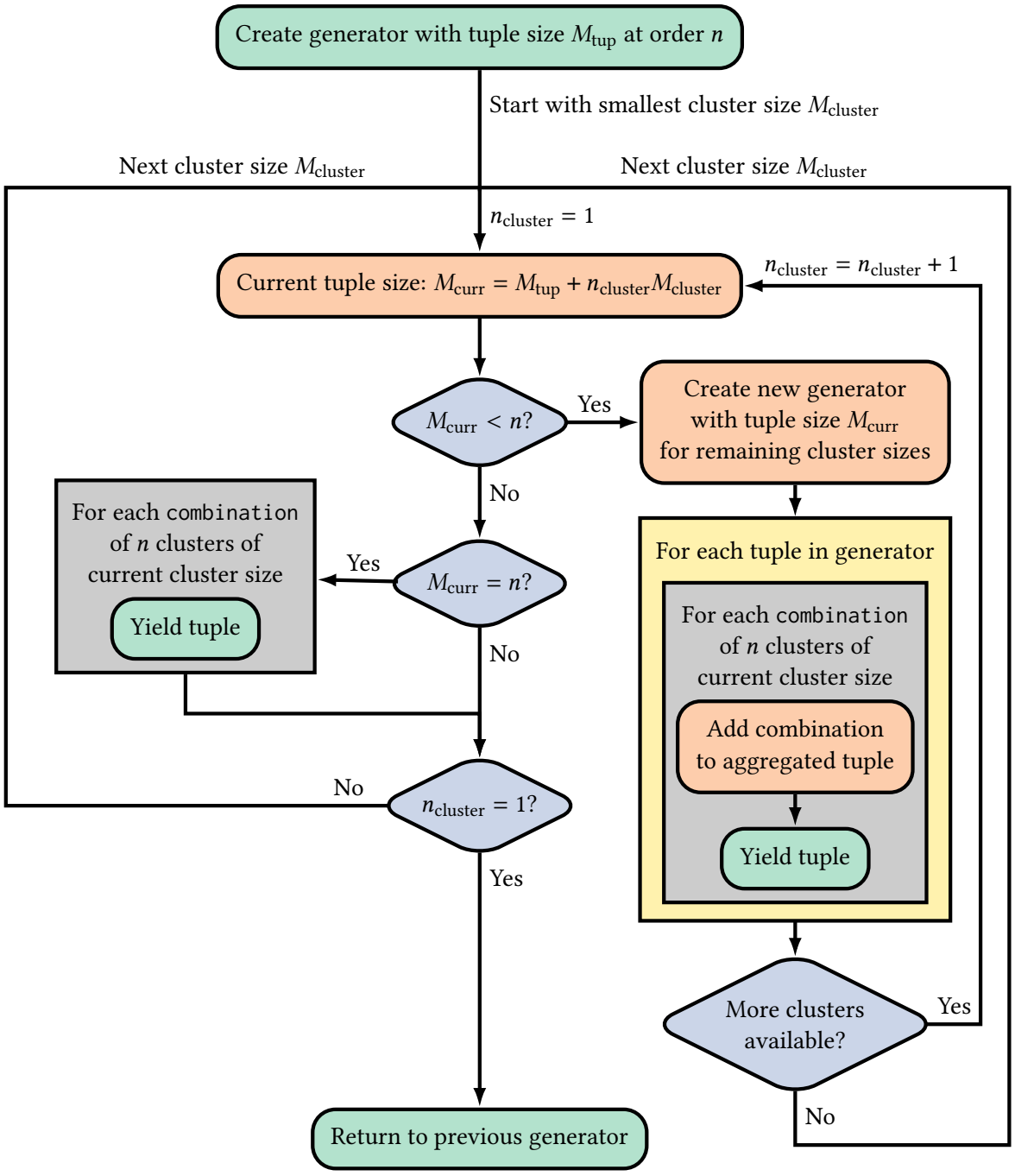

Figure 6.1: Flowchart of recursive cluster tuple generation. The generator function requires the orbital clusters to be sorted by size.

expansion space is formed from orbital clusters. The recursion depth of this generator corresponds to the number of differently sized clusters that are included in the tuple. A new generator is created recursively for every cluster size that is considered to be included in the tuples generated for this order until the sum of these reach the desired tuple size. The last generator then yields orbital tuples for all combinations of clusters that correspond to its cluster size. The previous generators add their clusters to the aggregated tuple until the entire tuple is filled. As a result, all combinations of clusters that yield tuples contributing to the current MBE order can be obtained. The recursive generator used in PyMBE does not only produce tuples of a given number of expansion space orbitals (the MBE order) but additionally only produces tuples of a given occupation which is not described in Figure 6.1 for conciseness and clarity. The actual implementation therefore includes another loop over the number of virtual orbitals. Orbital tuples that will not contribute due to occupation are automatically avoided and are not produced by the recursive generator. The orbital clusters are required to be sorted by size and occupation which is done once at the very beginning of the MBE calculation.

The construction of increments requires the generation of all of a tuples' subtuples as described in Equation (2.68). Since it is necessary to generate the subtuples for all tuples at a given order, this recursive generator has to be called repeatedly which can become expensive. For orbital tuples that equal both in the size and occupation of their clusters, the size and occupation of the orbital clusters that produce valid subtuples will also equal. For this reason, an alternative non-generator implementation exists that generates the possible subtuple types and then just loops over all combinations that can be generated by assigning the tuple clusters to these subtuple types. The function that generates the subtuple types can be accelerated through *memoization*, the caching of function results such that repeated function calls with equivalent inputs can be avoided. On the basis of these developments, the PyMBE code is able to efficiently perform MBE calculations for arbitrary cluster choices.

While the MBEs of all cluster choices will yield an approximation to the correlation energy, some choices might accelerate convergence more than others. The consequence of orbital clustering will be that some correlation energy contributions of n orbitals will not contribute at the nth order but will instead be pushed to later orders in the expansion. The goal should be to choose the orbital clusters in a way such that these n-orbital contributions are less important than those explicitly considered at the nth order. For this reason, the `MBE` member function `cluster_orbs` chooses orbital clusters with the intent of maximizing the intracluster correlation while minimizing the intercluster correlation. This is achieved by attempting to form a set of clusters that is as homogenous as possible up to a given user-defined cluster size n_{max} and assigning orbitals to these clusters while maximizing the pair correlation up until a designated MBE order. The algorithm devised to assign orbitals to clusters is described in Figure 6.2 and starts by generating cluster types with homogenous size and occupation. Since the total number of expansion space orbitals and electrons is rarely divisible by the supplied maximum cluster size, the predetermined cluster types are often not perfectly homogenous. This step is followed by a single-orbital MBE calculation until a given maximum MBE order. The sum of the increment magnitudes is accumulated for all possible orbital pairs that can be constructed from a tuple's orbitals. Contributions from individual orbitals from calculations involving a non-empty reference space are not considered as these contributions do not benefit from clustering. The outlined procedure will form a symmetric matrix of pair contributions with a vanishing diagonal.

The sum of the intracluster contributions of the predetermined clusters (hereinafter referred to as the *score function*) can be maximized through permutations of the orbitals in this matrix. This combinatorial optimization problem exhibits numerous local maxima and must therefore be solved by employing algorithms suitable for global optimization. A frequently applied method for the global optimization within large, discrete search spaces is simulated annealing.[504] While simulated

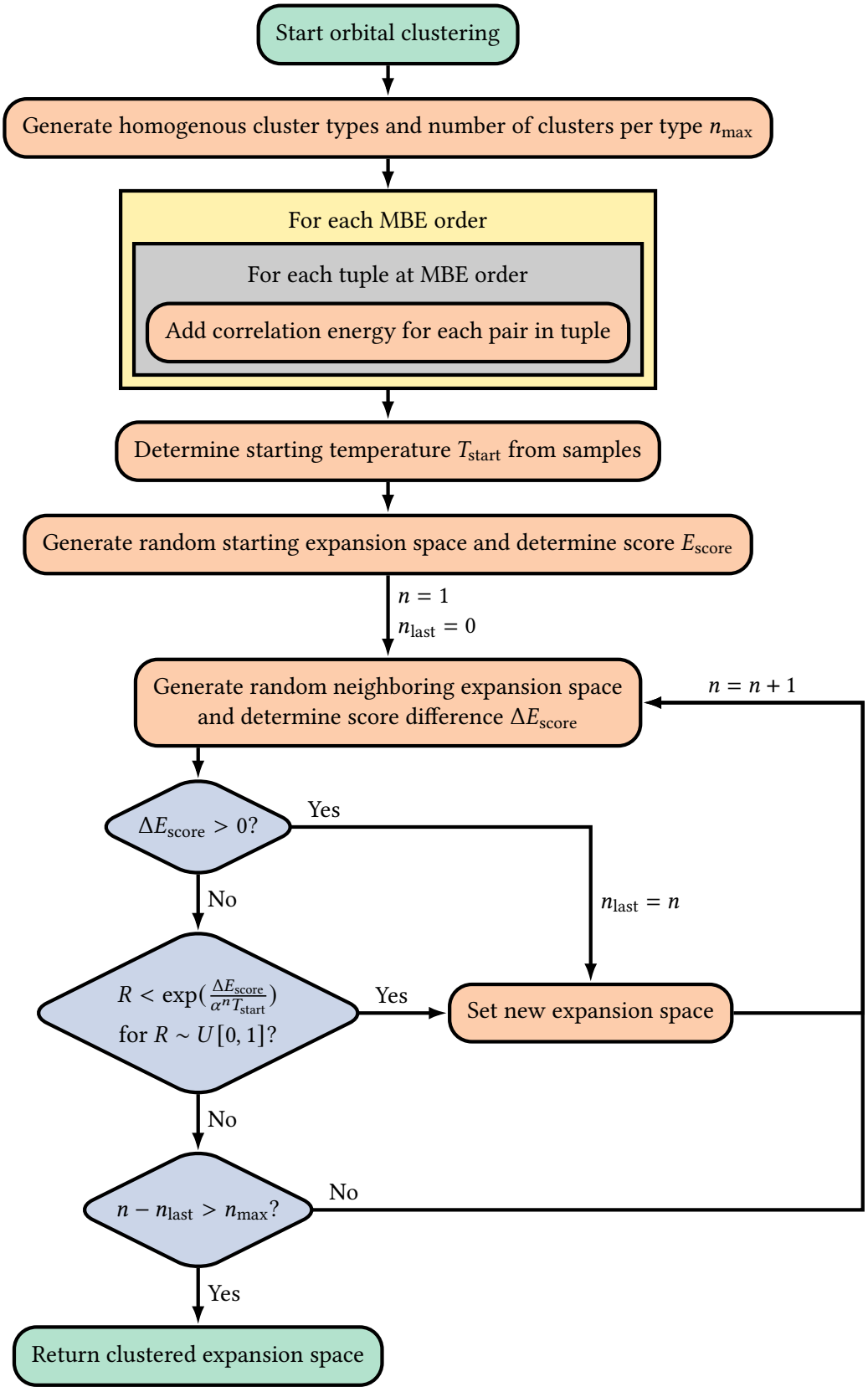

Figure 6.2: Flowchart of orbital clustering.

annealing often requires many function evaluations to reach the global maximum, the computational cost of evaluating the score function is comparatively low. A slow, exponential cooling schedule is employed. An important hyperparameter of simulated annealing is the starting temperature T_{start} which affects both performance and the ability of the method to reach a global optimum. When T_{start} is too high, the algorithm spends many iterations randomly walking through the search space without improving the score function. Conversely, a value set too low will get stuck in the well of a local optimum. Instead, T_{start} can be determined automatically through an iterative method by maintaining an acceptance rate of the Metropolis condition described in Figure 6.2 for a number of random samples.[505] In this thesis, a target acceptance rate of 0.99 and 1000 random samples were used to determine T_{start}. Annealing is continued until the score function has not increased for $n_{\text{max}} = 100000$ iterations and the temperature scheduling parameter α is chosen such that the temperature decreases to 10^{-5} over n_{max} iterations. After the simulated annealing procedure has converged, the resulting clusters will automatically replace the expansion space in PyMBE and a clustered MBE calculation can be started by invoking the `kernel` function.

6.2 Results

The orbital clusters produced by the clustering algorithm can be investigated through heatmaps of the accumulated increment magnitudes for all possible orbital pairs. These heatmaps and the clusters constructed using the outlined algorithm from MBE information until order 4 are presented for canonical MOs and PM LMOs of benzene[a] (C_6H_6) in a cc-pVDZ basis set[404] for different cluster sizes in Figure 6.3. In the canonical MO basis, the pair correlation matrix does not exhibit a significant level of sparsity. Nevertheless, the non-linear scale of the heatmaps in Figure 6.3 exaggerates the absence of sparsity but is crucial to reveal structure and draw insights from these heatmaps. The accumulated increment magnitude between occupied orbital pairs will generally be larger for standard calculations because the total correlation energy of the system is distributed among a larger number of virtual orbitals such that these will have fewer increment contributions. The orbitals within the clusters in Figure 6.3 are sorted by orbital index. The occupied orbitals can clearly be distinguished from the virtual orbitals in the clusters. The largest pair contributions to the correlation energy are concentrated in the cluster blocks highlighted in cyan. Larger cluster sizes are clearly able to accommodate a greater proportion of significant pair contributions. Substantial contributions outside these clusters cannot be recovered unless the cluster occupation and size constraints are relaxed. These occupation constraints are necessary to treat the occupied and virtual orbitals on an equal footing during the clustering procedure and to ensure uniform cluster properties. In the LMO basis, clustering is generally more efficient due to increased sparsity in the pair correlation contributions. LMO pairs will generally have much larger correlation energy contributions whenever both orbitals are spatially local. The resulting cyclical structure is clearly visible on the right side of Figure 6.3.

While the utilization of larger orbital clusters will generally recover a greater fraction of the correlation energy at early orders of the expansion, this comes at the price of more expensive individual CASCI calculations. Choosing an appropriate cluster size is therefore highly dependent on the computational scaling of the targeted quantum chemical method. To investigate how the cluster size affects the time-to-solution for different targeted quantum chemical methods, wall times[b] are presented in Figure 6.4 for methane[c] (CH_4) in different Dunning correlation-consistent basis sets.[404] All expansions are

[a] Geometry from Ref. 135

[b] Computer architecture: Four Intel Xeon CPUs E5-4620 on a single node (64 threads, 32 cores @ 2.4 GHz, 7.80 GB/thread), only 4 threads / 2 cores are employed for the MBE-CCSD calculations (124.75 GB/thread)

[c] $R(\text{C}-\text{H}) = 1.1015\,\text{Å}$

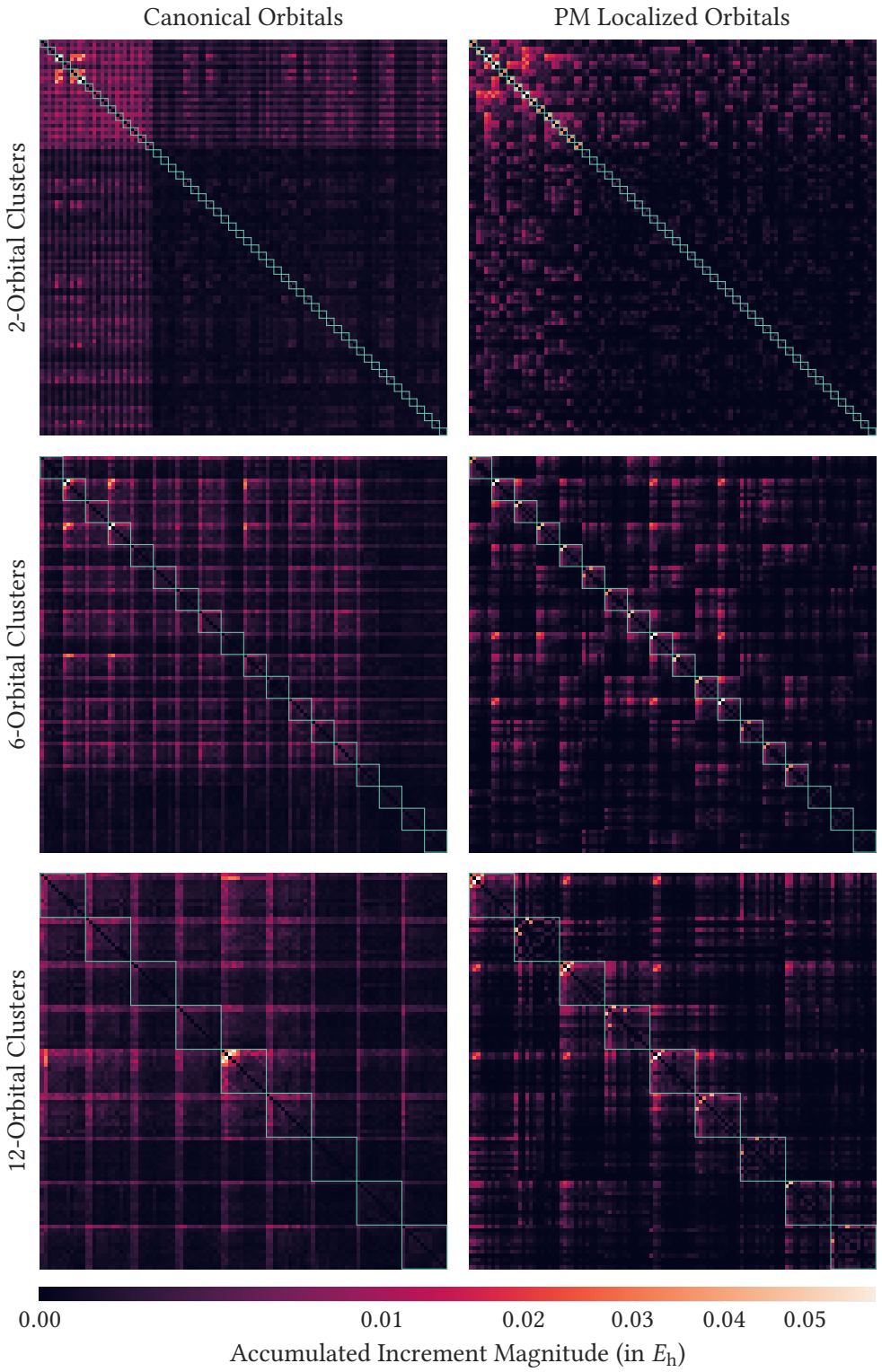

Figure 6.3: Accumulated increment magnitudes for canonical and PM LMO orbital pairs of C_6H_6 in a cc-pVDZ basis set from an MBE truncated at order 4. The orbitals are rearranged according to the outlined clustering algorithm for different cluster sizes. The cyan outlines describe the respective optimized orbital clusters.

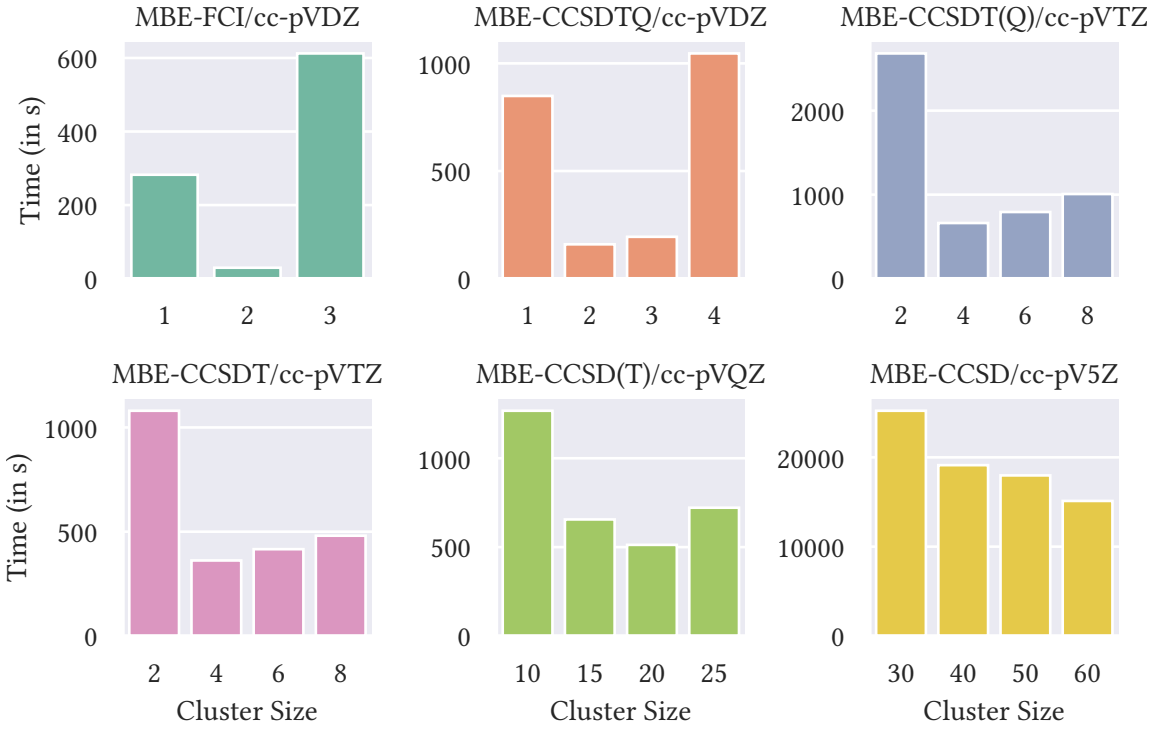

Figure 6.4: Timings for MBE-FCI and a variety of MBE-CC methods for CH_4 in different basis sets and for different cluster sizes. All expansions are terminated at the order corresponding to six times the cluster size.

terminated such that all six-orbital contributions are recovered. Therefore, the calculations will in all cases be more accurate than the calculations involving smaller cluster sizes as additional contributions involving multiple orbitals from the same clusters are taken into account. For MBE-FCI, a cluster size of two orbitals appears to offer an optimal compromise between the computational effort required to perform individual increment calculations and the total necessary number of increment calculations. For clusters involving three orbitals, the last-order increments involve 18 orbitals and therefore become too expensive, negatively affecting the timings. The optimal cluster size for the MBE of a given quantum chemical method also depends on the termination order of the expansion. When the termination order increases, the cost of the increment calculations at the last orders might overshadow any possible gains from a reduced number of calculations. Therefore, the optimal cluster size will decrease as the termination order is increased. Additionally, a larger number of reference space orbitals will also favor smaller cluster sizes.

As a general trend, the MBE-CC expansions in Figure 6.4 will benefit from larger cluster sizes as the computational scaling with respect to increment size decreases. For MBE-CCSDTQ, cluster sizes of two or three orbitals appear optimal. When comparing MBE-FCI and MBE-CCSDTQ, the former appears to outperform the latter. This is caused by the large prefactor of the highly nonlinear CC equations for small calculations and the fact that the ncc backend is not optimized for repeatedly performing many calculations involving only few orbitals. Nevertheless, CCSDTQ will demonstrate superior performance for the larger increment calculations stemming from increased cluster sizes as FCI succumbs to its exponential scaling. MBE-CCSDT(Q) and MBE-CCSDT appear to perform optimally employing cluster sizes of four orbitals while small increases in computational cost are observed for clusters involving more orbitals. From these results, MBEs of high-level CC methods such as CCSDT, CCSDT(Q), or CCSDTQ will be able to compete with conventional CC methods for

the treatment of large systems when employing orbital clustering.

Moving on towards approximations of the *gold standard of quantum chemistry*, CCSD(T), clusters of about 20 orbitals are required to perform MBE-CCSD(T) calculations in an optimal manner. Employing these large cluster sizes will generally cause the MBE to become memory-bound as the required two-electron integrals and intermediates increase the memory footprint of the individual increment calculations. As a result, the MBE-CCSD calculations in Figure 6.4 are only performed on two computational cores. For MBE-CCSD, the computational cost continues to decrease as the cluster size is increased. If the MBE is terminated after six orbital clusters are included in the increment calculations, MBE-CCSD is not expected to be able to compete with the conventional CCSD computation due to similar scaling. A memory-optimized MBE code employing a resolution-of-identity[506–509] or Cholesky decomposition[365,366] approach to reduce the memory requirements of the two-electron integrals could be applied to larger systems which are out of reach for conventional CCSD calculations.

Further investigations and applications of orbital clusters in the context of MBE-based methods are presented in Chapters 7 and 9 in combination with controlled truncation of the MBE through screening and error estimation and with symmetry exploitation.

7 Screening and Error Estimation in MBE-FCI

The errors of approximate FCI methods that are introduced through thresholding are often difficult to gauge for systems for which FCI reference calculations are not feasible. For this reason, many approximate FCI methods offer strategies to approximate and control errors. ASCI,[121,122] iCI,[123] and SHCI[120] use a subset of important determinants on the basis of which the CI problem is solved. The remaining contribution of a larger subset of important determinants (ASCI) or all remaining determinants (iCI and SHCI) is then approximated perturbatively. The error of this perturbative contribution is often estimated by performing these calculations for differing numbers of determinants and extrapolating the variational energy against the perturbative correction using a linear or higher polynomial fit.[120–123] The variational energy of this fit at vanishing perturbative correction is taken as the final result. A similar procedure is commonly used in DMRG as described Section 2.3.2.[119,314,329,330] For both SCI and DMRG, the error of this approximate energy can be determined from the accuracy of the involved fit,[121,122] from the differences between extrapolated values from different fits,[120] or by taking a fraction of the extrapolation distance.[119] In general, both the quality of the fit itself and the extrapolation distance should affect the accuracy of the obtained result. The resulting errors will only provide a rigorous estimate if the fit function correctly describes the underlying correlation between the respective variable and the error. For QMC methods, the sampling error is commonly estimated through a blocking analysis.[118] This chapter proposes an algorithm for screening and the estimation of errors for the MBE-FCI method. The work in this chapter was published in Ref. 496.

7.1 Theory and Implementation

MBE-based methods are only practically feasible when the expansion is terminated after a certain accuracy threshold has been reached. Since the MBE method is not variational and often exhibits oscillatory convergence, the state of convergence and the potential error of MBE calculations is difficult to assess by only considering the total increment at a given order. With the fixed screening procedure outlined in Section 3.1.3, the same number of orbitals is screened away regardless of the convergence behavior of the MBE towards the target property. This shortcoming motivates the need for a systematic screening procedure that dynamically adjusts for the state of convergence and associates error bars with the final results.

The convergence of the MBE is rooted in two assumptions:

1. The mean of the increment magnitudes for a distinct number of orbitals decreases as the number of orbitals increases. For this to lead to convergence, the mean absolute magnitude of the increments has to drop faster than the total number of increments increases throughout the MBE.

2. The majority of the increments will cancel out due to differing signs and similar magnitudes at late orders of the expansion.

The latter of these assumptions accelerates the convergence dictated by the former. A possible approach to estimate contributions at later orders is through random sampling. Unfortunately, the recursively constructed increments require all subtuple increments such that only the $n + 1$-order increments can be readily sampled at order n. Instead, the screening and error estimation algorithm introduced in this chapter will exploit an empirical relationship of the mean increment magnitude in conjunction with Monte-Carlo importance sampling current-order increments to make predictions at future orders. The absolute increments $|\Delta\epsilon|$ generally decrease exponentially with the expansion order, as showcased in Figure 7.1 for water[a] (H_2O), ammonia[b] (NH_3), and methane[c] (CH_4) in a cc-pVTZ basis set.[404] For all three systems, the increments at every order follow a log-normal distribution and the geometric mean (GM) decreases exponentially as the expansion order increases. The number of increments grows at a lower rate, indicating convergence of the MBE. At later orders, the increment distributions will start to deteriorate because many increments approach the convergence criterion of the increment calculations (set to $10^{-10}\ E_\mathrm{h}$ by default) and the numerical threshold for double-precision floating point operations.

When orbital clusters are used as expansion objects as described in Chapter 6, combinations of differently sized clusters can contribute at a given MBE order. To illustrate, combinations of four single orbitals, one pair cluster and two single orbitals, two pair clusters, and one triple cluster and one single orbital can contribute at MBE order 4. As a result, the increment magnitude will no longer be strictly correlated to the MBE order. Instead, contributions from orbital combinations that would otherwise show up at earlier orders in a single-orbital MBE are now only recovered at the current order. In the above example, the increment formed from one pair cluster and two single orbitals will not only add the four-orbital contribution but also those three-orbital contributions that require orbitals from all three clusters. The increments formed from two pair clusters and from one triple cluster and a single orbital will also include the two- and three-orbital contributions requiring orbitals from both clusters. In a single-orbital expansion, all of these lower-order contributions would instead appear at the respective MBE order. The corresponding increments directly describe these individual contributions. As the magnitudes of these increments decrease exponentially with the MBE order (or the number of tuple orbitals), a clustered MBE increment magnitude will mostly be correlated to the number of orbitals in the orbital contribution involving the smallest number of orbitals that is not considered in the subtuple increments. This number is equal to the number of clusters N_cluster in the tuple because all contributions formed by a single orbital from every cluster in this tuple cannot be included in any subtuple calculation involving only a subset of these clusters. Additionally, the increment magnitude will be larger when a greater number of these contributions N_contrib occur for a given cluster tuple. The quantity N_contrib can be calculated from the product of the cluster sizes of said orbital tuple. Returning to the illustrative example, $N_\mathrm{cluster} = 3$ and $N_\mathrm{contrib} = 2$ for the tuple of one pair cluster because two three-orbital contributions involving either one of the pair orbitals and both single orbitals have not been considered. Correspondingly, the tuple of two pair clusters will correspond to $N_\mathrm{cluster} = 2$ and $N_\mathrm{contrib} = 4$ while the tuple of one triple cluster and one single orbital will produce $N_\mathrm{cluster} = 2$ and $N_\mathrm{contrib} = 3$. The tuple of four single orbitals is equivalent to the single-orbital case and will therefore produce $N_\mathrm{cluster} = 4$ and $N_\mathrm{contrib} = 1$, in correspondence with the increment magnitude correlation being correlated to the MBE order in Figure 7.1. From this discussion, the empirical relationship of the increment magnitude for a clustered MBE can be defined as follows:

$$|\Delta\epsilon| = aN_\mathrm{contrib} \cdot \exp\left(bN_\mathrm{cluster}\right) + \bar{\varepsilon}. \tag{7.1}$$

[a] $R(\mathrm{O{-}H}) = 0.9668\ \text{Å}$, $\sphericalangle(\mathrm{H-O-H}) = 101.9°$
[b] $R(\mathrm{N{-}H}) = 1.0277\ \text{Å}$, $\sphericalangle(\mathrm{H-N-H}) = 103.5°$, $\sphericalangle(\mathrm{H-N-H-H}) = 107.7°$
[c] $R(\mathrm{C{-}H}) = 1.1015\ \text{Å}$

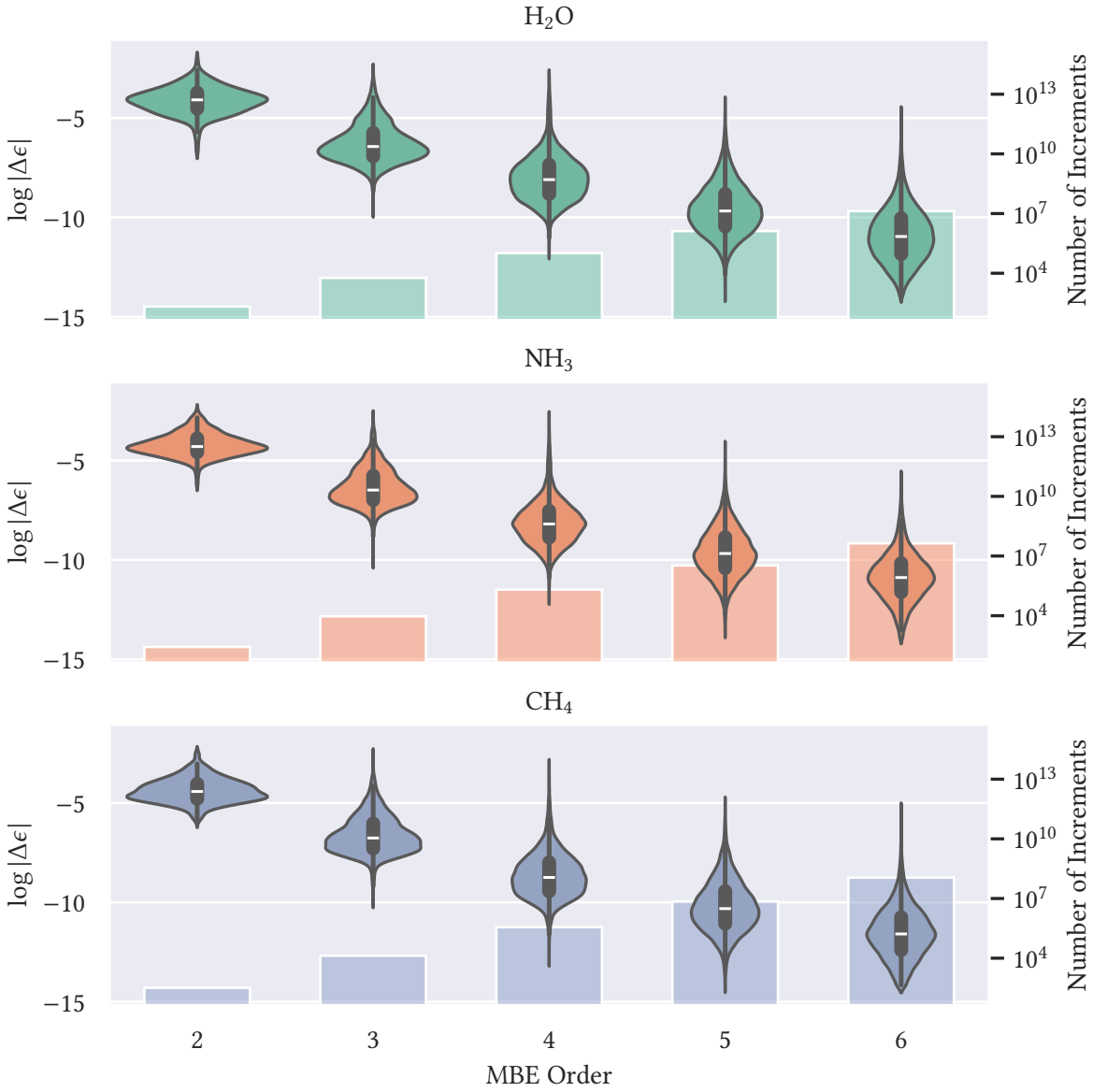

Figure 7.1: Distribution of log-transformed absolute increments $\log|\Delta\epsilon|$ at different expansion orders ($k \leq 6$) for a single-orbital MBE-FCI calculation of H_2O, NH_3, and CH_4 based on an empty reference space in a cc-pVTZ basis. The symmetric kernel density estimate of the distributions is displayed in green, orange, and blue, while the white lines describe the median, the boxes describe upper and lower quartiles, and the whiskers indicate data points within 150 % of the interquartile range. The orange bar plot describes the number of increments. Both y-axes operate on the same scale. Adapted with permission from Ref. 496. Copyright 2024 American Chemical Society.

a and b are the fitting parameters. $\bar{\varepsilon}$ is the error that leads to the log-normal distribution and is caused by other effects, such as increment occupation and varying interaction between the involved orbitals, that are not considered in this rather simple model.

The increment magnitudes $|\Delta\epsilon|$ can be normalized by dividing by N_{contrib}. The resulting distribution of these normalized increment magnitudes are showcased in Figure 7.2. The normalized increment magnitudes are again distributed log-normally and the GM decreases exponentially with the number

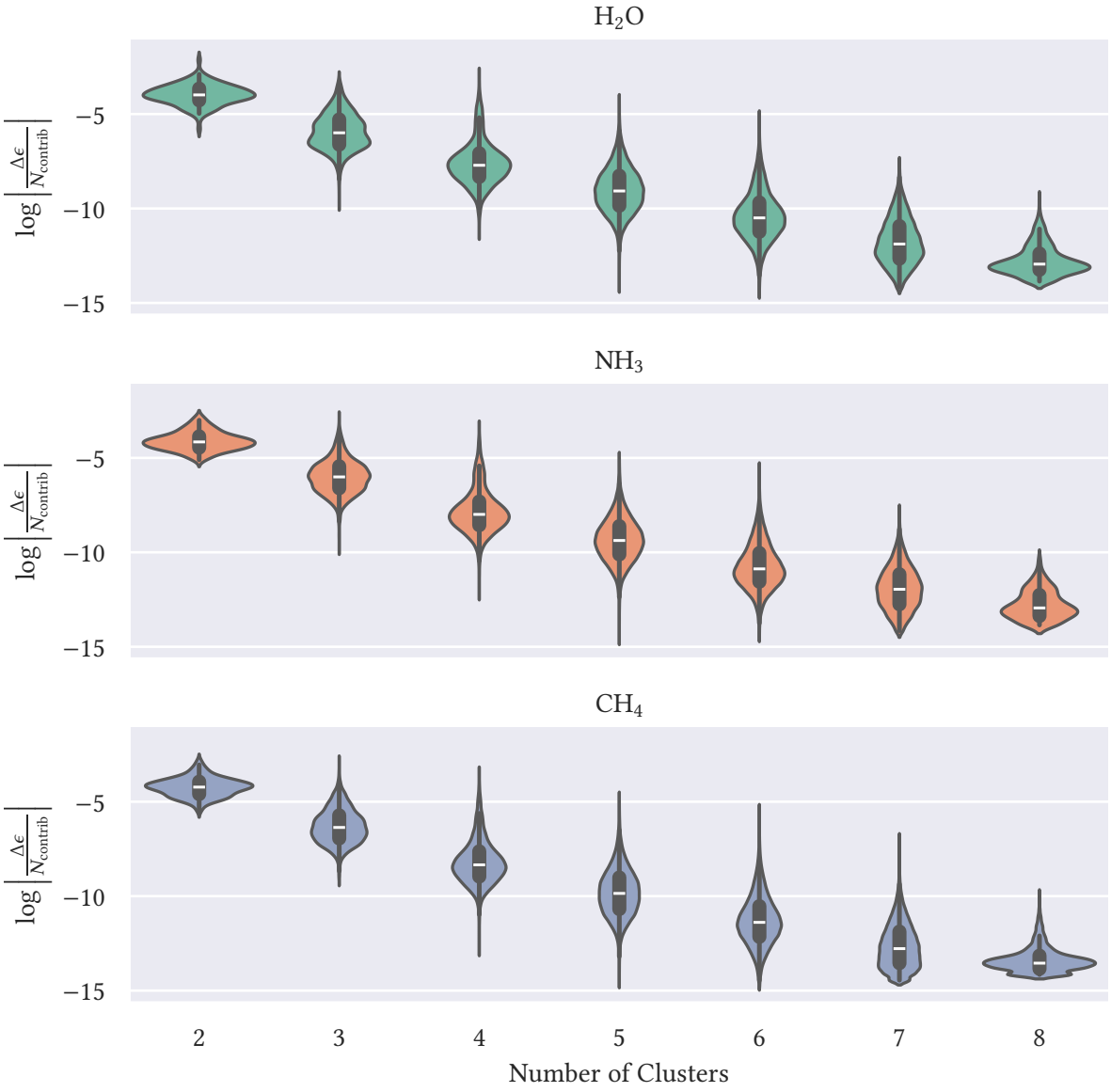

Figure 7.2: Distribution of log-transformed normalized absolute increments $\log|\Delta\epsilon/N_{\text{contrib}}|$ at different MBE orders ($k \leq 8$) for a clustered MBE-FCI calculation of H_2O, NH_3, and CH_4 based on an empty reference space in a cc-pVTZ basis. Orbital clusters comprising between one and four MOs have been selected at random. Adapted with permission from Ref. 496. Copyright 2024 American Chemical Society.

of clusters. For increments involving a larger number of clusters, the distributions are censored due to finite convergence criteria and the limits of floating-point precision and as a result the empirical linear relationship deteriorates as shown in Figure 7.3. When tighter convergence criteria are employed, these deviations from linearity are mostly caused by the limits of double-precision floating point operations. The resulting distributions in Equation (7.1) will be skewed towards larger increment energies. This behavior is generally not problematic unless extremely high accuracy is targeted since the increments at late orders are small in magnitude and exhibit completely random signs such that the majority will cancel out.

The ability to predict the magnitude of individual increments by employing Equation (7.1) is severely

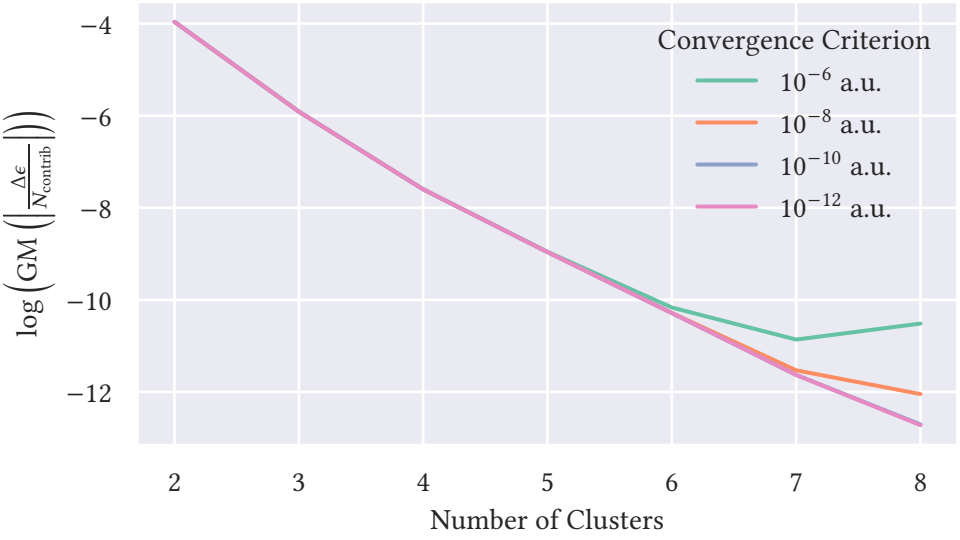

Figure 7.3: Log-transformed GM of the normalized increment magnitude $\log\left(\mathrm{GM}(|\Delta\epsilon/N_{\mathrm{contrib}}|)\right)$ plotted against number of clusters for different CASCI convergence criteria for the H_2O/cc-pVTZ example in Figure 7.2. Adapted with permission from Ref. 496. Copyright 2024 American Chemical Society.

limited by the high variance of the data in Figure 7.2. Instead, the proposed algorithm targets the sum of the contributions at future orders which is of much greater interest for screening and error estimation purposes. The GM of the normalized increment magnitude $|\Delta\epsilon/N_{\mathrm{contrib}}|$ can be subjected to a weighted linear regression in the log-transformed scale. The weights can be obtained from the reciprocal of the variance of the geometric sample mean in the logarithmic scale. The resulting predictions at different MBE orders for H_2O are presented in Figure 7.4. The predictions at early orders in the expansion will often underestimate the GM of the observed increment magnitudes as a result of the departure from the linear relationship that is caused by the finite convergence criteria and the limits of floating-point precision. When the resulting model is used for screening and error estimation purposes, prediction intervals are estimated and added to the predicted GMs in an attempt to mitigate any deviations from linearity of the underlying data.

Since the increments follow a log-normal distribution, the arithmetic mean (AM) and the variance of the normal distributions in the log-transformed scale can be used to construct the AM in the original scale. The AM in the log-transformed scale and the logarithm of the GM are equivalent. The variance can be used from previous data points as the variance first increases and then stays fairly constant after a certain sample size has been reached. The sum of the predicted AMs for all possible combinations of N_{contrib} and N_{cluster} that can be produced by an orbital cluster at order k will yield a prediction of the *potential* contribution

$$|\mathcal{E}^{(k)}| = \sum_{\Delta\epsilon} N_{\mathrm{contrib}}(\Delta\epsilon) \cdot \mathrm{AM}\left(\left|\frac{\Delta\epsilon}{N_{\mathrm{contrib}}}\right|\right)_{N_{\mathrm{cluster}}(\Delta\epsilon)} \tag{7.2}$$

of this orbital cluster at order k. This potential cluster contribution will equal the actual absolute cluster contribution

$$|E^{(k)}| = F_k \cdot |\mathcal{E}^{(k)}| \tag{7.3}$$

whenever sign cancellation occurs among the increments. In practice, this will only happen at the start of a calculation when all increments are negative ($F_k = 1$). At later orders, it becomes

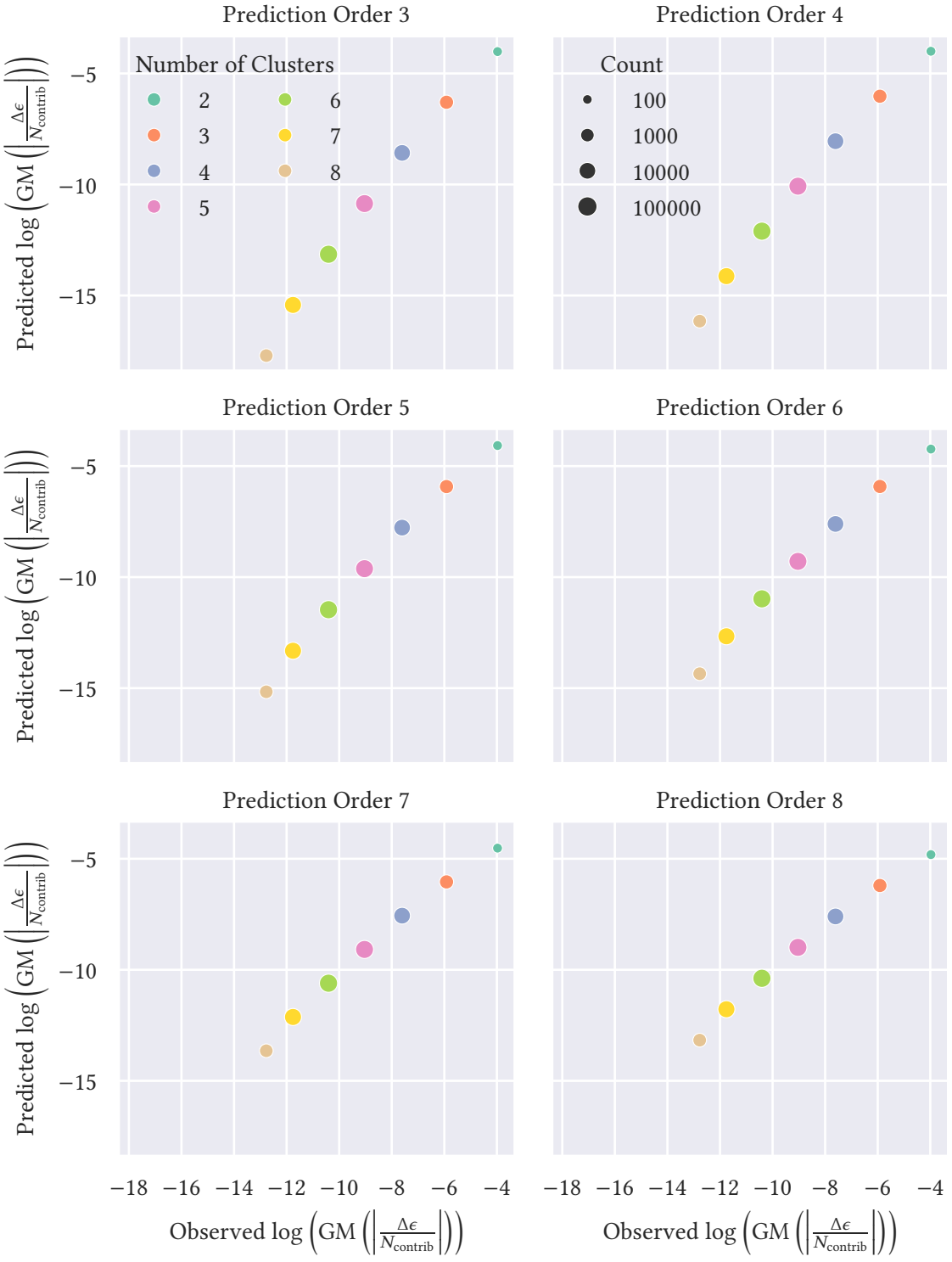

Figure 7.4: Predicted vs. observed logs of the GM of normalized increment magnitudes at different prediction orders for the H_2O/cc-pVTZ example in Figure 7.2. Adapted with permission from Ref. 496. Copyright 2024 American Chemical Society.

increasingly likely for an n-orbital contribution to also lead to an increase of the correlation energy and the distribution of the increments will slowly become symmetric and center around zero ($F_k \to 0$). The exact value of F_k at different orders of the MBE is inherently difficult to predict, so a conservative estimate is attempted by sampling the predicted distributions at later orders obtained using Equation (7.1) from the current-order increments by employing importance sampling.

The resulting screening protocol requires a single input, the maximum target error ΔE_{thres}, and then screens away orbitals by estimating their contributions at future orders and removing orbitals with the smallest contribution such that the accumulated error estimate stays within the targeted error bounds. A schematic overview is given in Figure 7.5. For each orbital cluster and future MBE order, the errors are estimated in two steps: fitting and sampling. The samples for the sampling step are

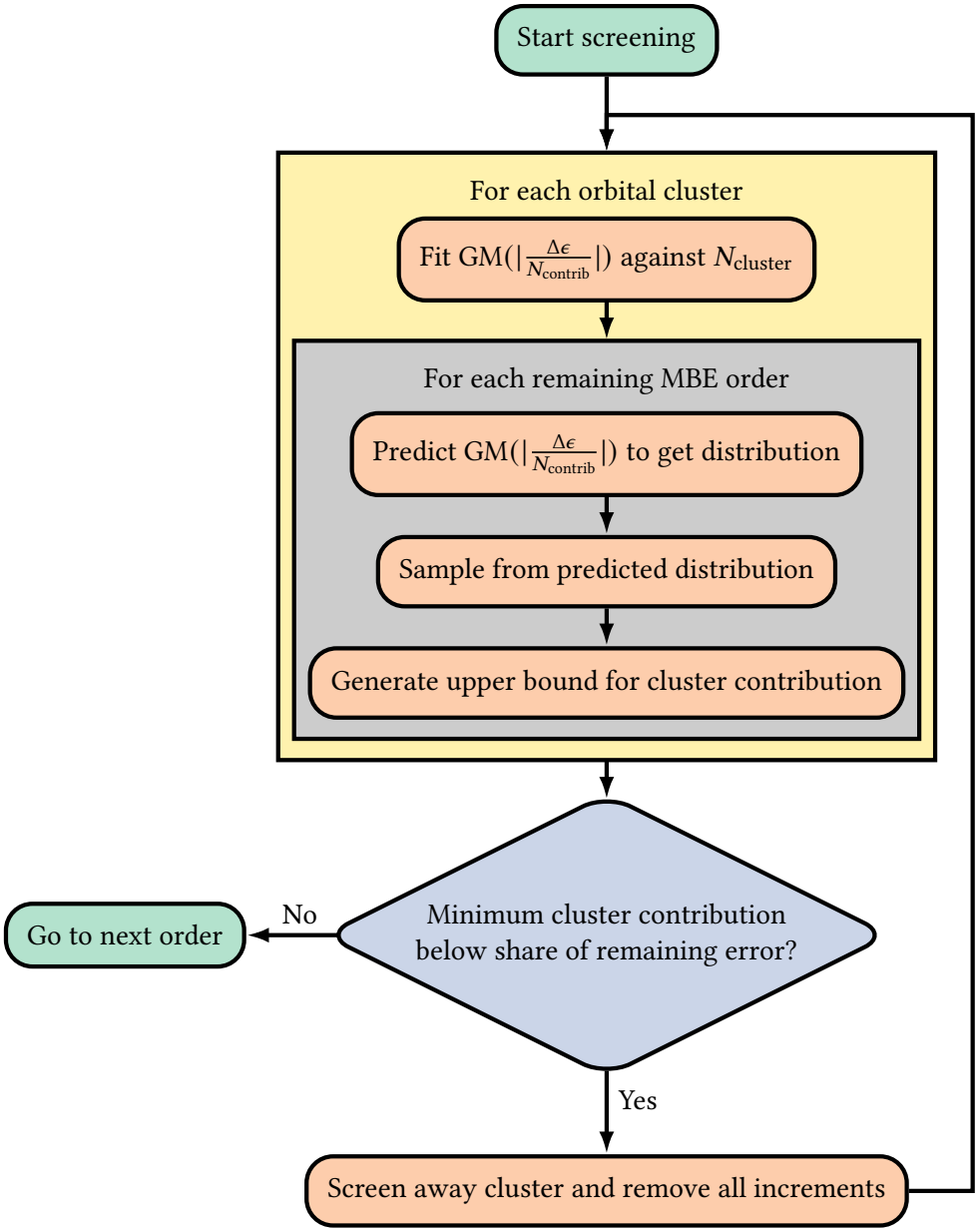

Figure 7.5: Flowchart for the screening and error estimation procedure.

randomly chosen with replacement from all increments of the last $\max_i(n(S_i))$ orders. A sample of 10000 increments is generally enough to reproduce the increment distribution at these orders. The value $\max_i(n(S_i))$ defines the maximum cardinality of the set of all expansion space clusters S_i. Drawing samples from the last $\max_i(n(S_i))$ orders ensures that increments of all clusters are included in the sample even when heterogeneous cluster types are employed. These samples can then be used to predict a probability density function by employing kernel density estimation (KDE).[510,511] The KDE implementation from SciPy[512] is used in combination with Scott's rule for bandwidth estimation.[513] After sample preparation, the iteration over the orbital clusters and remaining MBE orders in Figure 7.5 commences.

The fitting step of error estimation is only started if a minimum of three data points in Figure 7.2 is present. Additionally, all $x + 1$-orbital contributions, where x is the negative exponent of ΔE_{thres} in scientific notation, need to have been calculated. These two restrictions ensure a sufficient amount of data is present to permit confident error predictions within the supplied error bounds. If this is the case, a weighted linear least squares fit of Equation (7.1) in the logarithmic scale is carried out. The upper prediction interval for a designated confidence level γ is calculated and added to the predicted $\text{GM}(|\Delta\epsilon/N_{\text{contrib}}|)$. The employed γ is chosen based on the current progress towards convergence according to Table 7.1. By employing a dynamic confidence level, the reality that less confidence in the error estimation is required when the last few orders already contribute less than the remaining target error is encoded into the screening procedure. Incidentally, this approach also prevents the errors from being excessively overestimated for large prediction intervals and ensures appropriate termination of the calculation once convergence is reached. From the predicted $\text{GM}(|\Delta\epsilon/N_{\text{contrib}}|)$ and the variance of the last data point, normal distributions in the log-transformed scale can be constructed for the importance sampling step.

Table 7.1: Confidence levels used for error estimation.

Number of Orders where $\sum_k E^{(k)} < \Delta E_{\text{thres}}$	Confidence Level γ
$>= 0$	95 %
$>= \max_i(n(S_i))$	80 %
$>= 2 \cdot \max_i(n(S_i))$	50 %
$>= 3 \cdot \max_i(n(S_i))$	15 %

In the sampling step, the prepared current- and previous-order increments are sampled according to the predicted distributions by employing importance sampling. The probabilities are determined from the predicted probability density function and from the KDE obtained from the sample of current- and previous-order increments. The increments are sampled according to the logarithm of their magnitude while $|E^{(k)}|$ is estimated by summing these sampled increments including their signs. Sampling is done for all possible distributions (described by the different values of N_{cluster} and N_{contrib}) that contribute at the current error estimation order to Equation (7.2). Additional samples are drawn until the γth quantile of $|E^{(k)}|$ has converged which is used as a conservative upper bound for the contribution of the current cluster at this order. Estimation of $E^{(k)}$ is repeated over increasingly high orders while possible cancellation at different orders k due to differing signs are not factored into the error estimation. Once the last $\max_i(n(S_i))$ orders do not contribute to more than 1 % of the total accumulated error for this cluster, the error estimation for this cluster is terminated.

After error estimation is completed, the orbital cluster with the smallest potential contribution is considered to be screened away. If the potential contribution accounts for less than the share of

the remaining error threshold allocated to this cluster, the orbital is removed from the expansion space. The share allocated to a given cluster is defined through the ratio of the number of increments produced by this cluster and the total number of increments resulting from the next $\max_i(n(S_i))$ orders. After a cluster is screened away, the current- and previous-order increments produced by this cluster are removed from $\mathrm{AM}(|\Delta\epsilon/N_{\mathrm{contrib}}|)$ and new samples are drawn. The outlined procedure is repeated until either the smallest potential contribution exceeds the share allocated to this cluster or until the remaining expansion space is unable to produce any increments at future orders.

7.2 Results

The proposed screening and error estimation algorithm requires extensive testing and numerical verification to ensure that the errors introduced through screening are appropriately assessed. Underestimated errors could cause the results to exceed targeted error bounds while overestimated errors can result in unnecessary work due to delayed termination of the MBE. In combination with the reference space detection introduced in Chapter 5 and the orbital clustering presented in Chapter 6, the screening and error estimation algorithms are tested on the `FCI21` benchmark set,[514] a set of 21 small molecules, and compared to conventional FCI results for these systems.

7.2.1 Investigations of the FCI21 Benchmark Set

The `FCI21` benchmark set includes 21 systems in cc-pVDZ and SV basis sets.[404,515] The utilized parameters for all investigated systems are summarized in Table 7.2. Four systems are removed from

Table 7.2: Systems from the `FCI21` benchmark set and corresponding parameters.[514] Adapted with permission from Ref. 496. Copyright 2024 American Chemical Society.

Molecule	Bond Length (in Å)	Angle (in degree)	Dihedral Angle (in degree)	Ground State	Correlated Orbitals	Basis
LiH	1.6136	—	—	$^1\Sigma^+$	all-electron	cc-pVDZ
BeH	1.3570	—	—	$^2\Sigma^+$	all-electron	cc-pVDZ
BH	1.2551	—	—	$^1\Sigma^+$	all-electron	cc-pVDZ
CH	1.1424	—	—	$^2\Pi$	all-electron	cc-pVDZ
NH	1.0557	—	—	$^3\Sigma^-$	all-electron	cc-pVDZ
OH	0.9796	—	—	$^2\Pi$	all-electron	cc-pVDZ
HF	0.9200	—	—	$^1\Sigma^+$	all-electron	cc-pVDZ
Li_2	2.7139	—	—	$^1\Sigma_g^+$	frozen-core	cc-pVDZ
Be_2	4.4269	—	—	$^1\Sigma_g^+$	frozen-core	cc-pVDZ
B_2	1.6240	—	—	$^3\Sigma_g^-$	frozen-core	cc-pVDZ
C_2	1.2728	—	—	$^1\Sigma_g^+$	frozen-core	cc-pVDZ
N_2	1.1368	—	—	$^1\Sigma_g^+$	frozen-core	SV
O_2	1.2786	—	—	$^3\Sigma_g^-$	frozen-core	SV
F_2	1.4186	—	—	$^1\Sigma_g^+$	frozen-core	SV
CH_4	1.1015	109.5	120.0, 240.0	$^1A_1$	frozen-core	SV
NH_3	1.0277	103.5	107.7	$^1A_1$	frozen-core	cc-pVDZ
H_2O	0.9668	101.9	—	$^1A_1$	frozen-core	cc-pVDZ

the set to adapt it to the purposes of this investigation: H_2 is removed because it converges very quickly, Li_2 and Be_2 (all-electron) are already represented by the frozen-core calculations on these systems which correspond with the other homonuclear diatomic molecules in the set, and HF (frozen-core) is already represented by the all-electron calculation in accordance with the other diatomic hydrides in the set. In contrast to Ref. 514, the triplet states and the corresponding equilibrium bond lengths are used for NH and B_2 as these describe the ground state. RHF and ROHF states exhibiting the multiplicity and symmetry in Table 7.2 were used for all systems except for OH, in which case the broken-symmetry B_2 solution in the C_{2v} subgroup was employed. The converged MBE energies of these systems are compared to reference FCI calculations performed with PySCF.

MBE-FCI calculations of these systems were compared in the canonical MO basis, the CCSD NO basis, the PM LMO basis, and the FB LMO basis. Optimal reference spaces in these different MO bases were identified through a single-orbital MBE-FCI calculation truncated at MBE order 5 according to the procedure outlined in Chapter 5. The reference space sizes chosen for these systems in all four MO bases using a starting quantum fidelity threshold of 0.95 from a single-orbital MBE-FCI calculation truncated at order 5 are provided in Figure 7.6. While the minimum reference space for closed-shell systems is empty, the minimum reference space for open-shell systems involves all singly occupied orbitals to guarantee the correct spin state can be targeted for all increment active spaces. For the diatomic hydrides in Figure 7.6, the majority does not require the addition of orbitals beyond the minimum reference space. An atypical exception is the OH system in the FB LMO basis which requires a total of eight MOs in the reference space to ensure MBE-FCI convergence. The diatomics in the `FCI21` set will generally require some orbitals to be added to the reference space since the ground

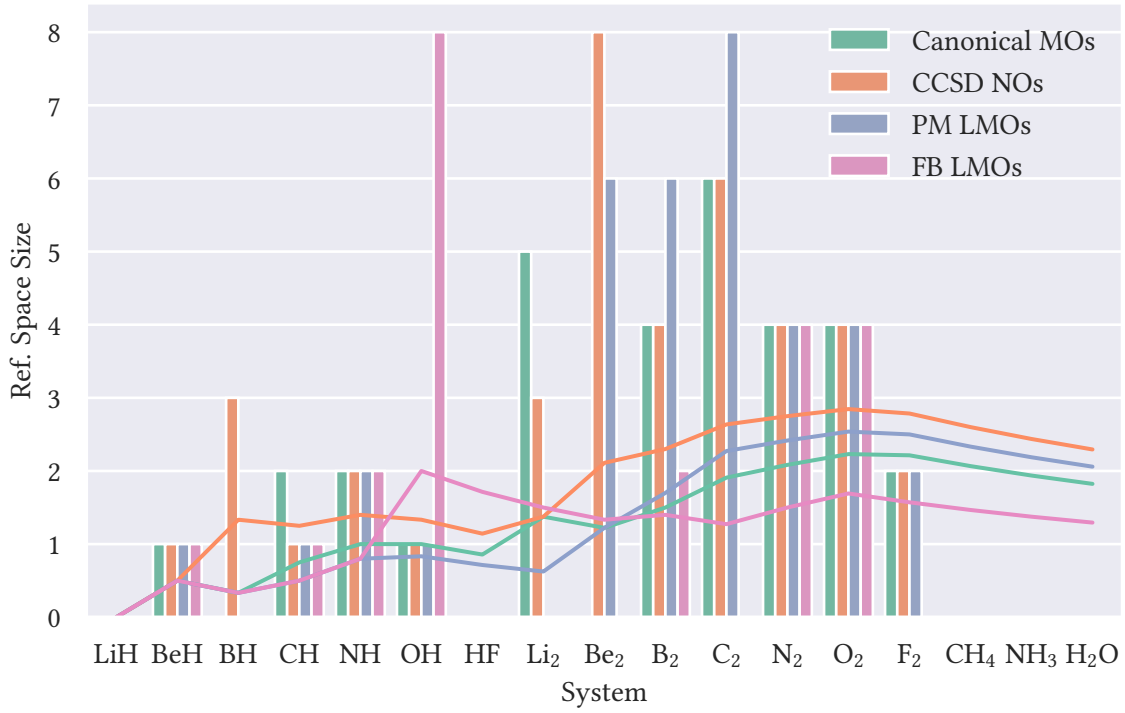

Figure 7.6: Sizes of reference active spaces expressed in different orbital bases across the `FCI21` set. The bars indicate sizes of individual reference spaces for the various systems, while the horizontal lines depict the corresponding cumulative average size of the reference spaces. Adapted with permission from Ref. 496. Copyright 2024 American Chemical Society.

states of many of these systems (e.g., Be_2, B_2, and C_2) exhibit some degree of multireference character by requiring contributions from more than a single determinant. Systems such as CH_4, NH_3, and H_2O are dominated by dynamic correlation and can therefore be described using empty reference spaces. The remaining expansion spaces are split into clusters of at most two MOs following the clustering algorithm described in Chapter 6.

The errors of these MBE-FCI calculations for the `FCI21` set and different targeted error bounds are displayed in Figure 7.7 for all four MO bases. As is to be expected, observed errors decrease as the screening threshold is tightened. The outlined screening and error estimation algorithm is consistently able to truncate the expansion such that results stay within the targeted error bounds. Observed errors will only rarely exceed targeted error bounds which is usually caused by the low

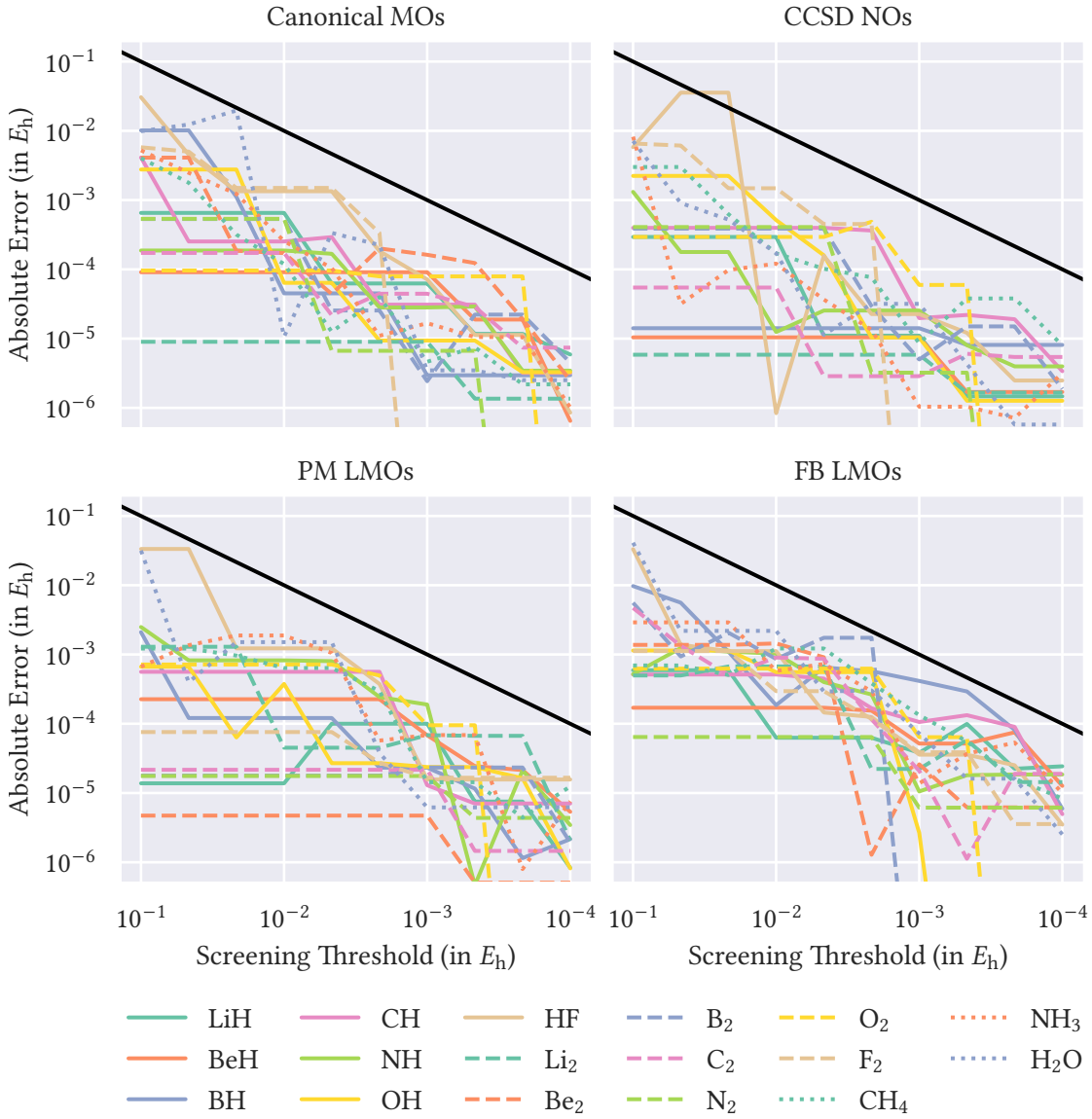

Figure 7.7: Absolute errors across the `FCI21` set for different screening thresholds and MO bases. Black lines indicate perfect correspondence between actual and predefined errors. Adapted with permission from Ref. 496. Copyright 2024 American Chemical Society.

amount of statistical information present in the expansion for these small systems and basis sets and the resulting limited sample sizes.

Utilizing different MO bases will affect the time-to-solution of MBEs converged up to a given error threshold. While localized and therefore mutually exclusive MOs will often accelerate convergence, the individual increment calculations will become more expensive whenever a larger reference space is required to obtain a converging expansion when LMO bases are employed. It is reasonable to assume that compact, delocalized orbital bases, such as CCSD NOs or CASSCF MOs describing a small active space, might produce smaller reference spaces by folding a large amount of electron correlation into very few orbitals, either the partially occupied orbitals or the orbitals of the active space. Therefore, a combination of a delocalized reference space and a localized expansion space could synergize well and minimize the resulting time-to-solution. Nevertheless, the results in Figure 7.6 do not appear to support this assumption as the LMO bases will not necessarily result in larger reference spaces. Additionally, a delocalized reference space could limit the localizability of the remaining expansion space by removing degrees of freedom. In addition to the four MO bases investigated in Figures 7.6 and 7.7, timings for MBE-FCI calculations were also compared for the following combinations of delocalized (canonical MOs, CCSD NOs, and CASSCF MOs) and localized orbital bases (PM LMOs) for the reference and expansion spaces: CASSCF MOs optimizing a reference space determined from canonical MOs, CASSCF MOs optimizing a reference space determined from CCSD NOs, a canonical MO reference space combined with a PM LMO expansion space, a CCSD NO reference space combined with a PM LMO expansion space, a CASSCF optimized reference space starting from canonical MOs combined with a PM LMO expansion space, and a CASSCF optimized reference space starting from CCSD NOs combined with a PM LMO expansion space. The CCSD solutions for the calculation of NOs and the CASSCF solutions targeted the correct state except for CH and OH which targeted the broken-symmetry B_2 solution in the C_{2v} subgroup. The CASCI solver in PySCF is limited to Abelian and linear symmetries and hence the A' state is targeted during the CASSCF optimization for CH_4 and NH_3. The effects of employing a variety of orbital bases and the resulting reference spaces on the wall times[d] of MBE-FCI calculations converged to an error bound of 1 mE_h are investigated in Figure 7.8.

The small systems included in the `FCI21` benchmark set will generally not substantially benefit from LMO bases. Nevertheless, significant improvements are evident for some larger systems in the set, e.g., N_2, F_2, CH_4, and NH_3. For F_2, convergence is accelerated by almost three orders of magnitude when an LMO basis is employed. Whenever the results from LMOs are compared, the PM LMO basis appears to generally outperform the FB LMO basis. Therefore, PM LMOs were used for all combined delocalized and localized MO bases in Figure 7.8. The superiority of the PM LMO basis could be rooted in the ability of the PM method to maintain σ-π separation which might be relevant for many of the linear systems in this set. This effect is particularly detrimental for B_2, C_2, and OH. For the former two systems, the smaller reference spaces result in slower convergence which is remedied in all other investigated orbital bases. Conversely, the very large reference space chosen for the OH system in the FB LMO basis does not positively affect time-to-solution. While it appears necessary to choose this enormous reference space in this MO basis, the cost of performing the individual increment calculations grows substantially, making the calculation unnecessarily expensive.

For a few systems (e.g., LiH, BeH, NH, O_2, H_2O), the necessary computational effort to converge the MBE below the targeted error bound appears to be largely unaffected by the chosen MO basis. These calculations also exhibit equally sized reference spaces in all orbital bases. Treatment of the BH system only requires a reference space in the CCSD NO basis. The resulting expansion is

[d]Computer architecture: Four Intel Xeon CPUs E5-4620 on a single node (64 threads, 32 cores @ 2.4 GHz, 7.80 GB/thread)

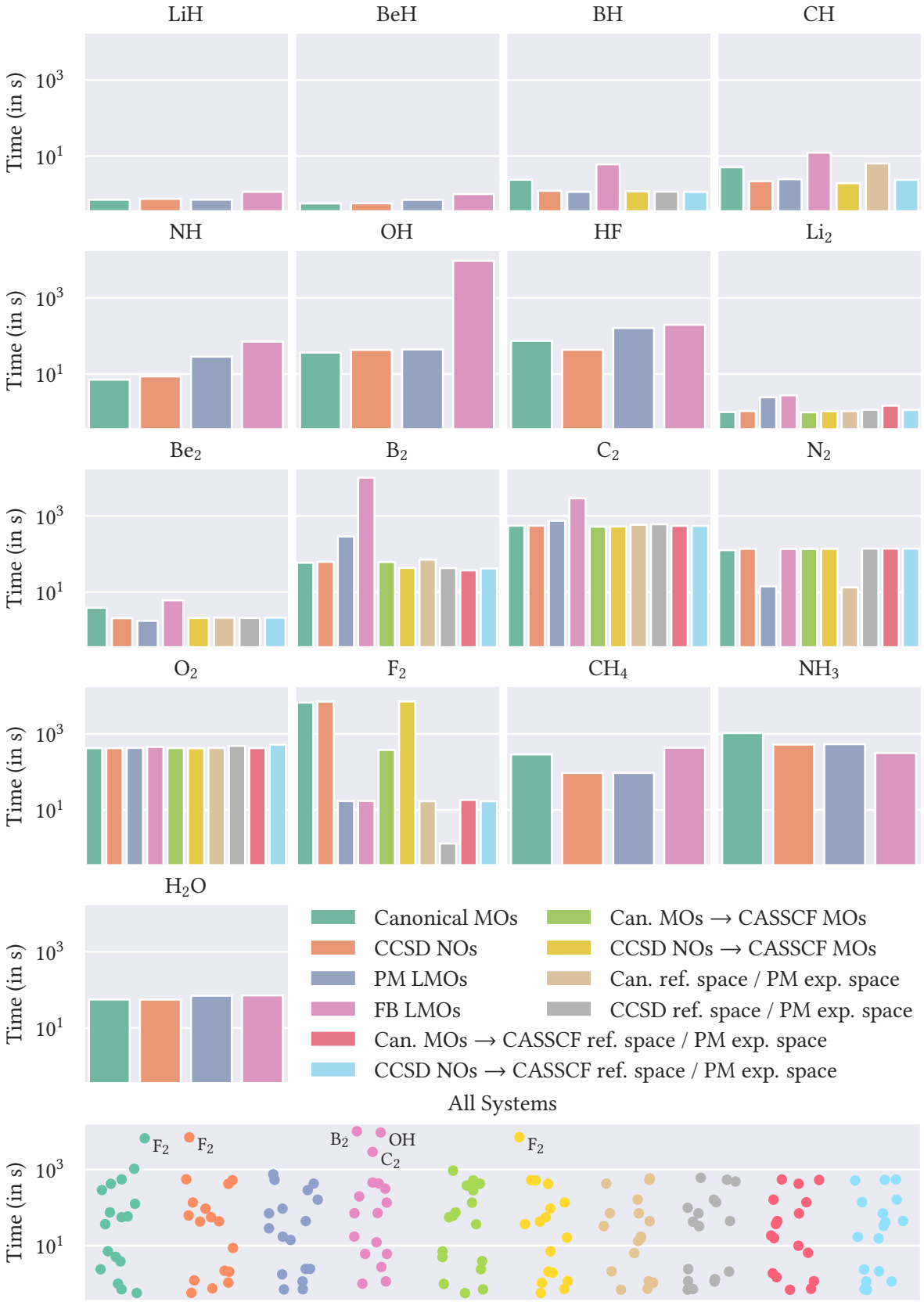

Figure 7.8: MBE-FCI timings for the `FCI21` set for different choices of MO basis. Adapted with permission from Ref. 496. Copyright 2024 American Chemical Society.

able to outperform the canonical orbital basis while being on par with the PM LMO basis which requires no reference space. For CH, calculations employing the symmetry-broken B_2 solution in the C_{2v} subgroup appear to accelerate convergence in comparison to the canonical MO basis that describes the correct symmetry state. The PM LMOs rival the performance of the orbital bases involving the CCSD NO reference space for this system. Calculations involving Li_2, Be_2, B_2, and C_2 do not appear to benefit from optimized reference spaces or localized expansion spaces. Nevertheless, the orbital bases involving delocalized reference spaces and localized expansion spaces appear to generally outperform the purely localized MO bases while producing very similar timings compared to the canonical and CCSD NOs. Contrastingly, the calculations on N_2 benefit from a purely localized MO basis instead.

For all systems considered in Figure 7.8, both the explicit optimization of the reference space orbitals through CASSCF and the combination of delocalized reference and localized expansion spaces appears to offer little benefit over the PM LMO basis. The CASSCF optimization could instead be repeated every time orbitals are added to the reference space, as this can potentially discourage more orbitals from being added to the reference space by folding the remaining static correlation into the present reference space. Additionally, these experiments could be repeated on a set of more statically correlated systems to determine whether additional benefits from these mixed orbital bases exist for the purpose of accelerating MBE-FCI calculations.

The systems in the `FCI21` benchmark set are generally quite small which enables comparisons with conventional FCI. It might be premature to draw definitive conclusions on the convergence behavior of different orbital bases on such compact systems. Nevertheless, the observed superiority of the PM LMOs will generalize when moving towards larger systems as increased distance between the LMOs will allow an increased number of orbital combinations to produce vanishing increments due to negligible overlap between the involved orbitals. For this reason, the PM LMO basis is employed to apply the outlined screening and error estimation algorithm to a group of larger systems.

7.2.2 Screening and Error Estimation for Larger Systems

The applicability of the screening and error estimation algorithm to MBE calculations involving orbital clusters is demonstrated on larger systems: ethene (C_2H_4), methanol (CH_3OH), formaldehyde (H_2CO), hydrogen peroxide (H_2O_2), hydrogen cyanide (HCN), and hydrazine (N_2H_4).[e] MBE-CCSD calculations are performed in the cc-pVTZ basis set[404] and compared to conventional CCSD calculations since FCI is intractable for systems of this size. Empty reference spaces and eight-orbital clusters are used to treat these predominately dynamically correlated systems. Errors of these calculations for different screening thresholds are displayed in Figure 7.9. The energy errors of these larger systems substantiate the findings on the smaller systems in Section 7.2.1. The outlined algorithm consistently produces errors close to or below the predefined error bound. The projected errors can in rare cases fall below the actual errors if the increments depart from the observed empirical relationship in Equation (7.1). For larger error bounds, errors will often fall significantly below these bounds since the algorithm will only start to screen away orbitals once enough statistical information is available. Additionally, the sign cancellation factor F_k will still be close to one and the upper error bound can be accurately estimated from the predicted mean absolute increments alone. Smaller error bounds will require the algorithm to venture further into the MBE where the actual errors caused by screening will be closer to the predicted increment magnitudes. Furthermore, the increment magnitudes can sometimes not be perfectly described through a log-normal distribution and heavy

[e] CCSD/cc-pVTZ geometries

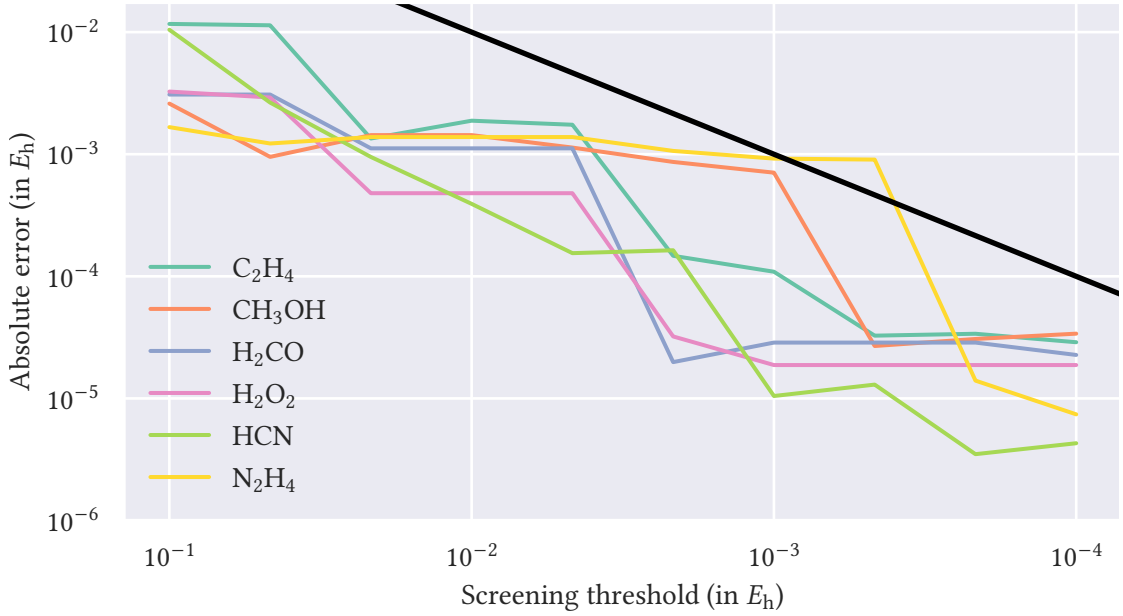

Figure 7.9: Absolute errors of MBE-CCSD/cc-pVTZ calculations on C_2H_4, CH_3OH, H_2CO, H_2O_2, HCN, and N_2H_4 for different screening thresholds using bases of PM LMOs. Adapted with permission from Ref. 496. Copyright 2024 American Chemical Society.

tails can be observed which significantly affect the arithmetic mean and lead to the underestimation of potential errors.

For narrow error bounds, the majority of the increments far into the expansion are expected to fall close to or below the convergence criterion of the individual increment calculations. The noise introduced through these increments will result in an overestimation of the mean absolute increment and can delay or in the worst case prevent MBE termination. One possible remedy could be the treatment of these increments through a censored log-normal distribution for which the real distribution is recovered through maximum likelihood estimation.[516] This would only be necessary for practical thermochemical applications if an accuracy below 0.1 mE_h is desired.

8 Exploiting Point-Group Symmetry in MBE-FCI

The exploitation of symmetry has extended the applicability of many quantum chemical methods beyond their usual domain. While the majority of molecules that can be constructed and synthesized in the realm of chemistry do not exhibit molecular symmetry, those accessible by highly accurate approximate FCI methods often are symmetric due to the limited number of atoms that they are constructed from. Therefore, the efficient exploitation of point-group symmetry has been a cornerstone of approximate FCI method development[41,119,294,318,517] and possible directions in the context of the MBE-FCI framework are investigated in this chapter. A similar approach which involves the construction of symmetry-equivalent occupied orbital domains of FB LMOs has been successfully applied in the context of the incremental method.[36] The work in this chapter was published in Refs. 518 and 519.

8.1 Theory

In symmetry-adapted orbital bases, taking advantage of molecular symmetry involves exploiting the inherent symmetry properties of any tensors by lowering memory footprint and reducing the number of operations of any tensor contractions as described in Section 2.7. This method can easily be applied to MBE-FCI theory by utilizing a CASCI solver that is able to exploit symmetry. In MBE-FCI, both the interfaces to PySCF and MBECC backends can be used with symmetry by passing irreducible representation assignment information for the orbitals. Unfortunately, the speed-ups afforded by this implementation in the context of MBE calculations often leave something to be desired as the overhead from the symmetry treatment in very small CASCI or CASCC calculations and the limited number of irreducible representations present in the active spaces often thwart any possible gains. On top of that, as was demonstrated in Refs. 41 and 42 and in Chapter 7, MBE-FCI calculations often benefit from an LMO basis. For LMOs, individual orbitals are rarely invariant with respect to the transformation induced by a symmetry operation as is the case for symmetry-adapted orbital bases. Instead, the LMOs produced by PM or FB localization procedures are generally symmetry-equivalent to the majority of symmetry operations such that the orbitals transform among each other whenever a symmetry operation is applied as exemplified in Figure 8.1b.[36,520] LMOs will only be symmetry-invariant to a given symmetry operation (Figure 8.1a) when the orbital is localized at the respective symmetry element whether it be an inversion point, rotation axis, rotation-reflection axis, or mirror plane. While this type of symmetry will not produce vanishing integrals, it will cause integrals of symmetry-equivalent orbitals to be equal. It should be noted that the same is true for symmetry-adapted orbital integrals whenever orbitals transform as multidimensional irreducible representations when non-Abelian point groups are considered. Unfortunately, symmetry properties of the orbitals produced from localization procedures have to be classified after the orbitals were optimized because the symmetry properties of these orbitals are not explicitly constrained during localization but are rather a consequence of the symmetric orbital space and the symmetry properties

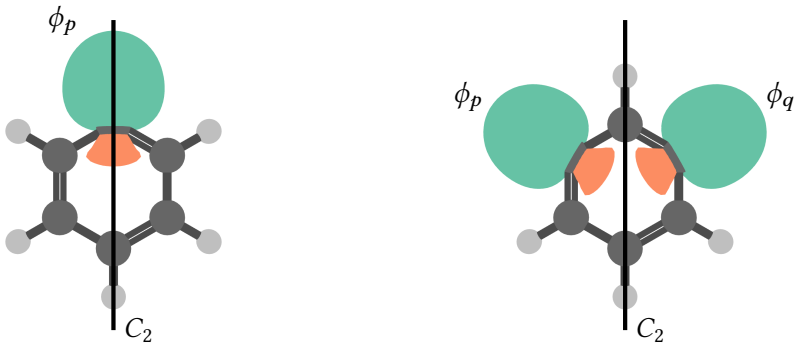

(a) Symmetry-invariant orbital (b) Symmetry-equivalent orbitals

Figure 8.1: Localized orbitals of benzene that are symmetric with respect to a two-fold rotation axis. Adapted with permission from Ref. 518. Copyright 2023 American Chemical Society.

of the localization cost function. For FB LMOs, which maximize the distance between orbital centroids, this identification can be achieved by only considering the symmetry properties of these centroids.[36] As an additional complication, localization cost functions often produce numerous densely clustered minima[440,521] such that the optimized LMOs will not necessarily respect the molecular symmetry of the system. Especially for virtual orbitals in large basis sets which are notoriously difficult to localize, the LMOs will often only exhibit approximate symmetry properties. If symmetry is to be exploited by assuming integrals and coefficients of these symmetry-equivalent orbitals are identical, the symmetry properties of these orbitals need to be enforced in a numerically exact manner without sacrificing their spatial locality.

8.1.1 Symmetrization of Localized Orbitals

The LMOs can be symmetrized by minimizing an objective cost function $\mathcal{J}$. This cost function is constructed by identifying and enforcing the approximate symmetry properties inherently present in the set of LMOs. For a given symmetry operation $\hat{G}$, the matrix element $\langle\phi_p|\hat{G}|\phi_q\rangle$ describes the overlap between orbital ϕ_p and the transformed orbital $\hat{G}\phi_q$. Certain elements of the matrix representation G_{pq} will vanish whenever orbitals are exactly symmetry-equivalent with respect to $\hat{G}$ because the transformation will produce a different set of orbitals S_2 that are orthonormal to the original set S_1. Only those matrix elements G_{pq} describing symmetry-equivalent orbitals will contribute. All other elements must be included in the objective cost function such that the approximate symmetry properties can be enforced through minimization. Unitary orbital transformations that will lead to this symmetrization can be expressed by the exponential of an anti-Hermitian operator as in Equation (2.40). When expressed in the AO basis, the objective function

$$\mathcal{J} = \sum_{G}^{h} \sum_{(S_1,S_2)\in\mathcal{S}_G} \sum_{p\in S_1} \sum_{\bar{q}\notin S_2} \left(\sum_{t,u} \sum_{\mu,\nu} \exp(\boldsymbol{\kappa}^\dagger)_{tp} \exp(\boldsymbol{\kappa})_{u\bar{q}} c^*_{\mu p} c_{\nu\bar{q}} \langle\chi_\mu|\hat{G}|\chi_\nu\rangle \right)^2 \tag{8.1}$$

is described by adding the symmetry constraints for all h symmetry operations of the molecular point group. The set $\mathcal{S}_G$ describes all pairs of symmetry-equivalent orbital sets S_1 and S_2. The cost function is designed to be quadratic to guarantee that there is no cancellation between different symmetry-equivalent orbital pairs or symmetry operations and to ensure that all of these symmetry constraints can be enforced simultaneously. Alternatively, an absolute cost function could be used,

but this can lead to issues during optimization due to inflated step sizes near the minimum. Equation (8.1) is minimized by employing unitary optimization which guarantees orthonormality.[522] The symmetrization of the LMOs is of special importance in MBE calculations because the increment properties at lower orders are contributing to the final property with a large prefactor due to the recursive nature of the MBE.

The symmetrization procedure modifies the orbitals *a posteriori*. For this reason, it is of utter importance that the degree of spatial localization is not affected by this procedure. This restriction can be justified by the assumption that only small orbital rotations will be necessary to symmetrize the orbitals since the LMOs already exhibit approximate symmetry properties. The spatial locality of an MO can be quantified through the second- and fourth-moment orbital spreads in Equation (2.80).[413–415]

8.1.2 Petite List Method

Symmetry-equivalent orbitals can be exploited in MBE-FCI by utilizing the property that active spaces from orbitals that can be transformed into another tuple of different orbitals using a symmetry operation will produce the same correlation energy. Illustrative orbital tuples which will produce equivalent correlation energies are presented in Figure 8.2. For symmetrized LMOs, the MBE will produce many redundant increment calculations that can be avoided to increase computational efficiency. A method that can be used for this purpose is the *petite* list method by Dupuis and King.[128] This method loops over all orbital combinations (the *grande* list) and applies all symmetry operations of the molecular point group to establish whether the current orbital tuple is lexicographically larger than any other symmetry-equivalent orbital tuple. Only the lexicographically largest orbital tuple for a set of symmetry-equivalent orbital tuples will be explicitly calculated. These orbital combinations form the *petite* list. Even though this technique was originally devised for AO integrals, it can easily be generalized to arbitrary orbital tensors such as the increments of the MBE. The only requirement is that the objects of the expansion must have numerically exact symmetry properties which is enforced through symmetrization. Earlier developments in the context of the incremental method did not enforce these symmetry properties and were therefore restricted to occupied orbitals in the expansion space as these are often approximately symmetry-equivalent.[36] Nevertheless, even for occupied orbitals these deviations from exact symmetry properties will cause issues when moving to higher orders in the MBE.

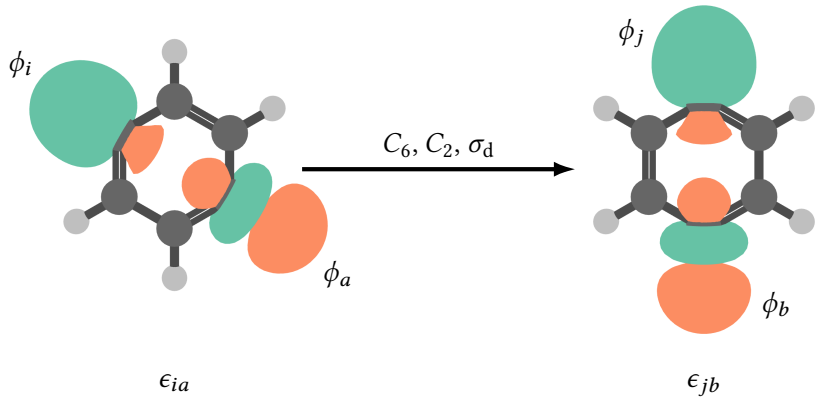

Figure 8.2: Localized orbitals of benzene for two symmetry-equivalent active spaces that can be transformed into each other and have equal correlation energy contributions.

8.2 Implementation

MBE-FCI calculations exploiting LMO point-group symmetry need to be prepared by detecting the approximate symmetries present in the orbitals after the localization procedure is complete. The LMOs then need to be optimized such that these symmetries hold up to the numerical precision of the used floating-point representation. Both of these steps are implemented in the SymLo program[523] from which the `symmetrize_mos` function can be called after localization is complete and before the PyMBE kernel is invoked.

8.2.1 The SymLo Program

The `symmetrize_mos` function starts by generating the necessary transformation matrices in the orthogonalized AO basis. This step requires the system to be shifted to the symmetry center and rotated to a predetermined set of symmetry axes such that symmetry operations can be applied along these. The necessary transformations are generated for arbitrary point groups on the basis of functionality from the PySCF *symm* module. After the AOs have been rotated to the symmetry axes, the symmetry operation of interest can be applied to individual AOs. The SymLo program includes functionality to generate the necessary transformation matrices for arbitrary point groups. While identity and inversion matrices can be trivially generated for spherical harmonics, the rotation matrices are generated by utilizing Wigner D-matrices[524] which can be constructed from Euler angles in PySCF. Reflection matrices can be constructed by combining two-fold rotation and inversion while rotation-reflection matrices are constructed from rotation and reflection matrices. After the AOs have been transformed, AOs at atoms that permute under a given symmetry operation are swapped. The resulting AO transformation matrices are then transformed to the orthogonalized AO basis and can then be used to transform any MO coefficients under the action of a symmetry operation. The procedure for the subsequent symmetry detection and symmetrization is outlined in Figure 8.3. To start with, blocks of $\mathbf{G}$ are identified which are symmetry-invariant with respect to all symmetry operations. This is done by constructing the sum of all absolute contributions for all symmetry operations, $\mathbf{G}^{\Sigma} = \sum_G |\mathbf{G}|$. All elements below a certain threshold

$$\lambda_p = \gamma \max_q G^{\Sigma}_{pq} \tag{8.2}$$

can be set to zero in order to deduce any block structure from this matrix. These blocks can be identified using the reverse Cuthill-McKee algorithm[525,526] which orders the orbitals such that the bandwidth of the resulting matrix is minimized. The SciPy implementation of the reverse Cuthill-McKee algorithm is used in SymLo.[512] The orbitals can be optimized with respect to these symmetry-invariant blocks by minimizing Equation (8.1) for all elements that were previously set to zero.

Since the desired root of the objective cost function has a multiplicity of two, it cannot be determined solely on the basis of gradient information due to instabilities. Instead, a Newton algorithm can be used to optimize the orbitals with respect to Equation (8.1). In SymLo, the co-iterative augmented Hessian method[527] and its implementation in PySCF is used for this purpose. The orbital gradient $\frac{d\mathcal{J}}{d\kappa_{rs}}$, Hessian diagonal $\frac{d^2\mathcal{J}}{d{\kappa_{rs}}^2}$, and Hessian matrix contracted with a trial function $\sum_t \frac{d^2\mathcal{J}}{d{\kappa_{rt}}^2} x_{ts}$ can be constructed by adding expressions to specific elements depending on whether the indices r and s are included in the orbital sets S_1 and S_2. The Hessian diagonal is Hermitian while the orbital gradient and

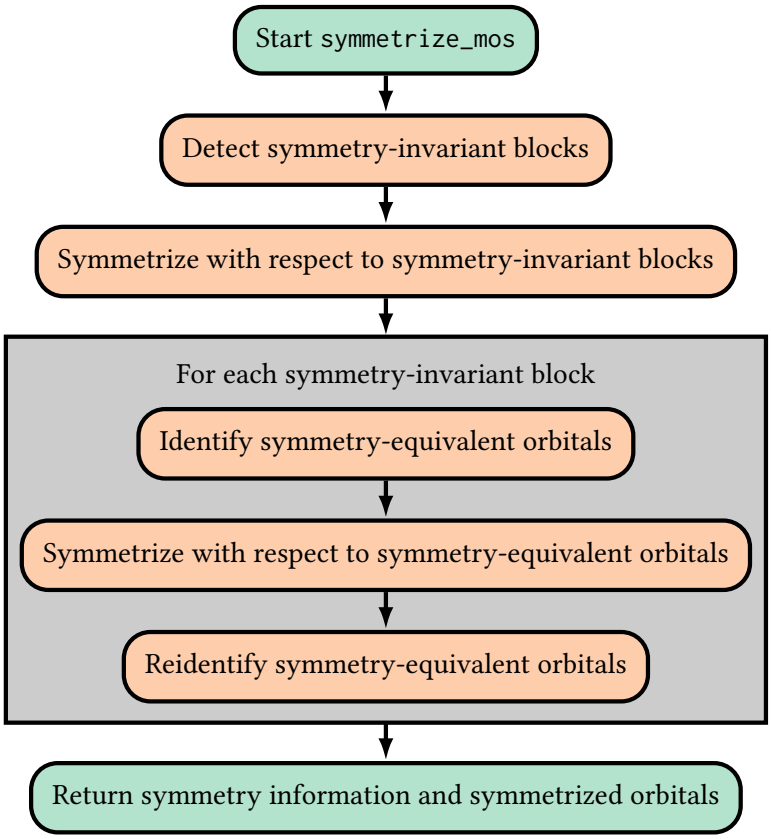

Figure 8.3: Flowchart of LMO symmetry detection and symmetrization.

Hessian matrix contracted with a trial function are anti-Hermitian due to the unitarity constraint. The expression

$$-2\sum_{G}^{h}\sum_{(S_1,S_2)\in\mathcal{S}_G}\sum_{\bar{q}\notin S_2}\sum_{\mu,\nu,\sigma,\rho} c'^{*}_{\mu r}c^{*}_{\sigma s}c'_{\nu\bar{q}}c'_{\rho\bar{q}}G_{\mu\nu}G_{\sigma\rho} \tag{8.3}$$

is added to all elements of the orbital gradient where $r \in S_1$. The starting MO coefficients are described by $\mathbf{c}$ and the current transformed MO coefficients

$$\mathbf{c}' = \mathbf{c}\exp(\boldsymbol{\kappa})^T \tag{8.4}$$

are constructed by a unitary transformation of these. Whenever $s \in S_1$, the negative Hermitian transpose of this expression is added to the orbital gradient. If $r \notin S_2$, the expression

$$-2\sum_{G}^{h}\sum_{(S_1,S_2)\in\mathcal{S}_G}\sum_{p\in S_1}\sum_{\mu,\nu,\sigma,\rho} c'_{\nu r}c_{\rho s}c'^{*}_{\mu p}c'^{*}_{\sigma p}G_{\mu\nu}G_{\sigma\rho} \tag{8.5}$$

is added to the orbital gradient while its negative Hermitian transpose is added whenever $s \notin S_2$.

For the Hessian diagonal, the expression

$$2\sum_{G}^{h}\sum_{(S_1,S_2)\in\mathcal{S}_G}\sum_{\bar{p}\notin S_2}\sum_{\mu,\nu,\sigma,\rho} c^{*}_{\mu s}c^{*}_{\sigma s}c'_{\nu\bar{p}}c'_{\rho\bar{p}}G_{\mu\nu}G_{\sigma\rho} \tag{8.6}$$

is added to every element where $r \in S_1$ while its Hermitian transpose is added for $s \in S_1$. If $r \notin S_2$, the expression

$$2 \sum_{G}^{h} \sum_{(S_1,S_2)\in\mathcal{S}_G} \sum_{p\in S_1} \sum_{\mu,\nu,\sigma,\rho} c_{\nu s} c_{\rho s} c'^{*}_{\mu p} c'^{*}_{\sigma p} G_{\mu\nu} G_{\sigma\rho} \tag{8.7}$$

is added to the Hessian diagonal and its Hermitian transpose is added whenever $s \notin S_2$. Additionally, the expression

$$-2 \sum_{G}^{h} \sum_{(S_1,S_2)\in\mathcal{S}_G} \sum_{\mu,\nu,\sigma,\rho} \left(c'^{*}_{\mu r} c_{\nu r} c^{*}_{\sigma s} c'_{\rho s} + 2 c'^{*}_{\mu r} c'_{\nu s} c^{*}_{\sigma s} c_{\rho r} + c^{*}_{\mu s} c'_{\nu s} c'^{*}_{\sigma r} c_{\rho r} \right) G_{\mu\nu} G_{\sigma\rho} \tag{8.8}$$

is added to every element of $\frac{d^2\mathcal{J}}{d\kappa_{rs}{}^2}$ for which $r \in S_1$ and $s \notin S_2$. Its Hermitian transpose is added when $r \notin S_2$ and $s \in S_1$.

The Hessian matrix multiplied by a trial function can be constructed by adding the expression

$$4 \sum_{G}^{h} \sum_{\mu,\nu,\sigma,\rho} \sum_{u} \left(\sum_{t\in S_1} \sum_{(S_1,S_2)\in\mathcal{S}_G} \sum_{\bar{p}\notin S_2} \delta_{rt} c^{*}_{\mu u} c'_{\nu\bar{p}} c^{*}_{\sigma s} c'_{\rho\bar{p}} + \sum_{t\notin S_2} c^{*}_{\sigma s} c'^{*}_{\mu r} \left(c'_{\rho t} c_{\nu u} + c_{\rho u} c'_{\nu t} \right) \right) G_{\mu\nu} G_{\sigma\rho} x_{tu} \tag{8.9}$$

to every element where $r \in S_1$ and its negative Hermitian transpose to every element where $s \in S_1$. The expression

$$4 \sum_{G}^{h} \sum_{\mu,\nu,\sigma,\rho} \sum_{u} \left(\sum_{t\in S_1} c'_{\nu r} c_{\rho s} \left(c^{*}_{\mu u} c'^{*}_{\sigma t} + c'^{*}_{\mu t} c^{*}_{\sigma u} \right) + \sum_{t\notin S_2} \sum_{(S_1,S_2)\in\mathcal{S}_G} \sum_{p\in S_1} \delta_{rt} c'^{*}_{\mu p} c_{\nu u} c'^{*}_{\sigma p} c_{\rho s} \right) G_{\mu\nu} G_{\sigma\rho} x_{tu} \tag{8.10}$$

is added to every element where $r \notin S_2$. Its negative Hermitian transpose is added to every element where $s \notin S_2$. The expressions for the gradient, Hessian diagonal, and Hessian matrix multiplied by a trial function are scaled by a factor of $\sqrt{10^{14}}$ which ensures that the orbitals can be symmetrized up to the numerical limit of double-precision floating point representation ($\approx 10^{-14}$). The matrix $\mathbf{G}^{\Sigma}$ for the PM occupied orbitals of benzene is showcased in Figure 8.4 before and after sorting and after symmetrization with respect to the symmetry-invariant orbital blocks. Applying the reverse Cuthill-McKee algorithm correctly orders the orbitals into approximately symmetry-invariant blocks. The symmetrization procedure further ensures that the elements outside these blocks will numerically vanish such that the application of any symmetry operation will only produce contributions within the same block. The symmetrization is assumed to be converged, when the maximum absolute element of $\mathbf{G}^{\Sigma}$ falls below a convergence criterion $u_{\text{block}} = 10^{-13}$.

After the orbitals are symmetrized with respect to the symmetry-invariant blocks, the approximately symmetry-equivalent orbitals within these blocks can be detected by applying symmetry operations to the MOs and identifying which elements contribute above a second threshold λ_p in $\mathbf{G}$. This is done for every individual orbital and whenever there are intersections with the orbitals that other orbitals transform into, these can be consolidated. Using this procedure both single orbitals and orbital sets that are symmetry-invariant or symmetry-equivalent can be identified. The orbitals are then symmetrized by minimizing Equation (8.1) according to the outlined procedure until the maximum absolute element of $\mathbf{G}$ falls below a convergence criterion $u_{\text{orb}} = 10^{-12}$. Due to the finite threshold λ_p, there can be cases where not all symmetry relationships between the orbitals are correctly identified before symmetrization. In this case, the symmetrization procedure will generally passively enforce these relationships as a consequence of the symmetry relations with other symmetry operations or sets of symmetry-equivalent orbitals. For this reason, the identification of symmetry-equivalent orbitals is repeated with a threshold λ_p that is twice the symmetrization convergence criterion u_{orb} to ensure all symmetry relationships are correctly assigned and can be exploited.

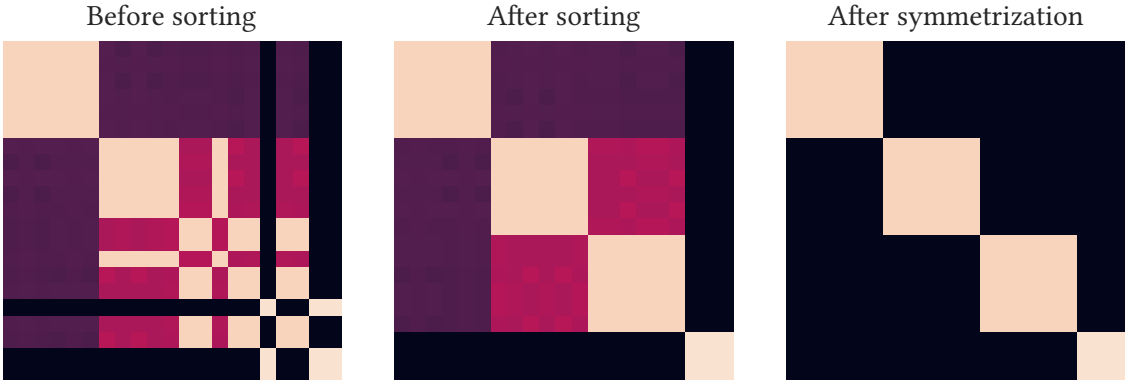

Figure 8.4: Heatmaps of $\boldsymbol{G}^{\Sigma}$ for PM localized occupied orbitals of benzene before symmetrization, after sorting according to the reverse Cuthill-McKee algorithm, and after symmetrization. Orbital indices are plotted along both the x-/y-axes and the employed color map is logarithmic, ranging in values of $\boldsymbol{G}^{\Sigma}$ from 10^{-13} (black) to 1 (bright beige tone). Adapted with permission from Ref. 518. Copyright 2023 American Chemical Society.

8.2.2 Exploiting Localized Orbital Symmetry in PyMBE

When LMO symmetry is exploited in MBE-based calculations, the total number of increments and CASCI calculations is effectively reduced. In PyMBE, the number of increments at a given MBE order has to be known before any increments are calculated to allocate the associative arrays required for increment storage in shared-memory. For calculations exploiting point-group symmetry, determining the number of non-redundant increments through a closed-form expression as described in Section 3.1.1 is significantly more complicated due to its dependence on the symmetry properties of the LMO basis. Instead, a *dry run* of the increment calculation is employed which generates all orbital tuples, applies all symmetry operations, and only counts those that are lexicographically greatest in each set of symmetry-equivalent orbitals. This *dry run* is parallelized by distributing the orbital tuples among all processes which results in negligible cost in comparison to the calculation of the actual increments.

During the calculation of increments in Section 3.1.2, only symmetry-unique increments are calculated and stored in the allocated associative arrays. It is important to note that while symmetry-equivalent active spaces will produce equal correlation energies, the increments calculated through Equation (2.68) will only be equal if all subtuple active spaces are also symmetry-equivalent. Illustrative examples where symmetry-equivalent active spaces do not result in symmetry-equivalent increments are provided in Figure 8.5. In the upper section of Figure 8.5, two increments formed from an occupied π-orbital and two different virtual orbitals belonging to a symmetry-equivalent set of size 12. This set of 12 symmetry-equivalent orbitals can be completely constructed from a symmetry-unique member through C_6, C_3, C_2, C_3^2, and C_6^5 rotations and the three σ_v mirror planes, among others. For instance, the two orbitals in the upper section of Figure 8.5 can be related through a σ_v mirror plane. The occupied π-orbital cannot be transformed into the two other π-orbitals in the symmetry-equivalent set by transformation employing the σ_v mirror plane. As a result, these two orbitals will not produce the same correlation energies. In the lower section of Figure 8.5, the occupied space spanned by all three occupied π-orbitals is symmetry-invariant with respect to all symmetry operations. For this reason, the active spaces on the left and the right side can be transformed into each other through a σ_v mirror plane and the correlation energies are equal. However, the subtuple increments required to construct both increments for these orbital tuples, such as those described in the upper section of

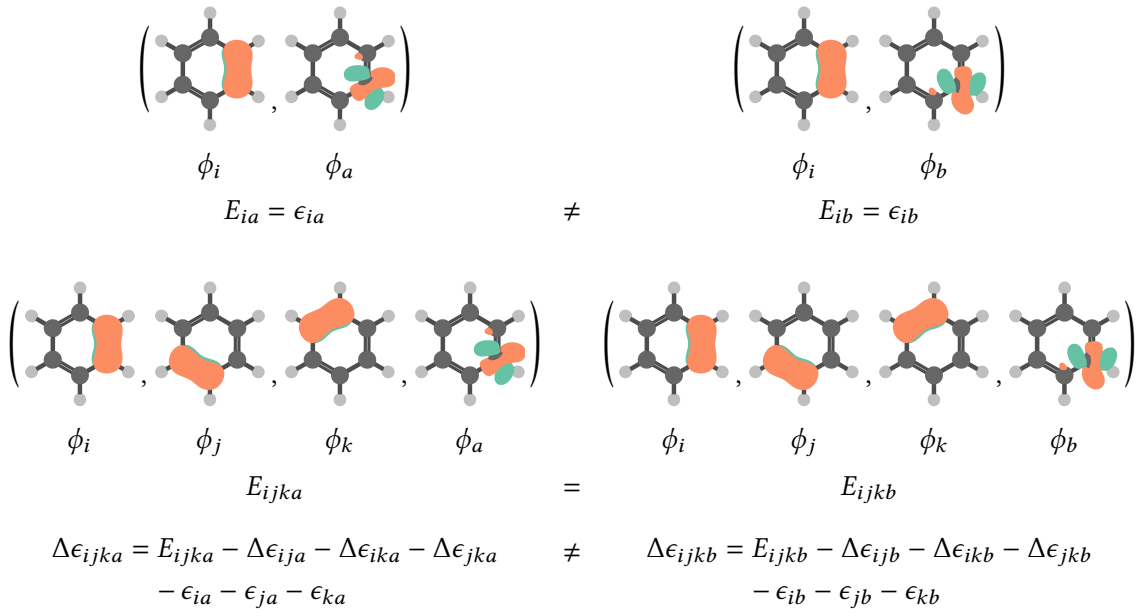

Figure 8.5: Illustrative example for orbital tuples which produce equivalent correlation energies but different increment energies. Adapted with permission from Ref. 519. Copyright 2024 American Chemical Society.

Figure 8.5, are not equal as the corresponding active spaces cannot be transformed into each other.

The increments of symmetry-equivalent active spaces will always be equal if all individual orbitals in the active space transform into another single orbital in the active space. When orbitals transform into a linear combination of orbitals, the resulting increments will often not be symmetry-equivalent. This condition is used in PyMBE to differentiate between symmetry-equivalent active spaces and symmetry-equivalent increments. For every generated orbital tuple, every symmetry-equivalent active space is generated and the CASCI calculation is only carried out for the symmetry-unique active space. All active spaces which produce different increment energies are then generated by only applying those symmetry operations which transform single orbitals among each other. Only these unique increments are calculated by subtracting the appropriate subtuple increments from the correlation energy of the symmetry-unique active space and are then added to the allocated associative arrays. The total number of CASCI calculations is monitored during the calculation of the increments as this number can be less than the number of increments for the previously mentioned reason. Every unique increment is multiplied by the total number of symmetry-equivalent increments and added to the total MBE property. Whether an active space or increment is chosen as symmetry-unique within the set of symmetry-equivalent quantities is determined by employing the *petite* list method schematically described in Figure 8.6. After an orbital tuple is generated, the involved orbitals are transformed by all symmetry operations of the molecular point group. The orbital tuple will only be considered when it is the lexicographically greatest in the generated symmetry-equivalent set. The contributions of all symmetry-equivalent increments to the correlation energy can be determined through multiplication with the number of unique orbital tuples in the symmetry-equivalent set. This number can be calculated by dividing the total number of symmetry operations of the point group by the order of the stabilizer. The stabilizer is the group of all symmetry operations that leave the tuple invariant.

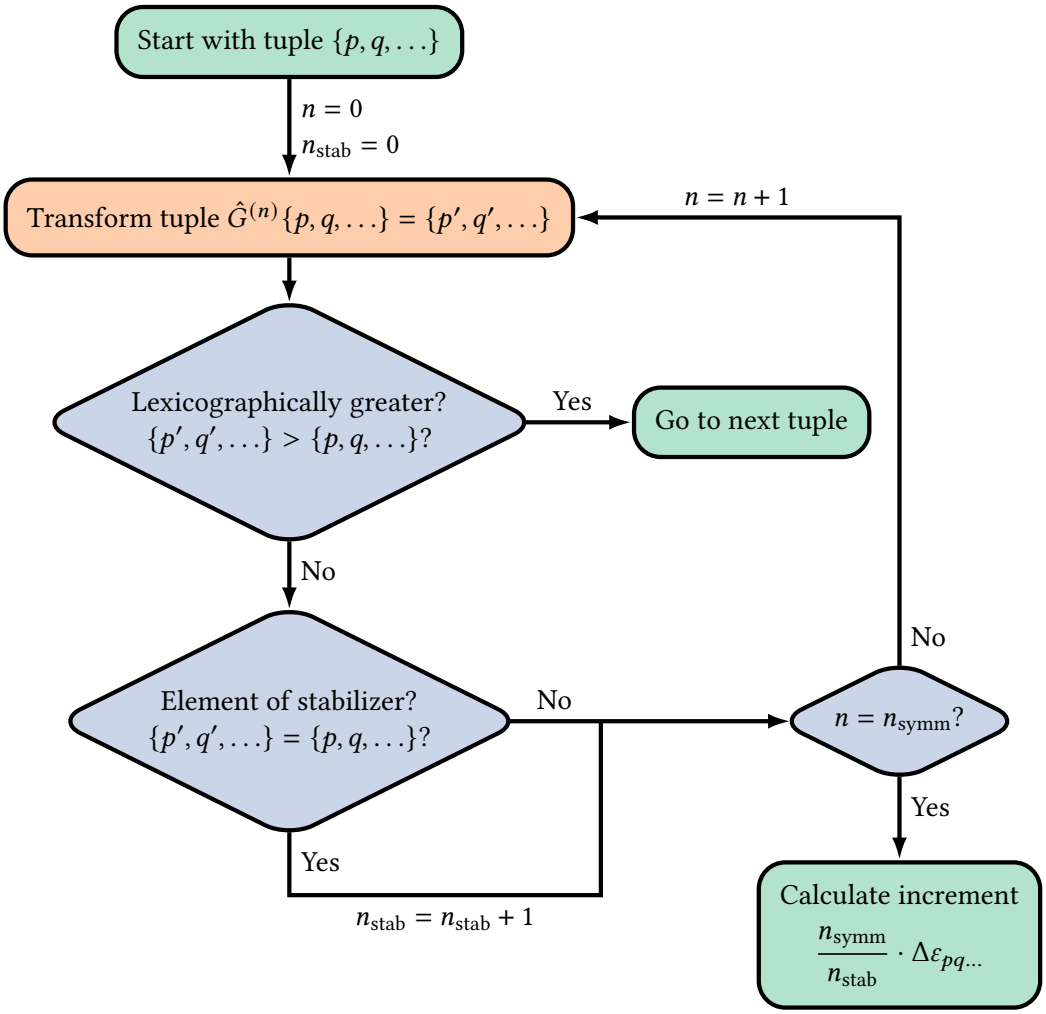

Figure 8.6: Flowchart of the *petite* list method. Adapted with permission from Ref. 519. Copyright 2024 American Chemical Society.

When the reference space is not invariant with respect to all symmetry operations, the application of symmetry operations to the reference space can produce contributions in the expansion space. For this reason, only symmetry transformations for orbital tuples which reproduce the entire reference space are considered in PyMBE. However, from a theoretical point-of-view, there is no reason to perform calculations with a non-symmetric reference space and these calculations are discouraged for performance reasons.

For calculations involving orbital clusters, only symmetry operations for orbital tuples which produce tuples of complete clusters are valid transformations considered in Figure 8.6. In general, orbital clustering in combination with symmetry-equivalent orbital sets can be challenging as the choice of the orbital clusters can significantly affect the ability to exploit LMO point-group symmetry. To limit this effect, orbital clustering is only performed among orbital sets which exhibit the same symmetry properties with respect to all symmetry operations. Additionally, the formation of clusters from orbitals that are part of the same symmetry-equivalent set will also render symmetry exploitation less effective. Using the outlined clustering procedure, these clusters are generally rare as the corresponding orbitals are not located at the same bonds or atoms and are therefore not explicitly prohibited in the clustering algorithm. Nevertheless, orbital clustering can lead to less effective

symmetry exploitation. However, this effect is always overshadowed by the computational gains resulting from a reduced number of expansion objects. When large orbital spaces are treated, the simulated annealing procedure in Section 6.1 will often converge to a local maximum. This local maximum will sometimes not be consistent with respect to the symmetry-equivalent orbital sets that form clusters with each other. This can be avoided by repeatedly restarting the annealing procedure for all remaining inconsistent symmetry-equivalent orbital sets which effectively reduces the orbital space to be clustered and guides the procedure towards the correct global maximum. The resulting clusters will enable optimal symmetry exploitation while allowing for sufficient freedom for the orbitals to form efficient clusters.

8.3 Results

Identifying and enforcing numerically exact symmetry properties while leaving the spatial locality of the LMOs unaffected is necessary for the applicability of LMO symmetry in local correlation methods. The symmetrization procedure is therefore tested extensively before exploiting point-group symmetry in MBE-FCI calculations with LMOs.

8.3.1 Symmetrization of Localized Orbitals

The symmetrization procedure is tested on a multitude of molecular systems for a variety of point groups: ammonia[a] (NH_3, C_{3v}), methane[b] (CH_4, T_d), boron trifluoride[c] (BF_3, C_{3h}), bromine pentafluoride[d] (BrF_5, C_{4v}), sulfur hexafluoride[e] (SF_6, O_h), benzene[f] (C_6H_6, D_{6h}), glucose[g] (C_6H_{12}, D_{3d}), pentaerythrityl tetrachloride[h] ($C_5H_8Cl_4$, S_4), sulfur[i] (S_8, D_{4d}), and buckminsterfullerene[j] (C_{60}, I_h). The cc-pVDZ basis set[404] is used to construct closed-shell HF orbitals which are then optimized using the PM, FB, and ER localization procedures as described in Section 2.6.2. The HF orbitals that are closest to the orthogonalized AO basis in a least-squares sense form the initial guess for orbital localization.[527,528] The symmetry detection is controlled by two different parameters, γ_{block} and γ_{orb}, for which a default value of 0.3 was chosen for all systems except for BF_3 and SF_6 with FB orbitals which required parameters of $\gamma_{\text{block}} = 0.4$ / $\gamma_{\text{orb}} = 0.1$ and $\gamma_{\text{block}} = 0.3$ / $\gamma_{\text{orb}} = 0.2$ to converge the symmetrization, respectively.

The degree to which symmetry properties are present in a set of LMOs differs depending on the localization procedure used. The elements of $\mathbf{G}^{\Sigma}$ for different sets of LMOs of benzene are showcased in Figure 8.7. Symmetry detection and the subsequent symmetrization is generally more difficult for virtual orbitals. This is particularly the case for FB and ER localization procedures which produce orbitals that deviate significantly from symmetry. Since the symmetrization algorithm depends on symmetry properties already present in the initial orbitals and due to the absence of symmetry in the ER virtual orbitals, the symmetrization procedure could not be converged for any of the considered

[a] $R(\text{N–H}) = 1.0043\,\text{Å}$, $\sphericalangle(\text{H–N–H}) = 110.9°$, $\sphericalangle(\text{H}-\text{N}-\text{H}-\text{H}) = 123.8°$
[b] $R(\text{C–H}) = 1.1030\,\text{Å}$
[c] $R(\text{B–F}) = 1.1130\,\text{Å}$
[d] $R(\text{Br–F}^{\text{ax}}) = 1.6890\,\text{Å}$, $R(\text{Br–F}^{\text{pla}}) = 1.7740\,\text{Å}$, $\sphericalangle(\text{F}^{\text{ax}}-\text{Br}-\text{F}^{\text{pla}}) = 84.8°$
[e] $R(\text{S–F}) = 1.5640\,\text{Å}$
[f] $R(\text{C–C}) = 1.3968\,\text{Å}$, $R(\text{C–H}) = 1.0874\,\text{Å}$
[g] $R(\text{C–C}) = 1.5260\,\text{Å}$, $R(\text{C–H}^{\text{ax}}) = 1.0930\,\text{Å}$, $R(\text{C–H}^{\text{eq}}) = 1.0980\,\text{Å}$
[h] $R(\text{C–C}) = 1.5400\,\text{Å}$, $R(\text{C–Cl}) = 1.7400\,\text{Å}$, $R(\text{C–H}) = 1.0900\,\text{Å}$
[i] $R(\text{S–S}) = 2.0711\,\text{Å}$, $\sphericalangle(\text{S}-\text{S}-\text{S}) = 108.2°$
[j] $R(\text{C–C}, 6:6) = 1.4010\,\text{Å}$, $R(\text{C–C}, 6:5) = 1.4590\,\text{Å}$

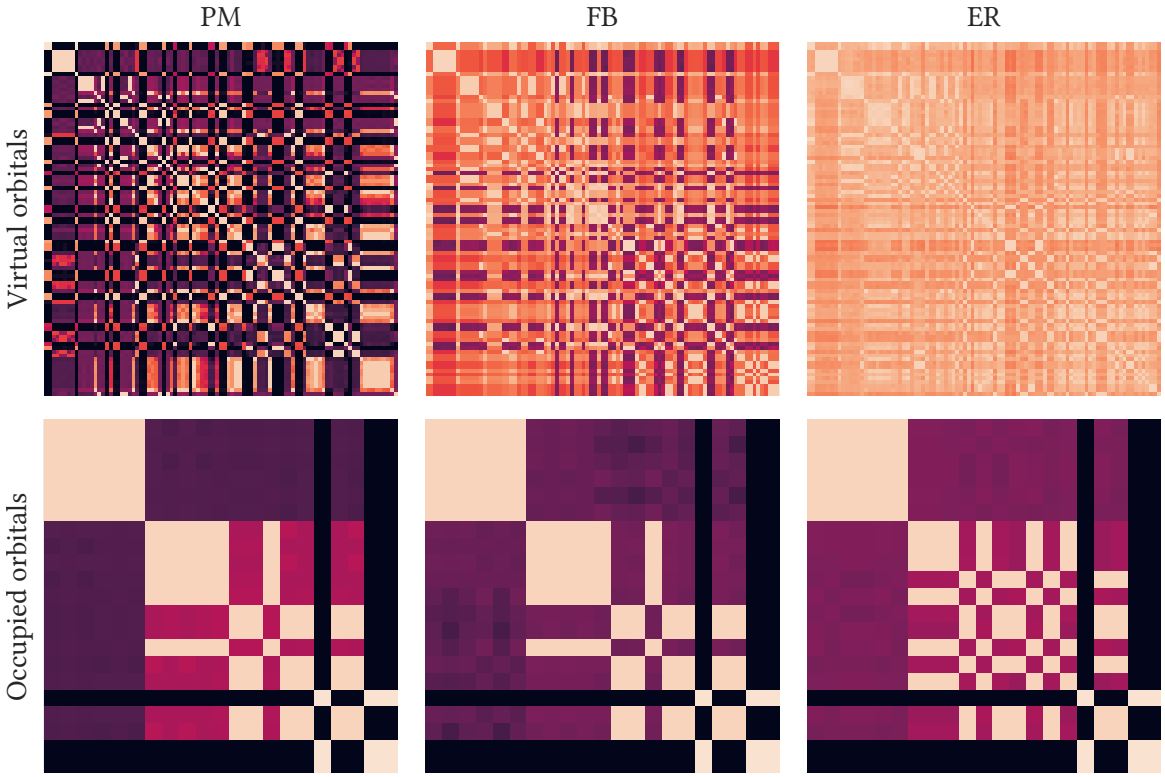

Figure 8.7: Heatmaps of $\mathbf{G}^{\Sigma}$ for different LMOs of benzene prior to symmetrization. Orbital indices are plotted along both the x-/y-axes and the color map is that of Figure 8.4. Adapted with permission from Ref. 518. Copyright 2023 American Chemical Society.

systems whenever ER LMOs were employed. For FB virtual orbitals, this effect is not as pronounced and the proposed algorithm is consistently able to symmetrize these orbitals. In general, ER orbitals are considered inferior, and their usefulness is limited in local correlation methods due to their spatial locality and the scaling of the localization procedure itself.[442]

The orbitals obtained after symmetrization generally do not represent a stationary point with respect to the used localization cost function unless the initial orbitals were already symmetric. For this reason, it is crucial that the spatial locality of the orbitals is not degraded when the orbitals are symmetrized. To confirm this property, the second and fourth-moment orbital spreads for PM and FB orbitals before and after symmetrization are compared in Figures 8.8 and 8.9 for all systems. The second-moment orbital spread is a measure for the general locality of the orbitals while the fourth-moment orbital spread penalizes the tails (which are usually a consequence of the orthogonality constraint) to a greater degree. Both of these properties are essential for the efficient implementation of local correlation methods.[415] The virtual orbitals will generally be less localized which is confirmed by the higher orbital spreads. Both quantities are entirely unaffected by the symmetrization which can be explained by the small orbital rotations that are necessary to symmetrize the orbitals. The orbitals after symmetrization are only described by a subset of markers in Figures 8.8 and 8.9 since only the symmetry-unique orbitals are plotted.

The initial orbitals provided by the two localization procedures do not only exhibit different spatial locality but also reveal different approximate symmetry properties. In all cases, the FB localization generates fewer symmetry-unique orbitals and the symmetrized orbitals will therefore offer a greater opportunity for exploitation and should be considered as an alternative to PM orbitals when applying

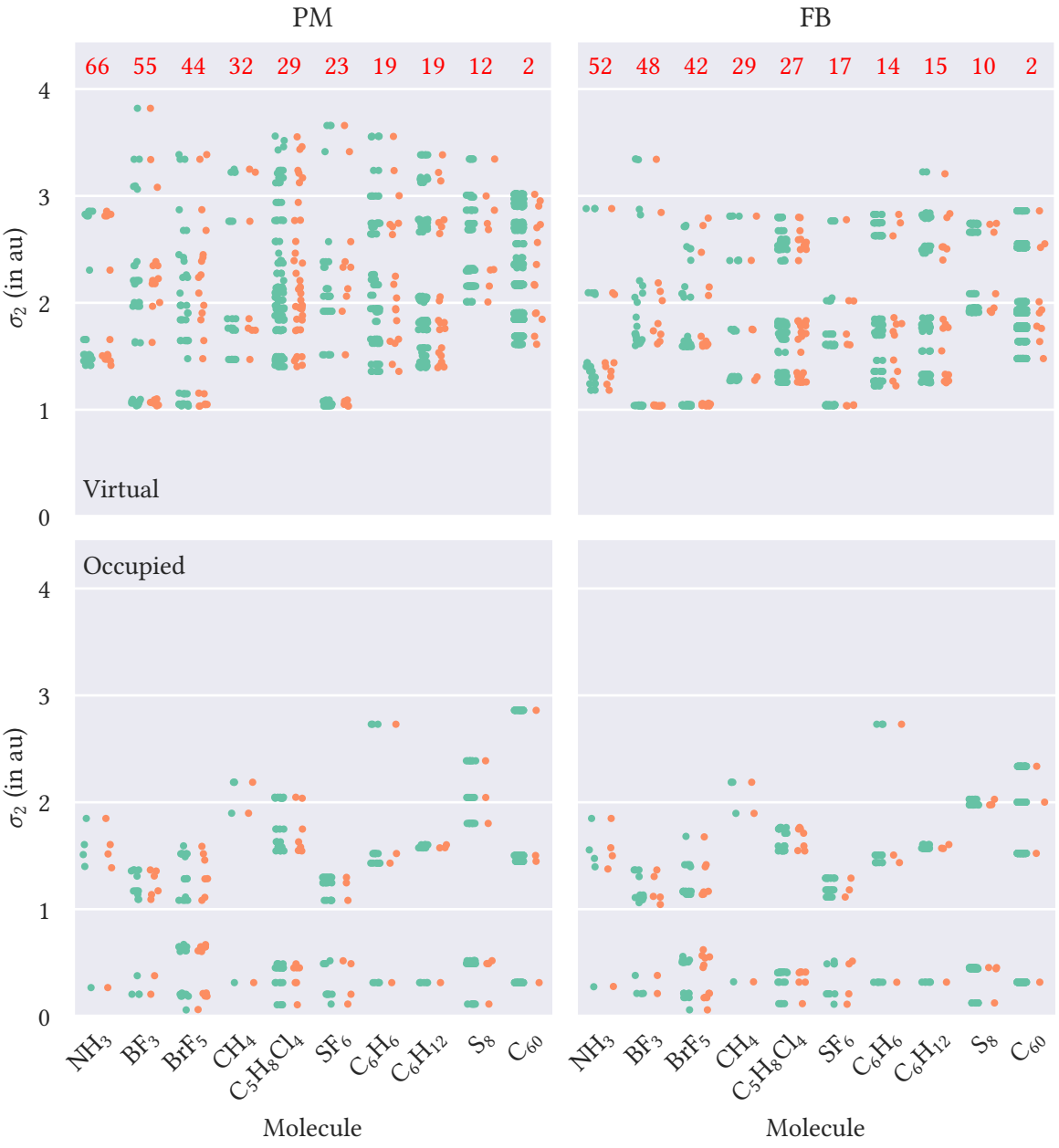

Figure 8.8: Second-moment orbital spreads (σ_2^p) of PM and FB LMOs. Results for orbitals before and after the symmetrization are displayed in green and orange, respectively. The percentage of symmetry-unique orbitals for every molecule is displayed in red. Adapted with permission from Ref. 518. Copyright 2023 American Chemical Society.

MBE-FCI to highly symmetric systems. Both methods produce orbitals with a similar degree of spatial locality while a smaller number of symmetrized FB LMOs is needed to construct the whole orbital space through the application of symmetry operations. The fact that the FB localization does not preserve σ-π separation but instead produces symmetry-equivalent τ orbitals could offer a plausible theory why a smaller number of symmetry-unique orbitals are required to span the orbital space.[429] Unfortunately, the results from Section 7.2.1 discourage the use of FB LMOs in the context of MBE-FCI.

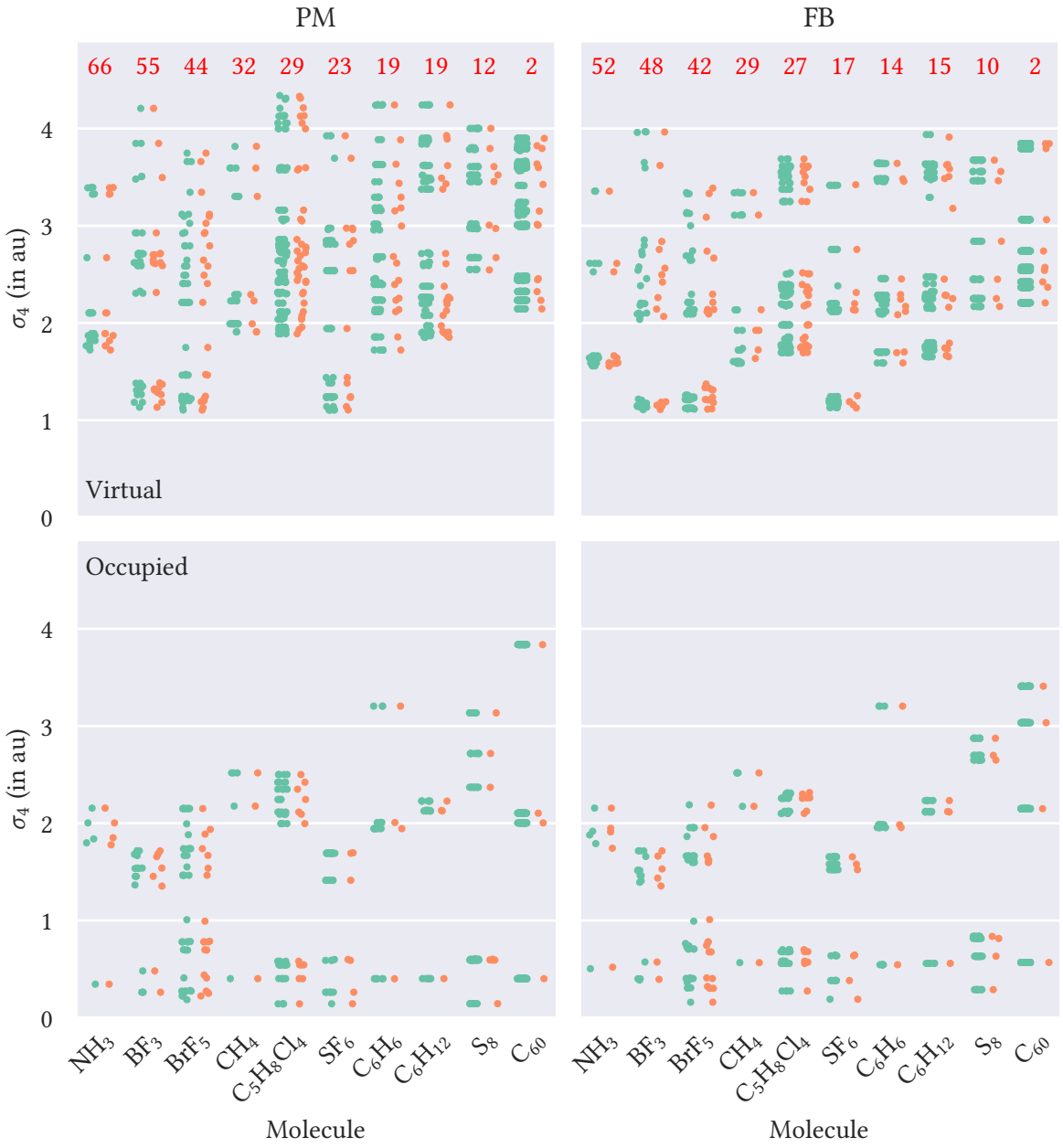

Figure 8.9: Fourth-moment orbital spreads (σ_4^p) of PM and FB LMOs. Results for orbitals before and after the symmetrization are displayed in green and orange, respectively. The percentage of symmetry-unique orbitals for every molecule is displayed in red. Adapted with permission from Ref. 518. Copyright 2023 American Chemical Society.

In addition to the effects of different localizations schemes, the number of symmetry-unique orbitals that are generated for a given set of orbitals is also influenced by the position of the atoms in the system and the order of the point group. These effects are investigated in Figure 8.10. As one would reasonably expect, the use of higher-order point groups generally leads to a smaller number of symmetry-unique orbitals. The limit for the minimum number of non-redundant orbitals will be inversely proportional to the order of the considered point group.[128] As already alluded to in Section 8.1, orbital centroids which coincide with symmetry elements will be symmetry-invariant and will not favorably contribute to the number of symmetry-unique orbitals. As LMOs are often

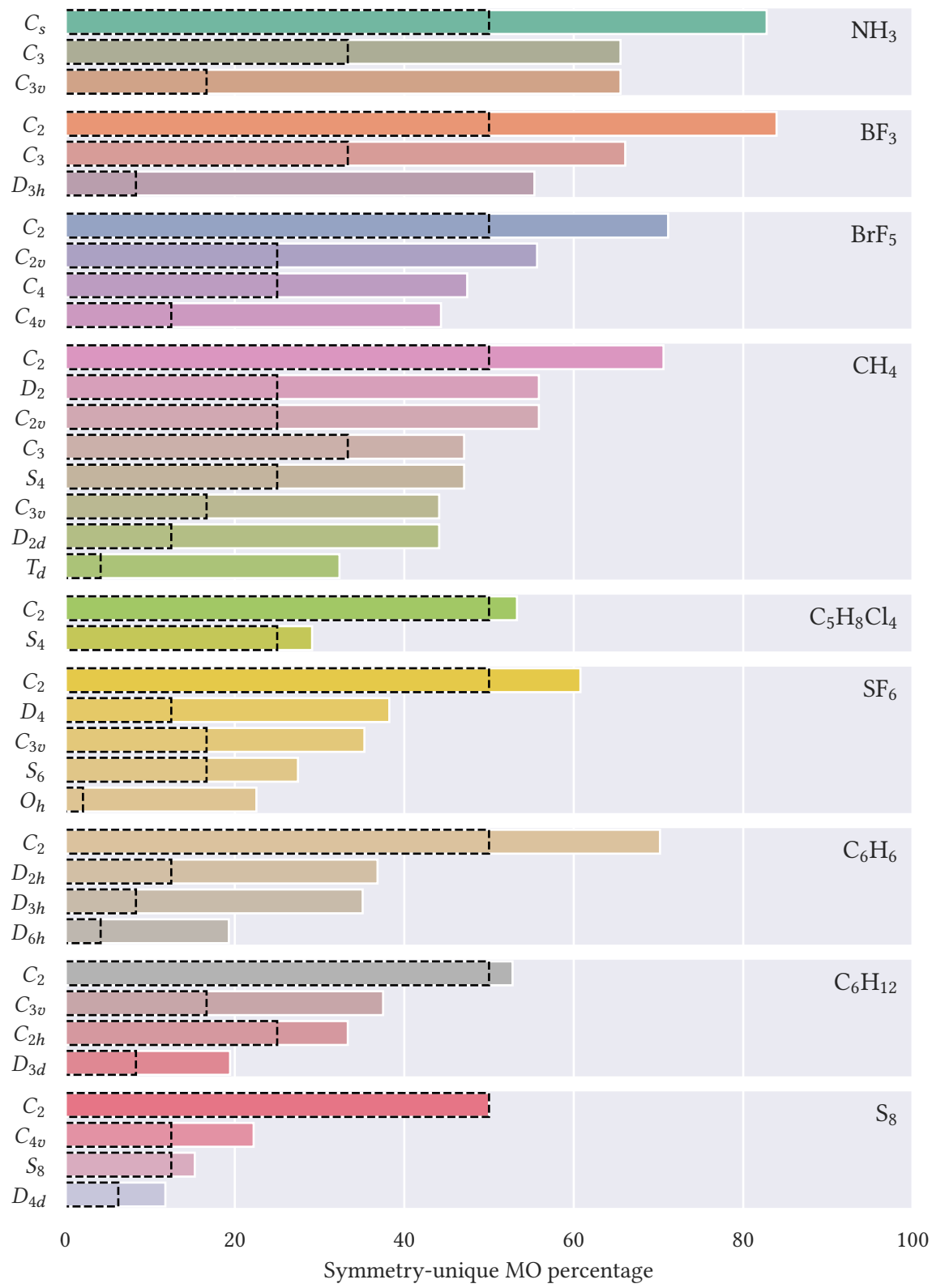

Figure 8.10: Ratio of symmetry-unique PM orbitals in the highest point group and selected subgroups for a range of molecules. Theoretical limits are superimposed using dashed lines. Adapted with permission from Ref. 518. Copyright 2023 American Chemical Society.

located at atoms and bonds, the number of non-redundant orbitals will increase whenever atoms are located on top of inversion points, rotation(-reflection) axes, or mirror planes. This result is apparent when comparing the symmetry-unique orbital ratios of NH_3 and C_6H_{12} in C_{3v} or BrF_5 and S_8 in C_{4v}.

An extreme case for which exploiting non-Abelian point-group symmetries in local correlation methods could yield unprecedented speed-ups is the buckminsterfullerene in the highly symmetric I_h point group. The high order of the point group ($h = 120$) and the fact that no atoms are located at the center of symmetry both promise an extreme compression of the orbital space to only a few symmetry-unique orbitals. In a cc-pVDZ basis set,[404] this system requires a total of 840 orbitals. Orbital examples from the symmetry-adapted canonical orbital basis and from both the symmetrized PM and FB LMO bases are presented in Figure 8.11. The symmetrization procedure is able to significantly condense

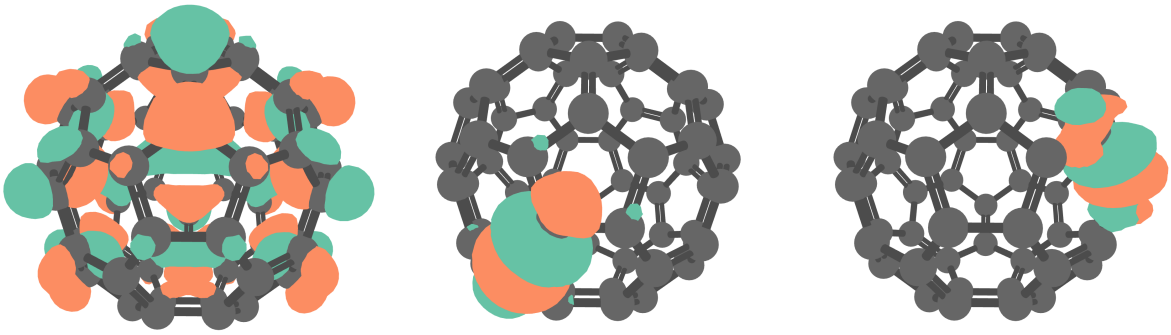

840 | 18 (2.1 %) | 14 (1.7 %)

(a) Symmetry-adapted canonical MO | (b) Symmetry-unique PM LMO | (c) Symmetry-unique FB LMO

Figure 8.11: Molecular orbitals of buckminsterfullerene. The total number of symmetry-unique orbitals is displayed below each example illustration alongside relative ratios. Adapted with permission from Ref. 518. Copyright 2023 American Chemical Society.

the orbital space by almost two orders of magnitude to 18 and 14 symmetry-unique orbitals starting from PM and FB LMOs, respectively. For both localization schemes, the total ratio comes close to the theoretical limit of 0.8 % while the mean differences of the second- and fourth-moment orbital spreads amount to less than 10^{-3} au. While the C_{60} system might currently still be out of reach for MBE-FCI theory, the potential of exploiting non-Abelian point-group symmetries by utilizing symmetry-equivalent LMOs is nevertheless tremendous.

8.3.2 Exploiting Arbitrary Point Group Localized Orbital Symmetry

The symmetry properties of the symmetrized LMOs can be exploited in MBE-FCI calculations, making numerous increment calculations redundant and therefore reducing the computational effort necessary to perform MBE-FCI calculations on symmetric molecules. The degree to which symmetry can be exploited depends on the order of the molecular point group and the nature of the LMOs themselves. The total number of redundant calculations for different molecular point groups are investigated in Figure 8.12 for water[k] (H_2O), ammonia[l] (NH_3), and methane[m] (CH_4) in a cc-pVDZ

[k] R(O–H) = 0.9580 Å, ∠(H – O – H) = 104.5°
[l] R(N–H) = 1.0043 Å, ∠(H – N – H) = 110.9°, ∠(H – N – H – H) = 123.8°
[m] R(C–H) = 1.1030 Å

basis set.[404] These all-electron calculations are performed using symmetrized FB LMOs employing an empty reference space and single orbitals in the expansion space. Both the total number of increments and the number of redundant calculations increase exponentially with the MBE order. Consequently, the percentage of redundant calculations of the total number of increments remains relatively stable throughout the expansion. For all systems, the percentage of redundant calculations is generally correlated to the order of the exploited molecular point group. The theoretical upper bound for this percentage is inversely related to the order of the molecular point group and will only be reached if the cardinality of all symmetry-equivalent orbital sets is equal to the order of the point group which will rarely be the case for systems with atoms or bonds located on top of symmetry elements.

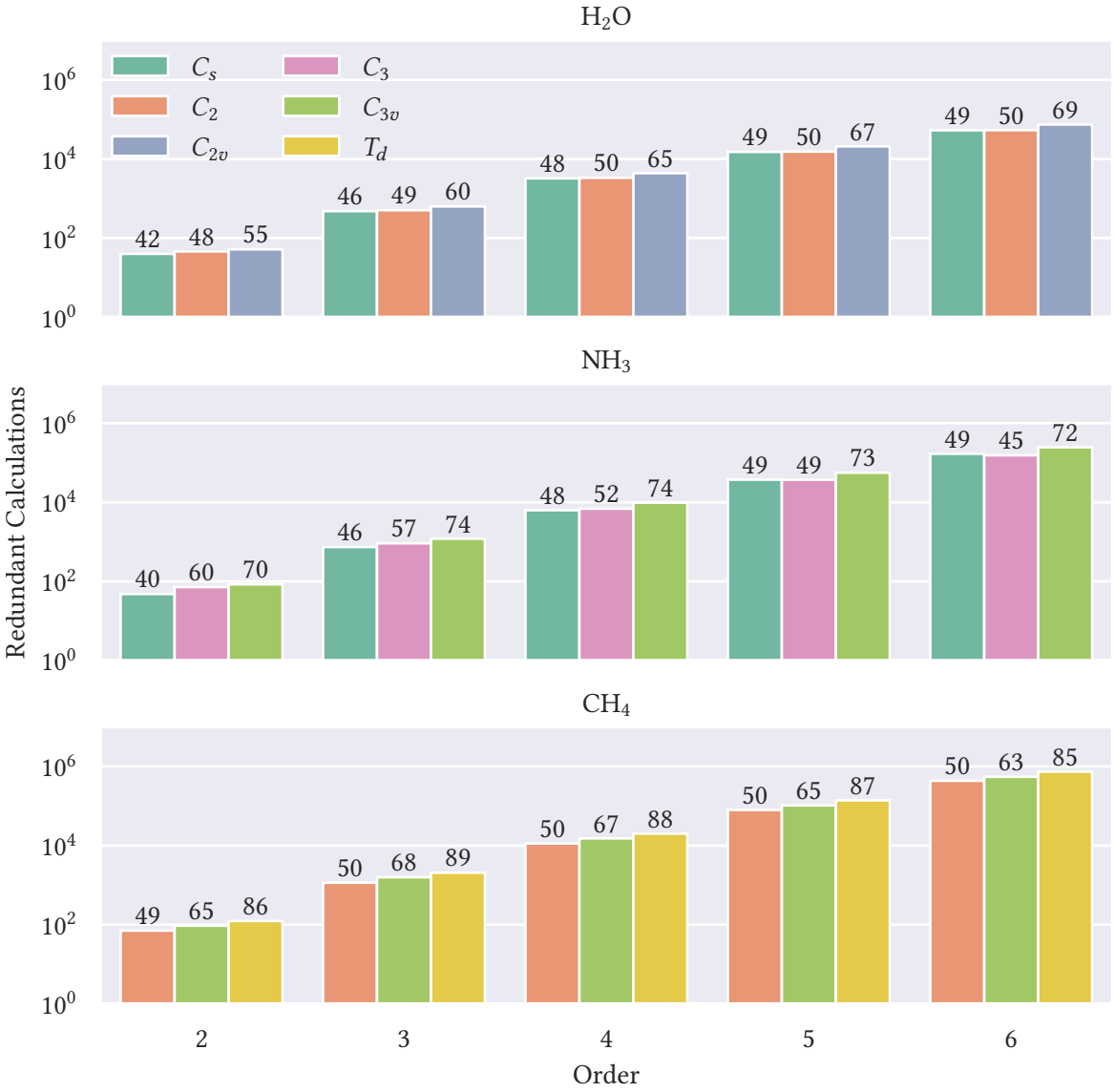

Figure 8.12: Total number of redundant calculations for specific point groups plotted against the MBE order for H_2O, NH_3, and CH_4. These all-electron calculations utilize symmetrized FB LMOs and an empty reference space. The percentage of redundant increments is displayed above the respective bar. The y-axis is logarithmic. Adapted with permission from Ref. 519. Copyright 2024 American Chemical Society.

Nevertheless, all calculations in Figure 8.12 approach this upper bound and a significant number of increment calculations can be skipped.

To investigate the effects of larger basis sets on the ability to exploit LMO point-group symmetry, the above calculations were repeated in the full molecular point group in Figure 8.13 employing the cc-pVTZ and cc-pVQZ basis sets.[404] Both the total number of increments and the number of redundant calculations increase with the cardinality of the basis set. For the virtual MOs of larger basis sets, the localization cost function will often exhibit numerous densely clustered minima and the symmetry properties of the identified minimum can affect the ability to exploit point-group

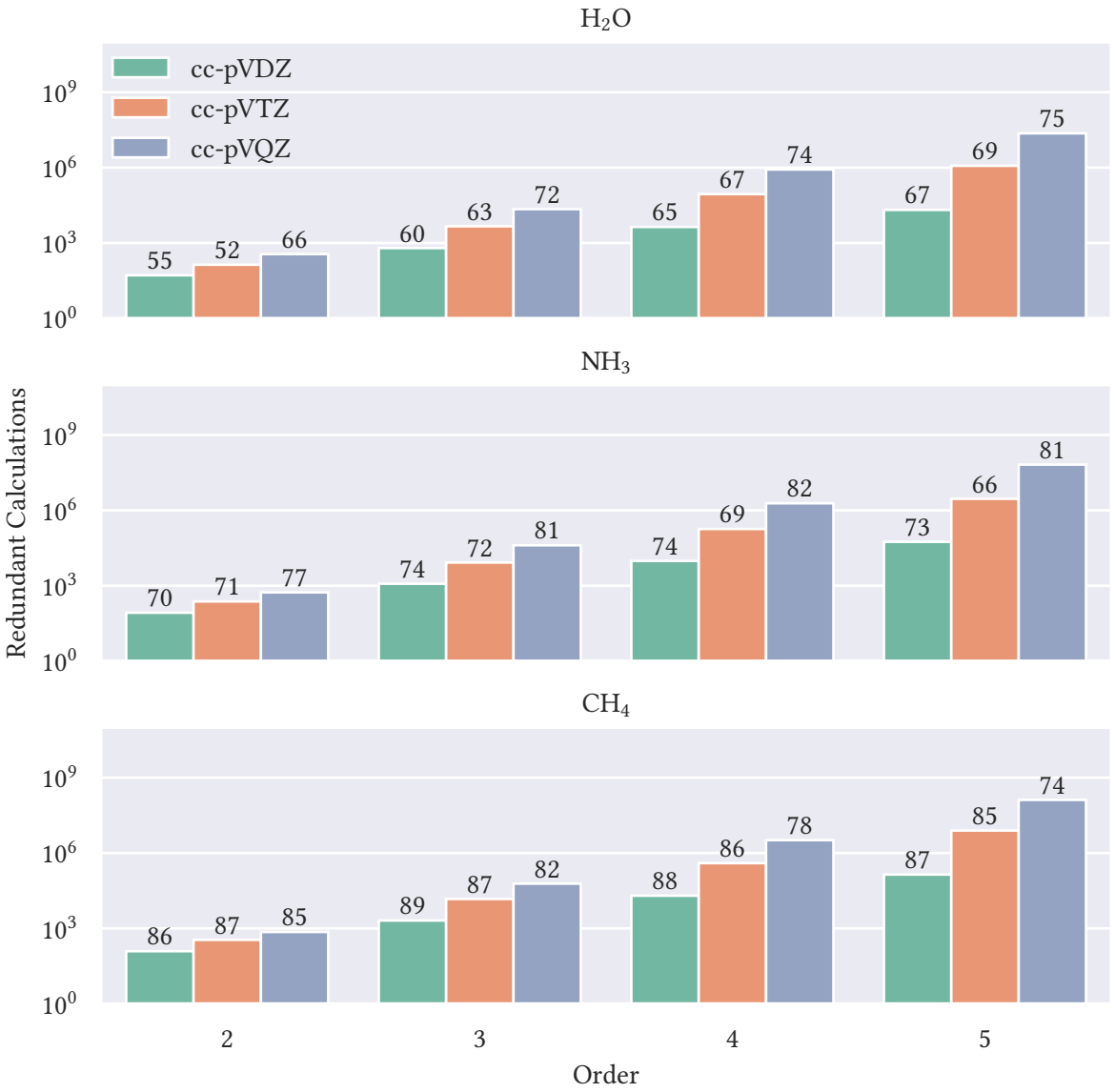

Figure 8.13: Total number of redundant calculations for the cc-pVDZ, cc-pVTZ, and cc-pVQZ basis sets plotted against the MBE order for H_2O, NH_3, and CH_4 in their respective full molecular point group. These all-electron calculations utilize symmetrized FB LMOs and an empty reference space. The percentage of redundant increments is displayed above the respective bar. The y-axis is logarithmic. Adapted with permission from Ref. 519. Copyright 2024 American Chemical Society.

symmetry. This effect can both increase and decrease the ratio of redundant calculations as can be seen for NH_3 in the cc-pVTZ and cc-pVQZ basis sets. In general, the percentage of redundant calculations exhibits no basis set dependence and symmetry can be exploited to a similar degree, regardless of basis set size. The additional LMOs introduced through larger basis sets appear to inherit similar symmetry properties to the LMOs of smaller basis sets. Hence, the exploitation of arbitrary point group LMO symmetries presented in this chapter is able to significantly reduce the computational effort of MBE-FCI calculations for highly symmetric systems. In combination with the developments in Chapter 6, a wider range of molecular systems in larger basis sets are now amenable to affordable and highly accurate MBE-FCI calculations.

9 The Ground-State Electronic Energy of Benzene

The benzene molecule is widely known as the prototypical aromatic base structure from which numerous chemically relevant derivatives can be formed. Due to its prevalence in organic chemistry and its large molecular size this system has been benchmarked in the cc-pVDZ basis set by a variety of state-of-the-art approximate FCI approaches through a blind study.[135] ASCI, SHCI, iCI, AS-FCIQMC, CAD-FCIQMC, DMRG, MBE-FCI, and FCCR were employed to target the frozen-core ground-state electronic energy of this system. Results from the *i*-FCIQMC approach are also available from previous work.[347] Additional post-blind results from ASCI employing localized orbitals and from SHCI utilizing further optimized orbitals and an alternative extrapolation function have also been generated for this system.[135] Since Ref. 135 was published, results from AFQMC,[529] CIPSI,[530] and iFCI[531] have emerged, corroborating the projected energy range. While the MBE-FCI method is able to converge to an energy right in the center of the range projected by the other methods, the calculation also required an overwhelming 1.7 million core hours parallelized over 4608 cores.[135] Its high symmetry, which has not been used in the MBE-FCI calculation in Ref. 135, makes the benzene system a perfect candidate for the exploitation of non-Abelian localized orbital symmetry in the context of the MBE-FCI method. In combination with the orbital clustering introduced in Chapter 6, this approach can significantly reduce computational costs and therefore enable more accurate calculations while also moving on to larger basis sets. The work in this chapter was published in Ref. 519.

The MBE-FCI calculation in Ref. 135 utilized a reference space including all six PM localized π-orbitals. When applied to an empty reference space MBE-FCI calculation employing PM orbitals, the automatic reference space identification introduced in Chapter 5 also suggests that these π-orbitals should be added to the reference space while leaving it empty could significantly slow convergence of the MBE. The development of the MBECC backend offers an alternative to the π-orbital reference space through high-level CC base models. Since these base models are able to capture the correlation of the π-orbitals to a large extent, convergence of the MBE will be accelerated even when an empty reference space is utilized. Empty reference spaces can be advantageous since the MBE can be converged to significantly higher orders before the CI and sigma vectors for individual increment calculations can no longer be stored in memory. For a π-orbital reference space, parallel calculations beyond MBE order 8 become difficult as a result of this memory boundary. Correspondingly, calculations involving an empty reference space can be reliably converged to MBE order 14. While MBE calculations involving single-orbital expansion spaces will never reach such high orders for systems of this size due to the prohibitive polynomial scaling of the number of increments with the size of the expansion space, calculations involving clusters of orbitals in the expansion space can easily be performed to higher orders. Hence, while including the highly correlated π-orbitals in the expansion space can be beneficial, empty reference space calculations can likely compete for base model MBE-FCI calculations involving a clustered expansion space.

Alternatively, the reference space can also be selected in the canonical orbital basis. Instead of including six localized π-orbitals in the reference space, the two degenerate sets of occupied and

virtual canonical π-orbitals might suffice to improve MBE convergence. These are significantly more correlated than the remaining π-orbitals. While this approach limits the localizability of the remaining orbitals, the reference space is also compressed such that higher MBE orders are easily accessible in calculations involving a clustered expansion space. This partitioning applies the combination of a delocalized reference space and a localized expansion space investigated in Section 7.2.1 to the larger benzene system.

It should be noted that the screening and error estimation techniques introduced in Chapter 7 are not utilized for the treatment of the benzene system. Since these calculations are mostly limited by memory, screening is not necessary before higher MBE orders become impractical. Additionally, the empirical relationship identified in Chapter 7 is not calibrated for the use with CC base models which represents a potential direction for future extension. For these reasons, all calculations in this chapter are truncated after a given MBE order.

The benzene calculations[a] employ a symmetrized, PM localized expansion space involving two-orbital clusters. These clusters are constructed from early-order MBE-FCI information (up to MBE order 4) using the clustering procedure outlined in Section 6.1. The results up to a maximum number of 14 orbitals in the increment active space for different reference spaces and CC base models are presented in Figure 9.1. Additionally, the results utilizing non-empty reference spaces and a CCSDT base model are augmented by additional MBE-CCSDTQ results for MBE orders which are intractable with MBE-FCI due to memory. The different reference space choices are easily compared when

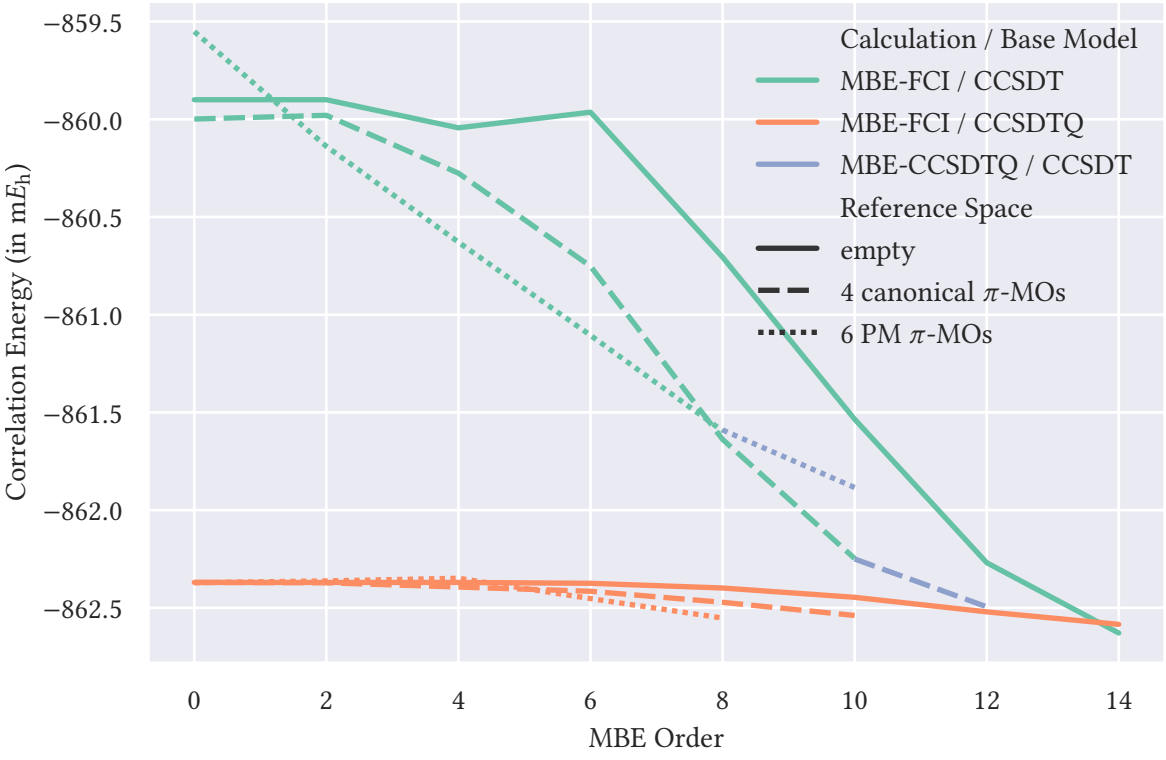

Figure 9.1: Correlation energies of the frozen-core electronic ground state energy of benzene obtained in MBE-FCI calculations using the cc-pVDZ basis set employing different reference spaces and CC base models. Adapted with permission from Ref. 519. Copyright 2024 American Chemical Society.

[a]Symmetrized geometry from Ref. 532 which was also used in Refs. 135 and 347

inspecting the calculations with the CCSDT base model. The calculation employing six PM π-orbitals in the reference space is unable to converge to the same energy as the other calculations before additional MBE orders become infeasible. When both sets of degenerate canonical π-orbitals are included in the reference space, a cost-effective balance between early MBE termination order and accelerated convergence caused by folding additional correlation into the reference space can be achieved, and the calculation is able to converge to a similar energy as the remaining expansions in Figure 9.1.

The CCSDTQ base model already recovers a great majority of the correlation effects present in this system. Therefore, all expansions utilizing this base model only yield a minor correction to the CCSDTQ energy of the full system. In any case, these calculations all converge to the same energy range which supports the assumption that the reference space choice is irrelevant for dynamically correlated systems when high-level base models are employed. All MBE convergence profiles follow a similar pattern as early-order contributions are often small since the CC base model can sufficiently describe small increment active spaces. Higher orders will then contribute to a greater degree until the MBE converges and the contributions vanish. When the MBE is truncated before full convergence is achieved, the resulting energy will nevertheless recover all contributions up to the base model level of theory.

The best estimate for the frozen-core MBE-FCI correlation energy of benzene in the cc-pVDZ basis set presented in this chapter is given by the MBE-FCI/CCSDTQ calculation employing an empty reference space which converges to an energy of $-862.6\,\mathrm{m}E_\mathrm{h}$. This calculation recovers all 7-orbital contributions at the FCI level of theory while the remaining orders are treated using the highly accurate CCSDTQ method. The FCI correction at the remaining orders will likely be minor. From these arguments, the MBE-FCI result presented in Ref. 135 only recovers up to 6-orbital contributions in their entirety and should therefore be less accurate. In comparison to this blind-study result, the calculations presented in this chapter are not only more accurate but also significantly cheaper. The empty reference space MBE-FCI/CCSDTQ calculation required a total of 40 300 core hours[b] which is significantly more affordable than the calculation in Ref. 135. The time-to-solution is reduced by a factor of 40. On the other hand, the MBE-FCI/CCSDT calculation employing four canonical π-orbitals required 1700 core hours while the corresponding MBE-FCI/CCSDTQ calculation required 2600 core hours.[b] In comparison to Ref. 135, the computational effort was reduced by a factor of 1000 and 650, respectively. About one order of magnitude can be traced to the symmetry exploitation since 89 % of the CASCI calculations were omitted due to symmetry equivalences, avoiding a total of 2.6 million redundant calculations. The remainder should be attributed to orbital clustering and other algorithmic improvements in the PyMBE program. It should be noted that these timings do not include the initial base model calculation which can become a bottleneck for larger calculations. For example, the CCSDTQ calculation in Ref. 135 required a total of 5500 core hours. When the MBE-FCI/CCSDT result is augmented by MBE-CCSDTQ/CCSDT results at the final order, the computational effort increases by around 15 600 core hours.[b] This increase is caused by numerous additional CCSDTQ increments that need to be calculated. The MBE-FCI/CCSDTQ calculation employing four canonical π-orbitals in the reference space yields the best compromise between accuracy and computational efficiency of all results presented in this chapter.

The results of a variety of other state-of-the-art approximate FCI approaches, all of which are described in Section 2.3, are compared to both types of base model calculations employing the four canonical π-orbitals in the expansion space in Figure 9.2. These predictions are divided into the CC *reference* calculations, the *blind* calculations that were performed without knowledge of the

[b]Computer architecture: Two Intel Gold 6130 per node (32 cores @ 2.1 GHz, 5.53 GB/core)

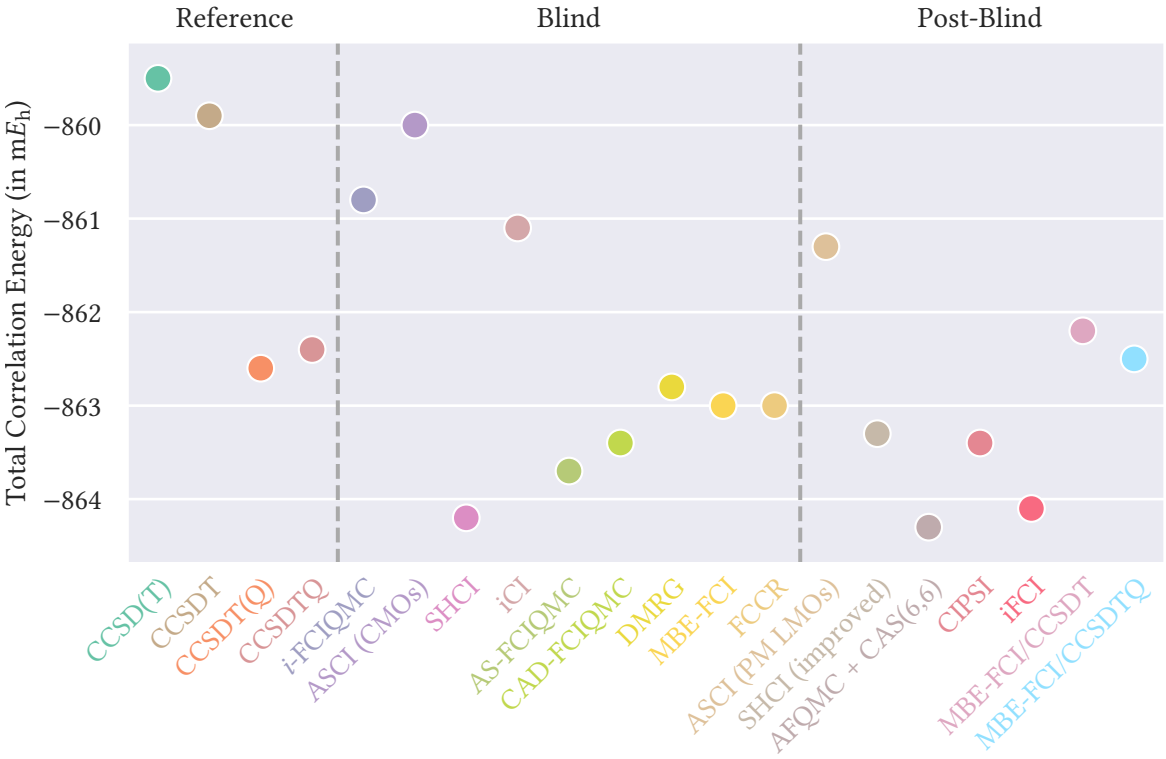

Figure 9.2: Correlation energies of the frozen-core electronic ground state energy of benzene in a cc-pVDZ basis set. All energies except those of the CCSDT(Q), MBE-FCI/CCSDT, and MBE-FCI/CCSDTQ methods were taken from Refs. 42, 347, 529, 530, and 531. Adapted with permission from Ref. 519. Copyright 2024 American Chemical Society.

results from other methods, and the *post-blind* calculations that were published after the results from Ref. 135 were available. The majority of the post-blind calculations predict energies below the average correlation energy in Ref. 135. The predicted correlation energies in this work are slightly higher and much closer to the CCSDT(Q) and CCSDTQ results.

Some developments presented in this thesis can enable calculations of unprecedented size. While MBE-FCI calculations on the benzene system in a cc-pVTZ basis involving a total of 254 orbitals would have been inconceivable when Ref. 135 was published in 2020, this system can now be efficiently treated in an attempt to reduce the remaining basis set error. Full CCSDTQ calculations are infeasible for systems of this size and MBE-FCI calculations hence need to rely on the CCSDT base model instead. While empty reference spaces yield the most accurate calculations in the cc-pVDZ basis set, these calculations become impractical when employing a cc-pVTZ basis as around 800 million and 20 billion increments would be required at MBE orders 12 and 14, respectively. Hence, an MBE-FCI/CCSDT calculation involving a reference space of four π-orbitals is performed, and the correlation energy can be compared to CC and AFQMC results in Figure 9.3.[530] The AFQMC calculation is computationally less expensive and less accurate than the corresponding result in Figure 9.2 because it is only based on a single-determinantal HF trial wave function. The correlation energy magnitude of the benzene system appears to be systematically overestimated by the AFQMC method.[529] The MBE-FCI/CCSDT result of $-1028.7\,\mathrm{m}E_\mathrm{h}$ is slightly above CCSDT(Q) which is plausible since the CCSDT(Q) result tends to overshoot the CCSDTQ energy.[222,533] The comparison to the results in Figure 9.1 indicates that the correlation energy will likely further decrease over the next few MBE orders. The resulting difference to the FCI result will presumably stay within a conservative estimate of 1 kcal/mol. Calculations

Figure 9.3: Correlation energies of the frozen-core electronic ground state energy of benzene in a cc-pVTZ basis set. The AFQMC energy is taken from Ref. 530. Adapted with permission from Ref. 519. Copyright 2024 American Chemical Society.

of this size can be routinely performed on large-scale parallel computer systems as the calculation required a mere 39 700 core hours.[b] An overwhelming number of around 238M CASCI calculations (90%) were skipped, underlining the importance of exploiting full D_{6h} symmetry for this system.

The investigation of the electronic ground state of the benzene molecule presented in this chapter has coupled many of the developments presented in this thesis and has exemplified how these advancements enable accurate calculations of unprecedented size on commodity computer hardware. Consequently, these developments can be applied to a variety of interesting molecular systems to provide reliable benchmark results needed both for quantum chemical method development and in thermochemical applications. The calculated correlation energies of the electronic ground state of benzene provide a reference point for other accurate approximations of FCI theory.

10 Conclusion and Outlook

Within the scope of this thesis, the capabilities of the MBE-FCI method have been extended to enable the efficient and highly accurate treatment of a variety of molecular systems. These developments have required a major overhaul of the PyMBE program and have resulted in greater accessibility, applicability, and performance of MBE-based methods. These advancements unlock the ability to perform massively parallel calculations of electronic energies beyond chemical accuracy for a wide range of systems which will become highly relevant for benchmarking and thermochemical applications. The key findings are summarized and future perspectives are explored in the present chapter.

The newly developed MBE-CASSCF method enables the treatment of statically correlated systems which require large active spaces. To achieve this, the CASCI step in conventional two-step CASSCF algorithms is replaced by a dedicated MBE-CASCI solver (e.g., PyMBE). The existing MBE targets in PyMBE were extended to facilitate the expansion of 1- and 2-RDMs and of generalized Fock matrices, both in a state-specific and state-averaged fashion, which allow for the approximation of the CASSCF orbital gradient. An interface to the CFOUR program package has enabled the efficient application of the MBE-CASSCF method. The description of the electronic structure of several polyacenes through the lens of MBE-CASSCF has revealed that rather crude approximations of the orbital gradient for the orbital optimization will nevertheless permit an accurate treatment of these systems. From a computational standpoint, the final energy evaluation employing the fully optimized orbitals turns out to be substantially more important. This finding enables the memory-efficient implementation of MBE-CASSCF orbital optimization through a recursive formulation of the MBE. Additionally, the orbital optimization benefits from the inclusion of important orbitals in a reference space and from a compact initial active orbital basis, such as LMOs. However, explicitly allowing for active-active orbital optimization will lead to convergence issues while offering little value. These problems caused by the redundancy of the active orbitals and the CI coefficients could be mitigated through an explicit coupling of the optimization of both sets of parameters.[271,479] Additionally, CASSCF calculations involving large active spaces often exhibit multiple local minima[305] which can cause issues and possibly needs to be remedied in the future. Nevertheless, given appropriate screening parameters, the MBE-CASSCF method is able to consistently reproduce conventional CASSCF results for smaller systems. The MBE-CASSCF method was then applied to the challenging description of the triplet-quintet spin gap of the iron(II) porphyrin system employing a variety of active spaces, up to a size of 50 electrons in 50 orbitals. While these calculations fail to reproduce the experimentally found ordering of the spin states, a decrease of the spin gap with increasing active space size signifies a possible interchange of the states if even more orbitals are included in the active space. The small magnitude of the spin gap and its high fluctuation for different active spaces indicate possible flaws in the CASSCF method for the qualitatively correct description of systems of this nature. These challenges could possibly be solved by incorporating the dynamic correlation outside the active space. In the context of MBE-FCI, this could be achieved by replacing the final energy MBE-CASCI evaluation by an MBE-FCI calculation where the orbitals outside the active space are screened away rather quickly. Nonetheless, the ability to treat large active spaces accurately and efficiently in the context of orbital-based MBEs is one of the key breakthroughs that have emerged from the

developments in this thesis. Possible applications involve not only extended statically correlated systems which might require these large active spaces to converge but also systems for which the choice of an optimal active space is ambiguous. The MBE-CASSCF method could additionally be extended to the calculation of molecular gradients which would facilitate geometry optimizations for systems requiring large active spaces.

An automatic procedure for the identification of statically correlated orbitals that are to be included in the reference space for MBE-FCI or MBE-CASCI calculations was proposed. This procedure exploits early-order MBE information through the quantum fidelity and streamlines the reference space identification process by only requiring a single input parameter. The resulting reference spaces of three statically correlated systems were compared to the active spaces obtained from DMRG-based autoCAS,[281,285] a common approach for solving the active space selection problem in the context of CASCI and CASSCF calculations. This comparison reveals high correlation between the results of both methods, indicating possible applications of the quantum-fidelity-based selection criterion in the context of both conventional and approximate CASSCF calculations. Additionally, the developed algorithm also ensures that the optimal eigenvalue is chosen from the spectrum of the individual increment calculations which prevents MBE convergence issues due to state switching along different orders of the MBE. This approach could be extended to the description of electronically excited states[112] which could be achieved by starting from a reference space which describes the dominant determinant in the configuration interaction with single excitations wave function of the targeted state and then following this state instead of the HF ground state determinant.

The cost of MBE-based methods can be reduced by merging single orbitals into orbital clusters and using these as objects of the expansion. Orbital clustering in MBE-FCI requires a careful balance between the total number of clusters and the size of the clusters themselves. In this thesis, an orbital clustering algorithm was developed which attempts to maximize intracluster correlations from early-order MBE information. The contributions at early orders of the MBE that can be constructed from these clusters are therefore maximized. An improved clustering method could involve explicit orbital optimization within the expansion space to maximize intracluster contributions, similar to the cluster mean-field method.[470] When approximating CC theory, orbital clustering becomes a necessity for MBE-based methods to become competitive with their conventional counterpart. The developments in the framework of this thesis have laid the groundwork for the practical application of MBE-CC approximations that will undoubtedly extend the range of systems that can be treated on the basis of high-level CC methods. MBE-based calculations employing orbital clusters could further be improved by removing the restriction that the clusters must be mutually exclusive. Instead, overlapping clusters would allow the expansion to recover additional intracluster contributions at early MBE orders if necessary. Similar efforts have been proposed in the context of fragment MBEs and been successfully applied to the description of condensed-matter systems.[71]

The orbital-based screening method proposed in this thesis enables the truncation of the MBE while controlling the accumulated errors. The proposed model uses empirical relationships and importance sampling to predict projected error bounds and removes orbitals from the expansion space to produce results within provided error bounds. The reference space detection, orbital clustering, and screening developments are applied to the `FCI21` benchmark set and compared to conventional FCI results. The outlined improvements to the MBE-FCI method enable the treatment of both statically and dynamically correlated systems in the benchmark set up to a range of different error bounds. Different localized and delocalized MO bases as well as various combinations of delocalized reference spaces and localized expansion spaces were tested on the systems in this benchmark set. For the small systems considered herein, PM LMOs seem to provide the lowest timings across the entire benchmark set while combinations of delocalized reference spaces and localized expansion spaces do not appear

to offer significant advantages over the localization of the entire orbital space. In the future, benefits of alternative localization methods which are able to improve locality of the virtual orbitals, such as fourth-moment localization, should be investigated.[415,430] These developments were also tested on a small group of larger molecules which showcase appropriate scaling of the error bounds with system size. Going forward, the screening and error estimation algorithm should be extended to MBE-FCI calculations employing CC base models. The algorithm could be further improved by factoring in information about those increments which fall below the convergence criterion of the individual CASCI calculations or below the numerical precision of the floating-point representation. Perhaps more sophisticated machine-learning models could be designed by accounting for additional information about the extent to which specific orbitals are correlated. This could possibly be achieved from distance- and orbital-spread-based measures for LMOs and could be applied to the additional pruning of individual increments. Furthermore, any insight on the cause behind why an increment exhibits a specific sign would be highly desirable for screening and error estimation purposes.

A novel algorithm for the symmetrization of LMOs was developed in the context of this thesis which enforces approximate symmetry properties present in both PM and FB LMOs. This algorithm was then applied to an extensive selection of molecular systems exhibiting a wide variety of (non-)Abelian point groups. It was found that the FB localization procedure will generally produce a smaller number of symmetry-unique MOs and will therefore exhibit a higher potential for symmetry exploitation than PM localization. Possible applications of the resulting symmetrized LMOs are not restricted to MBE-based methods but also show significant potential to speed up other local correlation methods employing orthogonal and linearly independent LMOs. The implementation of the *petite* list method in MBE-FCI has enabled the ability to exploit these (non-)Abelian LMO symmetries, culminating in a large reduction in the total number of necessary calculations for highly symmetric molecules.

The exploitation of LMO point-group symmetry and the use of orbital clustering have significantly extended the applicability of the MBE-FCI method and have enabled the calculation of a highly accurate approximation of the frozen-core electronic ground state energy of benzene in a cc-pVTZ basis set. This result closes the gap toward the non-relativistic ground state energy of benzene by removing a large proportion of the basis set error present in previously published results[135] and yields unparalleled accuracy for a system of this size at affordable computational costs.

Future applications will require MBE-FCI theory to venture beyond energies. Therefore, many of the developments presented in this thesis will need to be extended to other electronic properties to be broadly applicable across the wide spectrum of chemically interesting quantities. While all wave function properties can theoretically be expanded through an MBE and approximated through its truncation, the devil is often in the details, as this thesis has convincingly demonstrated. Nevertheless, when implemented effectively and applied appropriately MBE-based methods can offer affordable access to highly accurate approximations of the electronic Schrödinger equation.

Bibliography

(1) Von Neumann, J., The Mathematician In *Works of the Mind*, Heywood, R. B., Ed.; University of Chicago Press: Chicago, 1947, pp 180–196.

(2) Dirac, P. A. M. Quantum Mechanics of Many-Electron Systems. *Proc. R. Soc. A* **1929**, *123*, 714–733.

(3) Eyring, H.; Walter, J.; Kimball, G. E., *Quantum Chemistry*; John Wiley and Sons Inc.: New York, 1944.

(4) Mulliken, R. S. Spectroscopy, Molecular Orbitals, and Chemical Bonding, See: `https://www.nobelprize.org/uploads/2018/06/mulliken-lecture.pdf`, Nobel Prize lecture, 1966.

(5) Gupta, U.; Kim, Y. G.; Lee, S.; Tse, J.; Lee, H.-H. S.; Wei, G.-Y.; Brooks, D.; Wu, C.-J. In *2021 IEEE International Symposium on High-Performance Computer Architecture (HPCA)*, IEEE: Seoul, 2021.

(6) Li, B.; Basu Roy, R.; Wang, D.; Samsi, S.; Gadepally, V.; Tiwari, D. In *Proceedings of the International Conference for High Performance Computing, Networking, Storage and Analysis*, ACM: New York, 2023, pp 1–15.

(7) Kutzelnigg, W. Methods and Applications of Quantum Chemistry. Part I: Physical and Mathematical Basis. *Angewandte Chemie International Edition in English* **1966**, *5*, 823–835.

(8) Gauss, J., Molecular Properties, Winter school, 21-25 February 2000, Forschungszentrum Jülich, Germany In *Modern Methods and Algorithms of Quantum Chemistry*, Grotendorst, J., Ed., Second; NIC Series, Vol. 3; NIC: Jülich, 2000, pp 541–592.

(9) Karton, A. A Computational Chemist's Guide to Accurate Thermochemistry for Organic Molecules. *Wiley Interdiscip. Rev.: Comput. Mol. Sci.* **2016**, *6*, 292–310.

(10) Popelier, P., *Solving the Schrodinger Equation, Has Everything Been Tried?*; Imperial College Press: Singapore, 2014.

(11) Knowles, P.; Handy, N. A New Determinant-Based Full Configuration Interaction Method. *Chem. Phys. Lett.* **1984**, *111*, 315–321.

(12) Head-Gordon, M.; Artacho, E. Chemistry on the Computer. *Phys. Today* **2008**, *61*, 58–63.

(13) Piela, L., *Ideas of Quantum Chemistry*, 2nd ed.; Elsevier: Amsterdam, 2014.

(14) Helgaker, T.; Jørgensen, P.; Olsen, J., *Molecular Electronic-Structure Theory*; Wiley: Chichester, 2000.

(15) Di Felice, R. et al. A Perspective on Sustainable Computational Chemistry Software Development and Integration. *J. Chem. Theory Comput.* **2023**, *19*, 7056–7076.

(16) Huron, B.; Malrieu, J. P.; Rancurel, P. Iterative Perturbation Calculations of Ground and Excited State Energies from Multiconfigurational Zeroth-Order Wavefunctions. *J. Chem. Phys.* **1973**, *58*, 5745–5759.

(17) White, S. R. Density Matrix Formulation for Quantum Renormalization Groups. *Phys. Rev. Lett.* **1992**, *69*, 2863–2866.

(18) Zhang, S.; Carlson, J.; Gubernatis, J. E. Constrained Path Monte Carlo Method for Fermion Ground States. *Phys. Rev. B* **1997**, *55*, 7464–7477.

(19) Booth, G. H.; Thom, A. J. W.; Alavi, A. Fermion Monte Carlo without Fixed Nodes: A Game of Life, Death, and Annihilation in Slater Determinant Space. *J. Chem. Phys.* **2009**, *131*, 054106.

(20) Liu, W.; Hoffmann, M. R. iCI: Iterative CI toward Full CI. *J. Chem. Theory Comput.* **2016**, *12*, 1169–1178.

(21) Tubman, N. M.; Lee, J.; Takeshita, T. Y.; Head-Gordon, M.; Whaley, K. B. A Deterministic Alternative to the Full Configuration Interaction Quantum Monte Carlo Method. *J. Chem. Phys.* **2016**, *145*, 044112.

(22) Holmes, A. A.; Tubman, N. M.; Umrigar, C. J. Heat-Bath Configuration Interaction: An Efficient Selected Configuration Interaction Algorithm Inspired by Heat-Bath Sampling. *J. Chem. Theory Comput.* **2016**, *12*, 3674–3680.

(23) Eriksen, J. J.; Lipparini, F.; Gauss, J. Virtual Orbital Many-Body Expansions: A Possible Route Towards the Full Configuration Interaction Limit. *J. Phys. Chem. Lett.* **2017**, *8*, 4633–4639.

(24) Zimmerman, P. M. Incremental Full Configuration Interaction. *J. Chem. Phys.* **2017**, *146*, 104102.

(25) Eriksen, J. J. The Shape of Full Configuration Interaction to Come. *J. Phys. Chem. Lett.* **2021**, *12*, 418–432.

(26) Williams, K. T. et al. Direct Comparison of Many-Body Methods for Realistic Electronic Hamiltonians. *Phys. Rev. X* **2020**, *10*, 011041.

(27) Nesbet, R. K. Atomic Bethe-Goldstone Equations. I. The Be Atom. *Phys. Rev.* **1967**, *155*, 51–55.

(28) Nesbet, R. K. Atomic Bethe-Goldstone Equations. II. The Ne Atom. *Phys. Rev.* **1967**, *155*, 56–58.

(29) Nesbet, R. K. Atomic Bethe-Goldstone Equations. III. Correlation Energies of Ground States of Be, B, C, N, O, F, and Ne. *Phys. Rev.* **1968**, *175*, 2–9.

(30) Stoll, H. The Correlation Energy of Crystalline Silicon. *Chem. Phys. Lett.* **1992**, *191*, 548–552.

(31) Stoll, H. On the Correlation Energy of Graphite. *J. Chem. Phys.* **1992**, *97*, 8449–8454.

(32) Stoll, H. Correlation Energy of Diamond. *Phys. Rev. B* **1992**, *46*, 6700–6704.

(33) Friedrich, J.; Hanrath, M.; Dolg, M. Error Analysis of Incremental Electron Correlation Calculations and Applications to Clusters and Potential Energy Surfaces. *Chem. Phys.* **2007**, *338*, 33–43.

(34) Friedrich, J.; Hanrath, M.; Dolg, M. Energy Screening for the Incremental Scheme: Application to Intermolecular Interactions. *J. Phys. Chem. A* **2007**, *111*, 9830–9837.

(35) Friedrich, J.; Hanrath, M.; Dolg, M. Fully Automated Implementation of the Incremental Scheme: Application to CCSD Energies for Hydrocarbons and Transition Metal Compounds. *J. Chem. Phys.* **2007**, *126*, 154110.

(36) Friedrich, J.; Hanrath, M.; Dolg, M. Using Symmetry in the Framework of the Incremental Scheme: Molecular Applications. *Chem. Phys.* **2008**, *346*, 266–274.

(37) Bytautas, L.; Ruedenberg, K. The Range of Electron Correlation between Localized Molecular Orbitals. A Full Configuration Interaction Analysis for the NCCN Molecule. *J. Phys. Chem. A* **2010**, *114*, 8601–8612.

(38) Boschen, J. S.; Theis, D.; Ruedenberg, K.; Windus, T. L. Correlation Energy Extrapolation by Many-Body Expansion. *J. Phys. Chem. A* **2017**, *121*, 836–844.

(39) Bytautas, L.; Ruedenberg, K. Correlation Energy Extrapolation by Intrinsic Scaling. I. Method and Application to the Neon Atom. *J. Chem. Phys.* **2004**, *121*, 10905–10918.

(40) Eriksen, J. J.; Gauss, J. Many-Body Expanded Full Configuration Interaction. I. Weakly Correlated Regime. *J. Chem. Theory Comput.* **2018**, *14*, 5180–5191.

(41) Eriksen, J. J.; Gauss, J. Many-Body Expanded Full Configuration Interaction. II. Strongly Correlated Regime. *J. Chem. Theory Comput.* **2019**, *15*, 4873–4884.

(42) Eriksen, J. J.; Gauss, J. Generalized Many-Body Expanded Full Configuration Interaction Theory. *J. Phys. Chem. Lett.* **2019**, *10*, 7910–7915.

(43) Eriksen, J. J.; Gauss, J. Incremental Treatments of the Full Configuration Interaction Problem. *Wiley Interdiscip. Rev.: Comput. Mol. Sci.* **2021**, *11*, e1525.

(44) Zimmerman, P. M. Singlet–Triplet Gaps through Incremental Full Configuration Interaction. *J. Phys. Chem. A* **2017**, *121*, 4712–4720.

(45) Zimmerman, P. M. Strong Correlation in Incremental Full Configuration Interaction. *J. Chem. Phys.* **2017**, *146*, 224104.

(46) Abraham, V.; Mayhall, N. Cluster Many-Body Expansion: A Many-Body Expansion of the Electron Correlation Energy about a Cluster Mean-Field Reference. *J. Chem. Phys.* **2021**, *155*, 054101.

(47) Verma, P.; Huntington, L.; Coons, M. P.; Kawashima, Y.; Yamazaki, T.; Zaribafiyan, A. Scaling up Electronic Structure Calculations on Quantum Computers: The Frozen Natural Orbital Based Method of Increments. *J. Chem. Phys.* **2021**, *155*, 034110.

(48) Hankins, D.; Moskowitz, J. W.; Stillinger, F. H. Water Molecule Interactions. *J. Chem. Phys.* **1970**, *53*, 4544–4554.

(49) Xantheas, S. S. *Ab Initio* Studies of Cyclic Water Clusters $(H_2O)_n$, n=1–6. II. Analysis of Many-Body Interactions. *J. Chem. Phys.* **1994**, *100*, 7523–7534.

(50) Kaplan, I. G.; Santamaria, R.; Novaro, O. Non-Additive Forces in Atomic Clusters: The Case of Ag_n. *Mol. Phys.* **1995**, *84*, 105–114.

(51) Paulus, B.; Rosciszewski, K.; Gaston, N.; Schwerdtfeger, P.; Stoll, H. Convergence of the *Ab initio* Many-Body Expansion for the Cohesive Energy of Solid Mercury. *Phys. Rev. B* **2004**, *70*, 165106.

(52) Stoll, H.; Paulus, B.; Fulde, P. On the Accuracy of Correlation-Energy Expansions in Terms of Local Increments. *J. Chem. Phys.* **2005**, *123*, 144108.

(53) Dahlke, E. E.; Truhlar, D. G. Assessment of the Pairwise Additive Approximation and Evaluation of Many-Body Terms for Water Clusters. *J. Phys. Chem. B* **2006**, *110*, 10595–10601.

(54) Dahlke, E. E.; Truhlar, D. G. Electrostatically Embedded Many-Body Expansion for Large Systems, with Applications to Water Clusters. *J. Chem. Theory Comput.* **2007**, *3*, 46–53.

(55) Dahlke, E. E.; Truhlar, D. G. Electrostatically Embedded Many-Body Correlation Energy, with Applications to the Calculation of Accurate Second-Order Møller-Plesset Perturbation Theory Energies for Large Water Clusters. *J. Chem. Theory Comput.* **2007**, *3*, 1342–1348.

(56) Fedorov, D. G.; Kitaura, K. Extending the Power of Quantum Chemistry to Large Systems with the Fragment Molecular Orbital Method. *J. Phys. Chem. A* **2007**, *111*, 6904–6914.

(57) Hermann, A.; Krawczyk, R. P.; Lein, M.; Schwerdtfeger, P.; Hamilton, I. P.; Stewart, J. J. P. Convergence of the Many-Body Expansion of Interaction Potentials: From Van Der Waals to Covalent and Metallic Systems. *Phys. Rev. A* **2007**, *76*, 013202.

(58) Dahlke, E. E.; Truhlar, D. G. Electrostatically Embedded Many-Body Expansion for Simulations. *J. Chem. Theory Comput.* **2008**, *4*, 1–6.

(59) Dahlke, E. E.; Leverentz, H. R.; Truhlar, D. G. Evaluation of the Electrostatically Embedded Many-Body Expansion and the Electrostatically Embedded Many-Body Expansion of the Correlation Energy by Application to Low-Lying Water Hexamers. *J. Chem. Theory Comput.* **2008**, *4*, 33–41.

(60) Addicoat, M. A.; Collins, M. A. Accurate Treatment of Nonbonded Interactions within Systematic Molecular Fragmentation. *J. Chem. Phys.* **2009**, *131*, 104103.

(61) Řezáč, J.; Salahub, D. R. Multilevel Fragment-Based Approach (MFBA): A Novel Hybrid Computational Method for the Study of Large Molecules. *J. Chem. Theory Comput.* **2009**, *6*, 91–99.

(62) Beran, G. J. O.; Nanda, K. Predicting Organic Crystal Lattice Energies with Chemical Accuracy. *J. Phys. Chem. Lett.* **2010**, *1*, 3480–3487.

(63) Weiss, S. N.; Huang, L.; Massa, L. A Generalized Higher Order Kernel Energy Approximation Method. *J. Comput. Chem.* **2010**, *31*, 2889–2899.

(64) Góra, U.; Podeszwa, R.; Cencek, W.; Szalewicz, K. Interaction Energies of Large Clusters from Many-Body Expansion. *J. Chem. Phys.* **2011**, *135*, 224102.

(65) Gordon, M. S.; Fedorov, D. G.; Pruitt, S. R.; Slipchenko, L. V. Fragmentation Methods: A Route to Accurate Calculations on Large Systems. *Chem. Rev.* **2011**, *112*, 632–672.

(66) Bygrave, P. J.; Allan, N. L.; Manby, F. R. The Embedded Many-Body Expansion for Energetics of Molecular Crystals. *J. Chem. Phys.* **2012**, *137*, 164102.

(67) Gao, J.; Wang, Y. Communication: Variational Many-Body Expansion: Accounting for Exchange Repulsion, Charge Delocalization, and Dispersion in the Fragment-Based Explicit Polarization Method. *J. Chem. Phys.* **2012**, *136*, 071101.

(68) Le, H.-A.; Tan, H.-J.; Ouyang, J. F.; Bettens, R. P. A. Combined Fragmentation Method: A Simple Method for Fragmentation of Large Molecules. *J. Chem. Theory Comput.* **2012**, *8*, 469–478.

(69) Leverentz, H. R.; Maerzke, K. A.; Keasler, S. J.; Siepmann, J. I.; Truhlar, D. G. Electrostatically Embedded Many-Body Method for Dipole Moments, Partial Atomic Charges, and Charge Transfer. *Phys. Chem. Chem. Phys.* **2012**, *14*, 7669.

(70) Mayhall, N. J.; Raghavachari, K. Many-Overlapping-Body (MOB) Expansion: A Generalized Many Body Expansion for Nondisjoint Monomers in Molecular Fragmentation Calculations of Covalent Molecules. *J. Chem. Theory Comput.* **2012**, *8*, 2669–2675.

(71) Richard, R. M.; Herbert, J. M. A Generalized Many-Body Expansion and a Unified View of Fragment-Based Methods in Electronic Structure Theory. *J. Chem. Phys.* **2012**, *137*, 064113.

(72) Gillan, M. J.; Alfè, D.; Bygrave, P. J.; Taylor, C. R.; Manby, F. R. Energy Benchmarks for Water Clusters and Ice Structures from an Embedded Many-Body Expansion. *J. Chem. Phys.* **2013**, *139*, 114101.

(73) Richard, R. M.; Herbert, J. M. Many-Body Expansion with Overlapping Fragments: Analysis of Two Approaches. *J. Chem. Theory Comput.* **2013**, *9*, 1408–1416.

(74) Richard, R. M.; Lao, K. U.; Herbert, J. M. Achieving the CCSD(T) Basis-Set Limit in Sizable Molecular Clusters: Counterpoise Corrections for the Many-Body Expansion. *J. Phys. Chem. Lett.* **2013**, *4*, 2674–2680.

(75) Richard, R. M.; Lao, K. U.; Herbert, J. M. Approaching the Complete-Basis Limit with a Truncated Many-Body Expansion. *J. Chem. Phys.* **2013**, *139*, 224102.

(76) Tan, H.-J.; Bettens, R. P. A. *Ab Initio* NMR Chemical-Shift Calculations Based on the Combined Fragmentation Method. *Phys. Chem. Chem. Phys.* **2013**, *15*, 7541.

(77) Wang, X.; Liu, J.; Zhang, J. Z. H.; He, X. Electrostatically Embedded Generalized Molecular Fractionation with Conjugate Caps Method for Full Quantum Mechanical Calculation of Protein Energy. *J. Phys. Chem. A* **2013**, *117*, 7149–7161.

(78) Mach, T. J.; Crawford, T. D. Computing Optical Rotation Via an *N*-Body Approach. *Theor. Chem. Acc.* **2014**, *133*, 1449.

(79) Ouyang, J. F.; Cvitkovic, M. W.; Bettens, R. P. A. Trouble with the Many-Body Expansion. *J. Chem. Theory Comput.* **2014**, *10*, 3699–3707.

(80) Richard, R. M.; Lao, K. U.; Herbert, J. M. Understanding the Many-Body Expansion for Large Systems. I. Precision Considerations. *J. Chem. Phys.* **2014**, *141*, 014108.

(81) Richard, R. M.; Lao, K. U.; Herbert, J. M. Aiming for Benchmark Accuracy with the Many-Body Expansion. *Accounts Chem. Res.* **2014**, *47*, 2828–2836.

(82) Medders, G. R.; Götz, A. W.; Morales, M. A.; Bajaj, P.; Paesani, F. On the Representation of Many-Body Interactions in Water. *J. Chem. Phys.* **2015**, *143*, 104102.

(83) Cisneros, G. A.; Wikfeldt, K. T.; Ojamäe, L.; Lu, J.; Xu, Y.; Torabifard, H.; Bartók, A. P.; Csányi, G.; Molinero, V.; Paesani, F. Modeling Molecular Interactions in Water: From Pairwise to Many-Body Potential Energy Functions. *Chem. Rev.* **2016**, *116*, 7501–7528.

(84) Demerdash, O.; Head-Gordon, T. Convergence of the Many-Body Expansion for Energy and Forces for Classical Polarizable Models in the Condensed Phase. *J. Chem. Theory Comput.* **2016**, *12*, 3884–3893.

(85) Lao, K. U.; Liu, K.-Y.; Richard, R. M.; Herbert, J. M. Understanding the Many-Body Expansion for Large Systems. II. Accuracy Considerations. *J. Chem. Phys.* **2016**, *144*, 164105.

(86) Liu, J.; Herbert, J. M. Pair–Pair Approximation to the Generalized Many-Body Expansion: An Alternative to the Four-Body Expansion for Ab Initio Prediction of Protein Energetics Via Molecular Fragmentation. *J. Chem. Theory Comput.* **2016**, *12*, 572–584.

(87) Fedorov, D. G.; Kitaura, K. Many-Body Expansion of the Fock Matrix in the Fragment Molecular Orbital Method. *J. Chem. Phys.* **2017**, *147*, 104106.

(88) Lan, T. N.; Zgid, D. Generalized Self-Energy Embedding Theory. *J. Phys. Chem. Lett.* **2017**, *8*, 2200–2205.

(89) Liu, K.-Y.; Herbert, J. M. Understanding the Many-Body Expansion for Large Systems. III. Critical Role of Four-Body Terms, Counterpoise Corrections, and Cutoffs. *J. Chem. Phys.* **2017**, *147*, 161729.

(90) Yao, K.; Herr, J. E.; Parkhill, J. The Many-Body Expansion Combined with Neural Networks. *J. Chem. Phys.* **2017**, *146*, 014106.

(91) Herbert, J. M. Fantasy Versus Reality in Fragment-Based Quantum Chemistry. *J. Chem. Phys.* **2019**, *151*, 170901.

(92) Liu, K.-Y.; Herbert, J. M. Energy-Screened Many-Body Expansion: A Practical yet Accurate Fragmentation Method for Quantum Chemistry. *J. Chem. Theory Comput.* **2019**, *16*, 475–487.

(93) Liu, J.; Rana, B.; Liu, K.-Y.; Herbert, J. M. Variational Formulation of the Generalized Many-Body Expansion with Self-Consistent Charge Embedding: Simple and Correct Analytic Energy Gradient for Fragment-Based *Ab Initio* Molecular Dynamics. *J. Phys. Chem. Lett.* **2019**, *10*, 3877–3886.

(94) Peyton, B. G.; Crawford, T. D. Basis Set Superposition Errors in the Many-Body Expansion of Molecular Properties. *J. Phys. Chem. A* **2019**, *123*, 4500–4511.

(95) Veccham, S. P.; Lee, J.; Head-Gordon, M. Making Many-Body Interactions Nearly Pairwise Additive: The Polarized Many-Body Expansion Approach. *J. Chem. Phys.* **2019**, *151*, 194101.

(96) Heindel, J. P.; Xantheas, S. S. The Many-Body Expansion for Aqueous Systems Revisited: I. Water–Water Interactions. *J. Chem. Theory Comput.* **2020**, *16*, 6843–6855.

(97) Ballesteros, F.; Lao, K. U. Accelerating the Convergence of Self-Consistent Field Calculations Using the Many-Body Expansion. *J. Chem. Theory Comput.* **2021**, *18*, 179–191.

(98) Heindel, J. P.; Xantheas, S. S. Molecular Dynamics Driven by the Many-Body Expansion (MBE-MD). *J. Chem. Theory Comput.* **2021**, *17*, 7341–7352.

(99) Heindel, J. P.; Xantheas, S. S. The Many-Body Expansion for Aqueous Systems Revisited: II. Alkali Metal and Halide Ion–Water Interactions. *J. Chem. Theory Comput.* **2021**, *17*, 2200–2216.

(100) Herman, K. M.; Heindel, J. P.; Xantheas, S. S. The Many-Body Expansion for Aqueous Systems Revisited: III. Hofmeister Ion–Water Interactions. *Phys. Chem. Chem. Phys.* **2021**, *23*, 11196–11210.

(101) Paz, A. S. P.; Glover, W. J. Diabatic Many-Body Expansion: Development and Application to Charge-Transfer Reactions. *J. Chem. Theory Comput.* **2021**, *17*, 1497–1511.

(102) Schmitt-Monreal, D.; Jacob, C. R. Density-Based Many-Body Expansion As an Efficient and Accurate Quantum-Chemical Fragmentation Method: Application to Water Clusters. *J. Chem. Theory Comput.* **2021**, *17*, 4144–4156.

(103) Mato, J.; Tzeli, D.; Xantheas, S. S. The Many-Body Expansion for Metals. I. The Alkaline Earth Metals Be, Mg, and Ca. *J. Chem. Phys.* **2022**, *157*, 084313.

(104) Broderick, D. R.; Herbert, J. M. Scalable Generalized Screening for High-Order Terms in the Many-Body Expansion: Algorithm, Open-Source Implementation, and Demonstration. *J. Chem. Phys.* **2023**, *159*, 174801.

(105) Focke, K.; Jacob, C. R. Coupled-Cluster Density-Based Many-Body Expansion. *J. Phys. Chem. A* **2023**, *127*, 9139–9148.

(106) Herman, K. M.; Xantheas, S. S. A Formulation of the Many-Body Expansion (MBE) for Periodic Systems: Application to Several Ice Phases. *J. Phys. Chem. Lett.* **2023**, *14*, 989–999.

(107) Moore, G. E. Cramming More Components onto Integrated Circuits. *Electronics* **1965**, *38*, 1–4.

(108) Moore, G. E. In *International Electron Devices Meeting Technical Digest*, Institute of Electrical and Electronics Engineers (IEEE): Washington, D.C., 1975, pp 11–13.

(109) Leiserson, C. E.; Thompson, N. C.; Emer, J. S.; Kuszmaul, B. C.; Lampson, B. W.; Sanchez, D.; Schardl, T. B. There's Plenty of Room at the Top: What Will Drive Computer Performance After Moore's Law? *Science* **2020**, *368*, 1079.

(110) Greiner, J.; Eriksen, J. J. PyMBE: A Many-Body Expanded Correlation Code, See: `https://gitlab.com/januseriksen/pymbe`.

(111) Mata, R. A.; Stoll, H. An Incremental Correlation Approach to Excited State Energies Based on Natural Transition/Localized Orbitals. *J. Chem. Phys.* **2011**, *134*, 034122.

(112) Eriksen, J. J.; Gauss, J. Ground and Excited State First-Order Properties in Many-Body Expanded Full Configuration Interaction Theory. *J. Chem. Phys.* **2020**, *153*, 154107.

(113) Zimmerman, P. M.; Rask, A. E. Evaluation of Full Valence Correlation Energies and Gradients. *J. Chem. Phys.* **2019**, *150*, 244117.

(114) Dang, D.-K.; Zimmerman, P. M. Fully Variational Incremental CASSCF. *J. Chem. Phys.* **2021**, *154*, 014105.

(115) Veryazov, V.; Malmqvist, P. Å.; Roos, B. O. How to Select Active Space for Multiconfigurational Quantum Chemistry? *Int. J. Quantum Chem.* **2011**, *111*, 3329–3338.

(116) Keller, S.; Boguslawski, K.; Janowski, T.; Reiher, M.; Pulay, P. Selection of Active Spaces for Multiconfigurational Wavefunctions. *J. Chem. Phys.* **2015**, *142*, 244104.

(117) Shriver, D.; Atkins, P., *Inorganic Chemistry*; W. H. Freeman: 2010.

(118) Flyvbjerg, H.; Petersen, H. G. Error Estimates on Averages of Correlated Data. *J. Chem. Phys.* **1989**, *91*, 461–466.

(119) Olivares-Amaya, R.; Hu, W.; Nakatani, N.; Sharma, S.; Yang, J.; Chan, G. K.-L. The *Ab-Initio* Density Matrix Renormalization Group in Practice. *J. Chem. Phys.* **2015**, *142*, 034102.

(120) Li, J.; Otten, M.; Holmes, A. A.; Sharma, S.; Umrigar, C. J. Fast Semistochastic Heat-Bath Configuration Interaction. *J. Chem. Phys.* **2018**, *149*, 214110.

(121) Tubman, N. M.; Levine, D. S.; Hait, D.; Head-Gordon, M.; Whaley, K. B. An Efficient Deterministic Perturbation Theory for Selected Configuration Interaction Methods. **2018**, DOI: 10.48550/ARXIV.1808.02049.

(122) Tubman, N. M.; Freeman, C. D.; Levine, D. S.; Hait, D.; Head-Gordon, M.; Whaley, K. B. Modern Approaches to Exact Diagonalization and Selected Configuration Interaction with the Adaptive Sampling CI Method. *J. Chem. Theory Comput.* **2020**, *16*, 2139–2159.

(123) Zhang, N.; Liu, W.; Hoffmann, M. R. Iterative Configuration Interaction with Selection. *J. Chem. Theory Comput.* **2020**, *16*, 2296–2316.

(124) Goertzel, G. *Quota Sampling and Importance Functions in Stochastic Solution of Particle Problems*; tech. rep. ORNL-434; Oak Ridge National Laboratory, 1949.

(125) Kahn, H.; Harris, T. E. In *Monte Carlo Method*, ed. by Householder, A. S., National Bureau of Standards: 1951, pp 27–30.

(126) Pitzer, R. M. Electron Repulsion Integrals and Symmetry Adapted Charge Distributions. *J. Chem. Phys.* **1973**, *59*, 3308–3312.

(127) Davidson, E. R. The Iterative Calculation of a Few of the Lowest Eigenvalues and Corresponding Eigenvectors of Large Real-Symmetric Matrices. *J. Comput. Phys.* **1975**, *17*, 87–94.

(128) Dupuis, M.; King, H. F. Molecular Symmetry and Closed-Shell SCF Calculations. I. *Int. J. Quantum Chem.* **1977**, *11*, 613–625.

(129) Takada, T.; Dupuis, M.; King, H. F. Molecular Symmetry. IV. The Coupled Perturbed Hartree–Fock Method. *J. Comput. Chem.* **1983**, *4*, 234–240.

(130) Taylor, P. R. Symmetrization of Operator Matrix Elements. *Int. J. Quantum Chem.* **1985**, *27*, 89–96.

(131) Taylor, P. R. Symmetry-Adapted Integral Derivatives. *Theor. Chim. Acta* **1986**, *69*, 447–460.

(132) Čársky, P.; Schaad, L. J.; Hess, B. A.; Urban, M.; Noga, J. Use of Molecular Symmetry in Coupled-Cluster Theory. *J. Chem. Phys.* **1987**, *87*, 411–415.

(133) Häser, M.; Almlöf, J.; Feyereisen, M. W. Exploiting Non-Abelian Point Group Symmetry in Direct Two-Electron Integral Transformations. *Theor. Chim. Acta* **1991**, *79*, 115–122.

(134) Stanton, J. F.; Gauss, J.; Watts, J. D.; Bartlett, R. J. A Direct Product Decomposition Approach for Symmetry Exploitation in Many-Body Methods. I. Energy Calculations. *J. Chem. Phys.* **1991**, *94*, 4334–4345.

(135) Eriksen, J. J. et al. The Ground State Electronic Energy of Benzene. *J. Phys. Chem. Lett.* **2020**, *11*, 8922–8929.

(136) Bauschlicher, C. W.; Langhoff, S. R. Quantum Mechanical Calculations to Chemical Accuracy. *Science* **1991**, *254*, 394–398.

(137) Lee, T. J.; Scuseria, G. E., Achieving Chemical Accuracy with Coupled-Cluster Theory In *Quantum Mechanical Electronic Structure Calculations with Chemical Accuracy*, Langhoff, S., Ed.; Understanding Chemical Reactivity; Springer Netherlands: Dordrecht, 1995, pp 47–108.

(138) Helgaker, T.; Ruden, T. A.; Jørgensen, P.; Olsen, J.; Klopper, W. *A Priori* Calculation of Molecular Properties to Chemical Accuracy. *J. Phys. Org. Chem.* **2004**, *17*, 913–933.

(139) Feller, D.; Peterson, K. A. Probing the Limits of Accuracy in Electronic Structure Calculations: Is Theory Capable of Results Uniformly Better Than "Chemical Accuracy"? *J. Chem. Phys.* **2007**, *126*, 114105.

(140) Peterson, K. A.; Feller, D.; Dixon, D. A. Chemical Accuracy in Ab Initio Thermochemistry and Spectroscopy: Current Strategies and Future Challenges. *Theor. Chem. Acc.* **2012**, *131*, 1079.

(141) Bauschlicher, C. W.; Taylor, P. R. Benchmark Full Configuration-Interaction Calculations on H_2O, F, and F^-. *J. Chem. Phys.* **1986**, *85*, 2779–2783.

(142) Bauschlicher, C. W.; Langhoff, S. R.; Taylor, P. R.; Handy, N. C.; Knowles, P. J. Benchmark Full Configuration-Interaction Calculations on HF and NH_2. *J. Chem. Phys.* **1986**, *85*, 1469–1474.

(143) Bauschlicher, C. W.; Taylor, P. R. Full CI Benchmark Calculations for Molecular Properties. *Theor. Chim. Acta* **1987**, *71*, 263–276.

(144) Bauschlicher, C. W.; Langhoff, S. R. Full Configuration-Interaction Study of the Ionic–Neutral Curve Crossing in LiF. *J. Chem. Phys.* **1988**, *89*, 4246–4254.

(145) Bauschlicher, C. W.; Langhoff, S. R. Full Configuration-Interaction Benchmark Calculations for AlH. *J. Chem. Phys.* **1988**, *89*, 2116–2125.

(146) Bauschlicher, C. W. Full Configuration Interaction Benchmark Calculations for Titanium Monohydride. *J. Phys. Chem* **1988**, *92*, 3020–3023.

(147) Knowles, P. J.; Stark, K.; Werner, H.-J. A Full-CI Study of the Energetics of the Reaction F+H_2 $\rightarrow$ HF+H. *Chem. Phys. Lett.* **1991**, *185*, 555–561.

(148) Koch, H.; Harrison, R. J. Analytical Calculation of Full Configuration Interaction Response Properties: Application to Be. *J. Chem. Phys.* **1991**, *95*, 7479–7485.

(149) Evangelisti, S.; Bendazzoli, G. L.; Gagliardi, L. Full Configuration Interaction Calculations on Be_2. *Chem. Phys.* **1994**, *185*, 47–56.

(150) Van Mourik, T.; van Lenthe, J. H. Benchmark Full Configuration Interaction Calculations on the Helium Dimer. *J. Chem. Phys.* **1995**, *102*, 7479–7483.

(151) Olsen, J.; Jørgensen, P.; Koch, H.; Balkova, A.; Bartlett, R. J. Full Configuration–Interaction and State of the Art Correlation Calculations on Water in a Valence Double-Zeta Basis with Polarization Functions. *J. Chem. Phys.* **1996**, *104*, 8007–8015.

(152) Christiansen, O.; Koch, H.; Jørgensen, P.; Olsen, J. Excitation Energies of H_2O, N_2 and C_2 in Full Configuration Interaction and Coupled Cluster Theory. *Chem. Phys. Lett.* **1996**, *256*, 185–194.

(153) Sherrill, C. D.; Leininger, M. L.; Van Huis, T. J.; Schaefer, H. F. Structures and Vibrational Frequencies in the Full Configuration Interaction Limit: Predictions for Four Electronic States of Methylene Using a Triple-Zeta Plus Double Polarization (TZ2P) Basis. *J. Chem. Phys.* **1998**, *108*, 1040–1049.

(154) Larsen, H.; Olsen, J.; Hättig, C.; Jørgensen, P.; Christiansen, O.; Gauss, J. Polarizabilities and First Hyperpolarizabilities of HF, Ne, and BH from Full Configuration Interaction and Coupled Cluster Calculations. *J. Chem. Phys.* **1999**, *111*, 1917–1925.

(155) Halkier, A.; Larsen, H.; Olsen, J.; Jørgensen, P.; Gauss, J. Full Configuration Interaction Benchmark Calculations of First-Order One-Electron Properties of BH and HF. *J. Chem. Phys.* **1999**, *110*, 734–740.

(156) Rossi, E.; Bendazzoli, G. L.; Evangelisti, S.; Maynau, D. A Full-Configuration Benchmark for the N_2 Molecule. *Chem. Phys. Lett.* **1999**, *310*, 530–536.

(157) Braskén, M.; Lindberg, M.; Sundholm, D.; Olsen, J. Full Configuration Interaction Calculations of Electron-Hole Correlation Effects in Strain-Induced Quantum Dots. *Phys. Rev. B* **2000**, *61*, 7652–7655.

(158) Larsen, H.; Olsen, J.; Jørgensen, P.; Christiansen, O. Full Configuration Interaction Benchmarking of Coupled-Cluster Models for the Lowest Singlet Energy Surfaces of N_2. *J. Chem. Phys.* **2000**, *113*, 6677–6686.

(159) Larsen, H.; Hald, K.; Olsen, J.; Jørgensen, P. Triplet Excitation Energies in Full Configuration Interaction and Coupled-Cluster Theory. *J. Chem. Phys.* **2001**, *115*, 3015–3020.

(160) Braskén, M.; Corni, S.; Lindberg, M.; Olsen, J.; Sundholm, D. Full Configuration Interaction Studies of Phonon and Photon Transition Rates in Semiconductor Quantum Dots. *Mol. Phys.* **2002**, *100*, 911–918.

(161) Abrams, M. L.; Sherrill, C. D. A Comparison of Polarized Double-Zeta Basis Sets and Natural Orbitals for Full Configuration Interaction Benchmarks. *J. Chem. Phys.* **2003**, *118*, 1604–1609.

(162) Auer, A. A.; Gauss, J.; Pecul, M. Full Configuration-Interaction and Coupled-Cluster Calculations of the Indirect Spin–Spin Coupling Constant of BH. *Chem. Phys. Lett.* **2003**, *368*, 172–176.

(163) Dutta, A.; Sherrill, C. D. Full Configuration Interaction Potential Energy Curves for Breaking Bonds to Hydrogen: An Assessment of Single-Reference Correlation Methods. *J. Chem. Phys.* **2003**, *118*, 1610–1619.

(164) Abrams, M. L.; Sherrill, C. D. Full Configuration Interaction Potential Energy Curves for the X $^1\Sigma_g^+$, B $^1\Delta_g$, and B' $^1\Sigma_g^+$ States of C_2: A Challenge for Approximate Methods. *J. Chem. Phys.* **2004**, *121*, 9211–9219.

(165) Thøgersen, L.; Olsen, J. A Coupled Cluster and Full Configuration Interaction Study of CN and CN^-. *Chem. Phys. Lett.* **2004**, *393*, 36–43.

(166) Junquera-Hernández, J. M.; Sánchez-Marín, J.; Bendazzoli, G. L.; Evangelisti, S. Full Configuration Interaction Calculation of Be_3. *J. Chem. Phys.* **2004**, *120*, 8405–8411.

(167) Sherrill, C. D.; Piecuch, P. The $X^1\Sigma_g$,$B^1\Delta_g$, and $B'^1\Sigma_g$ States of C_2: A Comparison of Renormalized Coupled-Cluster and Multireference Methods with Full Configuration Interaction Benchmarks. *J. Chem. Phys.* **2005**, *122*, 124104.

(168) Gan, Z.; Grant, D. J.; Harrison, R. J.; Dixon, D. A. The Lowest Energy States of the Group-IIIA–Group-VA Heteronuclear Diatomics: BN, BP, AlN, and AlP from Full Configuration Interaction Calculations. *J. Chem. Phys.* **2006**, *125*, 124311.

(169) Pitarch-Ruiz, J.; Sánchez-Marín, J.; Velasco, A. M. Full Configuration Interaction Calculation of the Low Lying Valence and Rydberg States of BeH. *J. Comput. Chem.* **2007**, *29*, 523–532.

(170) Pieniazek, P. A.; Arnstein, S. A.; Bradforth, S. E.; Krylov, A. I.; Sherrill, C. D. Benchmark Full Configuration Interaction and Equation-Of-Motion Coupled-Cluster Model with Single and Double Substitutions for Ionized Systems Results for Prototypical Charge Transfer Systems: Noncovalent Ionized Dimers. *J. Chem. Phys.* **2007**, *127*, 164110.

(171) Pitarch-Ruiz, J.; Sánchez-Marin, J.; Velasco, A. M.; Martin, I. Full Configuration Interaction Calculation of BeH Adiabatic States. *J. Chem. Phys.* **2008**, *129*, 054310.

(172) Vetere, V.; Monari, A.; Bendazzoli, G. L.; Evangelisti, S.; Paulus, B. Full Configuration Interaction Study of the Metal-Insulator Transition in Model Systems: Li_N Linear Chains ($N = 2, 4, 6, 8$). *J. Chem. Phys.* **2008**, *128*, 024701.

(173) Ramachandran, C.; De Fazio, D.; Cavalli, S.; Tarantelli, F.; Aquilanti, V. Revisiting the Potential Energy Surface for the He + $H_2^+ \rightarrow HeH^+$ + H Reaction at the Full Configuration Interaction Level. *Chem. Phys. Lett.* **2009**, *469*, 26–30.

(174) Li, H.; Feng, H.; Sun, W.; Zhang, Y.; Fan, Q.; Peterson, K. A.; Xie, Y.; Schaefer, H. F. The Alkaline Earth Dimer Cations (Be_2^+, Mg_2^+, Ca_2^+, Sr_2^+, and Ba_2^+). Coupled Cluster and Full Configuration Interaction Studies. *Mol. Phys.* **2013**, *111*, 2292–2298.

(175) Tajti, A.; Szalay, P. G.; Császár, A. G.; Kállay, M.; Gauss, J.; Valeev, E. F.; Flowers, B. A.; Vázquez, J.; Stanton, J. F. HEAT: High Accuracy Extrapolated *Ab Initio* Thermochemistry. *J. Chem. Phys.* **2004**, *121*, 11599–11613.

(176) Feller, D.; Peterson, K. A.; Dixon, D. A. A Survey of Factors Contributing to Accurate Theoretical Predictions of Atomization Energies and Molecular Structures. *J. Chem. Phys.* **2008**, *129*, 204105.

(177) Helgaker, T.; Klopper, W.; Tew, D. P. Quantitative Quantum Chemistry. *Mol. Phys.* **2008**, *106*, 2107–2143.

(178) Curtiss, L. A.; Redfern, P. C.; Raghavachari, K. G*n* Theory. *Wiley Interdiscip. Rev.: Comput. Mol. Sci.* **2011**, *1*, 810–825.

(179) Karton, A.; Daon, S.; Martin, J. M. W4-11: A High-Confidence Benchmark Dataset for Computational Thermochemistry Derived from First-Principles W4 Data. *Chem. Phys. Lett.* **2011**, *510*, 165–178.

(180) Schrödinger, E. An Undulatory Theory of the Mechanics of Atoms and Molecules. *Phys. Rev.* **1926**, *28*, 1049–1070.

(181) Heitler, W.; London, F. Wechselwirkung Neutraler Atome und Homopolare Bindung nach der Quantenmechanik. *Z. für Phys.* **1927**, *44*, 455–472.

(182) Born, M.; Oppenheimer, R. Zur Quantentheorie der Molekeln. *Ann. Phys.* **1927**, *389*, 457–484.

(183) Griffiths, D. J.; Schroeter, D. F., *Introduction to Quantum Mechanics*; Cambridge University Press: Upper Saddle River, 2018.

(184) Fock, V. Näherungsmethode zur Lösung des Quantenmechanischen Mehrkörperproblems. *Z. für Phys.* **1930**, *61*, 126–148.

(185) Slater, J. C. Note on Hartree's Method. *Phys. Rev.* **1930**, *35*, 210–211.

(186) Slater, J. C. The Theory of Complex Spectra. *Phys. Rev.* **1929**, *34*, 1293–1322.

(187) Craig, D. P. Configurational Interaction in Molecular Orbital Theory. A Higher Approximation in the Non-Empirical Method. *Proc. R. Soc. A* **1950**, *200*, 474–486.

(188) Olsen, J.; Jørgensen, P.; Simons, J. Passing the One-Billion Limit in Full Configuration-Interaction (FCI) Calculations. *Chem. Phys. Lett.* **1990**, *169*, 463–472.

(189) Condon, E. U. The Theory of Complex Spectra. *Phys. Rev.* **1930**, *36*, 1121–1133.

(190) Roos, B. A New Method for Large-Scale Cl Calculations. *Chem. Phys. Lett.* **1972**, *15*, 153–159.

(191) Olsen, J.; Roos, B. O.; Jørgensen, P.; Jensen, H. J. Aa. Determinant Based Configuration Interaction Algorithms for Complete and Restricted Configuration Interaction Spaces. *J. Chem. Phys.* **1988**, *89*, 2185–2192.

(192) Vogiatzis, K. D.; Ma, D.; Olsen, J.; Gagliardi, L.; de Jong, W. A. Pushing Configuration-Interaction to the Limit: Towards Massively Parallel MCSCF Calculations. *J. Chem. Phys.* **2017**, *147*, 184111.

(193) Gao, H.; Imamura, S.; Kasagi, A.; Yoshida, E. Distributed Implementation of Full Configuration Interaction for One Trillion Determinants. *J. Chem. Theory Comput.* **2024**, *20*, 1185–1192.

(194) Hartree, D. R.; Hartree, W. Self-Consistent Field, with Exchange, for Beryllium. *Proc. R. Soc. Lond. A* **1935**, *150*, 9–33.

(195) Slater, J. C. The Self Consistent Field and the Structure of Atoms. *Phys. Rev.* **1928**, *32*, 339–348.

(196) Gaunt, J. A. A Theory of Hartree's Atomic Fields. *Math. Proc. Cambridge Philos. Soc.* **1928**, *24*, 328–342.

(197) Roothaan, C. C. J. New Developments in Molecular Orbital Theory. *Rev. Mod. Phys* **1951**, *23*, 69–89.

(198) Lennard-Jones, J. E. The Electronic Structure of Some Diatomic Molecules. *Trans. Faraday Soc.* **1929**, *25*, 668.

(199) Mulliken, R. S. Electronic Structures of Polyatomic Molecules and Valence VI. On the Method of Molecular Orbitals. *J. Chem. Phys.* **1935**, *3*, 375–378.

(200) Hall, G. G. The Molecular Orbital Theory of Chemical Valency VIII. A Method of Calculating Ionization Potentials. *Proc. R. Soc. Lond. A* **1951**, *205*, 541–552.

(201) Brillouin, L. Les Problèmes de Perturbations et les Champs Self-Consistents. *J. Phys. Radium* **1932**, *3*, 373–389.

(202) Brillouin, L. Le Champ Self-Consistent de Fock pour les Électrons des Métaux. *J. Phys. Radium* **1934**, *5*, 413–418.

(203) Roothaan, C. C. J. Self-Consistent Field Theory for Open Shells of Electronic Systems. *Rev. Mod. Phys* **1960**, *32*, 179–185.

(204) Pople, J. A.; Nesbet, R. K. Self-Consistent Orbitals for Radicals. *J. Chem. Phys.* **1954**, *22*, 571–572.

(205) Pratt, G. W. Unrestricted Hartree-Fock Method. *Phys. Rev.* **1956**, *102*, 1303–1307.

(206) Löwdin, P.-O. Quantum Theory of Many-Particle Systems. III. Extension of the Hartree-Fock Scheme to Include Degenerate Systems and Correlation Effects. *Phys. Rev.* **1955**, *97*, 1509–1520.

(207) Hollett, J. W.; Gill, P. M. W. The Two Faces of Static Correlation. *J. Chem. Phys.* **2011**, *134*, 114111.

(208) Coester, F.; Kümmel, H. Short-Range Correlations in Nuclear Wave Functions. *Nucl. Phys.* **1960**, *17*, 477–485.

(209) Čížek, J. On the Correlation Problem in Atomic and Molecular Systems. Calculation of Wavefunction Components in Ursell-Type Expansion Using Quantum-Field Theoretical Methods. *J. Chem. Phys.* **1966**, *45*, 4256–4266.

(210) Crawford, T. D.; Schaefer, H. F., An Introduction to Coupled Cluster Theory for Computational Chemists In *Reviews in Computational Chemistry*, Kenny B. Lipkowitz, D. B. B., Ed.; Reviews in Computational Chemistry, Vol. 14; Wiley: New York, 2000; Chapter 2, pp 33–136.

(211) Campbell, J. E. On a Law of Combination of Operators Bearing on the Theory of Continuous Transformation Groups. *Proc. London Math. Soc.* **1896**, *s1-28*, 381–390.

(212) Baker, H. F. Alternants and Continuous Groups. *Proc. London Math. Soc.* **1905**, *s2-3*, 24–47.

(213) Hausdorff, F. Die Symbolische Exponentialformel in der Gruppentheorie. *Ber. Verh. Kgl. Sächs. Ges. Wiss. Leipzig., Math.-Phys. Kl.* **1906**, *58*, 19–48.

(214) Purvis, G. D.; Bartlett, R. J. A Full Coupled-Cluster Singles and Doubles Model: The Inclusion of Disconnected Triples. *J. Chem. Phys.* **1982**, *76*, 1910–1918.

(215) Noga, J.; Bartlett, R. J.; Urban, M. Towards a Full CCSDT Model for Electron Correlation. CCSDT-*n* Models. *Chem. Phys. Lett.* **1987**, *134*, 126–132.

(216) Noga, J.; Bartlett, R. J. Erratum: The full CCSDT model for molecular electronic structure [J. Chem. Phys. 8 6, 7041 (1987)]. *J. Chem. Phys.* **1988**, *89*, 3401–3401.

(217) Scuseria, G. E.; Schaefer, H. F. A New Implementation of the Full CCSDT Model for Molecular Electronic Structure. *Chem. Phys. Lett.* **1988**, *152*, 382–386.

(218) Oliphant, N.; Adamowicz, L. Coupled-Cluster Method Truncated at Quadruples. *J. Chem. Phys.* **1991**, *95*, 6645–6651.

(219) Kucharski, S. A.; Bartlett, R. J. Recursive Intermediate Factorization and Complete Computational Linearization of the Coupled-Cluster Single, Double, Triple, and Quadruple Excitation Equations. *Theor. Chim. Acta* **1991**, *80*, 387–405.

(220) Raghavachari, K.; Trucks, G. W.; Pople, J. A.; Head-Gordon, M. A Fifth-Order Perturbation Comparison of Electron Correlation Theories. *Chem. Phys. Lett.* **1989**, *157*, 479–483.

(221) Bartlett, R. J.; Watts, J.; Kucharski, S.; Noga, J. Non-Iterative Fifth-Order Triple and Quadruple Excitation Energy Corrections in Correlated Methods. *Chem. Phys. Lett.* **1990**, *165*, 513–522.

(222) Bomble, Y. J.; Stanton, J. F.; Kállay, M.; Gauss, J. Coupled-Cluster Methods Including Noniterative Corrections for Quadruple Excitations. *J. Chem. Phys.* **2005**, *123*, 054101.

(223) Lyakh, D. I.; Musiał, M.; Lotrich, V. F.; Bartlett, R. J. Multireference Nature of Chemistry: The Coupled-Cluster View. *Chem. Rev.* **2011**, *112*, 182–243.

(224) Roos, B. O.; Taylor, P. R.; Siegbahn, P. E. M. A Complete Active Space SCF Method (CASSCF) Using a Density Matrix Formulated Super-CI Approach. *Chem. Phys.* **1980**, *48*, 157–173.

(225) Levine, B. G.; Durden, A. S.; Esch, M. P.; Liang, F.; Shu, Y. CAS without SCF—Why to Use CASCI and Where to Get the Orbitals. *J. Chem. Phys.* **2021**, *154*, 090902.

(226) Levy, B. Molecular MC–SCF Calculations. *Int. J. Quantum Chem.* **1970**, *4*, 297–313.

(227) Jensen, H. J. Aa.; Jørgensen, P. A Direct Approach to Second-Order MCSCF Calculations Using a Norm Extended Optimization Scheme. *J. Chem. Phys.* **1984**, *80*, 1204–1214.

(228) Grein, F.; Chang, T. Multiconfiguration Wavefunctions Obtained by Application of the Generalized Brillouin Theorem. *Chem. Phys. Lett.* **1971**, *12*, 44–48.

(229) Grein, F.; Banerjee, A. Variational Wavefunctions for Low-Lying Excited States. *Chem. Phys. Lett.* **1975**, *31*, 281–285.

(230) Grein, F.; Banerjee, A. A Multiconfiguration Method for Excited States of Atoms and Molecules. *Int. J. Quantum Chem.* **1975**, *9*, 147–154.

(231) Banerjee, A.; Grein, F. Convergence Behavior of Some Multiconfiguration Methods. *Int. J. Quantum Chem.* **1976**, *10*, 123–134.

(232) Ruedenberg, K.; Cheung, L. M.; Elbert, S. T. MCSCF Optimization through Combined Use of Natural Orbitals and the Brillouin–Levy–Berthier Theorem. *Int. J. Quantum Chem.* **1979**, *16*, 1069–1101.

(233) Roos, B. O. The Complete Active Space SCF Method in a Fock-Matrix-Based Super-CI Formulation. *Int. J. Quantum Chem.* **1980**, *18*, 175–189.

(234) Meier, U.; Staemmler, V. An Efficient First-Order CASSCF Method Based on the Renormalized Fock-Operator Technique. *Theor. Chim. Acta* **1989**, *76*, 95–111.

(235) Malmqvist, P. A.; Rendell, A.; Roos, B. O. The Restricted Active Space Self-Consistent-Field Method, Implemented with a Split Graph Unitary Group Approach. *J. Phys. Chem* **1990**, *94*, 5477–5482.

(236) Chaban, G.; Schmidt, M. W.; Gordon, M. S. Approximate Second Order Method for Orbital Optimization of SCF and MCSCF Wavefunctions. *Theor. Chem. Acc.* **1997**, *97*, 88–95.

(237) Angeli, C.; Evangelisti, S.; Cimiraglia, R.; Maynau, D. A Novel Perturbation-Based Complete Active Space–Self-Consistent-Field Algorithm: Application to the Direct Calculation of Localized Orbitals. *J. Chem. Phys.* **2002**, *117*, 10525–10533.

(238) Bates, J. E.; Shiozaki, T. Fully Relativistic Complete Active Space Self-Consistent Field for Large Molecules: Quasi-Second-Order Minimax Optimization. *J. Chem. Phys.* **2015**, *142*, 044112.

(239) Hohenstein, E. G.; Luehr, N.; Ufimtsev, I. S.; Martínez, T. J. An Atomic Orbital-Based Formulation of the Complete Active Space Self-Consistent Field Method on Graphical Processing Units. *J. Chem. Phys.* **2015**, *142*, 224103.

(240) Reynolds, R. D.; Yanai, T.; Shiozaki, T. Large-Scale Relativistic Complete Active Space Self-Consistent Field with Robust Convergence. *J. Chem. Phys.* **2018**, *149*, 014106.

(241) Kollmar, C.; Sivalingam, K.; Helmich-Paris, B.; Angeli, C.; Neese, F. A Perturbation-Based Super-CI Approach for the Orbital Optimization of a CASSCF Wave Function. *J. Comput. Chem.* **2019**, *40*, 1463–1470.

(242) Kreplin, D. A.; Knowles, P. J.; Werner, H.-J. MCSCF Optimization Revisited. II. Combined First- and Second-Order Orbital Optimization for Large Molecules. *J. Chem. Phys.* **2020**, *152*, 074102.

(243) Siegbahn, P. E. M.; Almlöf, J.; Heiberg, A.; Roos, B. O. The Complete Active Space SCF (CASSCF) Method in a Newton–Raphson Formulation with Application to the HNO Molecule. *J. Chem. Phys.* **1981**, *74*, 2384–2396.

(244) Liu, D. C.; Nocedal, J. On the Limited Memory BFGS Method for Large Scale Optimization. *Math. Program.* **1989**, *45*, 503–528.

(245) Fischer, T. H.; Almlöf, J. General Methods for Geometry and Wave Function Optimization. *J. Phys. Chem* **1992**, *96*, 9768–9774.

(246) Dalgaard, E.; Jørgensen, P. Optimization of Orbitals for Multiconfigurational Reference States. *J. Chem. Phys.* **1978**, *69*, 3833–3844.

(247) Dalgaard, E. A Quadratically Convergent Reference State Optimization Procedure. *Chem. Phys. Lett.* **1979**, *65*, 559–563.

(248) Jørgensen, P.; Albertsen, P.; Yeager, D. L. A Method to Reduce the Number of Two Electron Integral Transformations in a Second Order Multiconfigurational Hartree–Fock Procedure. *J. Chem. Phys.* **1980**, *72*, 6466–6473.

(249) Lengsfield, B. H. General Second Order MCSCF Theory: A Density Matrix Directed Algorithm. *J. Chem. Phys.* **1980**, *73*, 382–390.

(250) Shepard, R.; Simons, J. Multiconfigurational Wavefunction Optimization Using the Unitary Group Method. *Int. J. Quantum Chem.* **1980**, *18*, 211–228.

(251) Werner, H.-J.; Meyer, W. A Quadratically Convergent Multiconfiguration–Self-Consistent Field Method with Simultaneous Optimization of Orbitals and CI Coefficients. *J. Chem. Phys.* **1980**, *73*, 2342–2356.

(252) Yeager, D. L.; Albertsen, P.; Jørgensen, P. Mode Damping in Multiconfigurational Hartree–Fock Procedures. *J. Chem. Phys.* **1980**, *73*, 2811–2816.

(253) Yeager, D. L.; Jørgensen, P. A Numerical Study of the Convergency of Second and Approximate Second-Order Multiconfiguration Hartree-Fock Procedures. *Mol. Phys.* **1980**, *39*, 587–596.

(254) Jørgensen, P.; Olsen, J.; Yeager, D. L. Generalizations of Newton–Raphson and Multiplicity Independent Newton–Raphson Approaches in Multiconfigurational Hartree–Fock Theory. *J. Chem. Phys.* **1981**, *75*, 5802–5815.

(255) Lengsfield, B. H.; Liu, B. A Second Order MCSCF Method for Large CI Expansions. *J. Chem. Phys.* **1981**, *75*, 478–480.

(256) Werner, H.-J.; Meyer, W. A Quadratically Convergent MCSCF Method for the Simultaneous Optimization of Several States. *J. Chem. Phys.* **1981**, *74*, 5794–5801.

(257) Igawa, A.; Yeager, D. L.; Fukutome, H. A Method to Include Certain Infinite Order Contributions in a Multiconfigurational Self-Consistent Field (MCSCF) Calculation. *J. Chem. Phys.* **1982**, *76*, 5388–5396.

(258) Olsen, J.; Jørgensen, P.; Yeager, D. L. Multiconfigurational Hartree–Fock Studies of Avoided Curve Crossing Using the Newton–Raphson Technique. *J. Chem. Phys.* **1982**, *76*, 527–542.

(259) Olsen, J.; Jørgensen, P.; Yeager, D. L. Cubic Contributions in Multiconfigurational Self-Consistent-Field (MCSCF) Calculations. *J. Chem. Phys.* **1982**, *77*, 356–370.

(260) Yeager, D. L.; Lynch, D.; Nichols, J.; Jørgensen, P.; Olsen, J. Newton-Raphson Approaches and Generalizations in Multiconfigurational Self-Consistent Field Calculations. *J. Phys. Chem* **1982**, *86*, 2140–2153.

(261) Lengsfield, B. H. General Second-Order MCSCF Theory for Large CI Expansions. *J. Chem. Phys.* **1982**, *77*, 4073–4083.

(262) Jørgensen, P.; Swanstrøm, P.; Yeager, D. L. Guaranteed Convergence in Ground State Multiconfigurational Self-Consistent Field Calculations. *J. Chem. Phys.* **1983**, *78*, 347–356.

(263) Jensen, H. J. Aa.; Ågren, H. MC SCF Optimization Using the Direct, Restricted Step, Second-Order Norm-Extended Optimization Method. *Chem. Phys. Lett.* **1984**, *110*, 140–144.

(264) Knowles, P. J.; Werner, H.-J. An Efficient Second-Order MC SCF Method for Long Configuration Expansions. *Chem. Phys. Lett.* **1985**, *115*, 259–267.

(265) Werner, H.-J.; Knowles, P. J. A Second Order Multiconfiguration SCF Procedure with Optimum Convergence. *J. Chem. Phys.* **1985**, *82*, 5053–5063.

(266) Jensen, H. J. Aa.; Ågren, H. A Direct, Restricted-Step, Second-Order MC SCF Program for Large Scale Ab Initio Calculations. *Chem. Phys.* **1986**, *104*, 229–250.

(267) Jensen, H. J. Aa.; Jørgensen, P.; Ågren, H. Efficient Optimization of Large Scale MCSCF Wave Functions with a Restricted Step Algorithm. *J. Chem. Phys.* **1987**, *87*, 451–466.

(268) Lipparini, F.; Gauss, J. Cost-Effective Treatment of Scalar Relativistic Effects for Multireference Systems: A CASSCF Implementation Based on the Spin-Free Dirac–Coulomb Hamiltonian. *J. Chem. Theory Comput.* **2016**, *12*, 4284–4295.

(269) Ma, Y.; Knecht, S.; Keller, S.; Reiher, M. Second-Order Self-Consistent-Field Density-Matrix Renormalization Group. *J. Chem. Theory Comput.* **2017**, *13*, 2533–2549.

(270) Sun, Q.; Yang, J.; Chan, G. K.-L. A General Second Order Complete Active Space Self-Consistent-Field Solver for Large-Scale Systems. *Chem. Phys. Lett.* **2017**, *683*, 291–299.

(271) Kreplin, D. A.; Knowles, P. J.; Werner, H.-J. Second-Order MCSCF Optimization Revisited. I. Improved Algorithms for Fast and Robust Second-Order CASSCF Convergence. *J. Chem. Phys.* **2019**, *150*, 194106.

(272) Nottoli, T.; Gauss, J.; Lipparini, F. Second-Order CASSCF Algorithm with the Cholesky Decomposition of the Two-Electron Integrals. *J. Chem. Theory Comput.* **2021**, *17*, 6819–6831.

(273) Roos, B. O., The Complete Active Space Self-Consistent Field Method and its Applications in Electronic Structure Calculations In *Advances in Chemical Physics*, Lawley, K. P., Ed.; Wiley: Chichester, 1987; Vol. 69, pp 399–445.

(274) Anglada, J.; Bofill, J. Practical Remarks on the Selection of the Active Space in the CAS-SCF Wavefunction. *Chem. Phys. Lett.* **1995**, *243*, 151–157.

(275) Pierloot, K., Nondynamic Correlation Effects in Transition Metal Coordination Compounds In *Computational Organometallic Chemistry*, Cundari, T. R., Ed., 1st ed.; CRC Press: Boca Raton, 2001, pp 123–158.

(276) Pierloot, K. The CASPT2 Method in Inorganic Electronic Spectroscopy: From Ionic Transition Metal to Covalent Actinide Complexes. *Mol. Phys.* **2003**, *101*, 2083–2094.

(277) Kerridge, A., The Complete-Active-Space Self-Consistent-Field Approach and Its Application to Molecular Complexes of the f-Elements In *Computational Methods in Lanthanide and Actinide Chemistry*, Dolg, M., Ed.; Wiley: Chichester, 2015, pp 121–144.

(278) Ashley, D. C.; Jakubikova, E. Ironing Out the Photochemical and Spin-Crossover Behavior of Fe(II) Coordination Compounds with Computational Chemistry. *Coordin. Chem. Rev.* **2017**, *337*, 97–111.

(279) Pulay, P.; Hamilton, T. P. UHF Natural Orbitals for Defining and Starting MC-SCF Calculations. *J. Chem. Phys.* **1988**, *88*, 4926–4933.

(280) Bofill, J. M.; Pulay, P. The Unrestricted Natural Orbital–Complete Active Space (UNO–CAS) Method: An Inexpensive Alternative to the Complete Active Space–Self-Consistent-Field (CAS–SCF) Method. *J. Chem. Phys.* **1989**, *90*, 3637–3646.

(281) Stein, C. J.; Reiher, M. Automated Selection of Active Orbital Spaces. *J. Chem. Theory Comput.* **2016**, *12*, 1760–1771.

(282) Sayfutyarova, E. R.; Sun, Q.; Chan, G. K.-L.; Knizia, G. Automated Construction of Molecular Active Spaces from Atomic Valence Orbitals. *J. Chem. Theory Comput.* **2017**, *13*, 4063–4078.

(283) Faulstich, F. M.; Máté, M.; Laestadius, A.; Csirik, M. A.; Veis, L.; Antalik, A.; Brabec, J.; Schneider, R.; Pittner, J.; Kvaal, S.; Legeza, Ö. Numerical and Theoretical Aspects of the DMRG-TCC Method Exemplified by the Nitrogen Dimer. *J. Chem. Theory Comput.* **2019**, *15*, 2206–2220.

(284) Sayfutyarova, E. R.; Hammes-Schiffer, S. Constructing Molecular π-Orbital Active Spaces for Multireference Calculations of Conjugated Systems. *J. Chem. Theory Comput.* **2019**, *15*, 1679–1689.

(285) Stein, C. J.; Reiher, M. autoCAS: A Program for Fully Automated Multiconfigurational Calculations. *J. Comput. Chem.* **2019**, *40*, 2216–2226.

(286) King, D. S.; Gagliardi, L. A Ranked-Orbital Approach to Select Active Spaces for High-Throughput Multireference Computation. *J. Chem. Theory Comput.* **2021**, *17*, 2817–2831.

(287) Bensberg, M.; Reiher, M. Corresponding Active Orbital Spaces along Chemical Reaction Paths. *J. Phys. Chem. Lett.* **2023**, *14*, 2112–2118.

(288) Evangelisti, S.; Daudey, J.-P.; Malrieu, J.-P. Convergence of an Improved CIPSI Algorithm. *Chem. Phys.* **1983**, *75*, 91–102.

(289) Cimiraglia, R.; Persico, M. Recent Advances in Multireference Second Order Perturbation CI: The CIPSI Method Revisited. *J. Comput. Chem.* **1987**, *8*, 39–47.

(290) Epstein, P. S. The Stark Effect from the Point of View of Schroedinger's Quantum Theory. *Phys. Rev.* **1926**, *28*, 695–710.

(291) Nesbet, R. K. Configuration Interaction in Orbital Theories. *Proc. R. Soc. A: Math. Phys. Sci.* **1955**, *230*, 312–321.

(292) Murphy, R. B.; Messmer, R. P. Generalized Møller–Plesset and Epstein–Nesbet Perturbation Theory Applied to Multiply Bonded Molecules. *J. Chem. Phys.* **1992**, *97*, 4170–4184.

(293) Sharma, S.; Holmes, A. A.; Jeanmairet, G.; Alavi, A.; Umrigar, C. J. Semistochastic Heat-Bath Configuration Interaction Method: Selected Configuration Interaction with Semistochastic Perturbation Theory. *J. Chem. Theory Comput.* **2017**, *13*, 1595–1604.

(294) Holmes, A. A.; Umrigar, C. J.; Sharma, S. Excited States Using Semistochastic Heat-Bath Configuration Interaction. *J. Chem. Phys.* **2017**, *147*, 164111.

(295) Liu, W.; Hoffmann, M. R. SDS: The 'Static–Dynamic–Static' Framework for Strongly Correlated Electrons. *Theor. Chem. Acc.* **2014**, *133*, 1481.

(296) Zhang, N.; Liu, W.; Hoffmann, M. R. Further Development of iCIPT2 for Strongly Correlated Electrons. *J. Chem. Theory Comput.* **2021**, *17*, 949–964.

(297) Wang, Z.; Li, Y.; Lu, J. Coordinate Descent Full Configuration Interaction. *J. Chem. Theory Comput.* **2019**, *15*, 3558–3569.

(298) Li, Y.; Lu, J. Optimal Orbital Selection for Full Configuration Interaction (OptOrbFCI): Pursuing the Basis Set Limit under a Budget. *J. Chem. Theory Comput.* **2020**, *16*, 6207–6221.

(299) Coe, J. P. Machine Learning Configuration Interaction. *J. Chem. Theory Comput.* **2018**, *14*, 5739–5749.

(300) Coe, J. P. Machine Learning Configuration Interaction for *Ab Initio* Potential Energy Curves. *J. Chem. Theory Comput.* **2019**, *15*, 6179–6189.

(301) Schriber, J. B.; Evangelista, F. A. Communication: An Adaptive Configuration Interaction Approach for Strongly Correlated Electrons with Tunable Accuracy. *J. Chem. Phys.* **2016**, *144*, 161106.

(302) Schriber, J. B.; Evangelista, F. A. Adaptive Configuration Interaction for Computing Challenging Electronic Excited States with Tunable Accuracy. *J. Chem. Theory Comput.* **2017**, *13*, 5354–5366.

(303) Abraham, V.; Mayhall, N. J. Selected Configuration Interaction in a Basis of Cluster State Tensor Products. *J. Chem. Theory Comput.* **2020**, *16*, 6098–6113.

(304) Smith, J. E. T.; Mussard, B.; Holmes, A. A.; Sharma, S. Cheap and near Exact CASSCF with Large Active Spaces. *J. Chem. Theory Comput.* **2017**, *13*, 5468–5478.

(305) Levine, D. S.; Hait, D.; Tubman, N. M.; Lehtola, S.; Whaley, K. B.; Head-Gordon, M. CASSCF with Extremely Large Active Spaces Using the Adaptive Sampling Configuration Interaction Method. *J. Chem. Theory Comput.* **2020**, *16*, 2340–2354.

(306) Guo, Y.; Zhang, N.; Lei, Y.; Liu, W. iCISCF: Iterative Configuration Interaction-Based Multiconfigurational Self-Consistent Field Theory for Large Active Spaces. *J. Chem. Theory Comput.* **2021**, *17*, 7545–7561.

(307) Park, J. W. Near-Exact CASSCF-Level Geometry Optimization with a Large Active Space Using Adaptive Sampling Configuration Interaction Self-Consistent Field Corrected with Second-Order Perturbation Theory (ASCI-SCF-PT2). *J. Chem. Theory Comput.* **2021**, *17*, 4092–4104.

(308) Park, J. W. Second-Order Orbital Optimization with Large Active Spaces Using Adaptive Sampling Configuration Interaction (ASCI) and Its Application to Molecular Geometry Optimization. *J. Chem. Theory Comput.* **2021**, *17*, 1522–1534.

(309) Smith, J. E. T.; Lee, J.; Sharma, S. Near-Exact Nuclear Gradients of Complete Active Space Self-Consistent Field Wave Functions. *J. Chem. Phys.* **2022**, *157*, 094104.

(310) Chan, G. K.-L.; Sharma, S. The Density Matrix Renormalization Group in Quantum Chemistry. *Annu. Rev. Phys. Chem.* **2011**, *62*, 465–481.

(311) White, S. R. Density-Matrix Algorithms for Quantum Renormalization Groups. *Phys. Rev. B* **1993**, *48*, 10345–10356.

(312) White, S. R.; Martin, R. L. *Ab Initio* Quantum Chemistry Using the Density Matrix Renormalization Group. *J. Chem. Phys.* **1999**, *110*, 4127–4130.

(313) Mitrushenkov, A. O.; Fano, G.; Ortolani, F.; Linguerri, R.; Palmieri, P. Quantum Chemistry Using the Density Matrix Renormalization Group. *J. Chem. Phys.* **2001**, *115*, 6815–6821.

(314) Chan, G. K.-L.; Head-Gordon, M. Highly Correlated Calculations with a Polynomial Cost Algorithm: A Study of the Density Matrix Renormalization Group. *J. Chem. Phys.* **2002**, *116*, 4462–4476.

(315) Legeza, Ö.; Röder, J.; Hess, B. A. Controlling the Accuracy of the Density-Matrix Renormalization-Group Method: The Dynamical Block State Selection Approach. *Phys. Rev. B* **2003**, *67*, 125114.

(316) Chan, G. K.-L. An Algorithm for Large Scale Density Matrix Renormalization Group Calculations. *J. Chem. Phys.* **2004**, *120*, 3172–3178.

(317) Sharma, S.; Chan, G. K.-L. Spin-Adapted Density Matrix Renormalization Group Algorithms for Quantum Chemistry. *J. Chem. Phys.* **2012**, *136*, 124121.

(318) Wouters, S.; Neck, D. V. The Density Matrix Renormalization Group for Ab Initio Quantum Chemistry. *Eur. Phys. J. D* **2014**, *68*, 272.

(319) Yanai, T.; Kurashige, Y.; Mizukami, W.; Chalupský, J.; Lan, T. N.; Saitow, M. Density Matrix Renormalization Group for *Ab Initio* Calculations and Associated Dynamic Correlation Methods: A Review of Theory and Applications. *Int. J. Quantum Chem.* **2014**, *115*, 283–299.

(320) Knecht, S.; Hedegård, E. D.; Keller, S.; Kovyrshin, A.; Ma, Y.; Muolo, A.; Stein, C. J.; Reiher, M. New Approaches for *Ab Initio* Calculations of Molecules with Strong Electron Correlation. *Chimia* **2016**, *70*, 244.

(321) Zgid, D.; Nooijen, M. The Density Matrix Renormalization Group Self-Consistent Field Method: Orbital Optimization with the Density Matrix Renormalization Group Method in the Active Space. *J. Chem. Phys.* **2008**, *128*, 144116.

(322) Ghosh, D.; Hachmann, J.; Yanai, T.; Chan, G. K.-L. Orbital Optimization in the Density Matrix Renormalization Group, with Applications to Polyenes and β-Carotene. *J. Chem. Phys.* **2008**, *128*, 144117.

(323) Yanai, T.; Kurashige, Y.; Neuscamman, E.; Chan, G. K.-L. Multireference Quantum Chemistry through a Joint Density Matrix Renormalization Group and Canonical Transformation Theory. *J. Chem. Phys.* **2010**, *132*, 024105.

(324) Wouters, S.; Poelmans, W.; Ayers, P. W.; Neck, D. V. CheMPS2: A Free Open-Source Spin-Adapted Implementation of the Density Matrix Renormalization Group for Ab Initio Quantum Chemistry. *Comput. Phys. Commun.* **2014**, *185*, 1501–1514.

(325) Nakatani, N.; Guo, S. Density Matrix Renormalization Group (DMRG) Method As a Common Tool for Large Active-Space CASSCF/CASPT2 Calculations. *J. Chem. Phys.* **2017**, *146*, 094102.

(326) Zgid, D.; Ghosh, D.; Neuscamman, E.; Chan, G. K.-L. A Study of Cumulant Approximations to n-Electron Valence Multireference Perturbation Theory. *J. Chem. Phys.* **2009**, *130*, 194107.

(327) Kurashige, Y.; Yanai, T. Second-Order Perturbation Theory with a Density Matrix Renormalization Group Self-Consistent Field Reference Function: Theory and Application to the Study of Chromium Dimer. *J. Chem. Phys.* **2011**, *135*, 094104.

(328) Guo, S.; Watson, M. A.; Hu, W.; Sun, Q.; Chan, G. K.-L. N-Electron Valence State Perturbation Theory Based on a Density Matrix Renormalization Group Reference Function, with Applications to the Chromium Dimer and a Trimer Model of Poly(p-Phenylenevinylene). *J. Chem. Theory Comput.* **2016**, *12*, 1583–1591.

(329) Legeza, Ö.; Fáth, G. Accuracy of the Density-Matrix Renormalization-Group Method. *Phys. Rev. B* **1996**, *53*, 14349–14358.

(330) Chan, G. K.-L.; Head-Gordon, M. Exact Solution (within a Triple-Zeta, Double Polarization Basis Set) of the Electronic Schrödinger Equation for Water. *J. Chem. Phys.* **2003**, *118*, 8551–8554.

(331) Neumann, J. v. Thermodynamik Quantenmechanischer Gesamtheiten. *Nachr. Akad. Wiss. Göttingen Math.-Phys. Kl.* **1927**, *1927*, 273–291.

(332) Rissler, J.; Noack, R. M.; White, S. R. Measuring Orbital Interaction Using Quantum Information Theory. *Chem. Phys.* **2006**, *323*, 519–531.

(333) Legeza, Ö.; Sólyom, J. Optimizing the Density-Matrix Renormalization Group Method Using Quantum Information Entropy. *Phys. Rev. B* **2003**, *68*, 195116.

(334) Legeza, Ö.; Sólyom, J. Two-Site Entropy and Quantum Phase Transitions in Low-Dimensional Models. *Phys. Rev. Lett.* **2006**, *96*, 116401.

(335) Boguslawski, K.; Tecmer, P.; Legeza, Ö.; Reiher, M. Entanglement Measures for Single- and Multireference Correlation Effects. *J. Phys. Chem. Lett.* **2012**, *3*, 3129–3135.

(336) Boguslawski, K.; Tecmer, P.; Barcza, G.; Legeza, Ö.; Reiher, M. Orbital Entanglement in Bond-Formation Processes. *J. Chem. Theory Comput.* **2013**, *9*, 2959–2973.

(337) Boguslawski, K.; Tecmer, P. Orbital Entanglement in Quantum Chemistry. *Int. J. Quantum Chem.* **2014**, *115*, 1289–1295.

(338) Greer, J. C. Estimating Full Configuration Interaction Limits from a Monte Carlo Selection of the Expansion Space. *J. Chem. Phys.* **1995**, *103*, 1821–1828.

(339) Greer, J. Monte Carlo Configuration Interaction. *J. Comput. Phys.* **1998**, *146*, 181–202.

(340) Győrffy, W.; Bartlett, R. J.; Greer, J. C. Monte Carlo Configuration Interaction Predictions for the Electronic Spectra of Ne, CH_2, C_2, N_2, and H_2O Compared to Full Configuration Interaction Calculations. *J. Chem. Phys.* **2008**, *129*, 064103.

(341) Troparevsky, M. C.; Franceschetti, A. An Optimized Configuration Interaction Method for Calculating Electronic Excitations in Nanostructures. *J. Phys. Condens. Matter* **2008**, *20*, 055211.

(342) Kelly, T. P.; Perera, A.; Bartlett, R. J.; Greer, J. C. Monte Carlo Configuration Interaction with Perturbation Corrections for Dissociation Energies of First Row Diatomic Molecules: C_2, N_2, O_2, CO, and NO. *J. Chem. Phys.* **2014**, *140*, 084114.

(343) Austin, B. M.; Zubarev, D. Y.; Lester, W. A. Quantum Monte Carlo and Related Approaches. *Chem. Rev.* **2011**, *112*, 263–288.

(344) Booth, G. H.; Alavi, A. Approaching Chemical Accuracy Using Full Configuration-Interaction Quantum Monte Carlo: A Study of Ionization Potentials. *J. Chem. Phys.* **2010**, *132*, 174104.

(345) Cleland, D.; Booth, G. H.; Alavi, A. Communications: Survival of the Fittest: Accelerating Convergence in Full Configuration-Interaction Quantum Monte Carlo. *J. Chem. Phys.* **2010**, *132*, 041103.

(346) Shepherd, J. J.; Scuseria, G. E.; Spencer, J. S. Sign Problem in Full Configuration Interaction Quantum Monte Carlo: Linear and Sublinear Representation Regimes for the Exact Wave Function. *Phys. Rev. B* **2014**, *90*, 155130.

(347) Blunt, N. S.; Thom, A. J. W.; Scott, C. J. C. Preconditioning and Perturbative Estimators in Full Configuration Interaction Quantum Monte Carlo. *J. Chem. Theory Comput.* **2019**, *15*, 3537–3551.

(348) Greene, S. M.; Webber, R. J.; Weare, J.; Berkelbach, T. C. Beyond Walkers in Stochastic Quantum Chemistry: Reducing Error Using Fast Randomized Iteration. *J. Chem. Theory Comput.* **2019**, *15*, 4834–4850.

(349) Greene, S. M.; Webber, R. J.; Weare, J.; Berkelbach, T. C. Improved Fast Randomized Iteration Approach to Full Configuration Interaction. *J. Chem. Theory Comput.* **2020**, *16*, 5572–5585.

(350) Zhang, T.; Evangelista, F. A. A Deterministic Projector Configuration Interaction Approach for the Ground State of Quantum Many-Body Systems. *J. Chem. Theory Comput.* **2016**, *12*, 4326–4337.

(351) Thomas, R. E.; Sun, Q.; Alavi, A.; Booth, G. H. Stochastic Multiconfigurational Self-Consistent Field Theory. *J. Chem. Theory Comput.* **2015**, *11*, 5316–5325.

(352) Manni, G. L.; Smart, S. D.; Alavi, A. Combining the Complete Active Space Self-Consistent Field Method and the Full Configuration Interaction Quantum Monte Carlo within a Super-CI Framework, with Application to Challenging Metal-Porphyrins. *J. Chem. Theory Comput.* **2016**, *12*, 1245–1258.

(353) Dobrautz, W.; Weser, O.; Bogdanov, N. A.; Alavi, A.; Manni, G. L. Spin-Pure Stochastic-CASSCF Via GUGA-FCIQMC Applied to Iron–Sulfur Clusters. *J. Chem. Theory Comput.* **2021**, *17*, 5684–5703.

(354) Blankenbecler, R.; Scalapino, D. J.; Sugar, R. L. Monte Carlo Calculations of Coupled Boson-Fermion Systems. I. *Phys. Rev. D* **1981**, *24*, 2278–2286.

(355) Sugiyama, G.; Koonin, S. Auxiliary Field Monte-Carlo for Quantum Many-Body Ground States. *Ann. Phys.* **1986**, *168*, 1–26.

(356) Lang, G. H.; Johnson, C. W.; Koonin, S. E.; Ormand, W. E. Monte Carlo Evaluation of Path Integrals for the Nuclear Shell Model. *Phys. Rev. C* **1993**, *48*, 1518–1545.

(357) Rom, N.; Charutz, D.; Neuhauser, D. Shifted-Contour Auxiliary-Field Monte Carlo: Circumventing the Sign Difficulty for Electronic-Structure Calculations. *Chem. Phys. Lett.* **1997**, *270*, 382–386.

(358) Jacobi, S.; Baer, R. The Well-Tempered Auxiliary-Field Monte Carlo. *J. Chem. Phys.* **2003**, *120*, 43–50.

(359) Al-Saidi, W. A.; Zhang, S.; Krakauer, H. Auxiliary-Field Quantum Monte Carlo Calculations of Molecular Systems with a Gaussian Basis. *J. Chem. Phys.* **2006**, *124*, 224101.

(360) Motta, M.; Zhang, S. *Ab Initio* Computations of Molecular Systems by the Auxiliary-Field Quantum Monte Carlo Method. *Wiley Interdiscip. Rev.: Comput. Mol. Sci.* **2018**, *8*, e1364.

(361) Trotter, H. F. On the Product of Semi-Groups of Operators. *Proc. Amer. Math. Soc.* **1959**, *10*, 545–551.

(362) Suzuki, M. Relationship between d-Dimensional Quantal Spin Systems and $(d+1)$-Dimensional Ising Systems: Equivalence, Critical Exponents and Systematic Approximants of the Partition Function and Spin Correlations. *Prog. Theor. Phys.* **1976**, *56*, 1454–1469.

(363) Thouless, D. Stability Conditions and Nuclear Rotations in the Hartree-Fock Theory. *Nucl. Phys.* **1960**, *21*, 225–232.

(364) Thouless, D. Vibrational States of Nuclei in the Random Phase Approximation. *Nucl. Phys.* **1961**, *22*, 78–95.

(365) Beebe, N. H. F.; Linderberg, J. Simplifications in the Generation and Transformation of Two-Electron Integrals in Molecular Calculations. *Int. J. Quantum Chem.* **1977**, *12*, 683–705.

(366) Koch, H.; Sánchez de Merás, A.; Pedersen, T. B. Reduced Scaling in Electronic Structure Calculations Using Cholesky Decompositions. *J. Chem. Phys.* **2003**, *118*, 9481–9484.

(367) Stratonovich, R. L. On a Method of Calculating Quantum Distribution Functions. *Sov. Phys. Dokl.* **1958**, *2*, 416.

(368) Hubbard, J. Calculation of Partition Functions. *Phys. Rev. Lett.* **1959**, *3*, 77–78.

(369) Loh, E. Y.; Gubernatis, J. E.; Scalettar, R. T.; White, S. R.; Scalapino, D. J.; Sugar, R. L. Sign Problem in the Numerical Simulation of Many-Electron Systems. *Phys. Rev. B* **1990**, *41*, 9301–9307.

(370) Spencer, J. S.; Blunt, N. S.; Foulkes, W. M. The Sign Problem and Population Dynamics in the Full Configuration Interaction Quantum Monte Carlo Method. *J. Chem. Phys.* **2012**, *136*, 054110.

(371) Cleland, D. M.; Booth, G. H.; Alavi, A. A Study of Electron Affinities Using the Initiator Approach to Full Configuration Interaction Quantum Monte Carlo. *J. Chem. Phys.* **2011**, *134*, 024112.

(372) Zhang, S.; Krakauer, H. Quantum Monte Carlo Method Using Phase-Free Random Walks with Slater Determinants. *Phys. Rev. Lett.* **2003**, *90*, 136401.

(373) Ghanem, K.; Lozovoi, A. Y.; Alavi, A. Unbiasing the Initiator Approximation in Full Configuration Interaction Quantum Monte Carlo. *J. Chem. Phys.* **2019**, *151*, 224108.

(374) Mazziotti, D. A.; Erdahl, R. M. Uncertainty Relations and Reduced Density Matrices: Mapping Many-Body Quantum Mechanics onto Four Particles. *Phys. Rev. A* **2001**, *63*, 042113.

(375) Mazziotti, D. A. Variational Minimization of Atomic and Molecular Ground-State Energies Via the Two-Particle Reduced Density Matrix. *Phys. Rev. A* **2002**, *65*, 062511.

(376) Mazziotti, D. A. Realization of Quantum Chemistry without Wave Functions through First-Order Semidefinite Programming. *Phys. Rev. Lett.* **2004**, *93*, 213001.

(377) Zhao, Z.; Braams, B. J.; Fukuda, M.; Overton, M. L.; Percus, J. K. The Reduced Density Matrix Method for Electronic Structure Calculations and the Role of Three-Index Representability Conditions. *J. Chem. Phys.* **2004**, *120*, 2095–2104.

(378) Cancès, E.; Stoltz, G.; Lewin, M. The Electronic Ground-State Energy Problem: A New Reduced Density Matrix Approach. *J. Chem. Phys.* **2006**, *125*, 064101.

(379) Fukuda, M.; Braams, B. J.; Nakata, M.; Overton, M. L.; Percus, J. K.; Yamashita, M.; Zhao, Z. Large-Scale Semidefinite Programs in Electronic Structure Calculation. *Math. Program.* **2006**, *109*, 553–580.

(380) Verstichel, B.; van Aggelen, H.; Van Neck, D.; Ayers, P. W.; Bultinck, P. Variational Determination of the Second-Order Density Matrix for the Isoelectronic Series of Beryllium, Neon, and Silicon. *Phys. Rev. A* **2009**, *80*, 032508.

(381) Mazziotti, D. A. Large-Scale Semidefinite Programming for Many-Electron Quantum Mechanics. *Phys. Rev. Lett.* **2011**, *106*, 083001.

(382) Verstichel, B.; van Aggelen, H.; Van Neck, D.; Bultinck, P.; De Baerdemacker, S. A Primal–Dual Semidefinite Programming Algorithm Tailored to the Variational Determination of the Two-Body Density Matrix. *Comput. Phys. Commun.* **2011**, *182*, 1235–1244.

(383) Mazziotti, D. A. Enhanced Constraints for Accurate Lower Bounds on Many-Electron Quantum Energies from Variational Two-Electron Reduced Density Matrix Theory. *Phys. Rev. Lett.* **2016**, *117*, 153001.

(384) Mazziotti, D. A. Dual-Cone Variational Calculation of the Two-Electron Reduced Density Matrix. *Phys. Rev. A* **2020**, *102*, 052819.

(385) Löwdin, P.-O. Quantum Theory of Many-Particle Systems. I. Physical Interpretations by Means of Density Matrices, Natural Spin-Orbitals, and Convergence Problems in the Method of Configurational Interaction. *Phys. Rev.* **1955**, *97*, 1474–1489.

(386) Tredgold, R. H. Density Matrix and the Many-Body Problem. *Phys. Rev.* **1957**, *105*, 1421–1423.

(387) Coleman, A. J. Structure of Fermion Density Matrices. *Rev. Mod. Phys* **1963**, *35*, 668–686.

(388) Garrod, C.; Percus, J. K. Reduction of the *N*-Particle Variational Problem. *J. Math. Phys.* **1964**, *5*, 1756–1776.

(389) Gidofalvi, G.; Mazziotti, D. A. Active-Space Two-Electron Reduced-Density-Matrix Method: Complete Active-Space Calculations without Diagonalization of the *N*-Electron Hamiltonian. *J. Chem. Phys.* **2008**, *129*, 134108.

(390) Fosso-Tande, J.; Nguyen, T.-S.; Gidofalvi, G.; DePrince, A. E. Large-Scale Variational Two-Electron Reduced-Density-Matrix-Driven Complete Active Space Self-Consistent Field Methods. *J. Chem. Theory Comput.* **2016**, *12*, 2260–2271.

(391) Mullinax, J. W.; Maradzike, E.; Koulias, L. N.; Mostafanejad, M.; Epifanovsky, E.; Gidofalvi, G.; DePrince, A. E. Heterogeneous CPU + GPU Algorithm for Variational Two-Electron Reduced-Density Matrix-Driven Complete Active-Space Self-Consistent Field Theory. *J. Chem. Theory Comput.* **2019**, *15*, 6164–6178.

(392) Van Aggelen, H.; Bultinck, P.; Verstichel, B.; Van Neck, D.; Ayers, P. W. Incorrect Diatomic Dissociation in Variational Reduced Density Matrix Theory Arises from the Flawed Description of Fractionally Charged Atoms. *Phys. Chem. Chem. Phys.* **2009**, *11*, 5558.

(393) Verstichel, B.; van Aggelen, H.; Van Neck, D.; Ayers, P. W.; Bultinck, P. Subsystem Constraints in Variational Second Order Density Matrix Optimization: Curing the Dissociative Behavior. *J. Chem. Phys.* **2010**, *132*, 114113.

(394) Van Aggelen, H.; Verstichel, B.; Bultinck, P.; Neck, D. V.; Ayers, P. W.; Cooper, D. L. Variational Second Order Density Matrix Study of F_3^-: Importance of Subspace Constraints for Size-Consistency. *J. Chem. Phys.* **2011**, *134*, 054115.

(395) Deustua, J. E.; Shen, J.; Piecuch, P. Converging High-Level Coupled-Cluster Energetics by Monte Carlo Sampling and Moment Expansions. *Phys. Rev. Lett.* **2017**, *119*, 223003.

(396) Deustua, J. E.; Magoulas, I.; Shen, J.; Piecuch, P. Communication: Approaching Exact Quantum Chemistry by Cluster Analysis of Full Configuration Interaction Quantum Monte Carlo Wave Functions. *J. Chem. Phys.* **2018**, *149*, 151101.

(397) Deustua, J. E.; Yuwono, S. H.; Shen, J.; Piecuch, P. Accurate Excited-State Energetics by a Combination of Monte Carlo Sampling and Equation-Of-Motion Coupled-Cluster Computations. *J. Chem. Phys.* **2019**, *150*, 111101.

(398) Yuwono, S. H.; Chakraborty, A.; Emiliano Deustua, J.; Shen, J.; Piecuch, P. Accelerating Convergence of Equation-Of-Motion Coupled-Cluster Computations Using the Semi-Stochastic CC(P;Q) Formalism. *Mol. Phys.* **2020**, *118*, e1817592.

(399) Xu, E.; Uejima, M.; Ten-no, S. L. Full Coupled-Cluster Reduction for Accurate Description of Strong Electron Correlation. *Phys. Rev. Lett.* **2018**, *121*, 113001.

(400) Xu, E.; Uejima, M.; Ten-no, S. L. Towards Near-Exact Solutions of Molecular Electronic Structure: Full Coupled-Cluster Reduction with a Second-Order Perturbative Correction. *J. Phys. Chem. Lett.* **2020**, *11*, 9775–9780.

(401) Slater, J. C. Atomic Shielding Constants. *Phys. Rev.* **1930**, *36*, 57–64.

(402) Boys, S. F. Electronic Wave Functions - I. A General Method of Calculation for the Stationary States of Any Molecular System. *Proc. R. Soc. A* **1950**, *200*, 542–554.

(403) Hehre, W. J.; Stewart, R. F.; Pople, J. A. Self-Consistent Molecular-Orbital Methods. I. Use of Gaussian Expansions of Slater-Type Atomic Orbitals. *J. Chem. Phys.* **1969**, *51*, 2657–2664.

(404) Dunning, T. H. Gaussian Basis Sets for Use in Correlated Molecular Calculations. I. The Atoms Boron through Neon and Hydrogen. *J. Chem. Phys.* **1989**, *90*, 1007–1023.

(405) Woon, D. E.; Dunning, T. H. Gaussian Basis Sets for Use in Correlated Molecular Calculations. III. The Atoms Aluminum through Argon. *J. Chem. Phys.* **1993**, *98*, 1358–1371.

(406) Wilson, A. K.; Woon, D. E.; Peterson, K. A.; Dunning, T. H. Gaussian Basis Sets for Use in Correlated Molecular Calculations. Ix. The Atoms Gallium through Krypton. *J. Chem. Phys.* **1999**, *110*, 7667–7676.

(407) Balabanov, N. B.; Peterson, K. A. Systematically Convergent Basis Sets for Transition Metals. I. All-Electron Correlation Consistent Basis Sets for the 3d Elements Sc–Zn. *J. Chem. Phys.* **2005**, *123*, 064107.

(408) Schütz, M.; Werner, H.-J. Local Perturbative Triples Correction (T) with Linear Cost Scaling. *Chem. Phys. Lett.* **2000**, *318*, 370–378.

(409) Bender, C. F.; Davidson, E. R. A Natural Orbital Based Energy Calculation for Helium Hydride and Lithium Hydride. *J. Phys. Chem* **1966**, *70*, 2675–2685.

(410) Jensen, H. J. Aa.; Jørgensen, P.; Ågren, H.; Olsen, J. Second-Order Møller–Plesset Perturbation Theory As a Configuration and Orbital Generator in Multiconfiguration Self-Consistent Field Calculations. *J. Chem. Phys.* **1988**, *88*, 3834–3839.

(411) Wouters, S.; Bogaerts, T.; Van Der Voort, P.; Van Speybroeck, V.; Van Neck, D. Communication: DMRG-SCF Study of the Singlet, Triplet, and Quintet States of Oxo-Mn(salen). *J. Chem. Phys.* **2014**, *140*, 241103.

(412) Khedkar, A.; Roemelt, M. Active Space Selection Based on Natural Orbital Occupation Numbers from *n*-Electron Valence Perturbation Theory. *J. Chem. Theory Comput.* **2019**, *15*, 3522–3536.

(413) Burke, L. A.; Leroy, G.; Daudel, R.; Stephens, M. E. Absolute Overlap and Second Moment Dispersions As Measures of Localizability in the Spatial and Energetic Methods. *Chem. Phys. Lett.* **1978**, *57*, 15–21.

(414) Jansík, B.; Høst, S.; Kristensen, K.; Jørgensen, P. Local Orbitals by Minimizing Powers of the Orbital Variance. *J. Chem. Phys.* **2011**, *134*, 194104.

(415) Høyvik, I.-M.; Jansík, B.; Jørgensen, P. Orbital Localization Using Fourth Central Moment Minimization. *J. Chem. Phys.* **2012**, *137*, 224114.

(416) Pulay, P. Localizability of Dynamic Electron Correlation. *Chem. Phys. Lett.* **1983**, *100*, 151–154.

(417) Pulay, P.; Saebø, S. Orbital-Invariant Formulation and Second-Order Gradient Evaluation in Møller-Plesset Perturbation Theory. *Theor. Chim. Acta* **1986**, *69*, 357–368.

(418) Boughton, J. W.; Pulay, P. Comparison of the Boys and Pipek–Mezey Localizations in the Local Correlation Approach and Automatic Virtual Basis Selection. *J. Comput. Chem.* **1993**, *14*, 736–740.

(419) Couty, M.; Bayse, C. A.; Hall, M. B. Extremely localized molecular orbitals (ELMO): a non-orthogonal Hartree-Fock method. *Theor. Chim. Acta* **1997**, *97*, 96–109.

(420) Schütz, M.; Hetzer, G.; Werner, H.-J. Low-Order Scaling Local Electron Correlation Methods. I. Linear Scaling Local MP2. *J. Chem. Phys.* **1999**, *111*, 5691–5705.

(421) Paulus, B.; Rościszewski, K.; Stoll, H.; Birkenheuer, U. *Ab Initio* Incremental Correlation Treatment with Non-Orthogonal Localized Orbitals. *Phys. Chem. Chem. Phys.* **2003**, *5*, 5523–5529.

(422) Christiansen, O.; Manninen, P.; Jørgensen, P.; Olsen, J. Coupled-Cluster Theory in a Projected Atomic Orbital Basis. *J. Chem. Phys.* **2006**, *124*, 084103.

(423) Yang, J.; Kurashige, Y.; Manby, F. R.; Chan, G. K. L. Tensor Factorizations of Local Second-Order Møller–Plesset Theory. *J. Chem. Phys.* **2011**, *134*, 044123.

(424) Yang, J.; Chan, G. K.-L.; Manby, F. R.; Schütz, M.; Werner, H.-J. The Orbital-Specific-Virtual Local Coupled Cluster Singles and Doubles Method. *J. Chem. Phys.* **2012**, *136*, 144105.

(425) Riplinger, C.; Neese, F. An Efficient and near Linear Scaling Pair Natural Orbital Based Local Coupled Cluster Method. *J. Chem. Phys.* **2013**, *138*, 034106.

(426) Riplinger, C.; Sandhoefer, B.; Hansen, A.; Neese, F. Natural Triple Excitations in Local Coupled Cluster Calculations with Pair Natural Orbitals. *J. Chem. Phys.* **2013**, *139*, 134101.

(427) Høyvik, I.-M.; Kristensen, K.; Kjærgaard, T.; Jørgensen, P., A Perspective on the Localizability of Hartree–Fock Orbitals In *Thom H. Dunning, Jr.* Springer: Berlin, 2013, pp 287–296.

(428) Foster, J. M.; Boys, S. F. Canonical Configurational Interaction Procedure. *Rev. Mod. Phys* **1960**, *32*, 300–302.

(429) Pipek, J.; Mezey, P. G. A Fast Intrinsic Localization Procedure Applicable for *Ab Initio* and Semiempirical Linear Combination of Atomic Orbital Wave Functions. *J. Chem. Phys.* **1989**, *90*, 4916–4926.

(430) Høyvik, I.-M.; Jørgensen, P. Characterization and Generation of Local Occupied and Virtual Hartree–Fock Orbitals. *Chem. Rev.* **2016**, *116*, 3306–3327.

(431) Pipek, J. Localization Measure and Maximum Delocalization in Molecular Systems. *Int. J. Quantum Chem.* **1989**, *36*, 487–501.

(432) Mulliken, R. S. Electronic Population Analysis on LCAO–MO Molecular Wave Functions. I. *J. Chem. Phys.* **1955**, *23*, 1833–1840.

(433) Löwdin, P.-O. On the Non-Orthogonality Problem Connected with the Use of Atomic Wave Functions in the Theory of Molecules and Crystals. *J. Chem. Phys.* **1950**, *18*, 365–375.

(434) Høyvik, I.-M.; Jansik, B.; Jørgensen, P. Pipek–Mezey Localization of Occupied and Virtual Orbitals. *J. Comput. Chem.* **2013**, *34*, 1456–1462.

(435) Sun, Q.; Chan, G. K.-L. Exact and Optimal Quantum Mechanics/Molecular Mechanics Boundaries. *J. Chem. Theory Comput.* **2014**, *10*, 3784–3790.

(436) Reed, A. E.; Weinhold, F. Natural Bond Orbital Analysis of Near-Hartree–Fock Water Dimer. *J. Chem. Phys.* **1983**, *78*, 4066–4073.

(437) Lehtola, S.; Jónsson, H. Pipek–Mezey Orbital Localization Using Various Partial Charge Estimates. *J. Chem. Theory Comput.* **2014**, *10*, 642–649.

(438) Edmiston, C.; Ruedenberg, K. Localized Atomic and Molecular Orbitals. *Rev. Mod. Phys* **1963**, *35*, 457–464.

(439) Edmiston, C.; Ruedenberg, K. Localized Atomic and Molecular Orbitals. II. *J. Chem. Phys.* **1965**, *43*, S97–S116.

(440) Subotnik, J. E.; Shao, Y.; Liang, W.; Head-Gordon, M. An Efficient Method for Calculating Maxima of Homogeneous Functions of Orthogonal Matrices: Applications to Localized Occupied Orbitals. *J. Chem. Phys.* **2004**, *121*, 9220–9229.

(441) Subotnik, J. E.; Sodt, A.; Head-Gordon, M. Localized Orbital Theory and Ammonia Triborane. *Phys. Chem. Chem. Phys.* **2007**, *9*, 5522.

(442) Folkestad, S. D.; Matveeva, R.; Høyvik, I.-M.; Koch, H. Implementation of Occupied and Virtual Edmiston–Ruedenberg Orbitals Using Cholesky Decomposed Integrals. *J. Chem. Theory Comput.* **2022**, *18*, 4733–4744.

(443) Lykos, P.; Pratt, G. W. Discussion on the Hartree-Fock Approximation. *Rev. Mod. Phys.* **1963**, *35*, 496–501.

(444) Čížek, J.; Paldus, J. Stability Conditions for the Solutions of the Hartree—Fock Equations for Atomic and Molecular Systems. Application to the Pi-Electron Model of Cyclic Polyenes. *J. Chem. Phys.* **1967**, *47*, 3976–3985.

(445) Paldus, J.; Čížek, J. Hartree–Fock Stability and Symmetry Breaking: Oxygen Doubly Negative Ion. *Can. J. Chemistry* **1985**, *63*, 1803–1811.

(446) Davidson, E. R. Use of Double Cosets in Constructing Integrals Over Symmetry Orbitals. *J. Chem. Phys.* **1975**, *62*, 400–403.

(447) Tinkham, M., *Group Theory and Quantum Mechanics*; McGraw-Hill Book Company, Inc.: New York, 1964; 340 pp.

(448) Harris, C. R. et al. Array Programming with Numpy. *Nature* **2020**, *585*, 357–362.

(449) Sun, Q.; Berkelbach, T. C.; Blunt, N. S.; Booth, G. H.; Guo, S.; Li, Z.; Liu, J.; McClain, J. D.; Sayfutyarova, E. R.; Sharma, S.; Wouters, S.; Chan, G. K.-L. PySCF: The Python-Based Simulations of Chemistry Framework. *Wiley Interdiscip. Rev.: Comput. Mol. Sci.* **2017**, *8*, e1340.

(450) Sun, Q. et al. Recent Developments in the PySCF Program Package. *J. Chem. Phys.* **2020**, *153*, 024109.

(451) Stanton, J. F.; Gauss, J.; Cheng, L.; Harding, M. E.; Matthews, D. A.; Szalay, P. G. CFOUR, Coupled-Cluster techniques for Computational Chemistry, a quantum-chemical program package, With contributions from A. Asthana, A.A. Auer, R.J. Bartlett, U. Benedikt, C. Berger, D.E. Bernholdt, S. Blaschke, Y. J. Bomble, S. Burger, O. Christiansen, D. Datta, F. Engel, R. Faber, J. Greiner, M. Heckert, O. Heun, M. Hilgenberg, C. Huber, T.-C. Jagau, D. Jonsson, J. Jusélius, T. Kirsch, M.-P. Kitsaras, K. Klein, G.M. Kopper, W.J. Lauderdale, F. Lipparini, J. Liu, T. Metzroth, L. Monzel, L.A. Mück, D.P. O'Neill, T. Nottoli, J. Oswald, D.R. Price, E. Prochnow, C. Puzzarini, K. Ruud, F. Schiffmann, W. Schwalbach, C. Simmons, S. Stopkowicz, A. Tajti, T. Uhlířová, J. Vázquez, F. Wang, J.D. Watts, P. Yergün. C. Zhang, X. Zheng, and the integral packages MOLECULE (J. Almlöf and P.R. Taylor), PROPS (P.R. Taylor), ABACUS (T. Helgaker, H.J. Aa. Jensen, P. Jørgensen, and J. Olsen), and ECP routines by A. V. Mitin and C. van Wüllen. For the current version, see http://www.cfour.de.

(452) Matthews, D. A.; Cheng, L.; Harding, M. E.; Lipparini, F.; Stopkowicz, S.; Jagau, T.-C.; Szalay, P. G.; Gauss, J.; Stanton, J. F. Coupled-Cluster Techniques for Computational Chemistry: The `CFOUR` Program Package. *J. Chem. Phys.* **2020**, *152*, 214108.

(453) MPI Forum: MPI: A Message Passing Interface Standard, See: `http://www.mpi-forum.org`.

(454) Dalcín, L.; Paz, R.; Storti, M. MPI for Python. *J. Parallel Distr. Com.* **2005**, *65*, 1108–1115.

(455) Dalcín, L.; Paz, R.; Storti, M.; D'Elía, J. MPI for Python: Performance Improvements and MPI-2 Extensions. *J. Parallel Distr. Com.* **2008**, *68*, 655–662.

(456) Dalcin, L. D.; Paz, R. R.; Kler, P. A.; Cosimo, A. Parallel Distributed Computing Using Python. *Adv. Water Resour.* **2011**, *34*, 1124–1139.

(457) Dalcin, L.; Fang, Y.-L. L. MPI4py: Status Update After 12 Years of Development. *Comput. Sci. Eng.* **2021**, *23*, 47–54.

(458) Edmiston, C.; Krauss, M. Pseudonatural Orbitals As a Basis for the Superposition of Configurations. I. He_2^+. *J. Chem. Phys.* **1966**, *45*, 1833–1839.

(459) Barr, T. L.; Davidson, E. R. Nature of the Configuration-Interaction Method In *Ab Initio* calculations. I. Ne Ground State. *Phys. Rev. A* **1970**, *1*, 644–658.

(460) Sosa, C.; Geertsen, J.; Trucks, G. W.; Bartlett, R. J.; Franz, J. A. Selection of the Reduced Virtual Space for Correlated Calculations. An Application to the Energy and Dipole Moment of H_2O. *Chem. Phys. Lett.* **1989**, *159*, 148–154.

(461) Taube, A. G.; Bartlett, R. J. Frozen Natural Orbital Coupled-Cluster Theory: Forces and Application to Decomposition of Nitroethane. *J. Chem. Phys.* **2008**, *128*, 164101.

(462) Fales, B. S.; Hohenstein, E. G.; Levine, B. G. Robust and Efficient Spin Purification for Determinantal Configuration Interaction. *J. Chem. Theory Comput.* **2017**, *13*, 4162–4172.

(463) Cmake, See: `https://cmake.org/`.

(464) Krylov, A. I.; Sherrill, C. D.; Byrd, E. F. C.; Head-Gordon, M. Size-Consistent Wave Functions for Nondynamical Correlation Energy: The Valence Active Space Optimized Orbital Coupled-Cluster Doubles Model. *J. Chem. Phys.* **1998**, *109*, 10669–10678.

(465) Parkhill, J. A.; Head-Gordon, M. A Truncation Hierarchy of Coupled Cluster Models of Strongly Correlated Systems Based on Perfect-Pairing References: The Singles+Doubles Models. *J. Chem. Phys.* **2010**, *133*, 124102.

(466) Parkhill, J. A.; Head-Gordon, M. A Tractable and Accurate Electronic Structure Method for Static Correlations: The Perfect Hextuples Model. *J. Chem. Phys.* **2010**, *133*, 024103.

(467) Ma, D.; Li Manni, G.; Gagliardi, L. The Generalized Active Space Concept in Multiconfigurational Self-Consistent Field Methods. *J. Chem. Phys.* **2011**, *135*, 044128.

(468) Parker, S. M.; Seideman, T.; Ratner, M. A.; Shiozaki, T. Communication: Active-Space Decomposition for Molecular Dimers. *J. Chem. Phys.* **2013**, *139*, 021108.

(469) Parker, S. M.; Shiozaki, T. Communication: Active Space Decomposition with Multiple Sites: Density Matrix Renormalization Group Algorithm. *J. Chem. Phys.* **2014**, *141*, 211102.

(470) Jiménez-Hoyos, C. A.; Scuseria, G. E. Cluster-Based Mean-Field and Perturbative Description of Strongly Correlated Fermion Systems: Application to the One- and Two-Dimensional Hubbard Model. *Phys. Rev. B* **2015**, *92*, 085101.

(471) Kim, I.; Parker, S. M.; Shiozaki, T. Orbital Optimization in the Active Space Decomposition Model. *J. Chem. Theory Comput.* **2015**, *11*, 3636–3642.

(472) Lehtola, S.; Parkhill, J.; Head-Gordon, M. Orbital Optimisation in the Perfect Pairing Hierarchy: Applications to Full-Valence Calculations on Linear Polyacenes. *Mol. Phys.* **2017**, *116*, 547–560.

(473) Hermes, M. R.; Gagliardi, L. Multiconfigurational Self-Consistent Field Theory with Density Matrix Embedding: The Localized Active Space Self-Consistent Field Method. *J. Chem. Theory Comput.* **2019**, *15*, 972–986.

(474) Hermes, M. R.; Pandharkar, R.; Gagliardi, L. Variational Localized Active Space Self-Consistent Field Method. *J. Chem. Theory Comput.* **2020**, *16*, 4923–4937.

(475) Pandharkar, R.; Hermes, M. R.; Cramer, C. J.; Gagliardi, L. Localized Active Space-State Interaction: A Multireference Method for Chemical Insight. *J. Chem. Theory Comput.* **2022**, *18*, 6557–6566.

(476) Greiner, J.; Gianni, I.; Nottoli, T.; Lipparini, F.; Eriksen, J. J.; Gauss, J. MBE-CASSCF Approach for the Accurate Treatment of Large Active Spaces. *J. Chem. Theory Comput.* **2024**, *20*, 4663–4675.

(477) Hellmann, H., *Einführung in die Quantenchemie*; Franz Deuticke: Leipzig, 1937.

(478) Feynman, R. P. Forces in Molecules. *Phys. Rev.* **1939**, *56*, 340–343.

(479) Yao, Y.; Umrigar, C. J. Orbital Optimization in Selected Configuration Interaction Methods. *J. Chem. Theory Comput.* **2021**, *17*, 4183–4194.

(480) C Foreign Function Interface for Python, See: `https://github.com/python-cffi/cffi`.

(481) Radoń, M. Spin-State Energetics of Heme-Related Models from DFT and Coupled Cluster Calculations. *J. Chem. Theory Comput.* **2014**, *10*, 2306–2321.

(482) Tarrago, M.; Römelt, C.; Nehrkorn, J.; Schnegg, A.; Neese, F.; Bill, E.; Ye, S. Experimental and Theoretical Evidence for an Unusual Almost Triply Degenerate Electronic Ground State of Ferrous Tetraphenylporphyrin. *Inorg. Chem.* **2021**, *60*, 4966–4985.

(483) Collman, J. P.; Hoard, J. L.; Kim, N.; Lang, G.; Reed, C. A. Synthesis, Stereochemistry, and Structure-Related Properties of α,β,γ,δ-Tetraphenylporphinatoiron(II). *J. Am. Chem. Soc.* **1975**, *97*, 2676–2681.

(484) Goff, H.; La Mar, G. N.; Reed, C. A. Nuclear Magnetic Resonance Investigation of Magnetic and Electronic Properties of "Intermediate Spin" Ferrous Porphyrin Complexes. *J. Am. Chem. Soc.* **1977**, *99*, 3641–3646.

(485) Lang, G.; Spartalian, K.; Reed, C. A.; Collman, J. P. Mössbauer Effect Study of the Magnetic Properties of $S = 1$ Ferrous Tetraphenylporphyrin. *J. Chem. Phys.* **1978**, *69*, 5424–5427.

(486) Boyd, P. D. W.; Buckingham, D. A.; McMeeking, R. F.; Mitra, S. Paramagnetic Anisotropy, Average Magnetic Susceptibility, and Electronic Structure of Intermediate-Spin $S = 1$ (5,10,15,20-Tetraphenylporphyrin)iron(II). *Inorg. Chem.* **1979**, *18*, 3585–3591.

(487) Kitagawa, T.; Teraoka, J. The Resonance Raman Spectra of Intermediate-Spin Ferrous Porphyrin. *Chem. Phys. Lett.* **1979**, *63*, 443–446.

(488) Mispelter, J.; Momenteau, M.; Lhoste, J. M. Proton Magnetic Resonance Characterization of the Intermediate ($S = 1$) Spin State of Ferrous Porphyrins. *J. Chem. Phys.* **1980**, *72*, 1003–1012.

(489) Choe, Y.-K.; Hashimoto, T.; Nakano, H.; Hirao, K. Theoretical Study of the Electronic Ground State of Iron(II) Porphine. *Chem. Phys. Lett.* **1998**, *295*, 380–388.

(490) Choe, Y.-K.; Nakajima, T.; Hirao, K.; Lindh, R. Theoretical Study of the Electronic Ground State of Iron(II) Porphine. II. *J. Chem. Phys.* **1999**, *111*, 3837–3845.

(491) Webb, L. E.; Fleischer, E. B. Crystal Structure of Porphine. *J. Chem. Phys.* **1965**, *43*, 3100–3111.

(492) Nagashima, U.; Takada, T.; Ohno, K. *Ab initio* SCF-CI Calculation on Free Base Porphin and Chlorin; Theoretical Analysis on Intensities of the Absorption Spectra. *J. Chem. Phys.* **1986**, *85*, 4524–4529.

(493) Roos, B. O.; Lindh, R.; Malmqvist, P.-Å.; Veryazov, V.; Widmark, P.-O. Main Group Atoms and Dimers Studied with a New Relativistic ANO Basis Set. *J. Phys. Chem. A* **2003**, *108*, 2851–2858.

(494) Roos, B. O.; Lindh, R.; Malmqvist, P.-Å.; Veryazov, V.; Widmark, P.-O. New Relativistic ANO Basis Sets for Transition Metal Atoms. *J. Phys. Chem. A* **2005**, *109*, 6575–6579.

(495) Stemmle, C.; Paulus, B. Quantification of Electron Correlation Effects: Quantum Information Theory vs Method of Increments. *Int. J. Quantum Chem.* **2019**, *119*, e26007.

(496) Greiner, J.; Gauss, J.; Eriksen, J. J. Error Control and Automatic Detection of Reference Active Spaces in Many-Body Expanded Full Configuration Interaction. *J. Phys. Chem. A* **2024**, *128*, 6806–6818.

(497) Uhlmann, A. The "Transition Probability" in the State Space of a *-Algebra. *Rep. Math. Phys.* **1976**, *9*, 273–279.

(498) Alberti, P. M. A Note on the Transition Probability Over C*-Algebras. *Lett. Math. Phys.* **1983**, *7*, 25–32.

(499) Peres, A. Stability of Quantum Motion in Chaotic and Regular Systems. *Phys. Rev. A* **1984**, *30*, 1610–1615.

(500) Jozsa, R. Fidelity for Mixed Quantum States. *J. Mod. Optic.* **1994**, *41*, 2315–2323.

(501) Boguslawski, K.; Marti, K. H.; Reiher, M. Construction of CASCI-Type Wave Functions for Very Large Active Spaces. *J. Chem. Phys.* **2011**, *134*, 224101.

(502) Butscher, W.; Kammer, W. Modification of Davidson's Method for the Calculation of Eigenvalues and Eigenvectors of Large Real-Symmetric Matrices: "Root Homing Procedure". *J. Comput. Phys.* **1976**, *20*, 313–325.

(503) Zhai, H.; Larsson, H. R.; Lee, S.; Cui, Z.-H.; Zhu, T.; Sun, C.; Peng, L.; Peng, R.; Liao, K.; Tölle, J.; Yang, J.; Li, S.; Chan, G. K.-L. `Block2`: A Comprehensive Open Source Framework to Develop and Apply State-Of-The-Art DMRG Algorithms in Electronic Structure and Beyond. *J. Chem. Phys.* **2023**, *159*, 234801.

(504) Kirkpatrick, S.; Gelatt, C. D.; Vecchi, M. P. Optimization by Simulated Annealing. *Science* **1983**, *220*, 671–680.

(505) Ben-Ameur, W. Computing the Initial Temperature of Simulated Annealing. *Comput. Optim. Appl.* **2004**, *29*, 369–385.

(506) Vahtras, O.; Almlöf, J.; Feyereisen, M. Integral Approximations for LCAO-SCF Calculations. *Chem. Phys. Lett.* **1993**, *213*, 514–518.

(507) Feyereisen, M.; Fitzgerald, G.; Komornicki, A. Use of Approximate Integrals in Ab Initio Theory. An Application in MP2 Energy Calculations. *Chem. Phys. Lett.* **1993**, *208*, 359–363.

(508) Weigend, F.; Häser, M. RI-MP2: First Derivatives and Global Consistency. *Theor. Chem. Acc.* **1997**, *97*, 331–340.

(509) Weigend, F.; Häser, M.; Patzelt, H.; Ahlrichs, R. RI-MP2: Optimized Auxiliary Basis Sets and Demonstration of Efficiency. *Chem. Phys. Lett.* **1998**, *294*, 143–152.

(510) Rosenblatt, M. Remarks on Some Nonparametric Estimates of a Density Function. *Ann. Math. Stat.* **1956**, *27*, 832–837.

(511) Parzen, E. On Estimation of a Probability Density Function and Mode. *Ann. Math. Stat.* **1962**, *33*, 1065–1076.

(512) Virtanen, P. et al. SciPy 1.0: Fundamental Algorithms for Scientific Computing in Python. *Nat. Methods* **2020**, *17*, 261–272.

(513) Scott, D. W., *Multivariate Density Estimation: Theory, Practice, and Visualization*; Wiley: Chichester, 1992.

(514) Chilkuri, V. G.; Neese, F. Comparison of Many-Particle Representations for Selected Configuration Interaction: II. Numerical Benchmark Calculations. *J. Chem. Theory Comput.* **2021**, *17*, 2868–2885.

(515) Weigend, F.; Ahlrichs, R. Balanced Basis Sets of Split Valence, Triple Zeta Valence and Quadruple Zeta Valence Quality for H to Rn: Design and Assessment of Accuracy. *Phys. Chem. Chem. Phys.* **2005**, *7*, 3297.

(516) Cox, D.; Oakes, D., *Analysis of Survival Data*; Chapman and Hall/CRC: Boca Raton, 2018.

(517) Booth, G. H.; Cleland, D.; Thom, A. J. W.; Alavi, A. Breaking the Carbon Dimer: The Challenges of Multiple Bond Dissociation with Full Configuration Interaction Quantum Monte Carlo Methods. *J. Chem. Phys.* **2011**, *135*, 084104.

(518) Greiner, J.; Eriksen, J. J. Symmetrization of Localized Molecular Orbitals. *J. Phys. Chem. A* **2023**, *127*, 3535–3542.

(519) Greiner, J.; Gauss, J.; Eriksen, J. J. Exploiting Non-Abelian Point-Group Symmetry to Estimate the Exact Ground-State Correlation Energy of Benzene in a Polarized Split-Valence Triple-Zeta Basis Set. *J. Phys. Chem. Lett.* **2024**, *15*, 9881–9887.

(520) Lennard-Jones, J. The Molecular Orbital Theory of Chemical Valency. II. Equivalent Orbitals in Molecules of Known Symmetry. *Proc. R. Soc. London Ser. A* **1949**, *198*, 14–26.

(521) Subotnik, J. E.; Dutoi, A. D.; Head-Gordon, M. Fast Localized Orthonormal Virtual Orbitals Which Depend Smoothly on Nuclear Coordinates. *J. Chem. Phys.* **2005**, *123*, 114108.

(522) Lehtola, S.; Jónsson, H. Unitary Optimization of Localized Molecular Orbitals. *J. Chem. Theory Comput.* **2013**, *9*, 5365–5372.

(523) Greiner, J.; Eriksen, J. J. SymLo: Code for the Symmetrization of Localized Orbitals, See: `https://github.com/jonas-greiner/symlo`.

(524) Wigner, E., *Gruppentheorie und Ihre Anwendung auf die Quantenmechanik der Atomspektren*; Vieweg+Teubner Verlag: 1931.

(525) Cuthill, E.; McKee, J. In *Proceedings of the 1969 24th National Conference*, ACM Press: New York, 1969.

(526) George, A.; Liu, J. W., *Computer Solution of Large Sparse Positive Definite Systems*; Prentice-Hall: Englewood Cliffs, 1981, p 324.

(527) Sun, Q. Co-Iterative Augmented Hessian Method for Orbital Optimization. **2016**, DOI: `10.48550/ARXIV.1610.08423`.

(528) Ziółkowski, M.; Jansík, B.; Jørgensen, P.; Olsen, J. Maximum Locality in Occupied and Virtual Orbital Spaces Using a Least-Change Strategy. *J. Chem. Phys.* **2009**, *131*, 124112.

(529) Lee, J.; Malone, F. D.; Reichman, D. R. The Performance of Phaseless Auxiliary-Field Quantum Monte Carlo on the Ground State Electronic Energy of Benzene. *J. Chem. Phys.* **2020**, *153*, 126101.

(530) Loos, P.-F.; Damour, Y.; Scemama, A. The Performance of CIPSI on the Ground State Electronic Energy of Benzene. *J. Chem. Phys.* **2020**, *153*, 176101.

(531) Rask, A. E.; Zimmerman, P. M. Toward Full Configuration Interaction for Transition-Metal Complexes. *J. Phys. Chem. A* **2021**, *125*, 1598–1609.

(532) Schreiber, M.; Silva-Junior, M. R.; Sauer, S. P. A.; Thiel, W. Benchmarks for Electronically Excited States: CASPT2, CC2, CCSD, and CC3. *J. Chem. Phys.* **2008**, *128*, 134110.

(533) Eriksen, J. J.; Matthews, D. A.; Jørgensen, P.; Gauss, J. Communication: The Performance of Non-Iterative Coupled Cluster Quadruples Models. *J. Chem. Phys.* **2015**, *143*, 041101.

List of Publications

- Greiner, J.; Eriksen, J. J. Symmetrization of Localized Molecular Orbitals. *J. Phys. Chem. A* **2023**, *127*, 3535–3542
- Greiner, J.; Gianni, I.; Nottoli, T.; Lipparini, F.; Eriksen, J. J.; Gauss, J. MBE-CASSCF Approach for the Accurate Treatment of Large Active Spaces. *J. Chem. Theory Comput.* **2024**, *20*, 4663–4675
- Greiner, J.; Gauss, J.; Eriksen, J. J. Error Control and Automatic Detection of Reference Active Spaces in Many-Body Expanded Full Configuration Interaction. *J. Phys. Chem. A* **2024**, *128*, 6806–6818
- Greiner, J.; Gauss, J.; Eriksen, J. J. Exploiting Non-Abelian Point-Group Symmetry to Estimate the Exact Ground-State Correlation Energy of Benzene in a Polarized Split-Valence Triple-Zeta Basis Set. *J. Phys. Chem. Lett.* **2024**, *15*, 9881–9887